

# **Analysis of corroded steel structures with local fatigue approaches**

- Untersuchung von korrodierten Stahlkonstruktionen  
mit lokalen Ermüdungskonzepten -

Von der Fakultät für Bauingenieurwesen und Geodäsie der  
Gottfried Wilhelm Leibniz Universität Hannover  
zur Erlangung des akademischen Grades

Doktor der Ingenieurwissenschaften

- Dr.-Ing -

genehmigte Dissertation  
von

Mohammad Sulaiman Shojai, M. Sc.  
geboren am 27. September 1991 in Kabul (Afghanistan)

2024

Doctoral Committee:

1st Examiner: Prof. Dr.-Ing. Peter Schaumann

2nd Examiner: Prof. DSc. (Tech.) Sören Ehlers

Commission member: Prof. Dr. sc. ETH Elyas Ghafoori

Chairman: Prof. Dr.-Ing. Fadi Aldakheel

Day of submission: 24.10.2023

Day of examination: 09.02.2024

---

## Acknowledgements

This dissertation was written during my research activities at the Institute for Steel Construction of Leibniz University Hannover. Like many other projects in our lives, this work is an outcome of close collaborative efforts of different people. Hence, I would like to express my deepest gratitude and appreciation to the following individuals and groups who have contributed significantly to the successful completion of my doctoral journey:

Prof. Dr.-Ing. Peter Schaumann, the former head of the Institute of Steel Construction and my supervisor, whose support, guidance, and mentorship have been instrumental in shaping this research. Prof. DSc. (Tech.) Sören Ehlers, my second reviewer, for his invaluable insights, constructive feedback, and critical evaluation of my work, which enriched the quality of my research. Prof. Dr. sc. ETH Elyas Ghafoori, as member of the doctoral committee and new head of the Institute of Steel Construction, deserves special thanks for his interest in my research, the valuable conversations in the hallway, and the scientific guidance. Prof. Dr.-Ing. Fadi Aldakheel is thanked for taking the chair of the doctoral committee.

The scientific work presented in this dissertation is based on the research projects ISyMOO, (funding number 0324254E), and the project CorroFAT (grant number 37 LN/1), of the Research Association for Steel Applications (FOSTA) e. V., both funded by the BMWK. I would like to extend my thanks to these institutions for their financial support of this work. Furthermore, I wish to express my appreciation to the research partner, especially Dr. Andreas Momber from Muehlhan AG, Dr. Christian Woitzik and Dr. Moritz Braun from TU Hamburg, who were highly involved in this research. The idea of using the replica technique, which is an important part of this work, originated from Dr. Momber. This was very much appreciated.

I extend my gratitude to my colleagues at the Institute of Steel Construction and technicians for the positive environment they provided. Special thanks are expressed to my senior desk mates, Joshua Possekel and Andre Stang for their welcoming atmosphere, when I joined the Institute, their guidance, and the deep talks about life and research. Moreover, I thank my colleague, co-author of many paper, and former student assistant M.Sc. Tim Brömer, for his dedication to scientific work, for his reliability, and trustworthiness throughout the years. His contributions were invaluable to the success of this thesis. Furthermore, I would like to express my appreciation to B.Sc. Finn Schönamsgruber, for his outstanding assistance as my student assistant for more than four years, which significantly eased the workload and allowed me to focus on my research.

I express deep appreciation to my beloved wife Dieba for her unconditional support, encouragement, and understanding throughout this challenging journey.

Lastly, my heartfelt thanks go to my family, especially my parents for their endless love, day by day encouragement, and sacrifices they made over their life to make this journey possible.

This work is dedicated to my parents, Khatol and Shafi Shojai.

Hannover, 24.10.2023

Sulaiman Shojai

---

## Abstract

Offshore steel structures are exposed to harsh environmental conditions. At the same time, they are susceptible to fatigue due to cyclic loads from wind, waves, and operation as well as traffic. Both the steel structures and the corrosion protection have a limited lifetime. When the corrosion protection reaches the end of its service life, the steel is exposed to free corrosion. To continue the operation, the influence of corrosion on the fatigue behaviour has to be evaluated. Therefore, new methods need to be developed to accurately assess the actual condition of corroded components and integrate this information into (remaining) service life predictions.

Motivated by these challenges, this work began with investigations on corroded steel plates (also referred to as base material). Initially, methods for capturing and numerically modelling the actual corroded condition were developed. A corroded steel surface was converted into a numerical model using a 3D scan, allowing the calculation of stress concentrations caused by corrosion. Subsequently, fatigue tests were conducted on pre-corroded steel samples. Prior to fatigue tests, the samples were 3D scanned to characterize the state of corrosion and determine the stress concentrations based on the real surface. It was demonstrated that the hotspots of stress concentrations correlated with the crack locations observed in the fatigue tests. To incorporate the stress concentrations into the fatigue analysis according to local fatigue concepts, various methods for considering the micro-support effect were investigated. The application of the implicit gradient model (IGM) yielded the most reliable results with the lowest scatter in the derived stress-life (SN) curve based on notch stresses. Using the parameters derived for the IGM and the corresponding notch stress SN-curve, a quantitative relationship between the real surface of a corroded steel component and the fatigue life was established.

Steel structures often include numerous welded connections, which behave differently to corrosion exposure, due to existing stress concentrations from the welding geometry and residual stresses from the welding process. Hence, additional fatigue tests were conducted on corroded fillet and butt-welded specimens. In addition, 3D scans and residual stress measurements were performed. Subsequently, the fatigue tests were evaluated using local fatigue approaches, taking the real weld geometry from the 3D scans and the measured residual stresses into account. It was shown that stress concentrations had a significant impact on the fatigue life prediction. Additionally, it was demonstrated that residual stresses played a crucial role and must be considered for assessing the remaining fatigue life of corroded steel components. The application of local methods minimized the scatter in the SN-curves and thus increased the reliability. It was shown, that the consideration of the actual condition of corroded components in the calculation of fatigue strength is possible, also for welded samples.

Finally, the replica technique was introduced. With the replica technique, imprints of corroded components can be created during inspections of the structures. These imprints are then scanned in the laboratory and analysed using the methods presented in this work to determine their stress concentrations, which are correlated with the endurable load cycles. The replica technique can be applied to both welded and non-welded components. This allows the transfer of the findings from executed fatigue tests and numerical calculations to real structures.



---

**Keywords**

Pitting corrosion; stress concentrations; local fatigue approach; micro-support effect; notch effect; welds

---

## Kurzfassung

Offshore Stahlstrukturen sind zum Teil harschen Umweltbedingungen ausgesetzt. Gleichzeitig sind sie aufgrund zyklischer Belastungen aus Wind, Wellen und Betriebs- bzw. Verkehrslasten ermüdungsgefährdet. Sowohl die ermüdungsgefährdete Stahlkonstruktion als auch der Korrosionsschutz, der über die Jahre degradiert, haben eine begrenzte Lebensdauer. Wenn der Korrosionsschutz seine Lebensdauer erreicht hat und ausfällt, ist der Stahl freier Korrosion ausgesetzt. Um die Tragwerke in diesen Zustand weiterzubetreiben, ist es notwendig, den Einfluss von Korrosion auf die Ermüdungsfestigkeit zu untersuchen. Hierfür sind neue Methoden zu entwickeln, mit denen der tatsächliche Zustand von korrodierten Komponenten der Tragstrukturen erfasst und in Prognosen für eine (Rest-) Lebensdauer integriert werden kann.

Aus dieser Motivation heraus wurden im Rahmen dieser Arbeit zunächst Untersuchungen an korrodierten Stahlblechen (auch bezeichnet als Grundmaterial) durchgeführt. Dafür wurden im ersten Schritt Möglichkeiten zur Erfassung und numerischen Modellierung des tatsächlichen korrodierten Zustands erarbeitet. Hierbei wurde zunächst eine korrodierte Stahloberfläche aus einem 3D-Scan in ein numerisches Modell überführt. An diesem konnten die Kerbspannungen aus Korrosion berechnet werden. Im Anschluss daran wurden Ermüdungsversuche an vorkorrodierten Stahlproben durchgeführt. Vor den Ermüdungsversuchen wurden die Proben mit 3D-Scans aufgenommen, um den Zustand der Korrosion zu charakterisieren und die Kerbspannungen auf Basis der realen Oberfläche zu ermitteln. Es konnte gezeigt werden, dass die Stellen mit hohen Kerbspannungen mit der Rissinitiierungsstellen aus den jeweiligen Ermüdungsversuchen korrelieren. Um die Kerbspannungen in die Berechnung der Ermüdungsfestigkeit gemäß den lokalen Ermüdungskonzepten zu integrieren, wurden anschließend verschiedene Methoden zur Berücksichtigung der Mikrostützwirkung untersucht. Die Anwendung des impliziten Gradientenmodells (IGM) führte dabei zu den zuverlässigsten Ergebnissen mit der geringsten Streuung in der daraus abgeleiteten Kerbspannungswöhlerkurve. Mit den hergeleiteten Parametern für das IGM und der entsprechenden Kerbspannungswöhlerkurve, konnte ein quantitativer Zusammenhang zwischen der realen Oberfläche eines korrodierten Stahlbauteils und den ertragbaren Lastspielen hergestellt werden.

Stahlkonstruktionen weisen i. d. R. zahlreiche geschweißte Verbindungen auf. Diese verhalten sich aufgrund der bereits vorhandenen Spannungskonzentrationen durch die Schweißnahtgeometrie sowie den Eigenspannungen aus dem Schweißvorgang anders als das Grundmaterial. Deshalb wurden weitere Ermüdungsversuche an korrodierten Kehlnaht- und Stumpfnahproben durchgeführt. Zusätzlich erfolgten 3D-Scans und Eigenspannungsmessungen. Anschließend wurden die Ermüdungsversuche mit lokalen Ermüdungskonzepten, unter Berücksichtigung der realen Probengeometrie aus den 3D-Scans und den gemessenen Eigenspannungen nachgerechnet. Es konnte gezeigt werden, dass auch hier die Kerbspannungen einen großen Einfluss auf die Prognose der Lebensdauer haben. Zusätzlich stellte sich heraus, dass die Eigenspannungen eine wichtige Rolle spielen und zur Bewertung der Restlebensdauer von korrodierten Stahlkomponenten in Betracht gezogen werden müssen. Mit der Anwendung von lokalen Methoden konnte die Streuung in den Wöhlerkurven minimiert und somit die Zuverlässigkeit gesteigert werden. Es konnte somit auch für geschweißte Proben gezeigt werden,

---

dass die Berücksichtigung des realen Zustandes von korrodierten Komponenten in der Berechnung der Ermüdungsfestigkeit möglich ist.

Schließlich wurde die Replikatechnik vorgestellt. Mit der Replikatechnik können Abdrücke von korrodierten Komponenten im Rahmen von Bauwerksinspektionen erstellt werden. Diese können anschließend im Labor gescannt und mit den vorgestellten Methoden hinsichtlich ihrer Kerbspannungen, die mit den ertragen Lastspielen gekoppelt sind, untersucht werden. Die Replikatechnik kann sowohl an geschweißten als auch ungeschweißten Komponenten angewendet werden. Hiermit ist eine Übertragung der Erkenntnisse aus den durchgeführten Ermüdungsversuchen und den numerischen Berechnungen auf reale Bauwerke möglich.

### **Schlagwörter**

Pitting Korrosion; Spannungskonzentrationen; Lokale Ermüdungskonzepte; Mikrostützwirkung; Kerbwirkung; Schweißnähte



## Contents

<b>1</b>	<b>INTRODUCTION.....</b>	<b>1</b>
1.1	Motivation.....	1
1.2	State of the art.....	2
1.2.1	Development and impact of corrosion on structural steel.....	2
1.2.2	Fatigue design of steel structures.....	3
1.2.3	Local fatigue approaches.....	6
1.2.4	Micro-support effect.....	7
1.2.5	Mean and residual stress effect.....	10
1.2.6	Consideration of residual stresses in local approaches.....	11
1.3	Research objectives and structure of the thesis.....	13
1.3.1	Research objectives.....	13
1.3.2	Structure of the thesis.....	13
1.4	Limitations.....	15
1.5	References.....	15
<b>2</b>	<b>MODELLING OF PITTING CORROSION (PAPER I).....</b>	<b>23</b>
2.1	Abstract.....	25
2.2	Introduction.....	25
2.3	Methods and Experiments.....	28
2.3.1	Karhunen-Loeve expansion for the random-field model.....	28
2.3.2	Pit data acquisition from 3D-scans.....	30
2.3.3	Reverse engineering method for real surface modelling with 3D-scans.....	32
2.4	Calculation.....	33
2.4.1	Numerical Modeling.....	33
2.4.2	Parameter Study.....	39
2.5	Results.....	42
2.6	Discussion and Conclusion.....	47
2.7	Acknowledgements.....	49
2.8	References.....	49
<b>3</b>	<b>INFLUENCE OF PITTING CORROSION BASED ON 3D SURFACE SCANS (PAPER II).....</b>	<b>53</b>
3.1	Abstract.....	55
3.2	Introduction.....	55
3.3	Test setup.....	57
3.3.1	Specimen.....	57
3.3.2	Fatigue tests and digital image correlation setup.....	58
3.3.3	Digital image correlation setup.....	59
3.3.4	Crack detection using DIC.....	60
3.3.5	3D-scanning of specimen and reverse engineering method.....	61

---

3.4	Numerical Analysis .....	64
3.4.1	Numerical model .....	64
3.4.2	Convergence study .....	65
3.5	Results and Discussion.....	66
3.5.1	Fatigue tests results .....	66
3.5.2	Digital image correlation results .....	69
3.5.3	Numerical analysis results .....	71
3.5.4	Findings .....	78
3.6	Conclusion.....	78
3.7	Acknowledgements .....	78
3.8	Appendix A: Fatigue test data.....	79
3.9	Appendix B: Results of DIC measurements .....	80
3.10	Appendix C: Results of numerical analysis .....	81
3.11	References .....	82
<b>4</b>	<b>MICRO-SUPPORT CONSIDERATION OF CORRODED STEEL (PAPER III) .....</b>	<b>87</b>
4.1	Abstract .....	89
4.2	Introduction .....	89
4.3	Theoretical background for the implicit gradient model (IGM) .....	92
4.4	Experiments.....	94
4.4.1	Material characterization tests .....	94
4.4.2	Fatigue tests .....	95
4.5	Numerical Analysis of effective notch stresses .....	96
4.5.1	Reverse Engineering.....	97
4.5.2	Structural Analysis .....	97
4.5.3	Thermal analysis.....	99
4.6	Fatigue strength analysis .....	106
4.6.1	Determination of weighting factor for the implicit gradient model .....	106
4.6.2	Comparison of TCD with IGM .....	108
4.6.3	Discussion .....	109
4.7	Application to existing structures.....	111
4.7.1	Replica imprint and 3D-scan .....	111
4.7.2	Reverse Engineering.....	112
4.7.3	Results and discussion.....	113
4.8	Summary and Outlook .....	114
4.9	Acknowledgements .....	115
4.10	References .....	115
<b>5</b>	<b>ASSESSMENT OF CORROSION FATIGUE IN WELDED JOINTS (PAPER IV) .....</b>	<b>121</b>
5.1	Abstract .....	123

---

5.2	Introduction .....	124
5.3	Experiments.....	125
5.3.1	Specimens geometry and surface preparation .....	125
5.3.2	Accelerated corrosion experiment .....	126
5.3.3	Surface characterization measurements .....	127
5.3.4	3D-scans of specimens .....	128
5.3.5	Geometrical weld parameters .....	129
5.3.6	Hardness and residual stress measurements .....	130
5.3.7	Fatigue tests .....	131
5.3.8	Crack detection with digital image correlation .....	132
5.4	Experimental results and discussion .....	133
5.4.1	Surface measurement results .....	133
5.4.2	Digital surface comparison.....	134
5.4.3	Results of geometrical parameter evaluations .....	136
5.4.4	Hardness measurements .....	138
5.4.5	Residual stress results.....	139
5.4.6	Fatigue tests results .....	140
5.4.7	Crack detection with digital image correlation .....	144
5.4.8	Discussion .....	145
5.5	Summary and Outlook .....	146
5.6	Acknowledgements .....	148
5.7	Appendix A .....	148
5.8	References .....	151
<b>6</b>	<b>FATIGUE ANALYSIS OF CORRODED WELDED JOINTS WITH LOCAL APPROACHES (PAPER V) .....</b>	<b>155</b>
6.1	Abstract .....	157
6.2	Introduction .....	158
6.3	Background of the notch stress methods.....	160
6.3.1	Notch stress analysis methods .....	160
6.3.2	Implicit gradient model (IGM) approach .....	161
6.3.3	Consideration of residual stresses and mean stress correction.....	162
6.4	Experiments.....	164
6.4.1	Fatigue tests .....	164
6.4.2	Fatigue test results .....	165
6.5	Numerical analysis and fatigue strength assessment .....	166
6.5.1	Reverse engineering and numerical model .....	166
6.5.2	Analysis of bending stresses.....	168
6.5.3	Numerical analysis of stress concentration .....	170
6.5.4	Consideration of micro-support effect with IGM.....	170
6.5.5	Comparison of DIC and effective stress concentrations .....	172

6.5.6	Fatigue strength assessment .....	174
6.5.7	Discussion .....	178
6.6	Engineering application .....	179
6.7	Summary and Outlook .....	180
6.8	Acknowledgements .....	181
6.9	Appendix A .....	181
6.10	References .....	183
<b>7</b>	<b>CONCLUSIONS AND OUTLOOK .....</b>	<b>187</b>
7.1	Investigations on corroded steel plates .....	187
7.2	Investigations on corroded weld seams.....	188
7.3	Outlook.....	190
<b>8</b>	<b>LISTS .....</b>	<b>193</b>
8.1	List of Figures .....	193
8.2	List of Tables.....	200



## Nomenclature

### Abbreviations

AM	Area Method
CP	Cathodic Protection
CSS	Cyclic-Stress-Strain
DNV	Det Norske Veritas
DIC	Digital Image Correlation
ERF	Environment Reduction Factor
EC	Eurocode
FC	Free Corrosion
IGM	Implicit Gradient Model
IIW	International Institute of Welding
LM	Line Method
OWT	Offshore Wind Turbine
PM	Point Method
PWT	Post Weld Treatment
SWT	Smith, Watson, Topper
SED	Strain Energy Density Method
SN	Stress-Life
TCD	Theory of Critical Distances
VM	Volume Method

### Symbols

$a$	Weighting factor/parameter
$d^*$	Critical distance
$f_{SWT}$	Mean stress correction factor based on SWT
$f(R)$	Mean stress correction factor IIW
$L$	Intrinsic material length
$N$	Load cycle number
$P_{SWT}$	Damage parameter based on SWT
$R$	Stress ratio
$r_f$	Fictitious radius
$R_{local}$	Local stress ratio
$r_{real}$	Real radius
$s$	Stress hypothesis factor
$\Delta K_{th}$	Fatigue crack propagation threshold
$\Delta\sigma$	Stress range
$\Delta\sigma_0$	Fatigue limit
$\Delta\sigma_f$	Effective notch stress range
$\Delta\sigma_{f,ref}$	Mean stress corrected notch stress range
$\varepsilon_a$	Local strain amplitude
$\rho^*$	Equivalent length
$\sigma_a$	Stress amplitude
$\sigma_f$	Effective notch Stress
$\sigma_k$	Elastic notch Stress
$\sigma_m$	Mean stress
$\sigma_{max}$	Maximum stress
$\sigma_{min}$	Minimum stress
$\sigma_n$	Nominal stress
$\sigma_S$	Structural stress
$\sigma_y$	Yield stress
$\sigma_u$	Ultimate stress



# 1 Introduction

## 1.1 Motivation

The durability of steel construction is a major challenge of engineering structures. In view of the high replacement costs and the associated additional environmental emissions, the focus has shifted to repair and service life extension, in order to contribute to the goal of NetZero 2050 [1] proclaimed by the United Nations.

Steel structures such as bridges, sheet piles, pipelines or support structures for offshore wind turbines (OWT) and platforms are highly susceptible to corrosion, see Figure 1-1. Especially for bridges and wind turbines, which are additionally exposed to cyclic loading, this aspect becomes important. In practice, the structures are protected against corrosion with corrosion protection systems. These can be in the form of protective coatings, sacrificial anodes, external current or a combination of these. Despite special requirements for the corrosion protection system, e. g. for OWT [2–4], damages to it cannot be completely avoided during their lifetime. Therefore, recent research projects aim to quantify the condition of corrosion protection using digital data from inspections [5–7] and to repair possible damages. Similar efforts are observed for bridge constructions, as they face the same problems. However, the repair of corrosion protection systems, such as coatings, is only possible if the damage is local and not yet spread over a large area. At the end of the service life, however, widespread damages may occur, where the repair of the corrosion protection system is either very expensive or technically not possible. In these cases, it is necessary to reliably determine the service life of structures under consideration of the actual corroded condition in order to make profound decisions about further operation of the structures.

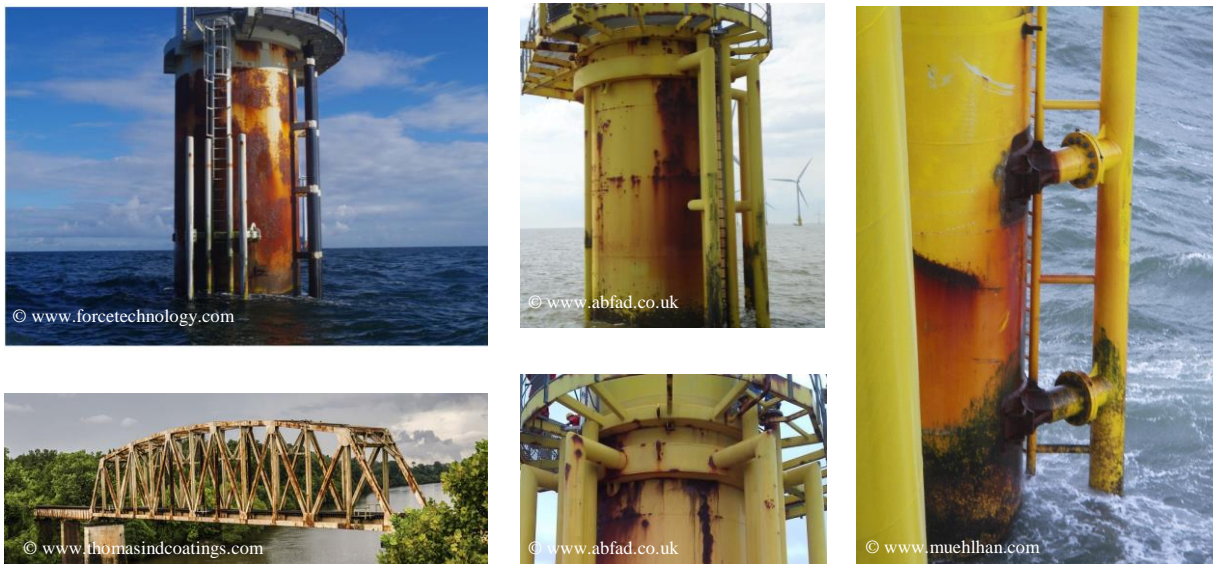


**Figure 1-1: Examples of corroded steel structures**

## 1.2 State of the art

### 1.2.1 Development and impact of corrosion on structural steel

Corrosion is a degradation process of metals caused by electrochemical reactions from the environment. Corrosion can be distinguished between uniform corrosion, which causes thickness reduction, and pitting corrosion, which leads to local stress concentrations on the steel surface. There is reliable knowledge about the thickness loss over time for structural steel [8] under different environmental conditions. For OWT, this is addressed in the standards with the so-called corrosion allowance [2–4]. However, the more crucial issue regarding cyclic loading is pitting corrosion.

The development of pits starts at several locations simultaneously, with some pits growing as stable pits over time in the direction of the plate thickness [9]. After a period of vertical pit growth, lateral propagation of corrosion occurs as individual pits collapse to form a new plateau. The initial pitting corrosion tends to become uniform corrosion over time [10]. According to Melchers [11], the described process from pitting corrosion to uniform corrosion can be repeated on the new plateau, resulting in a cyclic development process of corrosion.

The cyclic behaviour was also observed by Xu et al. [11], where in addition to the pitting depth, the ratio of pitting width to pitting depth (here called pit depth ratio) was documented. After initial needle-shaped pits, more hemispherical and wide pits were observed later during the corrosion process, which were attributed to the collapse of individual pits. Hence, according to the standards, a distinction is made between the form of pits, which can be hemispherical, crater-shaped or needle-shaped [12]. Liang et al. [13] and Xiang et al. [14] found that the pit geometry expressed by the pit depth ratio is the governing factor for the locally higher notch stress. In [11] and [15] it was shown by fatigue tests that the fatigue strength depends significantly on the pit depth ratio. Here, fatigue strength tests were carried out on pre-corroded specimens with different corrosion exposure durations. It was found that after a short exposure duration, the fatigue load cycles decreased significantly. However, as corrosion progressed, the pits became shallower and resulted in lower notch stresses, which eventually led to an increase in fatigue strength. This is consistent with the findings of Neuber's classical notch stress theory, where the notch stresses depend significantly on the notch radius, expressed by the pit depth ratio in case of pitting corrosion [16].

However, although there are some studies on the change of the surface geometry due to corrosion, including [17–19], the influence of corrosion on weld geometry has not been explicitly investigated. Yet, the findings in the above mentioned literature, where the geometrical aspect was only investigated on plane steel, allow the assumption, that corrosion changes the geometry and stress concentrations of weld seams as well.

In addition to the local stress concentrations due to pitting, corrosion affects the mechanical material properties. The service life of structures consists of the crack initiation and the crack propagation stage. Corrosion has an impact on the material in the crack initiation as well as in the crack propagation stage. As a result of the acidic conditions under the rust layer, reported by Melchers et. al [10], hydrogen can be generated and diffuse into the steel surface. According to Revie and Uhlig [20] and Marcus [21], the corrosion process includes an oxygen reaction and a hydrogen formation process in which hydrogen is released. The detailed chemical reaction process is presented in Li et al. [22]. This

leads to embrittlement of the material, which affects both the tensile strength of the material and both stages of the service life. Li et al. [22] showed that the tensile strength and corresponding elongation can be reduced significantly, if steel is subjected to acidic conditions as it is the case under the corrosion rust layer. Mehmanparast et al. [23] found that crack propagation in seawater is twice as high as in air as a result of embrittlement at the crack tip, which confirmed observations of earlier investigations [24,25]. An overview of the current state of research regarding the effects of corrosion on fatigue is provided in the report by Larrosa and Akid [26].

### 1.2.2 Fatigue design of steel structures

Because of the extensive cyclic loads, the fatigue analysis is often decisive in the design of bridges and OWT. Various standards and guidelines are available for this purpose, such as guidelines of Eurocode (EC) [27], Det Norske Veritas (DNV) [28] or International Institute of Welding (IIW) [29]. According to them, the fatigue design is carried out with different design approaches, which mainly differ in the definition and calculation of the stresses.

In Figure 1-2 the definition of stresses is illustrated on a steel plate with a non-load carrying transverse stiffener. It can be distinguished between the nominal stress  $\sigma_n$ , the structural stress  $\sigma_s$ , and the notch stress  $\sigma_k$ . Accordingly, the fatigue design can be carried out with the nominal, structural, and also with the notch stress approach, whereby the nominal stress approach is considered as a global and the notch stress approach as a local approach. The structural stress approach is considered as partly global and partly local approach.

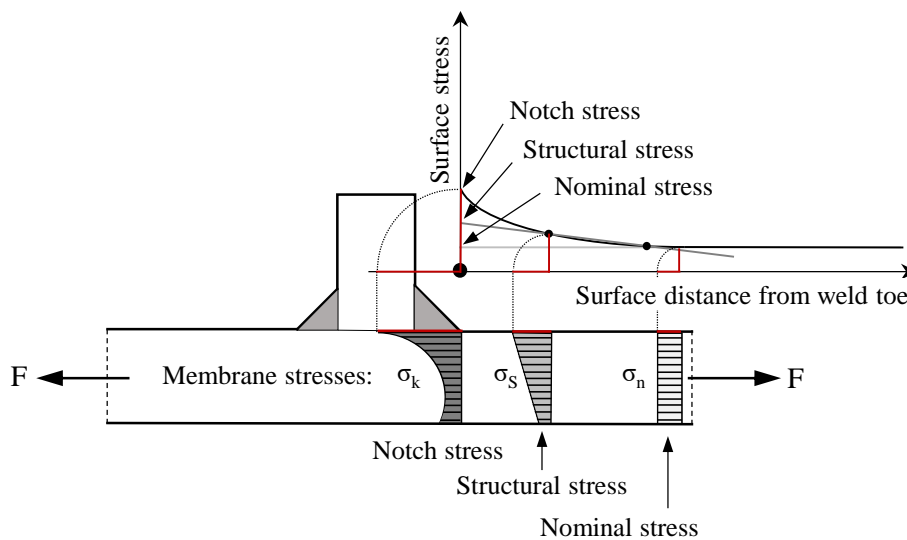


Figure 1-2: Definition of stresses in accordance with [28–30]

#### Nominal stress approach

The nominal stress approach is based on global (nominal) stresses, without consideration of stress concentrations from the structural detail (for example holes) or notch geometry (for example welds).

All potential stress concentrations are considered in the stress-life (SN) curves, which differ depending on the detail category. Each SN-curve is derived from fatigue tests on a specific structural detail. Based on these test results, a detail category is defined, which is later used in the design process.

### Structural stress approach (hot spot method)

The structural stress approach, also called hot spot method, is used when no SN-curves exist for the specific structural detail. Here, the structure-related stresses are determined using analytical formulas or a finite element (FE) analysis. In case of a stress analysis with FE, the so-called hotspot method is used. In this method, the stress on the surface is linearly extrapolated based on two predefined points (see Figure 1-2) towards the weld toe, in order to obtain the structural stress at the weld toe. The structural stresses are then used to perform fatigue analysis with an appropriate structural SN-curve. The structural SN-curve includes the impact from the stress concentrations resulting from the weld geometry, as this is not considered in the stress analysis.

### Effective notch stress approach

In the notch stress approach, the stresses are determined by FE-calculations, taking the impact of both, the structural and the notch geometry into account. The geometry of the weld notch is considered by idealized approximations in the CAD-model. The effect of the so-called micro-support effect is taken into account by modelling a notch with a fictitious radius of  $r_f = 1$  mm at the weld toe as well as at the weld root, see Figure 1-3. The notch stresses can then be used to perform the fatigue analysis by means of a notch stress SN-curve, which then mainly considers the material behaviour, as all potential stress increasing parameters are already considered.

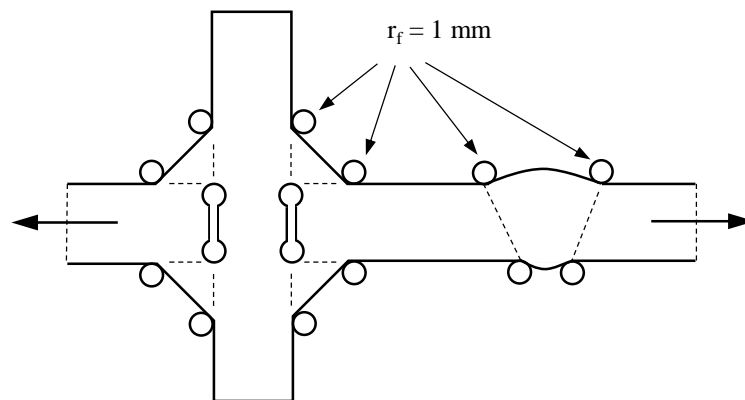


Figure 1-3: Analysis of effective notch stress according EC [27], DNV [28], and IIW [29] using a fictitious notch radius.

### Fatigue design curves according standards

For all approaches presented, there are different SN-curves in DNV for the environmental conditions air (A), cathodic protection (CP) and free corrosion (FC), see Figure 1-4a [28]. In the design, a fully intact corrosion protection is assumed and therefore the SN-curve for A is applied. Whenever there is no fully intact corrosion protection, the assumption is no longer fulfilled. The SN curves for free corrosion are then used as a conservative approach for determining the (residual) service life from the above-mentioned point in time [31].

The SN-curve of DNV for CP and FC are derived from the offshore oil and gas industry and are based on the guideline of the Health and Safety Executive UK [32]. The guideline in turn is based on fatigue tests carried out under artificially generated environmental conditions of CP and FC. The fatigue tests for CP and FC were performed at realistic frequencies of 0.1 Hz to 0.3 Hz to reflect the time dependence of corrosion. For the same structural details and load levels, different load cycles were determined for different environmental conditions. Based on this, the environment reduction factor (ERF) was introduced. The ERF describes the influence of the environment on the fatigue behaviour and is determined from the ratio of the load cycles from A to the load cycles from CP and FC:  $ERF = N_{Air}/N_{FC}$ .

In Figure 1-4b the ERF values from the tests are illustrated. Welded tubular joints had an  $ERF < 3.0$  in all tests, while welded plates reached values up to  $ERF = 5.2$ . Overall, ERF values between 0.8 and 5.2 were achieved, indicating a high degree of scatter. This included not only the scatter from the corrosive environment, but also from the weld geometry, which usually differs for every tested specimen.

It can be observed from the ERF values in Figure 1-4b, that the influence of corrosion on already heavily notched components (tubular joints) is smaller than the influence on weakly notched components (welded plates). Despite this, a constant design value of  $ERF = 3.0$  for FC environment was determined. The SN-curves for all structural and welded details for the FC environment were derived from the air SN-curves by reducing it with the design ERF. The reduction was applied to all fatigue design approaches anchored in DNV, including the nominal, structural and notch stress approach. In addition to the reduction, for the FC SN-curve, the break point at  $10^7$  load cycles is removed, see Figure 1-4a. This was seen as justified, because in the range of  $10^6$  load cycles no significant change of the ERFs could be observed.

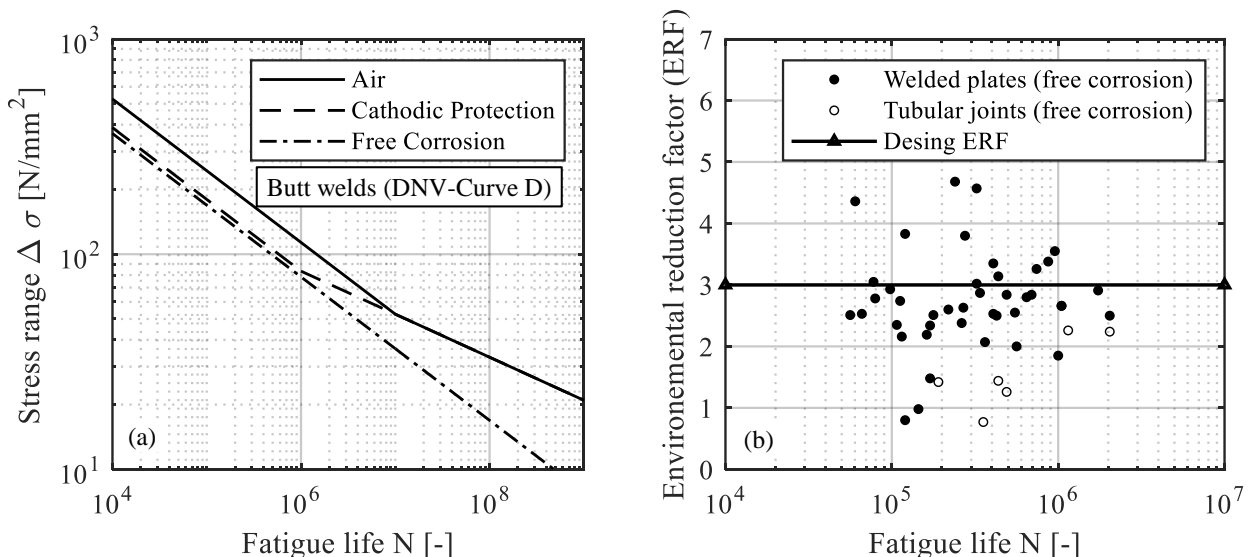


**Figure 1-4: (a) SN-curves for butt-welded plates (Curve D) for different environments according DNV [28], (b) diagram of ERF-values for welded plates and tubular joints for free corrosion environment according [32].**

However, considering the above, a general reduction with a single ERF value, as carried out in the DNV standards, is neither economical nor on the safe side. Hence, in the German BAW standard [33] a distinction between heavily and weakly notched components is made. Here, for FAT classes above FAT 125, the FAT classes have to be reduced by two category levels in case of free corrosion, while no reduction is necessary for FAT classes below FAT 56. Beside this, in the British standard BS 7608 [34] a reduction of the ERF depending on the relationship between the existing stress and the yield strength is considered. In case of welded specimen, where the local stresses are higher than in unwelded components, it leads to a reduction of the ERF values for heavily notched components. A distinction between welded and unwelded specimens is indirectly possible here, while it is missing in DNV and also in the IIW standard, where the impact of corrosion is considered by reduction of the SN-curves of at least 30 %, without any further specification. Nevertheless, as for strongly notched welded components the general reduction is on the safe side, it opens up the possibility of utilizing potential load-bearing reserves for existing structures and extending the service life.

In order to exploit potential load-bearing reserves, the remaining service life of structures must be evaluated on the basis of the actual condition of the structural component, including the weld geometry and potentially changes in the surface geometry due to corrosion. With the above-mentioned approaches, utilization of these reserves is not possible. Although in the notch stress approach of DNV notch stresses can be considered, it is limited to notch stresses concentrations from welds. It is not possible to consider the separate influence of the corrosion process, which consist of changes in the surface geometry as well as embrittlement of the material. Moreover, in the case of welded components, residual stresses have to be considered. In particular, clean blasting, which is used to prepare the surface for the application of corrosion protection, induces beneficial residual compressive stresses [35–37]. This has to be considered in order to exploit the beneficial effect and accurately predict the remaining service life of existing support structures.

In summary, the following issues cannot be addressed currently:

- Differentiation of heavily and mildly notched components, resulting in high degree of scatter in the ERF values
- Consideration of actual surface condition of the structural component in the fatigue analysis
- Consideration of beneficial residual stresses from clean blasting

### **1.2.3 Local fatigue approaches**

One possibility to consider the aforementioned issues is the application of local fatigue approaches. Local fatigue approaches are characterized by separate consideration of the stresses as well as the material resistance. Thereby, the increased stress in the notch is compared to the material resistance of an unnotched specimen. With this approach, the stress concentrations from corrosion and the stress concentrations already existing in the welds, as well as the global structural stresses, can be considered in a more differentiated way. The local approaches can be distinguished between the notch strain and the notch stress approach.



### **Notch strain approach**

The notch-strain approach relates notch-strain to the material strain-life curve and represents a more scientific approach [38–43]. With the notch-strain approach, load cycles are determined only up to crack initiation as the strain-life curves are obtained for specimens with relatively small cross-sections [44,45]. For the total service life, the crack propagation life has to be determined additionally using linear elastic fracture mechanics. Because of the scientific approach, many input parameters, including the definition of the crack initiation, are required here, which can thus strongly influence the results.

### **Notch stress approach**

In contrast to the notch strain approach, the notch stress approach covers the entire service life. The stresses are determined on the basis of the notch geometry and compared with correspondingly notch stress-based SN curves, which mainly consider the material effect. The notch stress approach is widely used for welded components [30,42,46–49] and is also, as already introduced in section 1.2.2, included in corresponding standards such as DNV [28], IIW [29] and Eurocode (EC) [27]. A main issue in the notch stress approach is the consideration of the micro-support effect, which is considered with a fictitious radius of  $r_f = 1$  mm, as shown in Figure 1-3. This procedure is limited to stress concentrations of weld seams for two reasons:

1. The modification with a radius of  $r_f = 1$  mm is calibrated on a high number of fatigue test data of welded specimens and is only applicable with the corresponding notch stress-based FAT 225 curve extracted within the calibration process. Thus, the modification includes the material behaviour of weld material, which is different to base material or the near-surface material of the corroded steel.
2. The use of rounding on pits cannot be implemented equally to the weld seams, because the decisive stress concentrations do not occur on a single pit, but in many cases on several interacting pits.

Thus, to apply the notch stress approach, alternative methods must be employed to account for the micro-support effect.

#### **1.2.4 Micro-support effect**

The micro-support effect is related to the behaviour of micro cracks during cyclic loading. Particularly, in case of sharp notches, the yield stress in the surface crystallites can be exceeded and lead to micro cracks, which do not propagate with continued cyclic loading. This behaviour reduces the stress concentrations and supports the fatigue resistance [38,50]. The reduced stress concentrations are referred to as effective (fatigue-driving) notch stresses. Various micro-support effect hypotheses can be found in the literature for calculating the effective notch stress, such as the strain energy density method (SED) [51–53], the theory of critical distances (TCD) [54–56], or the implicit gradient model (IGM) [57–59]. The main idea of all theories is, that the fatigue-driving stress (or strain) is not the stress at the surface of a component, but rather a stress in a certain depth or a stress (or strain) averaged

over a certain length, area or volume. In this work, the main focus is on the TCD and the IGM approach.

#### 1.2.4.1 Theory of critical distances (TCD) approach

The theory of critical distances is a summary of several theories that were considered independently for a long time, until they were unified by Taylor [54]. Peterson [60] proposed using the stress at a critical distance  $d^*$  from the stress peak according to Figure 1-6a. Neuber assumed that the effective notch stress is a stress averaged over the width of a microstructure particle in the notch base according to Figure 1-6b [61]. The width of the microstructure particle is called the equivalent length  $\rho^*$ , which depends on the material type and yield point of the material.

In the unified form by Taylor [54], Peterson's approach is the point method (PM) and Neuber's approach is the line method (LM). According to Taylor the critical distance for PM and the averaging length for LM can be related to the intrinsic material length  $L$ , which depends on the microstructure of the material and is derived on the basis of linear elastic fracture mechanics according to Figure 1-5 with:

$$L = \frac{1}{\pi} \left( \frac{\Delta K_{th}}{\Delta \sigma_0} \right)^2 \quad (1-1)$$

where  $\Delta K_{th}$  is the fatigue crack propagation threshold and  $\Delta \sigma_0$  is the fatigue limit.

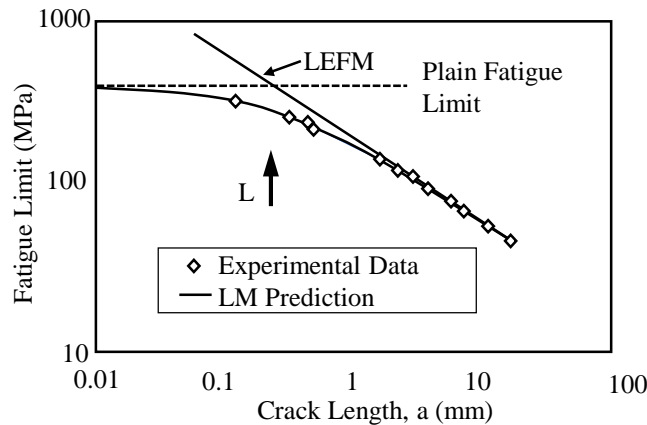


**Figure 1-5: Definition of the intrinsic material length  $L$  according Taylor [54]**

The intrinsic material length is related to the critical distance with  $d^* = L/2$ , while the equivalent averaging length is related to it with  $\rho^* = 2L$ . The aforementioned fictitious radius approach anchored in the codes is derived by Radaj from the LM [38] with the relation:

$$r_f = r_{real} + s \cdot \rho^* \quad (1-2)$$

where  $r_f$  is the fictitious radius,  $r_{real}$  is the real radius,  $s$  depending on the applied strength hypothesis (2.0 for the principal stress hypothesis and 2.5 for the von Mises equivalent stress), and  $\rho^*$  the equivalent length according to the LM. For the principal stress hypothesis, a recommended equivalent

length of  $\rho^* = 0.4$  [62], and a conservative assumption of the real notch radius  $r_{\text{real}} = 0$  mm, a fictitious radius of  $r_f = 1$  mm applied in the codes can be derived, see Figure 1-6d.

Further approaches are the area method (AM) defined by Sheppard [63], where the stress is averaged over a semicircular area with a radius of  $L$  and the volume method (VM) defined by Bellet [64], where the stress is averaged over a hemisphere with a radius of  $1.54L$ , respectively (see Figure 1-6c). The TCD methods have been extensively checked on standard notches [65,66] and also applied to weld seams (e. g., in [62,67,68]).

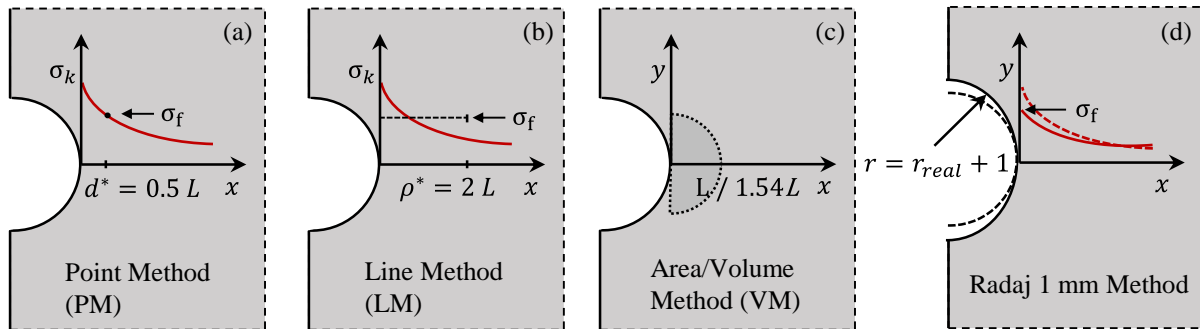


**Figure 1-6: Illustration of TCD-methods, (a) point method, (b) line method, (c) volume method and (d) Radaj 1 mm method**

The application to weld seams is possible because the potential crack locations are limited to the weld toe and weld root and thus only limited locations has to be evaluated. For components with a high number of notches, the stress evaluation requires an enormous effort in post processing, as it has to be performed separately for all potential notches. This issue has to be faced, when the TCD methods should be applied on corroded components, especially when the surface is based on the real 3D surface geometry, which includes several notches and potential crack locations.

#### 1.2.4.2 Implicit gradient model (IGM) approach

One way to overcome the post processing efforts in the TCD methods is by application of the implicit gradient model (IGM) approach, which allows the micro-support effect to be taken into account within the numerical analysis of the stress field. This enables the consideration of all notches of a corroded component in a single numerical analysis.

The IGM approach was derived by Peerlings [57,58,69] and among others already applied by Tovo and Livieri [70,71], Lang [72] and Schürmann [73] on standard notched specimen as well as on welded components. Analogous to the TCD methods, different approaches such as the PM, LM or VM can be implemented by choosing appropriate weighting functions [71,74]. By definition of a Dirac function, for example, the PM of TCD can be implemented in the IGM approach.

However, for the application it is important that the weighting functions are continuous in order to avoid boundary problems. Therefore, in the application of IGM, the VM has proven to be the most suitable, since it can be simply represented by a continuous Gaussian equation. Analogous to the VM

of TCD methods, the fatigue-driving effective stress  $\sigma_f(\mathbf{x})$  is assumed to be stress averaged over a volume around the notch peak stress according equation (1-3):

$$\sigma_f(\mathbf{x}) = \frac{1}{V_r(\mathbf{x})} \int_V G(\mathbf{x}, \mathbf{y}) \sigma_k(\mathbf{y}) dV_y \quad (1-3)$$

With some assumption the differential equation (1-4) can be derived from equation (1-3) as:

$$\sigma_f(\vec{x}) - \sigma_k(\vec{x}) - a \nabla^2 \sigma_f(\vec{x}) = 0 \quad (1-4)$$

where the parameter  $a (> 0)$  corresponds to the weighting factor of the surrounding volume at the notch and is linked to the intrinsic material length  $L$  with:

$$a = (\zeta \cdot L)^2 \quad (1-5)$$

With this, the impact of the material can be considered on the basis of linear elastic fracture mechanics and a relationship to the TCD methods can be defined.

For consideration of the micro-support effect with IGM, the differential equation (1-4) has to be solved to  $\sigma_f$ . For one- or two-dimensional problems, the equation can be solved by implementation into MATLAB. For three-dimensional problems, it is recommended to use the solvers of commercial FE-software. According to Lang et al. [48] and Lener et al. [72] it can be solved with the thermal analysis module of commercial FE-software, as equation (1-4) is similar to the differential equation of the thermal diffusion problem. For more details, it is referred to paper III and paper V.

However, as the IGM approach is not yet applied on real corroded surfaces, the main objectives to be solved are the following:

- Implementation of IGM approach in numerical analysis of corroded components based on a real surface geometry (for base material and weld seams).
- Derivation of a notch stress SN-curve and the weighting factor for application on corroded components, as the near surface material is different after corrosion exposure.

### 1.2.5 Mean and residual stress effect

In addition to the aforementioned aspects, the fatigue strength is affected by mean and residual stresses. The mean stress effect can be illustrated by a Haigh diagram according to Figure 1-7. Here, the fatigue strength, usually expressed by the stress range  $\Delta\sigma$  or the stress amplitude  $\sigma_a$  at a load cycle number of  $N = 2 \cdot 10^6$ , is presented as a function of the mean stresses  $\sigma_m$ . In the range of positive mean stresses, higher mean stresses lead to a reduction of the bearable stress amplitudes and hence to a reduction of the fatigue strength. In the region of negative mean stresses, the fatigue strength, due to the closure of cracks during cyclic loading, increases accordingly [75]. However, the magnification is more pronounced for high-strength steels than for structural steels and is therefore characterized with a constant approximation, which is also reflected in the relevant standards (EC, DNV, IIW). For very high negative mean stresses, the fatigue strength is limited by the static compressive strength.

The mean stresses can also be expressed by the stress ratio  $R$  as:

$$R = \frac{\sigma_{min}}{\sigma_{max}} = \frac{\sigma_m - \sigma_a}{\sigma_m + \sigma_a} \quad (1-6)$$

where  $\sigma_{min}$  and  $\sigma_{max}$  are the minimum and the maximum stress resulting from the cyclic load. The range of stress ratios that is decisive in practical applications is  $-1 \leq R < 1$ . There are various approximation formulas for this range, such as that of Gerber [76], Goodman [77], Soderberg [78] or Morrow [79].

In addition to the mean stresses, which result from external loads, steel components also contain residual stresses, which can arise from the manufacturing process as a result of rolling, welding or surface treatment. With regard to fatigue strength, residual stresses behave similarly as mean stresses and can therefore be regarded as mean stress increasing stresses. In contrast to the externally acting mean stresses, residual stresses can be relieved (relaxation) under cyclic loading, which has been investigated extensively in the context of post weld treatment (PWT) methods [80–82].

Normatively, the influence of mean and residual stresses is taken into account by fatigue strength enhancement factors. According to IIW, this is carried out using the diagram shown in Figure 1-8, in which the fatigue strength-enhancement factors  $f(R)$  are shown as a function of the stress ratios  $R$ . In addition, a distinction is made between low, medium and high residual stresses, whereas no increase is allowed for high residual stresses. This enables the residual stresses to be considered mainly in welded and unwelded components. For the consideration of beneficial residual stresses from PWT methods, such as shot peening, explicitly increased factors are given in IIW.

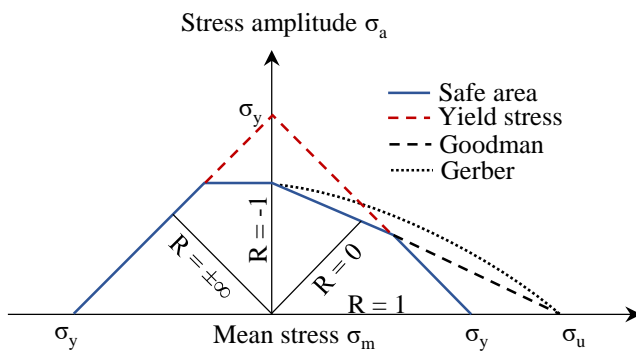


Figure 1-7: Haigh-diagram

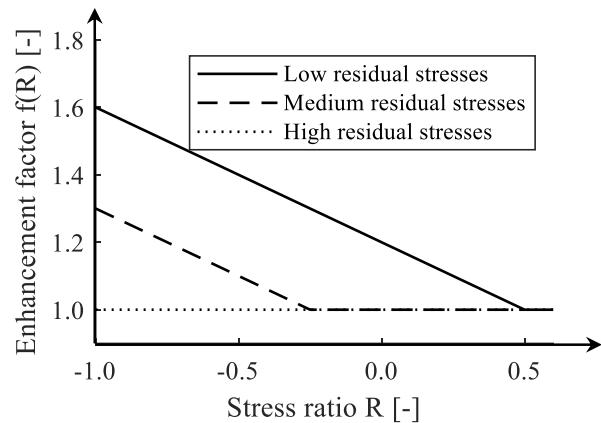


Figure 1-8: Mean stress effect according IIW

However, corroded welded components, which may also be clean blasted before application of corrosion protection, cannot be easily assigned to one of the curves shown in Figure 1-8, since there is no quantitative correlation between the residual stresses and the fatigue strength.

### 1.2.6 Consideration of residual stresses in local approaches

The correlation can be established with the mean stress correction factor based on Smith, Watson and Topper (SWT) [83], where the fatigue strength is assumed to depend on the product of the maximum

elastic-plastic local stress  $\sigma_{max}$  and the local strain amplitude  $\varepsilon_a$ . Usually, these are considered within the damage parameter  $P_{SWT}$  [39,84] as:

$$P_{SWT} = \sqrt{\sigma_{max} \cdot \varepsilon_a \cdot E} \quad (1-7)$$

Nykänen and Björk [85,86] employed the product  $\sigma_{max} \cdot \varepsilon_a$  and derived the mean stress correction factor  $f_{SWT}$  defined as:

$$f_{SWT} = \sqrt{1 - R_{local}} \quad (1-8)$$

where,  $R_{local}$  is the local mean stress ratio, which considers the residual stresses, the mean stresses and stress amplitudes at the notch base. The calculation of  $R_{local}$  is based on nonlinear material behaviour according to the cyclic stress-strain (CSS) curve by Ramberg and Osgood [87] for the first load step and according to the Masing-hypothesis [88] for any further load cycle, see Figure 1-9.

The mean stress correction factor  $f_{SWT}$  is subsequently applied to the effective notch stress range  $\Delta\sigma_f$  in order to obtain the mean stress corrected notch stress range  $\Delta\sigma_{f,ref}$  as follows:

$$\Delta\sigma_{f,ref} = \frac{\Delta\sigma_f}{\sqrt{1 - R_{local}}} \quad (1-9)$$

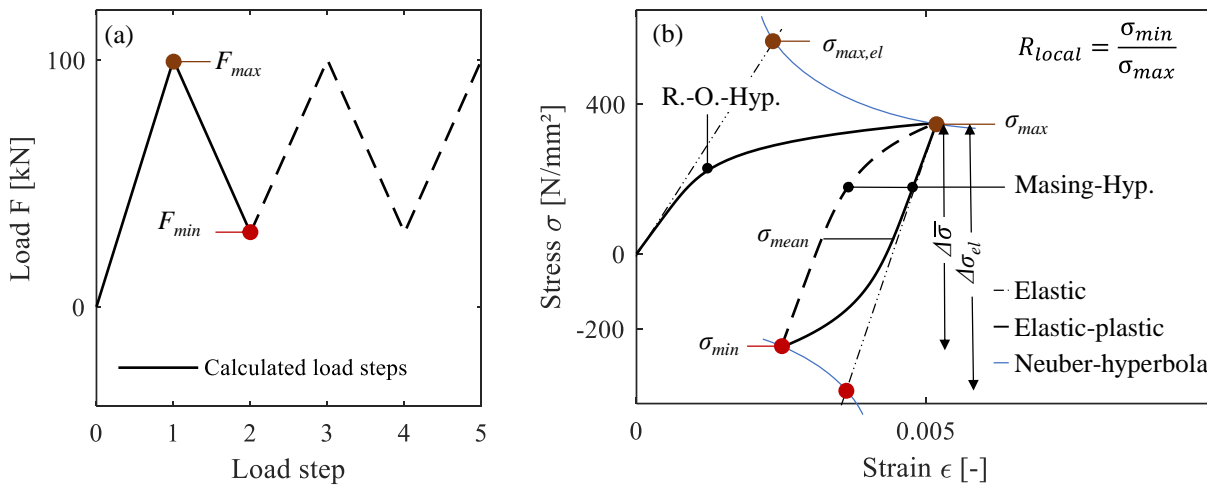


**Figure 1-9: Procedure of calculating the local mean stress ratio  $R_{local}$**

Nykänen and Björk [85,86] applied this approach to analyse the influence of residual stresses from shot peening on butt-welded joints while Ahola et al. [67,89,90] applied it on fillet-welded joints with different post weld treatments and on high-strength steels.

However, the presented approach is not applied on corroded welded components yet. Hence, another objective of this thesis is to apply this approach and evaluate the impact of residual stresses on the fatigue strength of corroded welded joints.

### 1.3 Research objectives and structure of the thesis

#### 1.3.1 Research objectives

In summary, the following research objectives can be identified from the state of the art, which will be addressed in this thesis:

- How can the actual corroded condition be captured and how can it be modelled numerically?
- If the actual corroded condition can be modelled based on 3D-scans of the real surface, can the stress concentrations be correlated to the fatigue strength?
- When the fatigue strength is not correlated to the elastic stress concentrations, can the effective stresses including the micro-support effect be correlated to the fatigue strength?
- If the micro-support has to be taken into account for the calculation of the fatigue-driving stresses, which methods are most suitable (TCD or IGM)?
- If the micro-support consideration can be incorporated in the numerical analysis with the IGM approach, how is the weighting factor of the surrounding volume determined?
- Which FAT curve should be used for the fatigue analysis, when fatigue-driving stresses are determined with the IGM approach?
- When the impact of geometrical changes due to pitting corrosion in plain steel or the change in weld geometry is considered in the analysis of stresses, how can the impact of material embrittlement due to corrosion be considered?
- How can the beneficial residual stresses from clean blasting be taken into account in order to exploit load-bearing reserves?
- How can the findings regarding the aforementioned objectives be applied on real corroded structures, as all analysis were carried out on pre-corroded specimen in the laboratory?

#### 1.3.2 Structure of the thesis

In order to tackle these objectives, a series of experimental and numerical analysis were performed in this thesis. The schematic structure of the thesis is depicted in Figure 1-10. Section 1 includes the motivation for this work and a short state of the art. In section 2 to 6 the papers are presented. Finally, in section 7 the work is summarized and an outlook for future research is given.

In the **first paper**, the impact of the surface geometry, particularly in the context of pitting corrosion, was investigated with different modelling techniques, as pitting corrosion can lead to significant stress concentrations.

In order to link the stress concentration analysed in the first paper to the fatigue strength, fatigue tests accompanied by digital image correlation (DIC) measurements were performed on corroded specimens in the **second paper**. Moreover, the specimens were transformed into 3D-models using the reverse engineering procedure, introduced in the first paper, and were analysed numerically in respect to their stress concentrations.

The fatigue tests in the second paper successfully established a qualitative link between hotspots of the stress concentrations and crack location. For a quantitative relationship between notch stress concentration and anticipated fatigue life, the micro-support effect, addressed by applying the implicit

gradient model (IGM), was considered in the **third paper**. Additionally, the third paper explored the practical applicability of these methods, including the potential use of the replica technique.

Steel structures often include numerous welded joints, which act differently to corrosion in base material, because of the already existing stress concentrations from weld geometry or residual stresses from welding. Hence, further experimental investigations were carried out in the **fourth paper**. This involved conducting fatigue tests on corroded fillet- and butt-welded specimens as well as comparative fatigue tests on as-welded and clean-blasted specimens as references. Additionally, 3D surface scans and residual stress measurements for various specimen geometries and surface conditions were performed.

To incorporate the findings of the fourth paper into predictions of fatigue strength of corroded welded joints, the **fifth paper** evaluated the fatigue tests using local fatigue approaches. Analogous to previous studies, 3D-models were established from scans and used for the numerical analysis. This approach enabled the consideration of stress concentrations arising from weld seams (including corrosion-induced changes) and structural stress magnifications from misalignments. The IGM was applied according the third paper to account for the micro-support effect, while mean stress correction factors were used to address the impact from residual stresses. Finally, the replica technique for welds is presented, enabling application of the findings on real structural components.

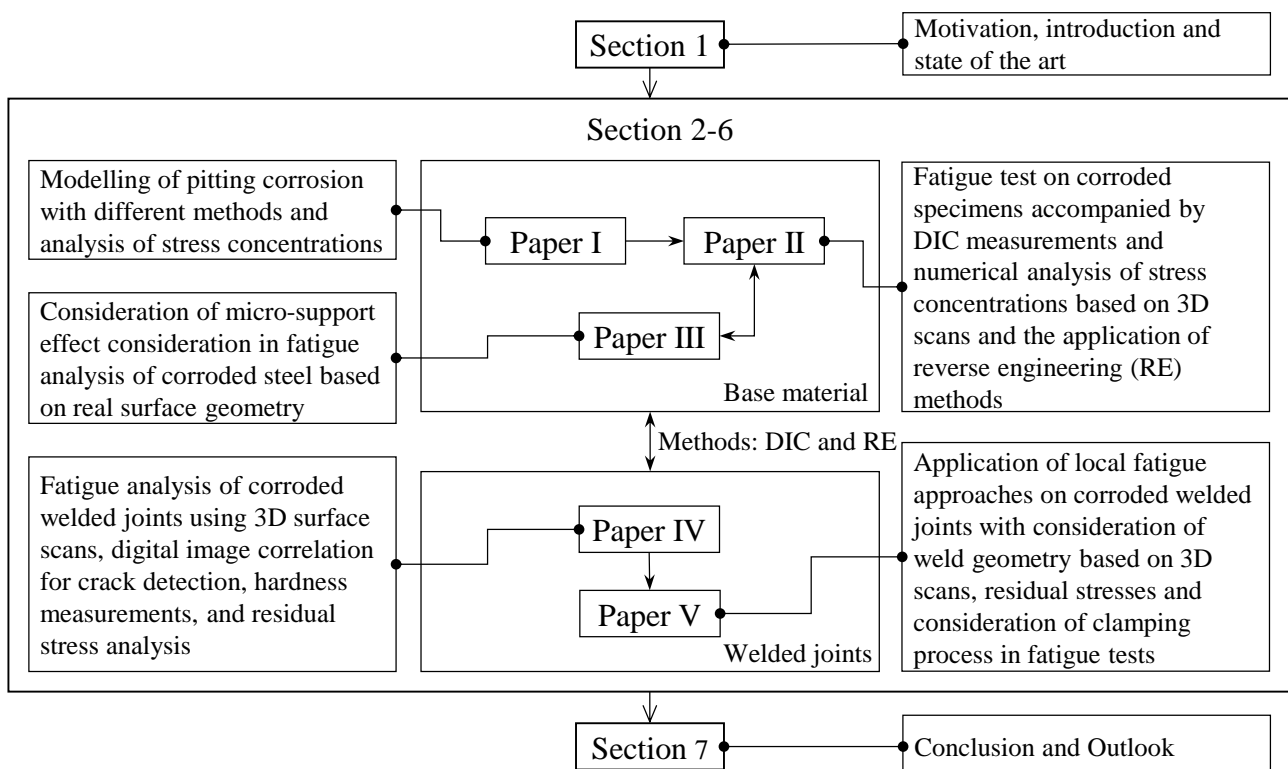


**Figure 1-10: Schematic overview of the thesis**



## 1.4 Limitations

The influence of corrosion on the fatigue strength of steel structures depends on many individual aspects that could not be addressed in this work to the full extent. Therefore, this work has some limitations, which are summarized as follows:

1. All experimental investigations were carried out on pre-corroded specimens. In papers I to III, the investigations were carried out on corroded base material taken from a ballast tank of a ship, without precise knowledge of the corrosion exposure. The specimens were assumed to represent a limiting condition due to the very strong formation of pitting corrosion. The welded specimens investigated in paper IV and V were stored for one month in salt spray chambers, which represents an accelerated corrosion test. However, a time-related correlation with real environmental conditions was not possible in either case.
2. In contrast to the mechanical impact of corrosion on the notch, the impact of embrittlement is not covered on a physical level. Within the framework of this work, the influence of corrosion on base material (paper III) was considered by calibration of the weighting factor on the fatigue test results, while in the case of welded joints (paper V), the use of reduction factors was recommended, based on visible differences in the SN-curves. However, investigations on a physical level requires the derivation of material parameters, such as the fatigue crack propagation threshold ( $\Delta K_{th}$ ) and the fatigue limit ( $\Delta\sigma_0$ ), for corroded materials. This was not part of the thesis.
3. The investigation provides only a snapshot of surface geometry and (for welded joints) residual stresses, neglecting change of both due to degradation processes. Moreover, it does not consider the simultaneous effects of corrosion and cyclic loading.
4. Finally, the study does not consider how cyclic loads may impact residual stresses in corroded welded joints.

## 1.5 References

- [1] Nations U. Net Zero Coalition | United Nations. [September 22, 2023]; Available from: <https://www.un.org/en/climatechange/net-zero-coalition>.
- [2] Det Norske Veritas. Corrosion protection for wind turbines(DNV-GL RP-0416); 2016.
- [3] Det Norske Veritas. Support structures for wind turbines(ST-0126); 2018.
- [4] Bundesanstalt für Wasserbau. Korrosionsschutz von Offshore-Bauwerken zur Nutzung der Windenergie - Teil 1: Allgemeines(VGB-S-021-01-2018-04-DE); 2018.
- [5] Momber AW, Nattkemper TW, Langenkämper D, Möller T, Brün D, Schaumann P et al. A data-based model for condition monitoring and maintenance planning for protective coating systems for wind tower structures. *Renewable Energy* 2022;186:957–73. <https://doi.org/10.1016/j.renene.2022.01.022>.

- 
- [6] Momber AW. Quantitative performance assessment of corrosion protection systems for offshore wind power transmission platforms. *Renewable Energy* 2016;94:314–27. <https://doi.org/10.1016/j.renene.2016.03.059>.
- [7] Momber A, Nattkemper T, Langenkämper D, Möller T, Brün D, Schaumann P et al. Digitalisierung und Verarbeitung von Sensordaten für die Zustandsbewertung von Oberflächenschutzsystemen stählerner Türme von Onshore-Windenergieanlagen. *Stahlbau* 2021. <https://doi.org/10.1002/stab.202100020>.
- [8] International Standards Organization. ISO 9233: Corrosion of metals and alloys — Corrosivity of atmospheres(ISO 9223); 2012.
- [9] Jeffrey R, Melchers RE. The changing topography of corroding mild steel surfaces in seawater. *Corrosion Science* 2007;49(5):2270–88. <https://doi.org/10.1016/j.corsci.2006.11.003>.
- [10] Melchers R. A Review of Trends for Corrosion Loss and Pit Depth in Longer-Term Exposures. *Corros. Mater. Degrad.* 2018;1(1):42–58. <https://doi.org/10.3390/cmd1010004>.
- [11] Xu S, Wang Y. Estimating the effects of corrosion pits on the fatigue life of steel plate based on the 3D profile. *International Journal of Fatigue* 2015;72:27–41. <https://doi.org/10.1016/j.ijfatigue.2014.11.003>.
- [12] Deutsches Institut für Normung e.V. Korrosion von Metallen in Seewasser und Seeatmosphäre – Teil 1: Begriffe, Grundlagen;(DIN 81249-1); 2011.
- [13] Liang X, Sheng J, Wang K. Investigation of the mechanical properties of steel plates with artificial pitting and the effects of mutual pitting on the stress concentration factor. *Results in Physics* 2019;14:102520. <https://doi.org/10.1016/j.rinp.2019.102520>.
- [14] Xiang L, Pan J, Chen S. Analysis on the stress corrosion crack inception based on pit shape and size of the FV520B tensile specimen. *Results in Physics* 2018;9:463–70. <https://doi.org/10.1016/j.rinp.2018.03.005>.
- [15] Xu S, Qiu B. Experimental study on fatigue behavior of corroded steel. *Materials Science and Engineering: A* 2013;584:163–9. <https://doi.org/10.1016/j.msea.2013.07.006>.
- [16] Neuber H. Kerbspannungslehre: Theorie der Spannungskonzentration ; genaue Berechnung der Festigkeit. 4th ed. Berlin: Springer; 2001.
- [17] Cerit M. Corrosion pit-induced stress concentration in spherical pressure vessel. *Thin-Walled Structures* 2019;136:106–12. <https://doi.org/10.1016/j.tws.2018.12.014>.
- [18] Huang Y, Wei C, Chen L, Li P. Quantitative correlation between geometric parameters and stress concentration of corrosion pits. *Engineering Failure Analysis* 2014;44:168–78. <https://doi.org/10.1016/j.engfailanal.2014.05.020>.
- [19] Hou J, Song L. Numerical Investigation on Stress Concentration of Tension Steel Bars with One or Two Corrosion Pits. *Advances in Materials Science and Engineering* 2015;2015:1–7. <https://doi.org/10.1155/2015/413737>.

- 
- [20] Revie RW, Uhlig HH. Corrosion and corrosion control: An introduction to corrosion science and engineering. Hoboken, New Jersey: Wiley-Interscience a John Wiley & Sons Inc. Publication; 2008.
- [21] Marcus P. Corrosion mechanisms in theory and practice. 3rd ed. Boca Raton, Fla.: CRC Press; 2012.
- [22] Le Li, Mojtaba Mahmoodian, Chun-Qing Li, Dilan Robert. Effect of corrosion and hydrogen embrittlement on microstructure and mechanical properties of mild steel.
- [23] Mehmanparast A, Brennan F, Tavares I. Fatigue crack growth rates for offshore wind monopile weldments in air and seawater: SLIC inter-laboratory test results. *Materials & Design* 2017;114:494–504. <https://doi.org/10.1016/j.matdes.2016.10.070>.
- [24] Vosikovskiy O. Fatigue-Crack Growth in an X-65 Line-Pipe Steel at Low Cyclic Frequencies in Aqueous Environments. *J. Eng. Mater. Technol* 1975;97(4):298–304. <https://doi.org/10.1115/1.3443302>.
- [25] Thorpe TW, Scott PM, Rance A, Silvester D. Corrosion fatigue of BS 4360:50D structural steel in seawater. *International Journal of Fatigue* 1983;5(3):123–33. [https://doi.org/10.1016/0142-1123\(83\)90025-7](https://doi.org/10.1016/0142-1123(83)90025-7).
- [26] Larrosa NO, Akid R, Ainsworth RA. Corrosion-fatigue: a review of damage tolerance models. *International Materials Reviews* 2018;63(5):283–308. <https://doi.org/10.1080/09506608.2017.1375644>.
- [27] European Committee for Standardization. Eurocode 3 - Design of steel structures - Part 1-9: Fatigue(EN 1993-1-9); 2020.
- [28] Det Norske Veritas - Germanischer Lloyd. Fatigue design of offshore steel structures(DNV-GL RP-C203); 2019.
- [29] Hobbacher AF. Recommendations for Fatigue Design of Welded Joints and Components. Cham: Springer International Publishing; 2016.
- [30] Braun M, Milaković A-S, Renken F, Fricke W, Ehlers S. Application of Local Approaches to the Assessment of Fatigue Test results obtained for Welded Joints at Sub-Zero Temperatures; 2020.
- [31] Det Norske Veritas. Fatigue Assessment of Ship Structures(Classification Notes No. 30.7); 2014.
- [32] Health & Safety Executive. Background to new fatigue guidance for steel joints and connections in offshore structures(OTH 92 390); 1998.
- [33] Bundesanstalt für Wasserbau. Merkblatt: Bewertung der Tragfähigkeit bestehender Verschlüsse im Stahlwasserbau (TbVS); 2018.
- [34] British Standards Institution. Guide to fatigue design and assessment of steel products(BS 7608:2014+A1:2015); 2014.

- [35] Hensel J, Eslami H, Nitschke-Pagel T, Dilger K. Fatigue Strength Enhancement of Butt Welds by Means of Shot Peening and Clean Blasting. *Metals* 2019;9(7):744. <https://doi.org/10.3390/met9070744>.
- [36] Guilemany JM, Llorca-Isern N, Szabo PJ. Residual stress characterisation of grit blasted steel surfaces. *Surface Engineering* 1996;12(1):77–9. <https://doi.org/10.1179/sur.1996.12.1.77>.
- [37] Gericke A, Glienke R. Untersuchung des Reinigungsstrahlens als Nahtnachbehandlungsmethode zur Verbesserung der Schwingfestigkeit geschweißter Strukturen. *DVS*;2018.
- [38] Radaj D, Vormwald M. Ermüdungsfestigkeit: Grundlagen für Ingenieure. 3rd ed. Berlin, Heidelberg: Springer-Verlag Berlin Heidelberg; 2007.
- [39] Fiedler M, Vormwald M. Introduction to the new FKM guideline which considers nonlinear material behaviour. *MATEC Web Conf.* 2018;165:10014. <https://doi.org/10.1051/matec-conf/201816510014>.
- [40] Masendorf L, Burghardt R, Wächter M, Esderts A. Determination of Local Stresses and Strains within the Notch Strain Approach: The Efficient and Accurate Calculation of Notch Root Strains Using Finite Element Analysis. *Applied Sciences* 2021;11(24):11656. <https://doi.org/10.3390/app112411656>.
- [41] Radaj D, Vormwald M. *Fatigue Assessment Methods*. Dordrecht: Springer; 2012.
- [42] Radaj D, Vormwald M. *Advanced methods of fatigue assessment*. Heidelberg: Springer; 2013.
- [43] Ladinek M, Niederwanger A, Lang R, Schmid J, Timmers R, Lener G. The strain-life approach applied to welded joints: Considering the real weld geometry. *Journal of Constructional Steel Research* 2018;148:180–8. <https://doi.org/10.1016/j.jcsr.2018.04.024>.
- [44] ASTM International. *Standard Test Method for Strain-Controlled Fatigue Testing (ASTM E606)*; 2019.
- [45] International Standards Organization. *Metallic materials - Fatigue testing - Axial-strain-controlled method (ISO 12106)*; 2017.
- [46] Radaj D, Sonsino CM, Fricke W. *Fatigue assessment of welded joints by local approaches*. 2nd ed. Cambridge: Woodhead Publ. [u.a.]; 2006.
- [47] Sonsino CM, Fricke W, Bruyne F de, Hoppe A, Ahmadi A, Zhang G. Notch stress concepts for the fatigue assessment of welded joints – Background and applications. *International Journal of Fatigue* 2012;34(1):2–16. <https://doi.org/10.1016/j.ijfatigue.2010.04.011>.
- [48] Lener G, Lang R, Ladinek M, Timmers R. A numerical method for determining the fatigue strength of welded joints with a significant improvement in accuracy. *Procedia Engineering* 2018;213:359–73. <https://doi.org/10.1016/j.proeng.2018.02.036>.
- [49] Schaumann P, Schürmann K, Pittner A, Rethmeier M. Automatically Welded Tubular X-Joints for Jacket Substructures: Prediction of the Technical Fatigue Crack Location. *ce/papers* 2019;3(3-4):823–8. <https://doi.org/10.1002/cepa.1140>.

- [50] Neuber H. Kerbspannungslehre: Grundlagen für genaue Festigkeitsberechnung mit Berücksichtigung von Konstruktionsform und Werkstoff. Berlin, Heidelberg, s.l.: Springer Berlin Heidelberg; 1958. <https://doi.org/10.1007/978-3-642-53069-2>.
- [51] Lazzarin P, Berto F. Some Expressions for the Strain Energy in a Finite Volume Surrounding the Root of Blunt V-notches. *Int J Fract* 2005;135(1-4):161–85. <https://doi.org/10.1007/s10704-005-3943-6>.
- [52] Berto F, Lazzarin P. A review of the volume-based strain energy density approach applied to V-notches and welded structures. *Theoretical and Applied Fracture Mechanics* 2009;52(3):183–94. <https://doi.org/10.1016/j.tafmec.2009.10.001>.
- [53] Song W, Liu X, Berto F, Wang P, Fang H. Fatigue failure transition analysis in load-carrying cruciform welded joints based on strain energy density approach. *Fat Frac Eng Mat Struct* 2017;40(7):1164–77. <https://doi.org/10.1111/ffe.12588>.
- [54] Taylor D. The theory of critical distances. *Engineering Fracture Mechanics* 2008;75(7):1696–705. <https://doi.org/10.1016/j.engfracmech.2007.04.007>.
- [55] Susmel L. The theory of critical distances: a review of its applications in fatigue. *Engineering Fracture Mechanics* 2008;75(7):1706–24. <https://doi.org/10.1016/j.engfracmech.2006.12.004>.
- [56] Susmel L, Taylor D. The Theory of Critical Distances to estimate lifetime of notched components subjected to variable amplitude uniaxial fatigue loading. *International Journal of Fatigue* 2011;33(7):900–11. <https://doi.org/10.1016/j.ijfatigue.2011.01.012>.
- [57] Peerlings RH, Borst R de, Brekelmans WAM, Vree JHP de. Computational Modelling of Gradient-Enhanced Damage for Fracture and Fatigue Problems. In: Owen DRJ, Oñate E, editors. *Computational plasticity: Fundamentals and applications ; proceedings of the fourth international conference held in Barcelona, Spain, 3th - 6th April, 1995 ; [a book in memoriam of Juan Carlos Simo*. Swansea: Pineridge Press; 1995, p. 975–986.
- [58] Peerlings RHJ, Brekelmans WAM, Borst R de, Geers MGD. Gradient-enhanced damage modelling of high-cycle fatigue. *Int. J. Numer. Meth. Engng.* 2000;49(12):1547–69.
- [59] Askes H, Livieri P, Susmel L, Taylor D, Tovo R. Intrinsic material length, Theory of Critical Distances and Gradient Mechanics: analogies and differences in processing linear-elastic crack tip stress fields. *Fatigue Fract Engng Mater Struct* 2013;36(1):39–55. <https://doi.org/10.1111/j.1460-2695.2012.01687.x>.
- [60] Peterson R. Notch sensitivity. *Metal Fatigue* 1959:293–306.
- [61] H Neuber. Neuber H (1968) Über die Berücksichtigung der Spannungskonzentration bei Festigkeitsberechnungen. *Konstruktion* 20(7):245–251. *Konstruktion* 1968;20(7):245.
- [62] Baumgartner J, Schmidt H, Ince E, Melz T, Dilger K. Fatigue assessment of welded joints using stress averaging and critical distance approaches. *Weld World* 2015;59(5):731–42. <https://doi.org/10.1007/s40194-015-0248-x>.

- [63] Sheppard SD. Field Effects in Fatigue Crack Initiation: Long Life Fatigue Strength. *J. Mech. Des* 1991;113(2):188–94. <https://doi.org/10.1115/1.2912768>.
- [64] Bellett D, Taylor D, Marco S, Mazzeo E, Guillois J, Pircher T. The fatigue behaviour of three-dimensional stress concentrations. *International Journal of Fatigue* 2005;27(3):207–21. <https://doi.org/10.1016/j.ijfatigue.2004.07.006>.
- [65] Taylor, Wang. The validation of some methods of notch fatigue analysis. *Fatigue & Fracture of Engineering Materials & Structures* 2000;23(5):387–94. <https://doi.org/10.1046/j.1460-2695.2000.00302.x>.
- [66] Susmel L, Taylor D. Fatigue design in the presence of stress concentrations. *The Journal of Strain Analysis for Engineering Design* 2003;38(5):443–52. <https://doi.org/10.1243/03093240360713496>.
- [67] Ahola A, Lipiäinen K, Afkhami S, Lilja H, Björk T. Fatigue performance of the welded details of an old, demolished steel railway bridge. *Engineering Structures* 2022;256:113966. <https://doi.org/10.1016/j.engstruct.2022.113966>.
- [68] Braun M, Müller AM, Milaković A-S, Fricke W, Ehlers S. Requirements for stress gradient-based fatigue assessment of notched structures according to theory of critical distance. *Fatigue & Fracture of Engineering Materials & Structures* 2020;43(7):1541–54. <https://doi.org/10.1111/ffe.13232>.
- [69] Peerlings R. Enhanced damage modelling for fracture and fatigue. Technische Universiteit Eindhoven; 1999.
- [70] Tovo R, Livieri P. An implicit gradient application to fatigue of sharp notches and weldments. *Engineering Fracture Mechanics* 2007;74(4):515–26. <https://doi.org/10.1016/j.engfrac-mech.2006.06.009>.
- [71] Tovo R, Livieri P. An implicit gradient application to fatigue of complex structures; 2008.
- [72] Lang R, Ladinek M, Lener G. Über die Anpassung eines fortschrittlichen Stützwirkungsansatzes für das Kerbspannungskonzept. *Stahlbau* 2017;86(6):470–82. <https://doi.org/10.1002/stab.201710494>.
- [73] Karsten Schürmann. Fatigue Behavior of Automatically Welded Tubular Joints for Offshore Wind Energy Substructures: Dissertation; 2021.
- [74] Zhang G. Method of effective stress for fatigue: Part I – A general theory. *International Journal of Fatigue* 2012;37:17–23. <https://doi.org/10.1016/j.ijfatigue.2011.09.018>.
- [75] Stüssi F. Zur Theorie der Dauerfestigkeit 1956. <https://doi.org/10.5169/SEALS-6085>.
- [76] Gerber H. Bestimmung der zulässigen Spannungen in Eisenkonstruktionen. *Zeitschrift der Bayerischen Architekten und Ingenieure Vereins*;1874(6):101–10.
- [77] Goodman J. *Mechanics applied to engineering*. 9th ed. New York: Longmans, Green & Co; 1899.

- [78] Soderberg CR. Factor of safety and working stress. *Journal of Applied Mechanics (ASME)* 1939(52):13–28.
- [79] Morrow J. Fatigue properties of metals. *Fatigue Design Handbook, Advances in Engineering* 1968:21–9.
- [80] Torres M. An evaluation of shot peening, residual stress and stress relaxation on the fatigue life of AISI 4340 steel. *International Journal of Fatigue* 2002;24(8):877–86. [https://doi.org/10.1016/S0142-1123\(01\)00205-5](https://doi.org/10.1016/S0142-1123(01)00205-5).
- [81] Dalaei K, Karlsson B, Svensson L-E. Stability of shot peening induced residual stresses and their influence on fatigue lifetime. *Materials Science and Engineering: A* 2011;528(3):1008–15. <https://doi.org/10.1016/j.msea.2010.09.050>.
- [82] Kim J-C, Cheong S-K, Noguchi H. Residual stress relaxation and low- and high-cycle fatigue behavior of shot-peened medium-carbon steel. *International Journal of Fatigue* 2013;56:114–22. <https://doi.org/10.1016/j.ijfatigue.2013.07.001>.
- [83] Smith K, Watson P, Topper T. A stress–strain function for the fatigue of metals (stress-strain function for metal fatigue including mean stress effect)-1970. *Journal of Materials* 1970;1970.
- [84] Fiedler M, Wächter M, Varfolomeev I, Vormwald M, Esderts A. *FKM-Richtlinie Nichtlinear: Rechnerischer Festigkeitsnachweis unter expliziter Erfassung nichtlinearen Werkstoffverformungsverhaltens für Bauteile aus Stahl, Stahlguss und Aluminiumknetlegierungen*. 1st ed. Frankfurt am Main: VDMA Verlag GmbH; 2019.
- [85] T. Nykänen and T. Björk. A new proposal for assessment of the fatigue strength of steel butt-welded joints improved by peening (HFMI) under constant amplitude tensile loading.
- [86] Nykänen T, Björk T. Assessment of fatigue strength of steel butt-welded joints in as-welded condition – Alternative approaches for curve fitting and mean stress effect analysis. *Marine Structures* 2015;44:288–310. <https://doi.org/10.1016/j.marstruc.2015.09.005>.
- [87] Ramberg W, Osgood WR. Description of stress-strain curves by three parameters. Washington D.C.: National Advisory Committee for Aeronautics; 1943.
- [88] G. Masing. *Eigenspannungen und Verfestigung beim Messing*.
- [89] Ahola A, Skriko T, Björk T. Fatigue strength assessment of ultra-high-strength steel fillet weld joints using 4R method. *Journal of Constructional Steel Research* 2020;167:105861. <https://doi.org/10.1016/j.jcsr.2019.105861>.
- [90] Ahola A, Muikku A, Braun M, Björk T. Fatigue strength assessment of ground fillet-welded joints using 4R method. *International Journal of Fatigue* 2021;142:105916. <https://doi.org/10.1016/j.ijfatigue.2020.105916>.





## 2 Modelling of pitting corrosion (Paper I)

This section contains a reprint of the article: Shojai, Sulaiman; Schaumann, Peter; Brömer, Tim (2022): Probabilistic modelling of pitting corrosion and its impact on stress concentrations in steel structures in the offshore wind energy. In: *Marine Structures* 84, S. 103232. DOI: 10.1016/j.marstruc.2022.103232.

### Background

Offshore steel structures and bridges are suspected to corrosion under harsh environmental conditions. This can lead to embrittlement of the near surface material and also to changes in the surface geometry. The latter in turn, can lead to high stress concentrations and thus to a reduction in fatigue strength, especially in the case of pitting corrosion, where changes in the surface geometry occur locally. The influence of the stress concentrations can be taken into account in local fatigue concepts such as the notch strain or notch stress approach. For this purpose, it is necessary to reliably model the stress concentrations resulting from the surface geometry.

### Overview

In this paper, different models for the determination of stress concentrations are investigated and compared. In particular, the single-pit, double-pit, random-field and real-surface model based on reverse engineering are examined. For the single-pit model, data of pit geometry (pit width and pit depth) were first obtained from corroded steel plates and then stress concentrations were calculated numerically on this basis. For the double-pit model, it was assumed that the decisive stresses do not occur at a single pit, but in the area of the overlap of two different pits. For the random-field model, corroded surfaces were created with a random-field generator and investigated numerically. Finally, the existing corroded plates were captured by 3D-scanners and then reverse engineered into numerical models (real-surface model). By examining a large number of samples and taking into account the statistical distributions of the input parameters (pit depth and pit width for single-pit and double-pit models), also the corresponding statistical distributions of the stress concentrations could be determined for all models.

### Conclusion

It has been shown in this paper that the random-field and single-pit model are not able to reproduce the stress concentrations with sufficient accuracy. From the results of the real-surface models, it was found that the highest stresses are not at the pit bottom of a single-pit, but in most cases at the overlap of two pits. These lead to high stress concentrations, which can only be reproduced by the double-pit model. Furthermore, it could be shown that there is good agreement between double-pit and the real-surface models regarding the statistical distribution of the stress concentrations. In addition to the deterministic fatigue strength analysis based on local fatigue approaches, the results allow a reliability-based analysis of corroded components.

It should be noted, that the stress concentrations were based on linear elastic material definition, neglecting the local effects from the fatigue process, such as the micro-support effect. A correlation between the elastic stress concentrations and their actual influence on the fatigue strength can only

be made if respective corroded specimens are tested against fatigue strength and the resulting effective stress concentrations are determined. Therefore, in the next article, fatigue tests were performed on corroded specimens, which were also numerically modelled with the reverse engineering method presented here.

### **Authors Contribution**

The experimental acquisition of the geometrical data, the numerical modelling, the paper conceptualization, methodology, validation, formal analysis, investigation, writing of the original draft and visualization were performed by the first author. Prof. Schaumann supervised the work presented in this paper and was responsible for the funding acquisition and project administration. Tim Brömer did preliminary research as part of his bachelor thesis under the supervision of the first author, generated the random-field models and co-wrote the respective part.

## **Probabilistic modelling of pitting corrosion and its impact on stress concentrations in steel structures in the offshore wind energy <sup>1</sup>**

### **2.1 Abstract**

Supporting structures for offshore wind turbines and the appropriate transformer platforms are highly susceptible to corrosion. Especially the phenomenon of pitting corrosion is very crucial, since this leads to local stress concentrations and hence has an impact on the fatigue life of marine structures. Despite corrosion protection systems, corrosion cannot be completely avoided, which can lead to pitting corrosion on the steel surface. Stress concentrations from pitting corrosion are not explicitly considered within the design of offshore structures. This is only possible by using local fatigue concepts, which requires a realistic modelling of corroded steel surfaces and the corresponding stress concentrations. Hence, in this work, three different models for evaluating the stress concentrations were developed: single-pit model, double-pit model and random fields model. The results were compared to the stress concentrations of a real corroded surface, which was analysed with the reverse engineering method. In all models, the probability-based determination of the stress concentration was the main focus in order to consider the characteristic scatter in pitting corrosion. The comparison of the three models with the real surface shows a good agreement with the double-pit model. It becomes evident, that the single-pit and the random fields model are not sufficient for modelling the stress concentrations. However, derived stress concentrations from the double-pit model and the real surface model can be utilized for risk and reliability-based analysis with local fatigue strength concepts.

Keywords: offshore-wind, corrosion, corrosion fatigue, pitting corrosion, stress concentrations, local fatigue concept, reverse engineering, random fields, monte-carlo

### **2.2 Introduction**

Marine structures such as sheet piles, pipelines, ships or support structures for offshore wind turbines (OWTs) and platforms are mainly made of steel and are highly susceptible to corrosion under maritime environmental conditions. Especially for OWTs, which in addition are exposed to cyclic loads, this aspect becomes more important. In practical applications, corrosion protection can be achieved by means of protective coatings, sacrificial anodes, external current or a combination of them. Therefore, special requirements are set for the corrosion protection system of OWTs [1–3]. Despite these preventive measures, corrosion cannot be completely avoided during the life time of OWTs of approx.

---

<sup>1</sup> [Shojai, S., Schaumann, P., Brömer, T., Marine Structures, 2022, 84, S.103232. DOI: 10.1016/j.marstruc.2022.103232.](https://doi.org/10.1016/j.marstruc.2022.103232)

20 to 25-years. Hence, some recently published research aims to quantify the state of corrosion protection as well as the state of corroded steel surfaces based on real data [4–6]. Since repairs of the corrosion protection system or recoating of the support structures at sea are very cost-intensive, the technical evaluation of further operation is of great importance, after (partial) degradation of the corrosion protection system. For this purpose, the remaining service life under degraded corrosion protection must be determined reliably.

The steel surface below the degraded corrosion protection system has a significant influence on the remaining service life. The steel surface can be uniformly corroded or subjected to pitting corrosion. In most cases it is a combination of both. Uniform corrosion has less influence on fatigue strength, especially since the wall thicknesses of offshore support structures are provided with the so-called "corrosion allowance" in the design process [1]. Pitting corrosion, on the other hand, is very crucial, since it leads to local stress concentrations on the steel surface. Thus, they have an impact on the fatigue life of the structures. The fatigue design of OWTs is predominantly carried out with the nominal stress concept, partly also with the structural stress concept [7]. Stress concentrations from pitting corrosion are not explicitly considered. This is only possible by using local fatigue concepts, like the notch stress or strain approach. This requires a realistic modelling of corroded steel surfaces and the corresponding stress concentrations due to pitting corrosion.

The most common model for pitting corrosion is the power function according to Romanoff [8], which describes the pit growth over time. A more accurate and at the same time complex model is proposed by Melchers in [9,10]. The probabilistic model according to Melchers takes the long-term behaviour, the statistical scatter of the pitting depth and the dependencies of physical and chemical parameters of the environment (temperature, oxygen content, etc.) into account. Other probabilistic models are from Williams et. al. [11] and Valor et. al. [12]. All probabilistic models aim to predict the depth of corrosion and hence avoid a perforation of steel components. However, in case of stress concentrations due to pitting corrosion, the pit width, which determines the shape of the pit, is a key factor. This has been published in many research works regarding stress concentrations due to pitting corrosion [13–16]. Yet in the mentioned probabilistic models, the pit width and the stress concentrations depending on that are not considered. The relationship between the pit width and the stress concentrations is shown as follows. According to DIN 81249-1 [17] pits can be hemispherical, crater-shaped or needle-shaped. In classical notch stress theory of Neuber, the shape of the notch, in this case the pits, can be expressed in terms of a notch radius [18]. The notch stress can then be expressed by:

$$\alpha_k = 1 + 2\sqrt{t/r} \quad (2-1)$$

Here,  $t$  corresponds to the pit depth and  $r$  to the notch radius, which in terms of hemispherical pits can be expressed as follows:

$$r = \frac{t(1 + a^2)}{2} \quad (2-2)$$

Here,  $a$  corresponds to the width ratio, which can be expressed by the ratio  $a=(D/2)/t$ , with the pit width  $D$  and the pit depth  $t$ . When equation (2-2) is inserted into (2-1), the notch stress concentration is given by:

$$\alpha_k = 1 + 2 \sqrt{\frac{2}{1 + a^2}} \quad (2-3)$$

The resulting formula for the notch stress concentration depends only on the width ratio. This matches with the formula from Ahn et. al. and is used mainly for fatigue analysis according to the crack growth concept [19].

$$K_t = 1 + C \sqrt{\frac{2}{1 + a^2}} \quad (2-4)$$

In this equation, C takes the shape of the pits into account. For hemispherical pits, where the stress concentrations occur at the deepest point of the pit, C=1.25 is suggested by Ahn et. al. [19]. Both equations assume that a fatigue failure is initiated at a single pit. However, investigations have shown that, in addition to the pit shape, the interaction of neighbouring pits and thus the spacing of the pits on the surface are relevant as well [20–22]. Moreover, Liang et. al [20] observed, that in case of neighbouring pits, the load direction has an impact on the stress concentrations.

In all the mentioned studies on stress concentrations, the relationship between the determined stress concentration and the actual stress concentration on a corroded surface is neglected. Rather, the studies focus on individual parameters that can influence the stress concentration. A prediction of the existing stresses on a real corroded surface is not given. Furthermore, these studies do not consider the probabilistic behaviour of pitting corrosion and the associated statistical scatter in the stress concentrations.

For this reason, the present paper examines methods and models that can be used to probabilistically determine the stress concentrations from pitting corrosion. This extends the research work on stress concentrations with probabilistic behaviour, which has so far been limited to pitting depth development and enables a more precise prediction of the remaining life time of corroded steel parts in offshore environment. In Figure 2-1 a schematic overview for the investigated models and the associated workflow is illustrated.

In this paper, the probabilistic distributions of a single pit model and a double pit model are investigated. The probabilistic distribution of stress concentrations is determined within a Monte-Carlo simulation. It is assumed, that the double pit model can represent the behaviour of multiple pits, since multiple pits can be simplified to multiple double pits. Data on pit width and pit depths were taken by enumeration from a real specimen.

Additionally, a random field model is introduced. The method has already been applied by Teixeira [23] for uniform corrosion and by Woloszyk et. al. [24,25] for pitting corrosion in order to investigate the tensile behaviour of corroded components. In this paper the random field model is used to investigate the stress concentrations, since the development of corrosion is assumed to be a random process [12].

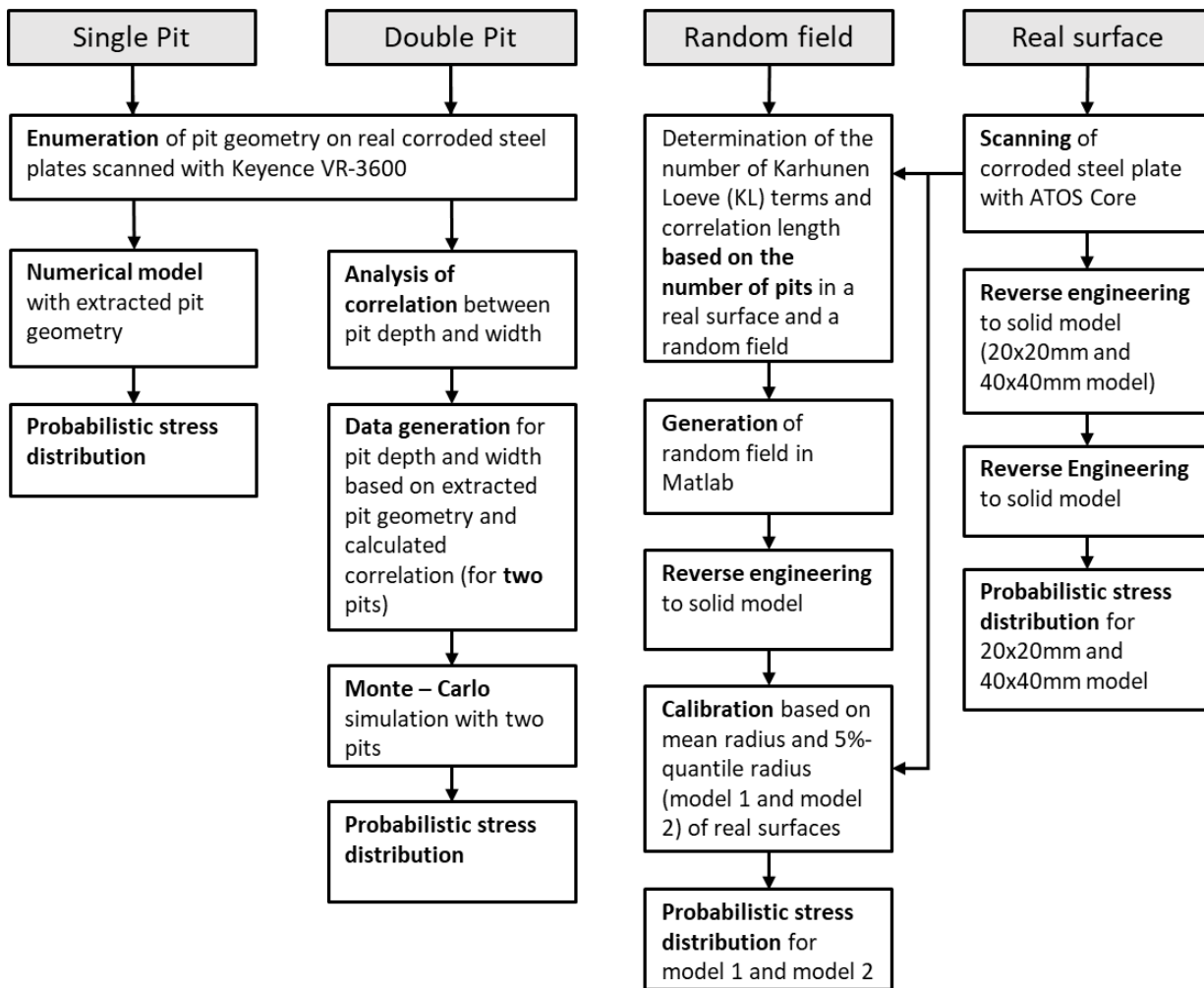


**Figure 2-1: Schematic overview of the investigated models and the associated workflow steps**

Finally, the stress concentrations are evaluated based on real corroded surfaces, as partially performed by Xu et. al. and Kainuma et. al. [26,27]. For obtaining the stress concentrations, in this paper, the reverse engineering method from Schaumann et. al. [28] is applied to corroded samples.

The novelties in this paper can be summarized as follows:

- the single-pit and the double-pit model for stress concentrations are extended to the probabilistic behaviour of pitting corrosion
- random fields are generated for the determination of stress concentrations
- a real steel surface is modelled with the reverse engineering method and the stress concentrations are represented probabilistically

## 2.3 Methods and Experiments

### 2.3.1 Karhunen-Loeve expansion for the random-field model

A random field can be modelled for example with the Karhunen-Loeve (KL) expansion. The theoretical background and the numerical realization are presented by Betz et. al. [29]. The KL expansion is

based on the assumption of a Gaussian random field. This method is based on the theory of a Gaussian random field  $H(x)$ , which is approximated by a series expansion  $\hat{H}(x, \theta)$ :

$$H(x, \theta) = \mu(x) + \sum_{i=1}^{\infty} \sqrt{\lambda_i} \xi_i(\theta) f_i(x) \quad (2-5)$$

The parameter  $\xi_i(\theta)$  is a set of standard normally distributed uncorrelated random variables with:

$$\begin{aligned} E(\xi_i) &= 0 \\ E(\xi_i \xi_j) &= 1 \end{aligned} \quad (2-6)$$

$\mu(x)$  is the function of the expected value of the random field and  $\lambda_i$  and  $f_i(x)$  are the eigenvalues and eigenfunctions of the covariance function  $C(x, x')$ , where  $x$  and  $x'$  are two different coordinates on a surface under consideration.

The covariance function results in

$$C(x, x') = \sum_{i=1}^{\infty} \lambda_i f_i(x) f_i(x') \quad (22-7)$$

and is referred to as a kernel function in this context. The KL extension can be approximated with the help of a series expansion. The eigenvalues  $\lambda_i$  and the associated eigenfunctions  $f_i(x)$  are sorted in descending order and the series is cut off after a finite term  $N$ :

$$\hat{H}(x, \theta) = \mu(x) + \sum_{i=1}^N \sqrt{\lambda_i} \xi_i(\theta) f_i(x) \quad (2-8)$$

The section obtained in this way no longer represents the exact random field, but is seen as an approximation of it. For further study [30] is recommended.

A MATLAB tool is available for generating such a random field using the KL method. This tool works with the OpenCOSSAN engine. More information can be obtained here [31,32].

For creating a random field, some inputs are required. A suitable covariance matrix must be created in conjunction with a variance  $\sigma$  and a correlation length  $L_c$ . The correlation length is a measure of the fluctuation, i.e. the changes in the individual nodes of the random field.

For this purpose, an exponential covariance function of the form

$$C(x, x') = \sigma^2 e^{-\frac{|x-x'|}{L_c}} \quad (2-9)$$

is used. This is followed by the definition of the random field in  $x$ - and  $y$ -direction using the "meshgrid" command. The "StochasticProcess" function integrated in OpenCOSSAN then delivers the series expansion. For this purpose, a set of standard normally distributed uncorrelated random variables, an expected value  $\mu$ , the covariance function, the number of KL-terms as well as the previously generated mesh are required.

### 2.3.2 Pit data acquisition from 3D-scans

The models according to Romanoff [8] and Melchers [9,10] aim mainly to predict perforation of the steel with models for pit growth. Therefore, no data on pit width and pit spacing were collected. In addition, the pit depth refers to the level of the plain surface and does not consider potentially overlying uniform corrosion. This could lead to underestimation of the notch radius and overestimation of the notch stress. Hence, in this work, an enumeration regarding the pit geometry is performed on a corroded sample of former ballast tank, which was investigated in aspects of power spectral density and pit distribution in [33,34]. For this purpose, the sample is recorded with a high-resolution 3D measuring system (Keyence VR-3000, Figure 2-2).

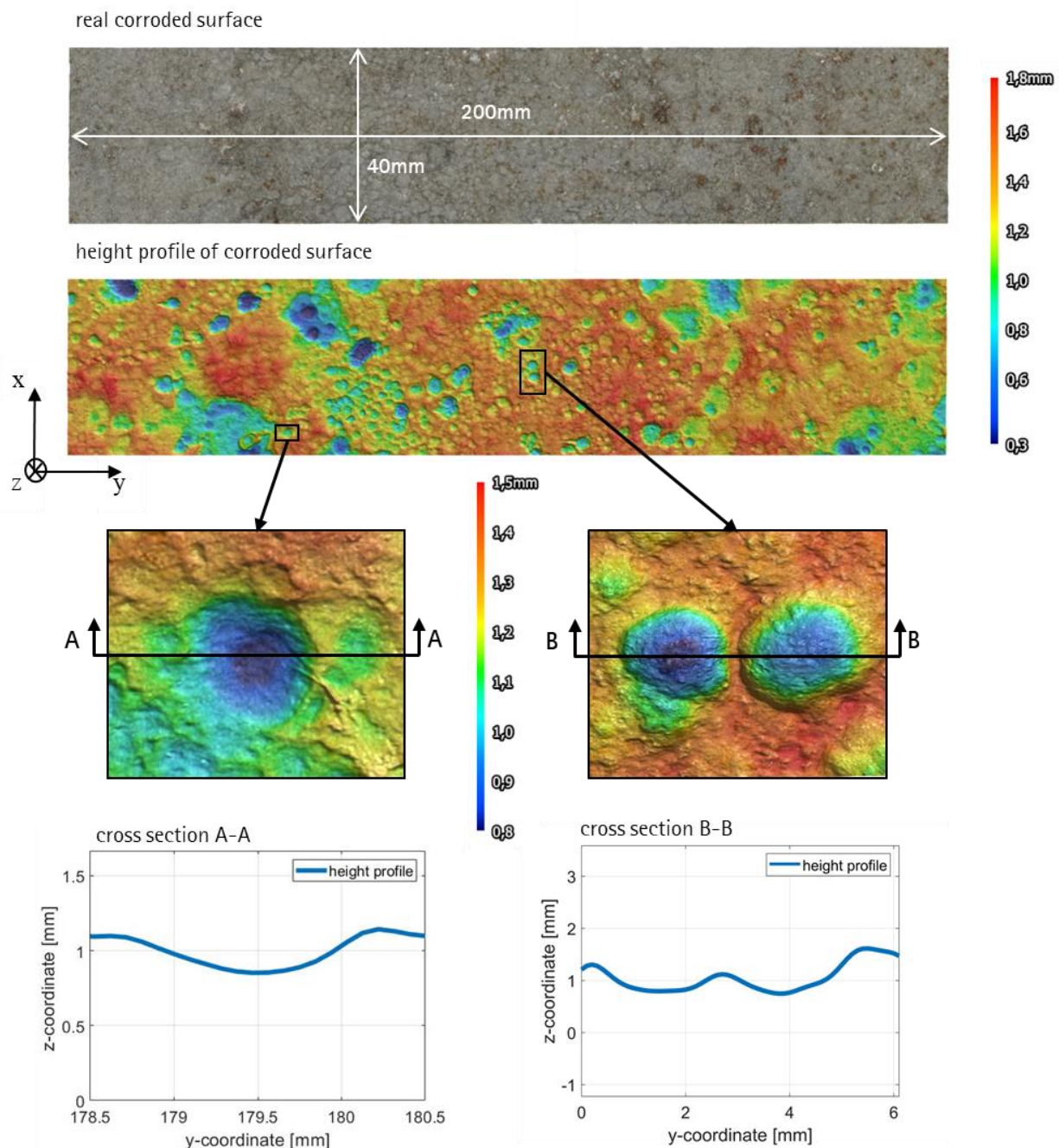


Figure 2-2: High resolution shot of a corroded sample



In Figure 2-3 some examples of interacting pits, mainly double pits, are illustrated. Moreover, some multiple pit interactions can be seen in the plots as well. This underlines the assumption, that multiple pits can be simplified to multiple double pits. Subsequently, data on the pit depth and pit width were collected, the width ratio was determined and statistically evaluated. In

Table 2-1 the obtained statistical data is listed.

Figure 2-4 shows the frequency distribution of the collected data. The pit ratio and the pit depth can be approximately considered as lognormal distributed with mean values of  $\mu=1.71$  and  $\mu=0.58$  and with deviation of  $\sigma=0.43$  and  $\sigma=0.22$ , respectively. The pit shapes are assumed to be hemispherical. Based on these data, the notch stresses can be investigated numerically in chapter 2.4.

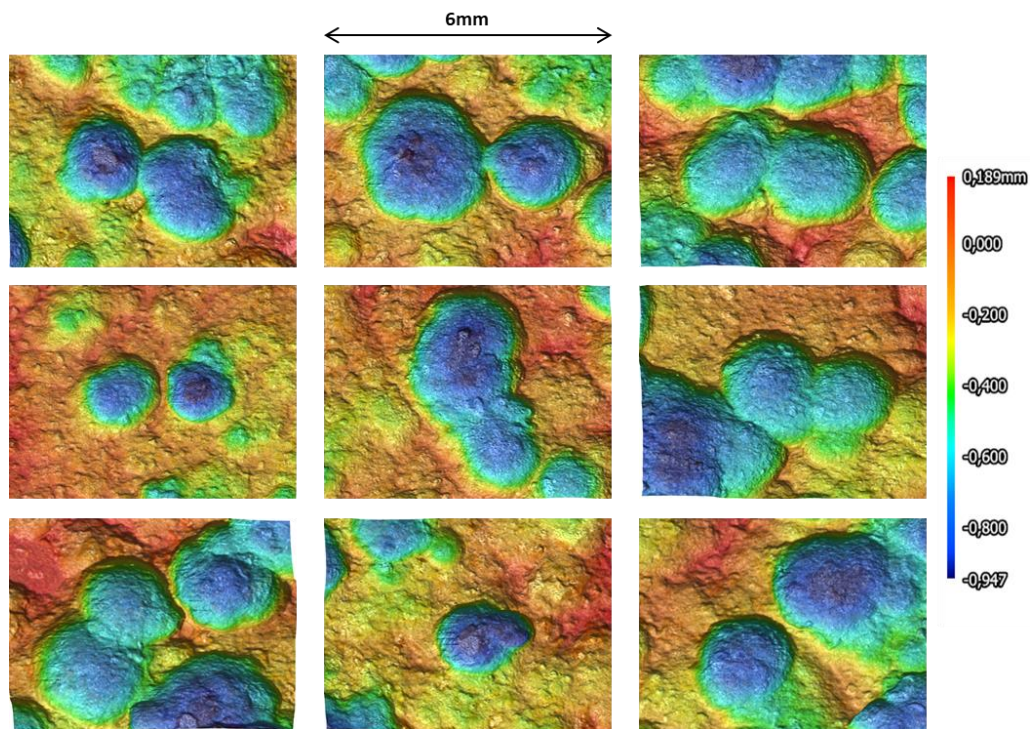
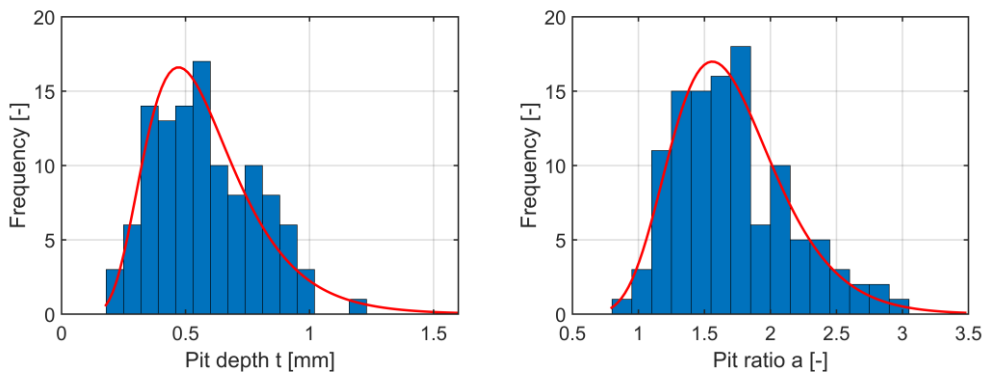


Figure 2-3: Examples for double pits on the real corroded surface scanned in high resolution

Table 2-1: Statistical evaluation of the geometric pit data

	Diameter D [mm]	Depth t [mm]	Ratio a [-]
Distribution	Lognormal	Lognormal	Lognormal
Mean E	1.89	0.58	1.71
Deviation	0.62	0.22	0.43



**Figure 2-4: Frequency diagram for pit depth (left) and pit width ratio (right)**

### 2.3.3 Reverse engineering method for real surface modelling with 3D-scans

For the validation of all other models, an evaluation of the stress concentration for the real corroded surfaces is necessary. For this purpose, the reverse engineering method is used. The reverse engineering method involves scanning the geometry of an existing surface with the aid of digital measuring systems and converting it into a numerical model. The basis for the process is the scanning of surfaces as point clouds. This is done with the industrial 3D-scanner ATOS Core from GOM. From this, faceted geometries can be generated in STL format by polygonization of the point clouds. These can then be assembled into complete components within the ATOS software if the component has been scanned from all perspectives (Figure 2-5, left). The closer the scanner is placed to the sample, the finer the faceting and hence more accurate the representation of the real geometry. The investigated sample is shown Figure 2-5 in STL-format (left) and in original format (right). The sample was scanned from a distance of 50 cm.

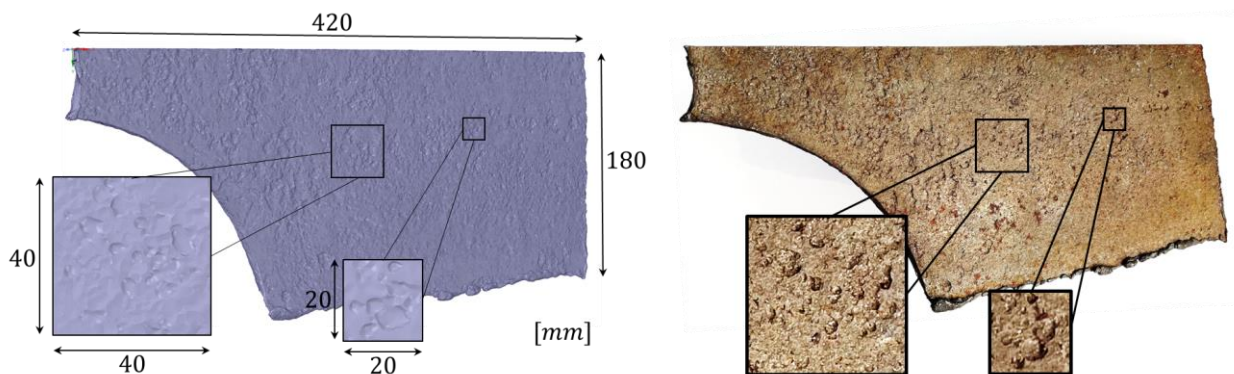


**Figure 2-5: Faceted 3D-scan of corroded sample with ATOS Core in STL-format (left) and original (right)**

## 2.4 Calculation

### 2.4.1 Numerical Modeling

The numerical simulation was performed in Ansys Workbench 2020 R2. For this purpose, quadratic tetrahedral elements (SOLID187) with linear elastic material definition (structural steel) were used. The convergence study was carried out with the adaptive convergence tool of Ansys Workbench. This led to element sizes of up to 0.03mm in the hotspot region.

**Single-Pit:** The numerical simulation was performed on a steel plate with boundary conditions as shown in Figure 2-6 (left). Exemplarily the result for  $a_1=1.60$  and  $t_1=1.0$ mm is shown.

**Double-Pit:** The single-pit method assumes that the relevant notch stress is influenced by the shape of a single pit. However, on the scanned corroded surface in Figure 2-2 and Figure 2-3, overlapping pits also can be observed. This requires the analysis of the notch stresses with the double-pit method. For this purpose, the same statistical data as for the single-pit analysis is used. The numerical analysis is carried out on a steel plate according to Figure 2-6 (right). The parameter  $c$  describes the pit distance (overlapping distance) of the two pits and is hence negative, when the pits overlap and positive when they don't. In Figure 2-6 (right) exemplarily the result for  $a_1=1.57$ ,  $a_2=1.11$ ,  $t_1=0.6$ mm,  $t_2=0.88$ mm,  $c=-0.13$ mm and  $r=0.1$  is shown.

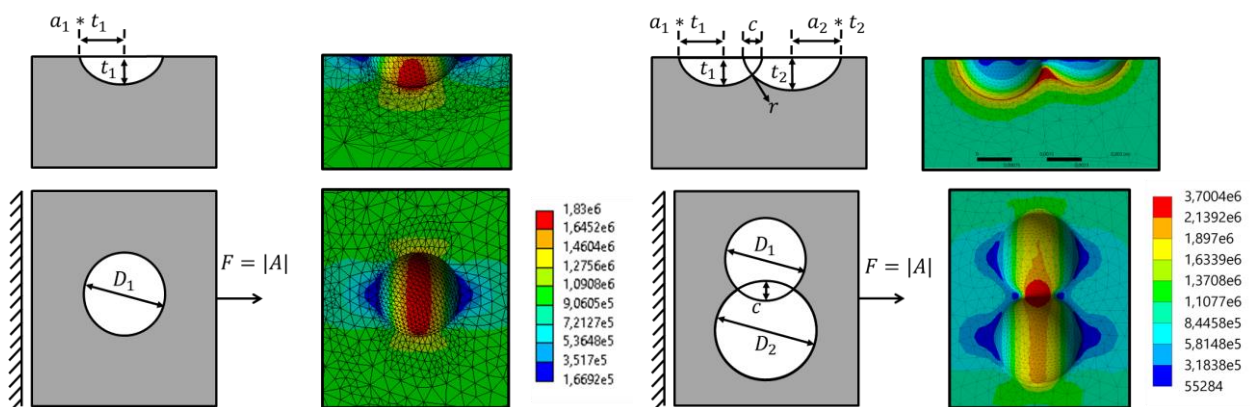


**Figure 2-6: Numerical model of single-pit (left) and double-pit (right) with corresponding stress concentrations (von Mises stress in [Pa])**

**Monte-Carlo-Simulation:** For evaluation of the relevant notch stresses a Monte-Carlo is carried out. The Monte-Carlo simulation requires data with corresponding statistical distribution and information about the statistical correlation for all the influencing parameters. The data for the Monte-Carlo simulation are listed in Table 2-2. For the pit geometry the data from the statistical evaluation is used. The overlapping distance  $c$  is assumed to follow a uniform distribution with values within the range of the listed boundary condition in Table 2-2. It is predefined, that the overlap  $c$  cannot be smaller than the diameter of the bigger pit, since the case of  $c = \max(-D_1; -D_2)$  leads to a single-pit model. Additionally,  $c$  should not be greater than 15% of the smaller pit diameter, since with greater distance the pits act like two single pits and thus not need to be considered in the double-pit model [20]. In addition to that, a rounding of the sharp edges, which arise due to overlapping of two pits, is considered. Based on spike study on the scanned surface Figure 2-2 a uniform distribution in the range of  $r=0.1-0.3$ mm is assumed for the rounding.

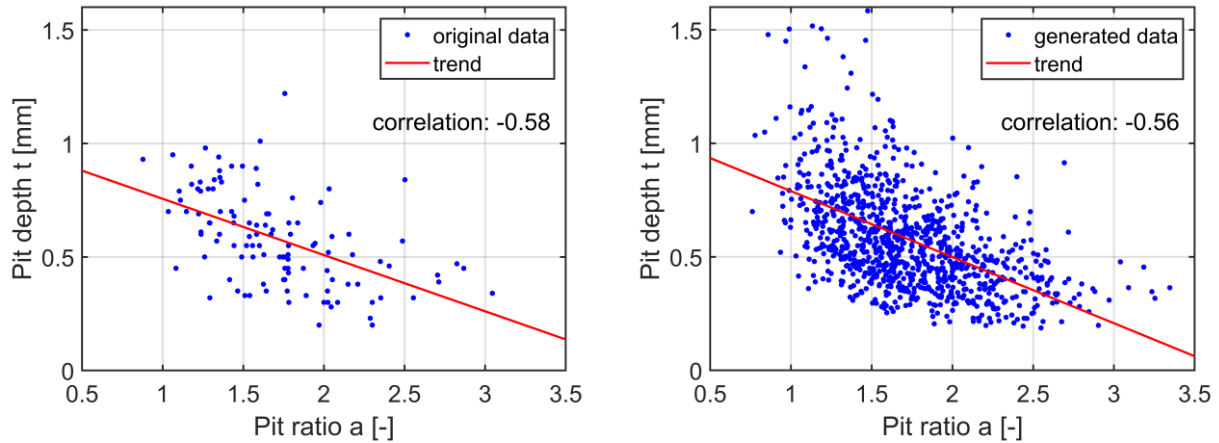


**Figure 2-7: Correlation between pit depth and pit ratio for original data (left) and generated data (right) for the Monte-Carlo simulation**

**Table 2-2: Input parameters for Monte-Carlo simulation**

	Depth $t_1$ [mm]	Depth $t_2$ [mm]	Ratio $a_1$	Ratio $a_2$	Overlap $c$ [mm]	Filleting $r$ [mm]
Distribution	lognormal		lognormal		uniform	uniform
Mean E	0.58		1.71		-	-
Deviation	0.22		0.43		-	-
Boundaries	-	-	-	-	$c > \max(-D_1; -D_2)$ $c < \min(0.3t_{1a_1}; 0.3t_{2a_2})$	$0.1 \leq r \leq 0.3$

**Table 2-3: Input data of 20 simulations and the corresponding stress concentrations**

Simulation number:	Depth $t_1$ [mm]	Depth $t_2$ [mm]	Ratio $a_1$	Ratio $a_2$	Overlap $c$ [mm]	Filleting $r$ [mm]	Stress concentration $\alpha_k$
1	0.51	1.97	0.46	1.72	-0.15	0.2	2.67
2	1.38	1.10	0.75	1.73	-0.93	0.2	2.94
3	1.00	1.20	0.45	2.73	-0.01	0.1	2.76
4	0.48	1.59	0.72	1.26	0.02	0.1	3.19
5	0.49	1.75	0.54	1.68	-0.01	0.2	2.79
6	0.54	1.48	0.50	1.31	-0.48	0.3	2.62
7	0.45	1.67	0.79	0.93	-0.67	0.1	2.79
8	0.66	1.60	0.87	1.56	0.13	0.3	2.18
9	0.34	2.40	0.96	1.60	-1.06	0.3	2.16
10	0.60	1.55	0.66	1.28	0.04	0.2	2.97
11	0.50	1.38	0.35	1.46	-0.86	0.2	2.12
12	0.52	1.62	0.80	2.20	0.19	0.1	1.98
13	0.93	1.04	0.90	1.54	-0.88	0.2	2.73
14	0.54	1.60	0.45	1.28	-0.15	0.3	3.10
15	0.53	1.22	0.87	1.47	-0.24	0.3	3.23
16	0.73	1.49	0.93	1.30	-1.05	0.1	2.50
17	0.32	2.84	0.66	1.52	-1.06	0.1	2.08
18	0.46	1.06	0.6	1.49	-0.32	0.1	3.15
19	0.35	1.67	0.31	2.49	-0.05	0.2	2.37
20	0.39	1.80	0.66	1.77	-0.21	0.3	2.65

In Figure 2-7 left the correlation between the pit depth and the pit ratio is illustrated. The pit depth is negatively correlated with the pit ratio, the correlation coefficient is  $-0.58$ . This means, that the pit depth is getting smaller with greater pit ratios and pits with big depth and big diameter are very rare. This has to be considered in the Monte-Carlo simulation through transformation of the generated random numbers to correlated random numbers. In Figure 2-7 right a realization of the pit parameters  $a$  and  $t$  for the Monte-Carlo simulation with consideration of the correlation is shown.

The generated data are similar to the original data and demonstrates the desired correlation. The correlation coefficient is  $-0.56$  and matches very well to the original data. The correlation coefficient was determined with the Spearman rank correlation. This provided the best match between the original and the generated data. Up to 1000 numerical simulations, according Figure 2-6 (right), were carried out with the generated data. In Table 2-3 the generated input data for 20 numerical simulation with corresponding stress concentrations are given as an example. The results will be discussed in chapter 2.5.

**Random field:** In the application of the random field method, some input parameters have to be defined first. A size of  $20 \times 20$  mm is chosen for the sample to be generated. In order to keep the computation time for generating a random field as low as possible and the accuracy of the field sufficiently precise, the number of nodes to be evaluated is set to  $N_x = N_y = 100$ . The correlation is considered with the exponential covariance function (9) and a correlation length of  $L_c=1.0$ . The number of KL-terms considered for the generation is set to  $KL=160$  (see chapter 2.4.2 Parameter study).

A realization of a random field is shown in Figure 2-8 (left). In the following steps the random field is calibrated. For the calibration data of up to 50 random fields and 50 real surfaces with sample size of  $20 \times 20$  mm were considered. The pit number and the pit radii were extracted with a matlab tool for the real surfaces as well as for the random fields Figure 2-9 (left). The mean value of the pit number is  $N_{pit}=30$  for the real surface and for the random field, when the random fields are generated with  $KL=160$  and  $L_c=1.0$ . The mean value for pit radius of the real surface is  $r=3.64$  mm, while for the random fields the initial mean radius is  $r=1.13$  mm. The Z-coordinates of the random fields were reduced by a scaling factor iteratively, until the mean value of the radii of the random field matched to that of the real surface. In this manner the scaling factor of  $0.293$  (model 1) was conducted. The scaling factor is then multiplied to Z-coordinates of all generated random fields.

In Figure 2-8 an initial random field (left) and the corresponding adjusted random field (right), model 1, is shown. It can be observed, that scaling the Z-coordinates makes the random field flatter, since the scaling factor is below  $1.0$ . Figure 2-9 (right) shows the frequency plot for the radii of the scaled random field and the real surface. It becomes evident, that the mean values with  $3.64$  and  $3.63$  and the distribution shape are matching very well, after scaling the random field. However, it is also observed that radii below  $r=1.0$  mm are very rare in the random field surfaces, when the calibration is based on the mean pit radius. The absence of small radii can lead to lower notch stresses, because the notch stresses depend on the notch radius. Hence, a calibration on the 5%-quantile value of the pit radii is considered in this investigation as well (model 2).

The 5%-quantile radius for the real surface is  $r=0.63$  mm, while the initial value for the random field is  $r=0.46$  mm. Again, the Z-coordinates of the random field are reduced until the 5%-quantile radius



of the random fields match with that of the real surface. The scaling factor for obtaining the same 5%-quantile radius is 0.69 (model 2) here. The random field and the frequency plot for the radii are illustrated in Figure 2-10. It can be observed that, when the 5%-quantile radius match, the distribution shape and the mean value do not match anymore. There are more small radii and less higher ones on the random field (model 2) now. However, the stress concentrations are calculated for both models.

In order to calculate the stress concentrations, the generated random fields have to be transformed into solid models. Therefore, the data of the random field is exported as a STL-file. The STL-file is then converted to a CAD model by using the reverse engineering module from Ansys SpaceClaim (see section: real corroded surfaces). The solid model created in this way, is shown in Figure 2-11. The boundary conditions, loads, mesh and convergence study are performed analogue to the real corroded surface (see section: real corroded surface).

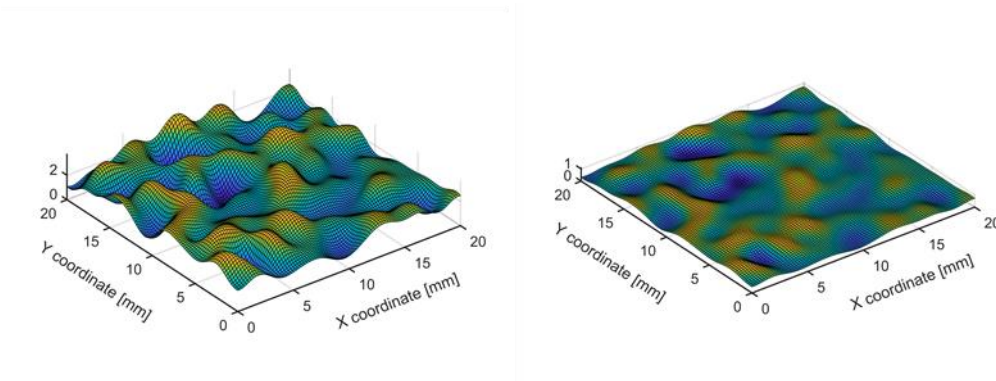


**Figure 2-8: Realization of random field (left) and calibrated random field, model 1 (right)**

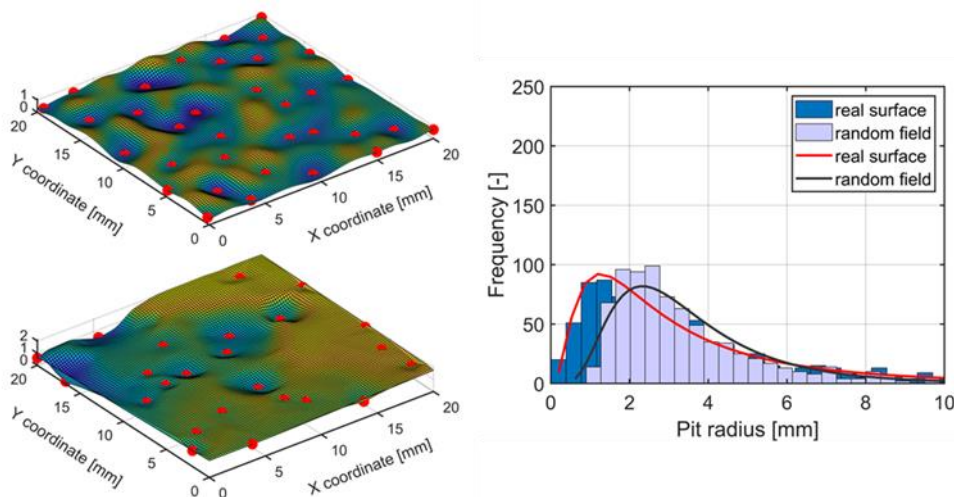


**Figure 2-9: Extraction of pit number and radius of model 1 (upper left) and real surface (lower left) with matlab tool and frequency plot for 50 samples for real surface and random fields (right)**

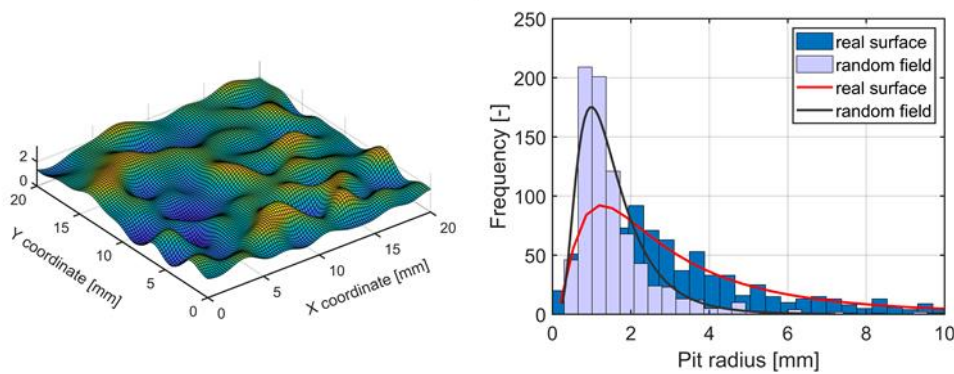


**Figure 2-10: Random field (model 2) calibrated on 5%-quantile radius (left) and frequency plot for 50 samples for real surface and random fields (right)**

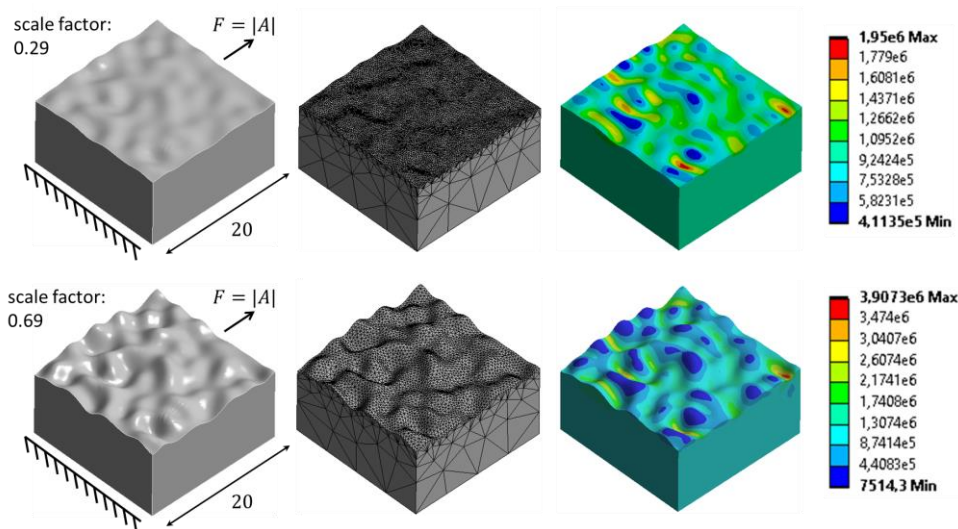


**Figure 2-11: Numerical model of random field, model 1 (upper), model 2 (lower) and corresponding stress concentrations (von Mises stress in [Pa])**

### Real corroded surface:

For stress concentration evaluation of the real surface, the reverse engineering method is used. The obtained faceted surfaces of Figure 2-5 require large amounts of data for illustration (high number of points, lines and surfaces) and are hence very complicated to handle. Beside this, the curvature of the surface is not continuous, which leads to singularities in the subsequent numerical analysis. Thus, the surfaces are approximated with so-called Non-Uniform Rational B-Spline (NURBS) surfaces. NURBS surfaces are described by two-dimensional, mathematically defined polynomial functions of higher order, which fit the shape of the cross-section lines of the faceted body. The NURBS surfaces get along with much less data for the description of the surface and have a continuous curvature. In this analysis the NURBS surfaces were created with ANSYS SpaceClaim. The quality of the created surface can be controlled through the number of the grid (in Ansys SpaceClaim: sample) and through the size of the surface being created. The higher the grid rate and smaller the surface size, the closer the fitting to the facets and thus more accurate. This is illustrated in Figure 2-12.

However, smaller rates offer a faster creation and higher usability in terms of further processing. In case of the sample, it has been necessary to cut smaller samples due to the high dimensions of the scanned steel plate, as shown in Figure 2-5.

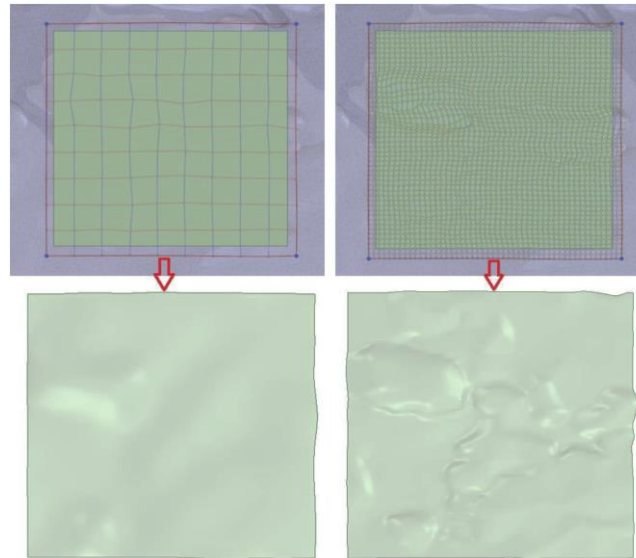


**Figure 2-12: NURBS-surface of a 20x20mm sample with grid rate 10 (left) and grid rate 50 (right)**

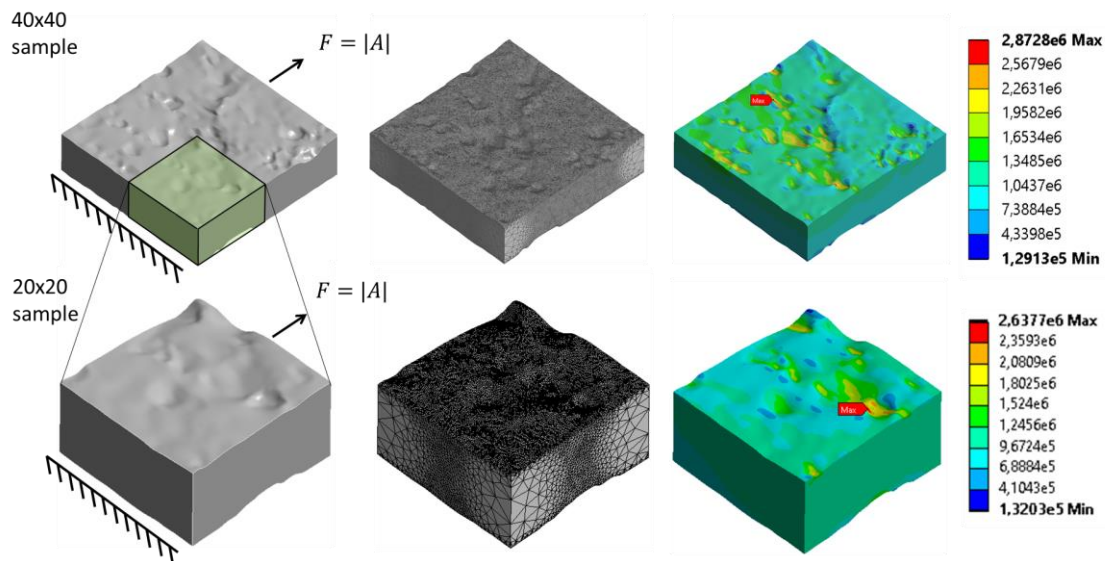


**Figure 2-13: Numerical model of real corroded samples with solid model (left), mesh (middle) and result plot of stress concentrations (right) for 40x40mm (upper) and 20x20mm (lower) sample size**

Two different sample sizes, 20x20 and 40x40 mm, are investigated here. The ideal grid rate for the 20x20 sample is  $R=50$  and for the 40x40 sample  $R=120$ . Higher grid sizes have not led to different results for the stress concentration. Hereafter, a solid model is generated by using the NURBS surfaces, shown in Figure 2-13 on the left. For the meshing tetrahedral elements were used. Element sizes smaller than 0.3 mm were needed, to fit the elements to the rough surface geometry. This ensures that the location of the maximum stress concentration doesn't change during the convergence study.



This in turn guarantees that the mesh is not refined in the wrong locations. In Figure 2-13 the meshed geometry is illustrated in the middle. Here, an element size of 0.2 mm was used for the analysis. For the refinement elements of up to 0.03mm were needed to reach a convergence of 4%. The boundary conditions are shown in Figure 2-13 as well. The applied force corresponds to the area, which has been extracted from the solid model. Up to 50 different surfaces for both sample sizes were investigated in this manner.

### 2.4.2 Parameter Study

**Single-Pit:** A parameter study was carried out with varying values for the width ratio  $a$  and the pitting depth  $t$ . Pit depths from  $t=0.5$  to 2mm and pit ratios from  $a=0.7$  to 2.0 were investigated. Here,  $a=1.0$  corresponds to a perfect hemispheric pit ( $r=t$ ),  $a>0$  to a wide pit ( $r>t$ ) and  $a<0$  to a narrow pit ( $r<t$ ). In Figure 2-14 the stress concentrations for a wide pit (left) and a narrow pit (right) are illustrated. The maximum notch stress for wide pits occur at the bottom of the pit. For narrow pits, the location of maximum notch stress shifts to the pit walls. The force flow is then no longer under the pit bottom, but along the pit wall. In the theoretical limit case of a fully penetrated pit, the force flow would correspond to a perforated plate. This disproves the idea that the notch stress increases with time.

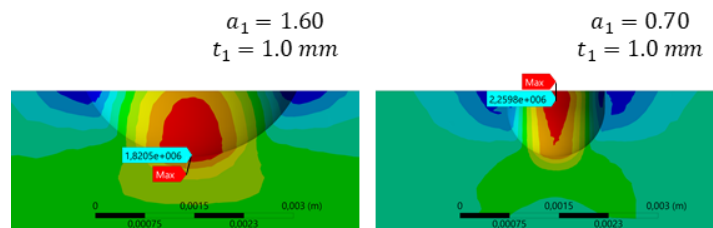


Figure 2-14: Stress concentrations for a wide pit  $a=1.60$  (upper) and narrow pit  $a=0.70$  (lower)

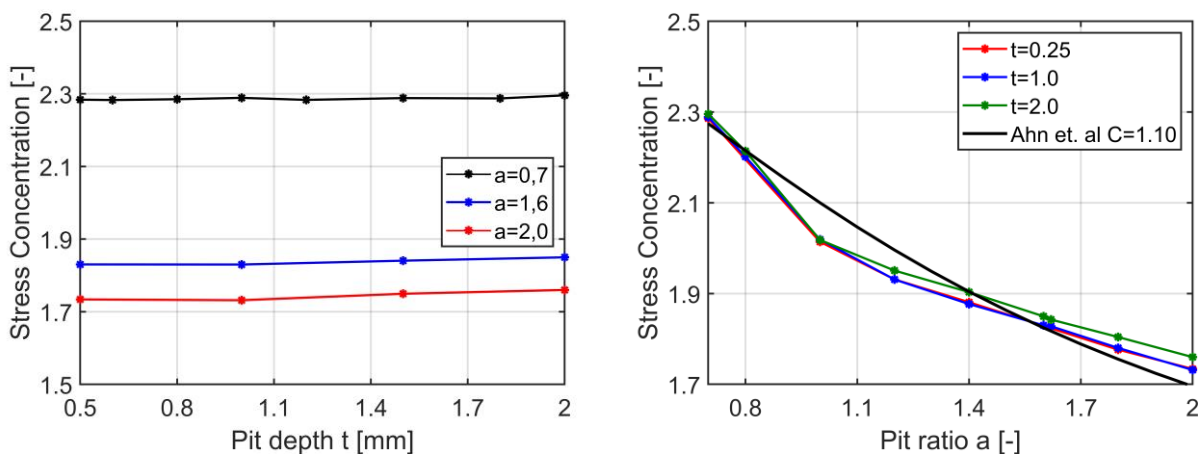
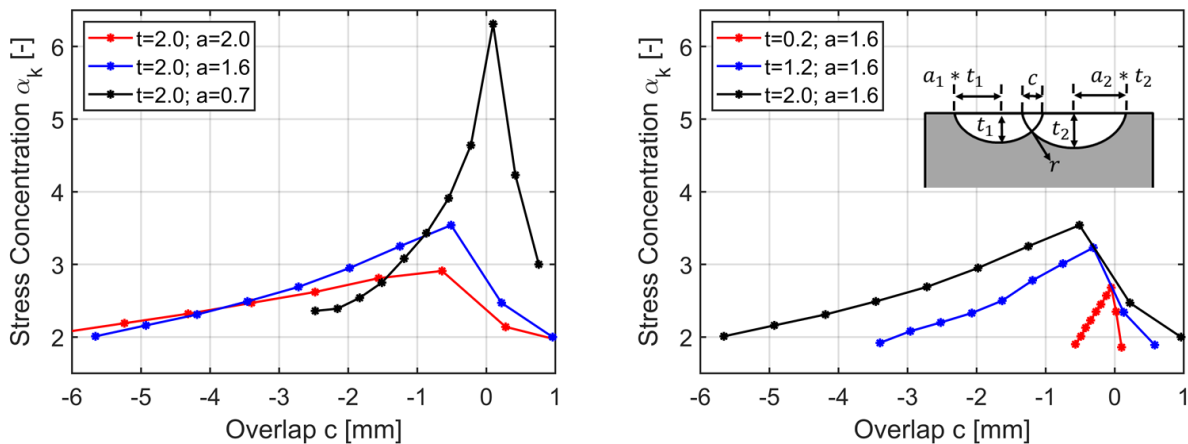


Figure 2-15: Stress concentration against pit depth (left) and pit ratio (right)

Figure 2-15 on the left shows the max. notch stress concentrations as a function of pit depth for different pit shapes, expressed with the width ratio. The pit depth plays a subordinate role for all pit shapes. Figure 2-15 on the right illustrates the max. notch stress as a function of the width ratio. The

notch stress decreases with increasing width ratio. The notch stress curve agrees with the formula derived in equation (2-3) from classical stress theory and the formula of Ahn. et. al. (2-4), when a shape factor of  $C=1.10$  is applied. The results for the parameter study of the single-pit model are in accordance to [13–16].

**Double-Pit:** For the relevant parameters  $a$ ,  $t$  and  $c$  (see Figure 2-6) a parameter study was carried out. For the study two identical pits with  $a_1=a_2$  and  $t_1=t_2$  were considered. To catch the influence of the pit ratio  $a$ , three different ratios were analysed ( $a=0.7$ ; 1.6; 2.0) with a constant value of  $t=2.0$ . For the impact of the pit depth  $t$ , three different depths were analysed ( $t=0.2$ ; 1.2; 2.0) with a constant value of  $a=1.6$ . The chosen values for  $a$  and  $t$  correspond mainly to those of Figure 2-4. Only with  $t=2.0$  a value outside the range was examined in order to analyse the impact of even deeper pits than conducted from the enumeration in Figure 2-4. In Figure 2-16 the results of the parameter study are shown. Here the notch stresses are plotted as a function of the pit distance for different cases. For all cases the maximum notch stresses occurred in the area of the overlap (see Figure 2-6). With small overlapping distance  $c$ , between  $-0.5$  and  $0$  mm, the notch stresses reach their maximum. With bigger overlapping distance, from the peaks on the left, the geometry of the double-pit model tends to a single-pit model, which leads to smaller notch stresses. The same can be observed, when the overlapping is reduced, from the peak on the right. It becomes evident, that the notch stresses increase exponentially with smaller pit ratios. The influence of the pit depth is smaller in comparison to the pit ratio but greater than in the single-pit model. The results for the parameter study of the double-pit model are in accordance to [20,22].



**Figure 2-16: Stress concentration as a function of overlapping distance and pit ratio (left) and overlapping distance and pit depth (right)**

**Random field:** For the random field model, a parameter study was carried out as well. Random values were generated for the correlation length and the number of KL-terms in order to investigate the impact on the number of pits, the mean and the 5%-quantile values of the pit radii and the mean pit depths.

In Figure 2-17, the impact of the parameters is shown in a correlation matrix. The matrix shows the correlation and the trend line of all parameters and the histograms of each parameter along the matrix diagonal, where the correlation is  $\rho=1.0$ . The histograms provide additional information about the

distribution of the parameter. It becomes evident, that there is a high positive correlation between the KL-terms and the number of generated pits ( $\rho=0.84$ ) and a negative correlation with the pit radius ( $\rho=-0.66$  and  $\rho=-0.70$ ). The correlation length is just correlated to the pit number ( $\rho=-0.34$ ). Moreover, there is a negative correlation between pit radius and pit depth ( $\rho=-0.51$  and  $\rho=-0.48$ ).

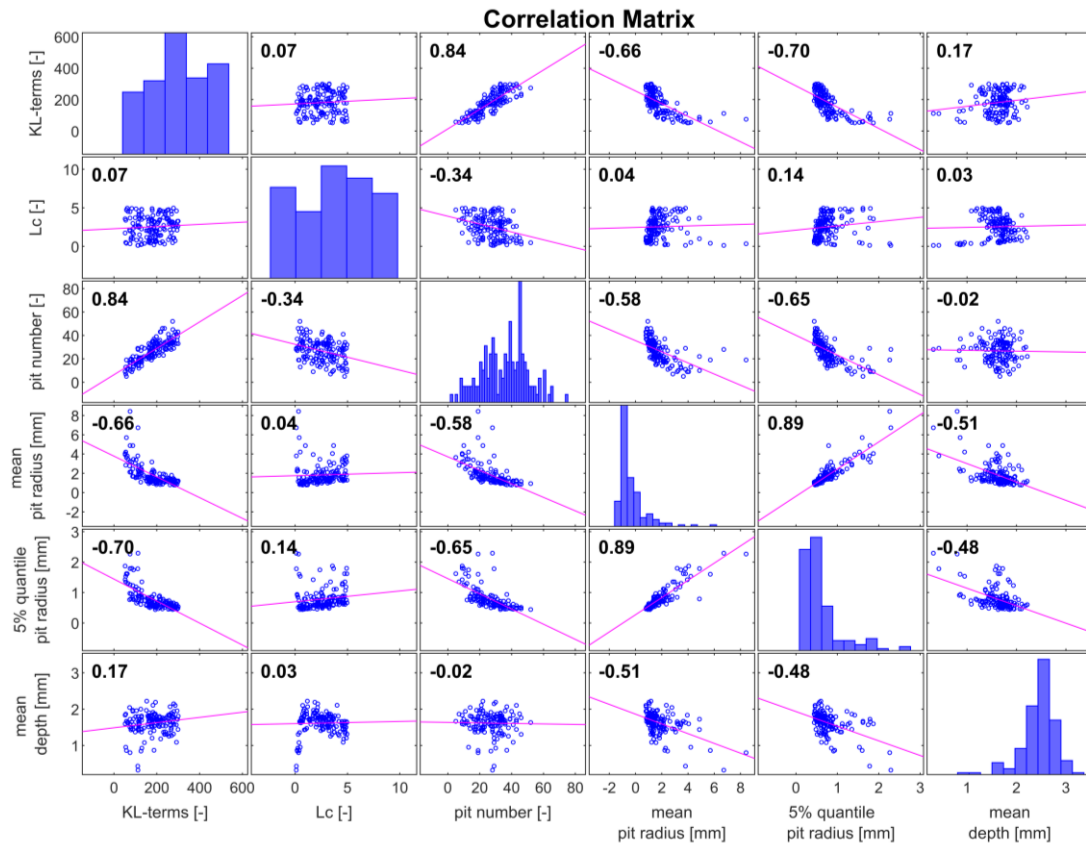


**Figure 2-17: Correlation matrix of random field parameters**

In Figure 2-18 samples of random field with varying correlation length and number of KL-terms are illustrated. The described impact of the KL-terms (upper plots) and the correlation length (lower plots) on the number pits becomes apparent. Furthermore, the correlation length has an influence on the steepness of the surface geometry, which is not considered in the element matrix. In order to generate random fields, a suitable number of KL-terms and a value for the correlation must be specified, which lead to a similar number of pits compared to the real corroded surfaces. The pit number were extracted with a matlab tool (see chapter 2.4.1 Numerical Modeling; Random field) and has a mean value of  $N_{\text{pit}}=30$ . A number of KL-terms of  $KL=160$  and a correlation length of  $L_c=1.0$  leads to the same mean pit number for random fields (see Figure 2-17). Hence, for the generation of random fields the combination of  $KL=160$  and  $L_c=1.0$  is chosen for investigations of the stress concentrations.

The calibration of the random field models to the pit depth and pit radius is performed after they have been generated with the scaling factors presented in section 2.4.1. It should be noted, that a calibration of the KL expansion on the pit radius is possible, but it results in a smaller pit number (see correlation matrix) and a poorer representation of the real corroded surface, as the pit number can't be scaled afterwards.

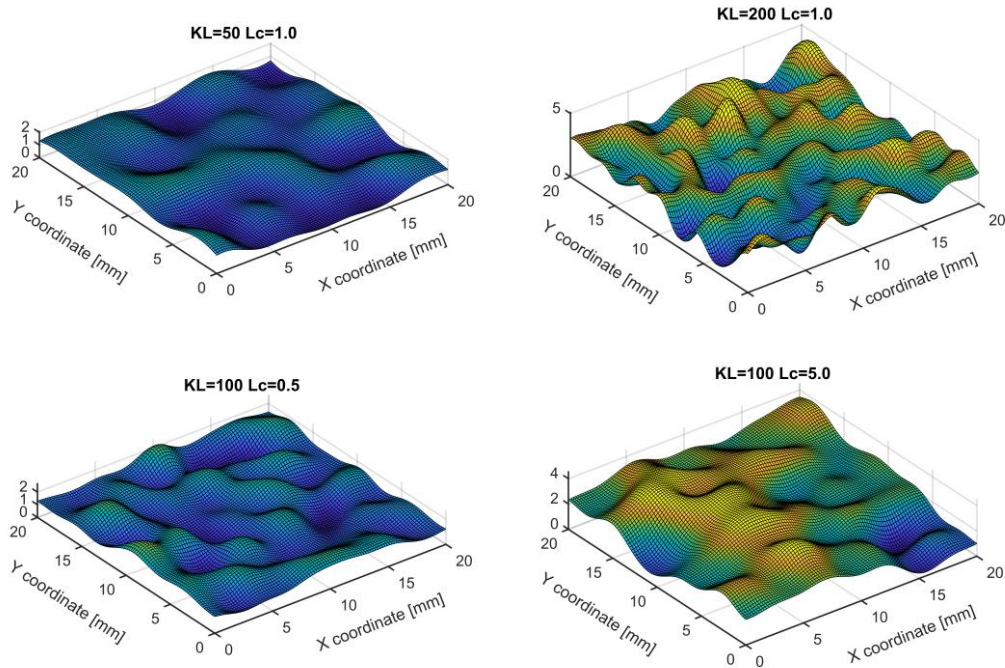


Figure 2-18: Random fields with varying KL-terms and correlation length

## 2.5 Results

**Single-Pit:** For all parameters of  $a$  from the frequency diagram (see Figure 2-4) and a constant depth of  $t=1.0\text{mm}$  the notch stresses were calculated. The depth can be constant, since it was shown in the parameter study, that the notch stress of a single pit depends only on the parameter  $a$ . Hence, the frequency plot for the notch stresses, illustrated in Figure 2-19 (left), corresponds exactly to the frequency plot of the pit ratio in Figure 2-4. The frequency diagram is transformed into a probability density function (PDF) and then used to calculate the 95% quantile value, see Figure 2-19 (right).

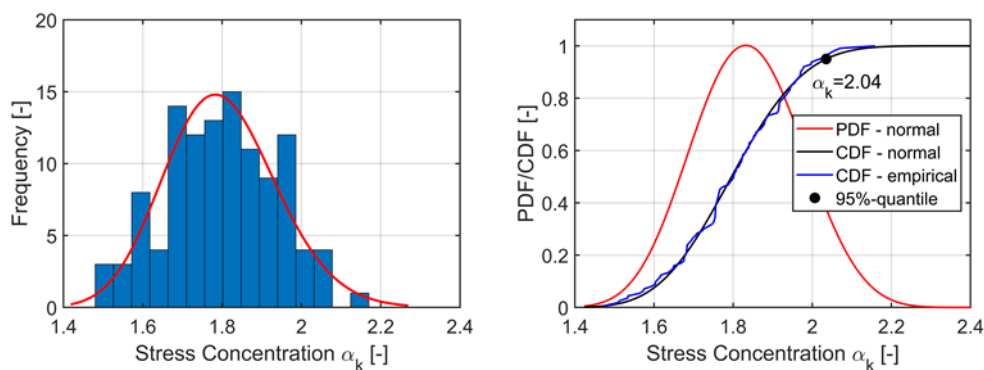


Figure 2-19: Results of numerical investigation of the single-pit model, frequency plot (left) and PDF/CDF plot (right)

The PDF follows a normal distribution, despite the input parameter was lognormal distributed. The mean value is  $\mu=1.8$  and the standard deviation is  $\sigma=0.14$ . The 95%-quantile value for the stress concentration is  $\alpha_k=2.04$ .

**Double-Pit:** Figure 2-20 (left) shows the results of stress concentrations, which were evaluated with the Monte-Carlo simulation. The frequency of the stress concentrations follows a three parametric Weibull distribution, which can be described by the following equation:

$$\text{PDF: } f(x) = \frac{B}{A} \left( \frac{x-C}{A} \right)^{B-1} \exp \left( - \left( \frac{x-C}{A} \right)^B \right) \quad (2-1)$$

$$\text{CDF: } F(x) = 1 - \exp \left( - \left( \frac{x-C}{A} \right)^B \right)$$

Herein A is the scale, B is the shape and C is the location parameter. With  $A=0.85$ ,  $B=1.71$  and  $C=1.66$  the probability density function (PDF) and cumulative density function (CDF) of the stress concentration can be described here. In Figure 2-20 on the right the PDF and the corresponding CDF for the approximation with the Weibull distribution is plotted as well as the empirical CDF with the results of the Monte-Carlo simulation.

The CDFs show good agreement and approve the approximation with the Weibull distribution. The mean value for the stress concentration is  $\mu=2.42$  and the standard deviation is  $\sigma=0.46$ . The 95%-quantile value is  $\alpha_k=3.35$ .

Based on the Monte-Carlo analysis a correlation matrix for all the random input parameter and the stress concentration was created, see Figure 2-21.

The highest correlations are between  $a_1$  and  $t_1$  and  $a_2$  and  $t_2$ , which was demonstrated before. Beside this, there is no correlation between the input parameters itself. However, there is a correlation between the input parameter with the stress concentration. The highest correlation and thus the impact on the stress concentration is from the overlap distance with correlation of  $\rho=0.46$  and the pit ratio with  $\rho=-0.41$ , while the impact from the pit depth is smaller ( $\rho=0.26$ ). The rounding value doesn't affect the stress concentration and thus the correlation is almost zero. The findings from the Monte-Carlo simulation match with the findings from the parameter study carried out before.

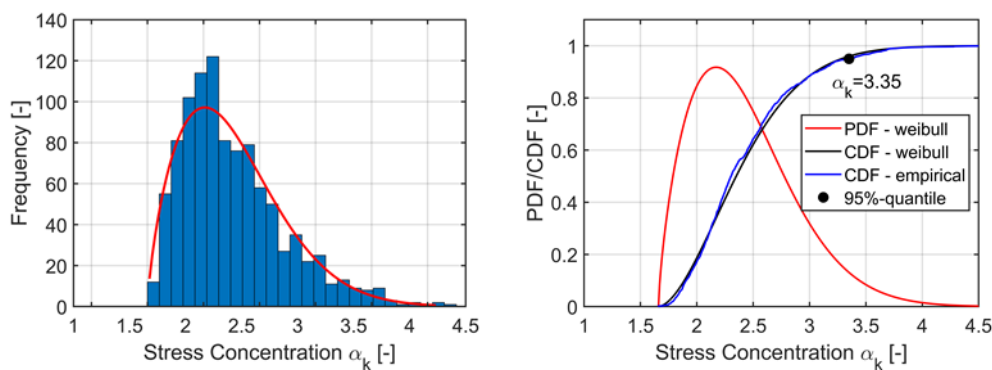


**Figure 2-20: Results of the Monte-Carlo simulation**

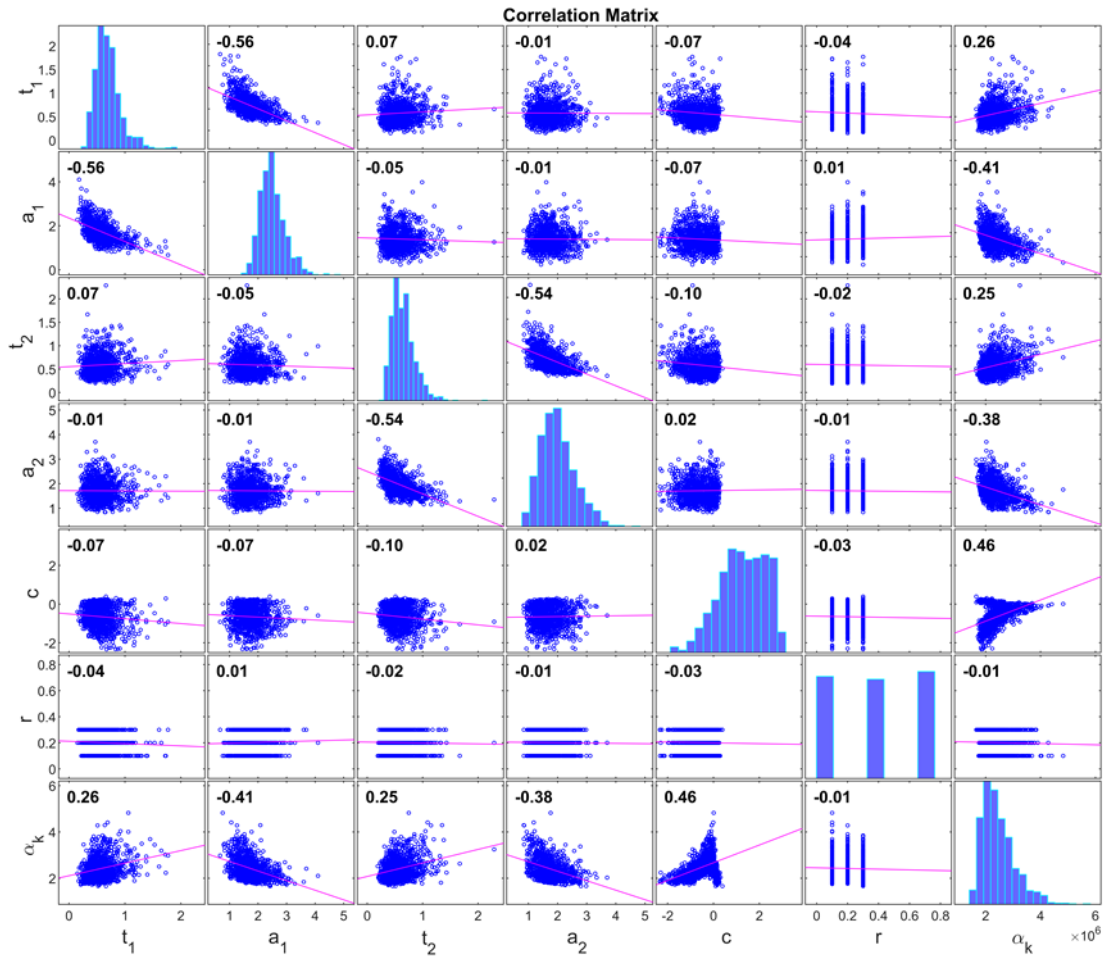


Figure 2-21: Correlation matrix from the Monte-Carlo simulation

### Random field:

For the investigation of the stress concentrations, a correlation length of  $L_c=1$  and a number of KL terms of 160 were set. A total of 100 random fields were generated and evaluated using the procedure described earlier. In Table 2-4 the statistical parameters are summed up. The results are illustrated in Figure 2-22. In Figure 2-22, on the right, the solid line represents the results of scale factor 0.69 (model 2), while the dashed line represents scale factor 0.29 (model 1).

The mean and the 95%-quantile values differ significantly. The high scale factor (model 2) leads to higher stress concentrations for the mean value as well as for the 95%-quantile value. This is related to the small radii for model 2 as illustrated earlier in Figure 2-10. Moreover, the deviation of the stress concentrations is higher with higher scale factor. Based on these results, no final conclusion about the optimal model can be made.



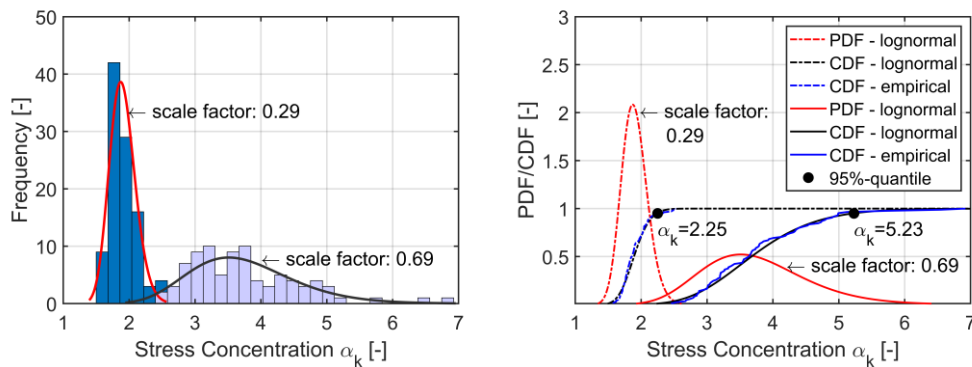


**Figure 2-22: Results of numerical investigation of random fields**

**Table 2-4: Statistical Data for stress concentration distribution of random fields**

	Model 1	Model 2
Scale factor	0.29	0.69
Distribution	Lognormal	Lognormal
Mean E	1.90	3.74
Deviation	0.19	0.86
95%-quantile	2.25	5.23

### Real corroded surface:

In Figure 2-23 some results of the numerical simulation of the 40x40mm specimen is shown. The maximum stress concentrations are in the bottom of single pits as well as in the intersection area of double pits.

In Figure 2-24 and Figure 2-25 the max. stress concentration for all simulations are plotted for the 40x40mm as well as 20x20mm specimens. The frequency follows in both cases a lognormal distribution with the statistical parameters shown in Table 2-5. This becomes also visible by the empirical and the fitted CDF plot for the corresponding frequency distribution shown in Figure 2-24 and Figure 2-25, on the right. The fitted CDFs show a good match to the empirical CDFs. The mean values with  $\mu=2.40$  and  $\mu=2.30$  as well as the standard deviation with  $\sigma=0.55$  and  $\sigma=0.53$  differ only slightly. The 95%-quantile value for the stress concentration differs in the same range. However, the value for the 40x40 sample with  $\alpha_k=3.43$  is just 4.9% higher than the value of the 20x20 sample with  $\alpha_k=3.27$ , even though only  $\frac{1}{4}$  of the corroded surfaces were modelled for the 20x20 samples. Considering the increased effort with modelling the 40x40 sample, it can be concluded that 20x20 samples are sufficient for a fast analysis.

**Table 2-5: Statistical Data for stress concentration distribution for real corroded surfaces**

Sample	40x40mm	20x20mm
Distribution	Lognormal	Lognormal
Mean E	2.40	2.30
Deviation	0.55	0.53
95%-quantile	3.43	3.27

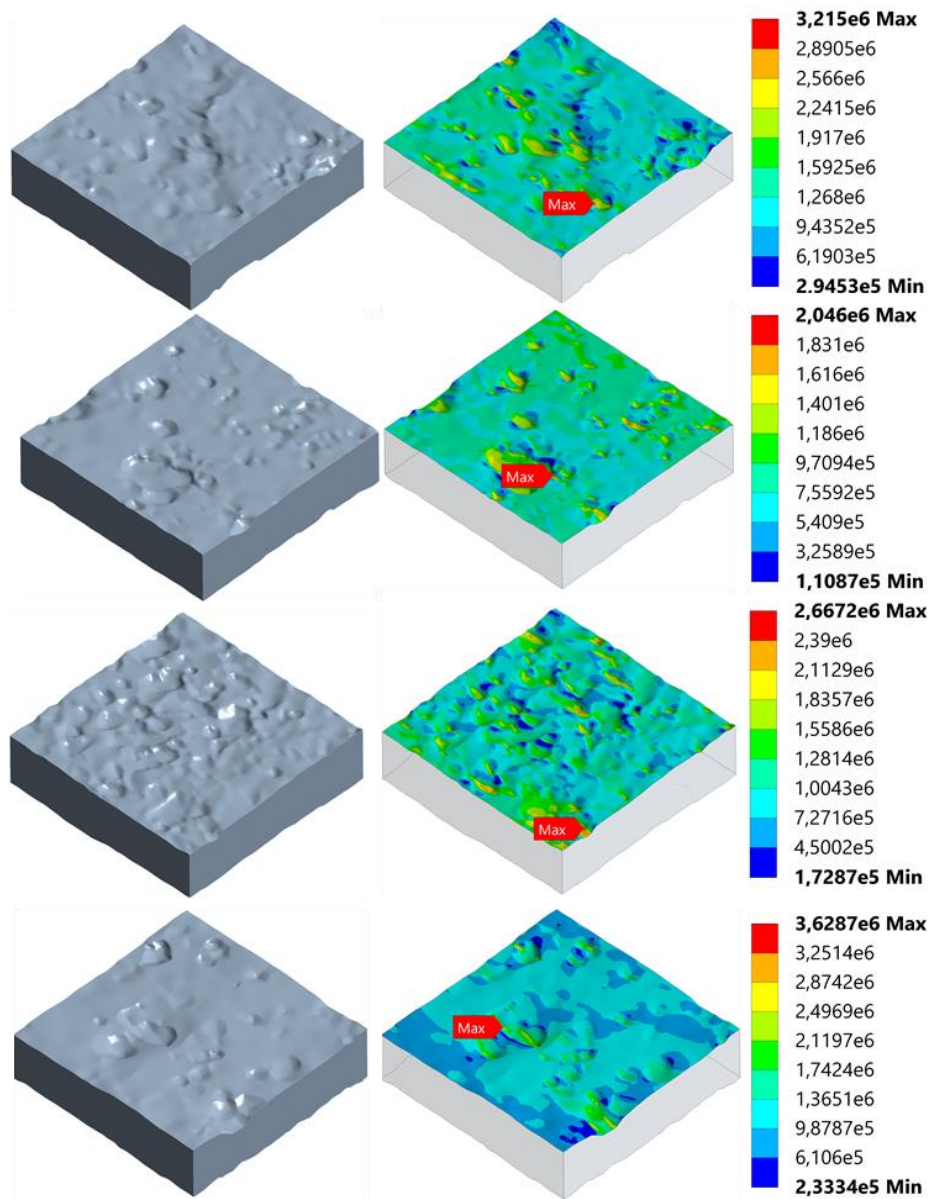
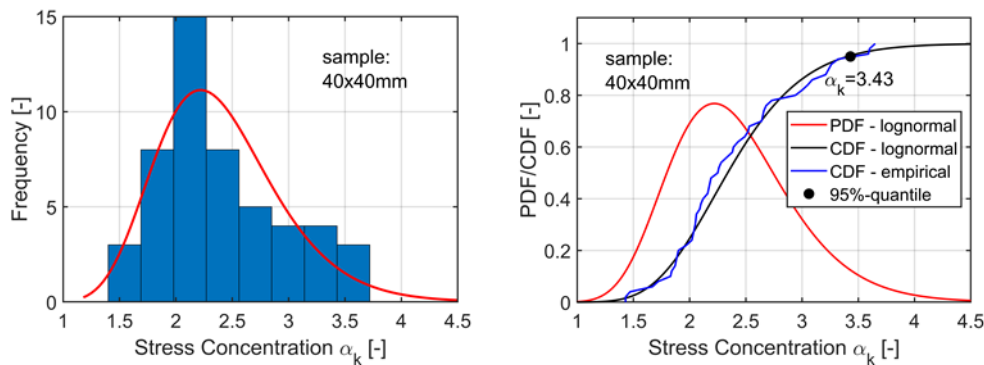
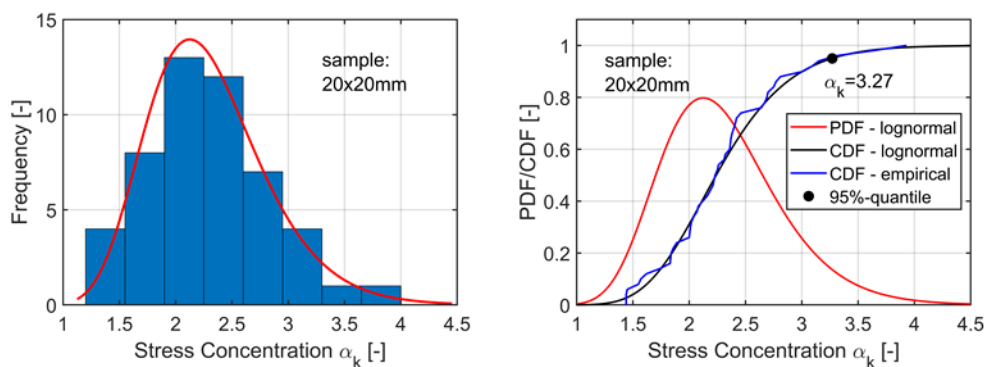


Figure 2-23: Exemplary results of 50 numerical simulation of 40x40mm real corroded surfaces





**Figure 2-24: Results of numerical investigation of 40x40mm samples with real corroded surface**



**Figure 2-25: Results of numerical investigation of 20x20mm samples with real corroded surface**

## 2.6 Discussion and Conclusion

As described, the single-pit model misses the interaction between neighbouring pits, which leads to very small stress concentration factors. Hence the model is not accurate. The double-pit model, on the other hand, matches very well with results of the real surfaces, see Figure 2-26 and Table 2-6.

The statistical parameter as well as the 95%-quantile values with  $\alpha_k=3.35$  for the double-pit model and  $\alpha_k=3.43$  for the real surface agree very well. The random field model was developed based on the frequency distribution of the pit radii of the real surface and calibrated on the mean value of the radii (model 1) and on the 5%-quantile value (model 2). Model 1 has a 95%-quantile stress concentration of  $\alpha_k=2.25$  with  $\sigma=0.19$  and matches with the results of the single-pit model. Model 2 has a 95%-quantile stress concentration of  $\alpha_k=5.23$  and is far beyond the results of the real surfaces.

Under the bottom line, the random field models are not able to model the stress concentrations with the desired accuracy, when the models are calibrated on the mean and the 5%-quantile value of the pit radii. In the parameter study of the double pit it was shown, that the stress concentration is not only dependent on the radius (expresses via  $a=r/t$ ), but to a high extent on the overlap distance. The overlap distance is not simulated in the generated random fields and hence they cannot represent the corroded surface properly, especially regarding stress concentrations. This also explains why random fields are appropriate for the investigation of tensile behaviour performed by Woloszyk et.al. [24,25] but not for fatigue issues. The tensile behaviour is mainly driven by the minimum cross-section of a

corroded specimen, for which the approach with random fields leads to satisfying results. In case of fatigue issues, the minimum cross section plays only a secondary role, since the stress concentrations are driven by the pit geometry and the overlap distance of interacting pits. For application of random fields on fatigue issues, further research on the implementation of the overlap distance is needed. Beside this, a more suitable parameter for calibration than the radius has to be established.

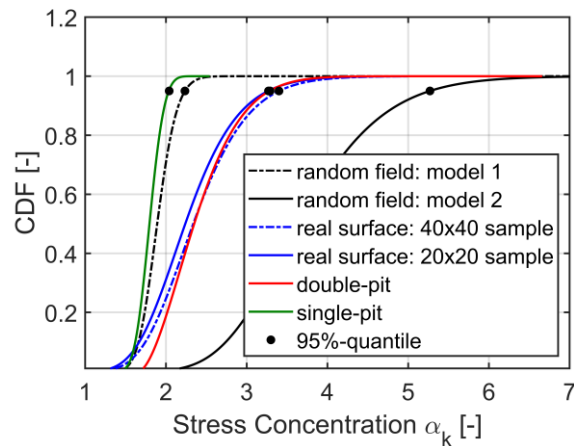


**Figure 2-26: CDF of stress concentration for all models and 95%-quantile values**

**Table 2-6: Comparison of stress concentration for different models**

Model	Single-Pit	Double-Pit	Random field		Real surface	
			Model 1	Model 2	20x20 sample	40x40 sample
Distribution	Lognormal	Weibull	Lognormal	Lognormal	Lognormal	Lognormal
Mean E	1.80	2.42	1.90	3.74	2.30	2.40
Deviation	0.14	0.46	0.19	0.86	0.53	0.55
95%-quantile	2.04	3.35	2.25	5.23	3.27	3.43

The investigations in this paper allows following conclusion:

- The enumeration of pits on the corroded specimen showed a negative correlation between pit depth and pit ratio
- The one pit model and the random field model are not able to represent the stress concentration of the real corroded surface with sufficient accuracy
- The double-pit model with additional Monte-Carlo simulation and consideration of input parameter correlation achieves the most accurate values compared to the real surfaces
- For the real surfaces 50 samples of 20x20mm and 40x40mm were modelled. The stress concentration value differs only slightly, although only ¼ of the corroded surfaces were modelled for the 20x20 samples.

The 95% quantile value of stress concentration, conducted in this way, can be used as an input in a deterministic fatigue strength analysis based on local fatigue approaches. With local concepts, the remaining lifetime for OWTs or other marine structures, where the corrosion protection is partially degraded, can be calculated. Furthermore, the stress concentration distribution can be utilized for a

risk and reliability-based analysis of corroded components subjected to cyclic loads. Thus, a reliability-based answer can be given to the initial question regarding the assessment of further operation after corrosion degradation.

However, for application of local fatigue approaches further research regarding the microstructural support and the influence of corrosion on the material has to be carried out and will be presented in future publications.

## 2.7 Acknowledgements

The project ISyMOO is funded by the German Federal Ministry of Economic Affairs and Climate Action (BMWK) through the 6<sup>th</sup> National Energy Research Program under the funding number 0324254A.

Further the authors would like to acknowledge the Institute for Ship Structural Design and Analysis from the Technical University Hamburg, especially Prof. DSc. (Tech.) Sören Ehlers and Dr.-Ing. Moritz Braun, for the provision of corroded material.

## 2.8 References

- [1] Det Norske Veritas. Corrosion protection for wind turbines(DNV-GL RP-0416); 2016.
- [2] Det Norske Veritas. Support structures for wind turbines(ST-0126); 2018.
- [3] Bundesanstalt für Wasserbau. Korrosionsschutz von Offshore-Bauwerken zur Nutzung der Windenergie - Teil 1: Allgemeines(VGB-S-021-01-2018-04-DE); 2018.
- [4] Momber AW, Nattkemper TW, Langenkämper D, Möller T, Brün D, Schaumann P et al. A data-based model for condition monitoring and maintenance planning for protective coating systems for wind tower structures. *Renewable Energy* 2022;186:957–73.  
<https://doi.org/10.1016/j.renene.2022.01.022>.
- [5] Momber AW. Quantitative performance assessment of corrosion protection systems for offshore wind power transmission platforms. *Renewable Energy* 2016;94:314–27.  
<https://doi.org/10.1016/j.renene.2016.03.059>.
- [6] Momber A, Nattkemper T, Langenkämper D, Möller T, Brün D, Schaumann P et al. Digitalisierung und Verarbeitung von Sensordaten für die Zustandsbewertung von Oberflächenschutzsystemen stählerner Türme von Onshore-Windenergieanlagen. *Stahlbau* 2021.  
<https://doi.org/10.1002/stab.202100020>.
- [7] Det Norske Veritas - Germanischer Lloyd. Fatigue design of offshore steel structures(DNV-GL RP-C203); 2019.
- [8] Szklarska-Smialowska Z. Pitting and crevice corrosion. Houston, Tex.: NACE International the Corrosion Society; 2005.

- [9] Melchers RE. Pitting Corrosion of Mild Steel in Marine Immersion Environment—Part 1: Maximum Pit Depth 2004.
- [10] Melchers RE, Jeffrey RJ. Probabilistic models for steel corrosion loss and pitting of marine infrastructure. *Reliability Engineering & System Safety* 2008;93(3):423–32. <https://doi.org/10.1016/j.ress.2006.12.006>.
- [11] Williams DE, Westcott C, Fleischmann M. Stochastic Models of Pitting Corrosion of Stainless Steels: I Modeling of the Initiation and Growth of Pits at Constant Potential. *J. Electrochem. Soc.* 1985;132(8):1796–804. <https://doi.org/10.1149/1.2114220>.
- [12] Valor A, Caleyó F, Alfonso L, Rivas D, Hallen JM. Stochastic modeling of pitting corrosion: A new model for initiation and growth of multiple corrosion pits. *Corrosion Science* 2007;49(2):559–79. <https://doi.org/10.1016/j.corsci.2006.05.049>.
- [13] Xiang L, Pan J, Chen S. Analysis on the stress corrosion crack inception based on pit shape and size of the FV520B tensile specimen. *Results in Physics* 2018;9:463–70. <https://doi.org/10.1016/j.rinp.2018.03.005>.
- [14] Cerit M. Corrosion pit-induced stress concentration in spherical pressure vessel. *Thin-Walled Structures* 2019;136:106–12. <https://doi.org/10.1016/j.tws.2018.12.014>.
- [15] Huang Y, Wei C, Chen L, Li P. Quantitative correlation between geometric parameters and stress concentration of corrosion pits. *Engineering Failure Analysis* 2014;44:168–78. <https://doi.org/10.1016/j.engfailanal.2014.05.020>.
- [16] Hou J, Song L. Numerical Investigation on Stress Concentration of Tension Steel Bars with One or Two Corrosion Pits. *Advances in Materials Science and Engineering* 2015;2015:1–7. <https://doi.org/10.1155/2015/413737>.
- [17] Deutsches Institut für Normung e.V. *Korrosion von Metallen in Seewasser und Seeatmosphäre – Teil 1: Begriffe, Grundlagen*; (DIN 81249-1); 2011.
- [18] Neuber H. *Kerbspannungslehre: Theorie der Spannungskonzentration ; genaue Berechnung der Festigkeit*. 4th ed. Berlin: Springer; 2001.
- [19] Ahn S-H, Lawrence FV, Metzger MM. CORROSION FATIGUE OF AN HSLA STEEL. *Fatigue & Fracture of Engineering Materials & Structures* 1992;15(7):625–42. <https://doi.org/10.1111/j.1460-2695.1992.tb01302.x>.
- [20] Liang X, Sheng J, Wang K. Investigation of the mechanical properties of steel plates with artificial pitting and the effects of mutual pitting on the stress concentration factor. *Results in Physics* 2019;14:102520. <https://doi.org/10.1016/j.rinp.2019.102520>.
- [21] Jakubowski M. Influence of Pitting Corrosion on Fatigue and Corrosion Fatigue of Ship and Offshore Structures, Part II: Load - Pit - Crack Interaction. *Polish Maritime Research* 2015;22(3):57–66. <https://doi.org/10.1515/pomr-2015-0057>.

- [22] Yan W, Xu Y, Zhou Y, Wang K. Investigation of Stress Concentration and Casing Strength Degradation Caused by Corrosion Pits. *International Journal of Corrosion* 2016;2016(3):1–6. <https://doi.org/10.1155/2016/6930234>.
- [23] Teixeira ÂP, Soares CG. Ultimate strength of plates with random fields of corrosion. *Structure and Infrastructure Engineering* 2008;4(5):363–70. <https://doi.org/10.1080/15732470701270066>.
- [24] Woloszyk K, Garbatov Y. An enhanced method in predicting tensile behaviour of corroded thick steel plate specimens by using random field approach. *Ocean Engineering* 2020;213:107803. <https://doi.org/10.1016/j.oceaneng.2020.107803>.
- [25] Woloszyk K, Garbatov Y. Random field modelling of mechanical behaviour of corroded thin steel plate specimens. *Engineering Structures* 2020;212:110544. <https://doi.org/10.1016/j.eng-struct.2020.110544>.
- [26] Xu S, Wang Y. Estimating the effects of corrosion pits on the fatigue life of steel plate based on the 3D profile. *International Journal of Fatigue* 2015;72:27–41. <https://doi.org/10.1016/j.ijfatigue.2014.11.003>.
- [27] Kainuma S, Jeong Y-S, Ahn J-H. Investigation on the stress concentration effect at the corroded surface achieved by atmospheric exposure test. *Materials Science and Engineering: A* 2014;602:89–97. <https://doi.org/10.1016/j.msea.2014.02.056>.
- [28] Schaumann P, Schürmann K, Pittner A, Rethmeier M. Automatically Welded Tubular X-Joints for Jacket Substructures: Prediction of the Technical Fatigue Crack Location. *ce/papers* 2019;3(3-4):823–8. <https://doi.org/10.1002/cepa.1140>.
- [29] Betz W, Papaioannou I, Straub D. Numerical methods for the discretization of random fields by means of the Karhunen–Loève expansion. *Computer Methods in Applied Mechanics and Engineering* 2014;271:109–29. <https://doi.org/10.1016/j.cma.2013.12.010>.
- [30] Ghanem RG, Spanos PD. *Stochastic finite elements: A spectral approach*. Mineola, NY: Dover Publ; 2003.
- [31] Patelli E, Alvarez DA, Broggi M, Angelis M de. Uncertainty Management in Multidisciplinary Design of Critical Safety Systems. *Journal of Aerospace Information Systems* 2015;12(1):140–69. <https://doi.org/10.2514/1.I010273>.
- [32] Tolo S, Patelli E, Beer M. An open toolbox for the reduction, inference computation and sensitivity analysis of Credal Networks. *Advances in Engineering Software* 2018;115:126–48. <https://doi.org/10.1016/j.advengsoft.2017.09.003>.
- [33] Neumann KM, Ehlers S. Power spectrum for surface description of corroded ship structure from laser scan. In: *Structures, safety, and reliability: Presented at ASME 2019 38th International Conference on Ocean, Offshore and Arctic Engineering, June 9-14, 2019, Glasgow, Scotland, UK*. New York, NY: The American Society of Mechanical Engineers; 2019.
- [34] Nugroho FA, Braun M, Ehlers S. Probability analysis of PIT distribution on corroded ballast tank. *Ocean Engineering* 2021;228:108958. <https://doi.org/10.1016/j.oceaneng.2021.108958>.



### 3 Influence of pitting corrosion based on 3D surface scans (Paper II)

This section contains a reprint of the article: Shojai, Sulaiman; Schaumann, Peter; Braun, Moritz; Ehlers, Sören (2022): Influence of pitting corrosion on the fatigue strength of offshore steel structures based on 3D surface scans. In: *International Journal of Fatigue* 164, S. 107128. DOI: 10.1016/j.ijfatigue.2022.107128.

#### Background

In the previous paper the possibilities of numerical modelling of stress concentrations were shown, whereby the double-pit model as well as the real-surface model led to similar results. In order to take these stress concentrations into account in local fatigue concepts, a correlation between the numerically determined stress concentrations and the fatigue strength must be ensured. This would enable predictions about the (remaining-) service life of already corroded steel structures on the basis of the real surface geometry.

#### Overview

In this research, a total of 36 fatigue tests were performed on pre-corroded specimens at different mean stress ratios. The fatigue tests were accompanied by digital image correlation (DIC) to observe the crack location and crack development. In addition, all specimens were digitized by means of 3D scans and transferred to a numerical model via the reverse engineering process, which allowed all possible notches from pitting corrosion to be considered in a single model. For the calculation, linear elastic material was defined and the boundary conditions were chosen according to the axial fatigue test.

#### Conclusion

From the fatigue tests it could be concluded, that the corroded specimens have a higher fatigue life endurance compared to the corresponding DNV curve C for rolled plates with pitting corrosion and for butt welds (category C1 and D, whether ground flushed or not) in air environment. It was shown, that there is a good match of the crack location captured by DIC and the numerical prediction based on the real-surface model for many specimens, underlining the leading impact of the notch effect on the crack initiation. In cases the crack locations did not match the maximum stress location, the stress gradients along the thickness was different, which indicated potential micro-support effects.

However, as mentioned, the stress concentrations were based on a linear elastic material definition, neglecting the micro-support effect. Although a qualitative correlation was found between stress concentrations and fatigue resistance, the stress concentrations could not be incorporated in local fatigue analysis as the micro-support has to be considered in the stress analysis.

#### Authors Contribution

The experiments and numerical analysis as well as the paper conceptualization, methodology, validation, formal analysis, investigation, writing of the original draft and visualization were performed by the first author. Prof. Schaumann supervised the work presented in this paper and was responsible

for the funding acquisition and project administration. Dr. Braun and Prof. Ehlers provided the corroded material, commented, reviewed and edited the paper.



## **Influence of pitting corrosion on the fatigue strength of offshore steel structures based on 3D surface scans<sup>2</sup>**

### **3.1 Abstract**

Support structures for offshore wind turbines and the corresponding transformer platforms are highly susceptible to corrosion. In particular, the phenomenon of pitting is crucial, as it leads to local stress concentrations and thus affects the fatigue life of structures. Despite corrosion protection systems, corrosion cannot be completely avoided, which can lead to pitting corrosion on the steel surface. This leads to fatigue life reduction, since the structures are exposed to high dynamic loads. Local stress concentrations can be considered in local concepts but so far, corrosion effects in local concepts are insufficiently defined. Hence, this paper aims to investigate the impact of pitting corrosion and the corresponding stress concentration on the fatigue life endurance of structural steel, used for offshore wind support structures. For this purpose, a total of 36 pre-corroded specimens with pitting were tested against fatigue failure and monitored with Digital Image Correlation. In addition, the specimens were scanned with a high-resolution 3D scanner and converted to numerical models by reverse engineering, to determine the stress concentrations on the surface. In most cases the hotspots from the numerical model coincide with the crack location detected with Digital Image Correlation. The notch effect has a significant impact on the crack location and crack path.

Keywords: offshore-wind, corrosion fatigue, stress concentrations, local fatigue concept, reverse engineering

### **3.2 Introduction**

Support structures for offshore wind turbines (OWTs) are mainly made of steel and are highly susceptible to corrosion under maritime environmental conditions. Therefore, special requirements are set for the corrosion protection of OWTs [1,2] Despite corrosion protection systems, corrosion cannot be completely avoided. Repairs of the corrosion protection system or even recoating of the support structures at sea are not feasible. For the technical assessment of further operation after (partial) failure of the corrosion protection system, the remaining service life under damaged corrosion protection must be determined reliably. Beside this, there is a growing interest in optimized design of support structures, due to the progressing use of the seas and associated cost increases. Both can be achieved by using more sophisticated fatigue strength concepts like the notch stress and the notch strain concept.

---

<sup>2</sup> [Shojai, S., Schaumann, P., Braun, M., Ehlers, S., International Journal of Fatigue, 2022, 164, S. 107128. DOI: 10.1016/j.ijfatigue.2022.107128.](https://doi.org/10.1016/j.ijfatigue.2022.107128)

Corrosion causes thickness reduction due to uniform corrosion and local stress concentrations due to pitting. There is reliable knowledge about the thickness loss over time for different locations of the OWT [1,3], which are addressed in the standards as corrosion allowance [1,4]. The more crucial issue is pitting corrosion, where pits act like small notches and cause local stress concentrations [5–11]. This leads to fatigue life reduction, since the structures are exposed to high dynamic loads. Local stress concentrations can be considered in local [12–20], but so far, corrosion effects in local concepts are insufficiently defined.

In case of OWTs, different design standards [21–23] exist for fatigue issues. According to DNV, the fatigue design is predominantly carried out with the nominal stress concept, partly also with the structural stress concept [22]. There are different stress-life (SN) curves for the environmental condition Air, Cathodic Protection (CP) and Free Corrosion (FC). In the design of OWTs, a fully intact corrosion protection is assumed and therefore the SN-curves for Air are applied. From the point of time when there is no fully intact corrosion protection, the SN-curve for FC is used as a conservative approach for determining the (remaining) service life [24]. The SN-curves for CP and FC are derived from SN-curves for Air by reducing the SN-curves with the so-called Environment Reduction Factor (ERF) [25]. For the CP case, the design ERF is 2.5, while for the FC case ERF is equal to 3.0. These values are based just on a few tests performed on welded tubular joints and welded plates [25]. The welded tubular joints had an  $ERF < 3.0$  in all tests, while the welded plates achieved values up to  $ERF = 5.2$ . Overall, ERF values between 0.8 to 5.2 were reported, indicating a high degree of scatter. This includes not only the scatter from the corrosive environment, but also the weld geometry, which is not documented. It is therefore assumed that the influence of corrosion on already heavily notched components (tubular joints) is smaller than the influence on weakly notched components (welded plates). A general reduction with a single ERF value, as carried out in the DNV standards, is then neither economical nor on the safe side. Hence, in the German BAW standard [26] a distinction between heavily and weakly notched components is made. Here, for FAT classes above FAT125, the FAT classes have to be reduced by two category levels in case of free corrosion, while no reduction is necessary for FAT classes below FAT56. Beside this, in the British standard BS 7608 [27] a reduction of the ERF depending on the relationship between the existing stress and the yield strength is considered. In case of welded specimen, where the local stresses are higher than in unwelded components, it leads to a reduction of the ERF values. A distinction between welded and unwelded specimens is indirectly possible here, while it is missing in DNV. However, a consideration of notch stresses with local concepts allows a distinction between strongly and mildly notched (corroded) components. Hence, in recently published research by Momber et. al. [28] a replica technique was developed, which enables the replication of the original topography of a corroded surface. This technique in combination with the findings of this paper, enables the evaluation of the remaining service life of corroded structures by using local concepts. Nevertheless, the application of local concepts requires a detailed consideration of the impact of corrosion on the service life of structures.

**Impact of corrosion:** the service life of structures consists of the crack initiation and the crack propagation stage. Corrosion has an impact on the material in the crack initiation as well as in the crack propagation stage. Due to the acidic conditions under the rust layer, reported by Melchers et. al. [29], hydrogen can be produced and diffuse into the steel surface. According to Revie and Uhlig [30], and Marcus [31] the corrosion process includes an oxygen reaction and a hydrogen development process,

in which hydrogen is released. The detailed chemical reaction process is illustrated in Li et. al. [32]. This leads to embrittlement of the material, which has an impact on the ultimate material strength as well as on both stages of the service life. Li et. al. [32] investigated the mechanical behaviour of low alloy mild steel G250 on specimen, which were exposed to different acidic conditions in an immersion test. With lower pH-values, the ultimate strength and the corresponding strain were reduced significantly. Mehmanparast et. al. [33] investigated that the crack propagation is two times higher in seawater than in air. Beside this, there is the already described impact on the surface geometry, which can accelerate the crack initiation stage due to high stress concentrations. This is of great importance, since the crack initiation time is supposed to be the leading life time in corroded specimens, according to recently published research of Qvale et. al. [34], where Digital Image Correlation (DIC) was used to identify crack initiations on a few corroded specimen extracted from offshore mooring chains. An overview of the current state of knowledge regarding the impact of corrosion on fatigue can be found in the review of Larrosa and Akid [10].

In this paper, the main focus is on the impact from the surface geometry on the fatigue performance. For this purpose, a total of 36 pre-corroded specimens are tested until fatigue failure occurs and monitored with DIC, in accordance with [34]. In addition, the specimens are scanned with a high-resolution 3D scanner and converted by reverse engineering to a numerical model that can be used to determine stress concentrations on the surface of the specimens. The stress concentrations are compared with the cracks recorded by DIC in order to make conclusions about the influence of the notch effect.

### **3.3 Test setup**

#### **3.3.1 Specimen**

The specimens were cut out from pre-corroded approx. 11mm transverse floor plates of a former bulk carrier. More information and first investigation on the surface geometry were carried out by Neumann [35] and Nugroho [36]. The exact exposure time to free corrosion environment and the environmental conditions are not recorded. The specimen geometry is shown in Figure 3-1. The specimens were made by waterjet cutting. The edges were chamfered manually with  $r = 1\text{mm}$  to avoid crack initiation on the sharp edges. The specimens were cleaned only with chemicals according to ASTM [37].

To determine the mechanical properties of the corroded steel, tensile tests were performed on 36 specimens by Biglu [38]. In Table 3-1 the results for ultimate tensile stress  $R_m$ , the yield stress  $R_{p0.2}$  and the E-module are shown. The mean yield stress is  $264\text{ N/mm}^2$  while the 95%-quantile value is  $250\text{ N/mm}^2$ . For the ultimate tensile stress, a mean value of  $414\text{ N/mm}^2$  and a 95% quantile value of  $371\text{ N/mm}^2$  was conducted. Based on these tests a low alloy mild steel between S235 and S355 is assumed.

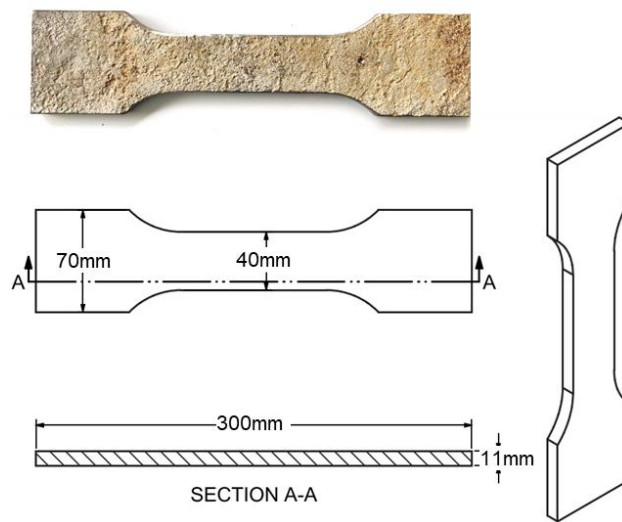


**Figure 3-1: Geometry of fatigue test specimen**

**Table 3-1: Mechanical properties from tensile tests by Biglu [38]**

	$R_{p0.2}$ [N/mm <sup>2</sup> ]	$R_m$ [N/mm <sup>2</sup> ]	E-module [kN/mm <sup>2</sup> ]
Mean:	264.18	414.09	180.27
Deviation:	7.99	17.40	18.86
95%-quantile:	249.95	371.43	134.60
min:	246.66	356.00	107.34
max:	304.38	444.31	286.31

### 3.3.2 Fatigue tests and digital image correlation setup

The fatigue test setup is shown Figure 3-2. The specimens were tested in a servo hydraulic testing machine, MFL HUS 60. The specimens were clamped at both ends. Some specimens were no longer straight after clamping at the upper end, which was due to the uneven surface at the clamping area. Clamping at the lower end straightened the specimen, resulting in out-of-plane moments. Since this is a constant moment, it can be interpreted as an additional mean stress, which has only a minor effect on fatigue. The testing frequency was 10 Hz. Up to 36 fatigue tests with  $R = -0.1$ ,  $R = 0.1$  and  $R = 0.5$  were carried out. Most of the tests were conducted at  $R = 0.1$ , see Table 3-2. These results are used to obtain a S-N curve. Further test with  $R = -0.1$  and  $R = 0.5$  are carried out in order to investigate the impact of the mean stress.

**Table 3-2: Fatigue testing scope**

R = 0.1	R = -0.1	R = 0.5
22 tests	6 tests	8 tests

Additionally, the fatigue tests were monitored with digital image correlation (DIC) in order to determine the exact location of crack initiation as well as the exact fatigue life endurance in the crack initiation and crack propagation stage. This is necessary for the calculation with local concepts, where only the fatigue life endurance until crack initiation is considered.

**Figure 3-2: Fatigue test setup**

### 3.3.3 Digital image correlation setup

The setup of the DIC system is shown in Figure 3-2. It contains four high resolution cameras (sensors), two on each side, in order to capture the crack on both sides. In addition, it can capture strains and deformation in three dimensions. The sensor distance is set to approx. 520mm, which allows to capture the specimens in a frame of approx. 120x90mm. The smaller the sensor distance, the higher the resolution and the smaller the capturing frame will become. Hence, the setting here is a compromise between the resolution and capturing frame.

The usual application of a black and white pattern for DIC is not necessary here because of rugged surface. The rugged surface leads to shadows, which are used to correlate the images, and to lower reflections on the surface. Comparison shots have shown that the difference between specimen with pattern and without pattern is negligible. However, in this work a white spray paint was applied on the surface to light up the specimen surface (see Figure 3-4). This allows to set a lower exposure time of the camera. A lower exposure time leads in turn to a lower delay between the trigger and the actual shot, which is an important issue in the application of DIC on fatigue test, where the loads alternate at high speed. However, the shadow correlation remains unaffected by the application of white spray paint. It should be mentioned that the pattern correlation can provide more accurate values for strain than the shadow correlation. For our application in this work, where the cameras are relatively far

away from the sample and the crack locations are of more interest than the exact strains, the shadow correlation is sufficient.

**DIC calibration:** Beside the mentioned delay due to the exposure time, there exist further delays between the testing machine signal and the DIC system. To ensure, that cracks are captured in every shot, the trigger has to be calibrated to the tensile load peak. Therefore, a static test has been run beforehand, in order to obtain the load-displacement relationship of a specific point on the specimen. In the second step, a dynamic test was run with 10Hz (and also 5 Hz for further comparison) on the desired load level. Then, the displacement for the desired load level was compared. In Figure 3-3 force and displacement over time are illustrated. The displacement for  $F=80\text{kN}$  is  $u=0.31\text{mm}$  in the static test,  $u=0.30\text{mm}$  at 5Hz frequency and  $u=0.27\text{mm}$  at 10Hz frequency. This corresponds to 96,7% (for 5Hz) and 87% (for 10Hz) of the load peak. To ensure a shot on the load peak, the trigger must be reduced respectively. Nevertheless, cracks are visible in both cases. This is also reported in [39].

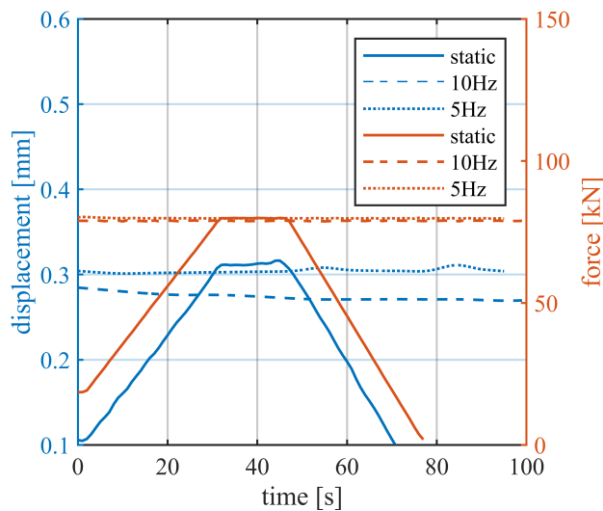


**Figure 3-3: Force-displacement diagram for static and dynamic test**



**Figure 3-4: Specimen preparation for DIC, white sprayed surface**

For the fatigue tests, the trigger was set to approx. 85% of the load peak. Depending on the load level, at every 1000 or 2000 load cycle a shot was taken.

### 3.3.4 Crack detection using DIC

With the application of DIC it is possible to capture the strains as well as the crack initiation and the crack propagation over the testing period. All 36 specimens were investigated with DIC. For all specimens the fatigue life until crack initiation was obtained by going manually through the DIC shot series, until the cracks became visible. Two values were documented in this way, the fatigue lifetime  $N_{C1}$  and  $N_{C2}$ .



The definition of  $N_{C2}$  is based on Radaj in [15] and Radaj and Vormwald [40], where the technical crack is defined as a crack between 0.5-2mm length and 0.5mm depth, see also Braun et al. [41]. This definition also corresponds to the definition in the background documentation of Eurocode 3 [42], where the technical crack is defined as the first crack either detected visually or by measuring the deformation behaviour. However, there are several methods to determine the technical crack using DIC. According to Friedrich and Ehlers [39,43], the technical crack is reached at a strain of more than 1% over a length of 2mm. Hutt and Cawley [44] and Schürmann [45] defined the crack by the displacement in axial direction. Schürmann used the strain to detect the crack location and the displacement to detect the number of load cycles to crack initiation. This is possible since a displacement gap occurs in the area of the crack, whereby a gap of approx. 0.004mm was chosen as an indicator. Alternatively, Qvale et. al. [34] defined the macroscopic crack at an inter-node displacement of 0.002mm. In the investigations carried out here, the approach according to Friedrich and Ehlers was chosen for the detection of the technical crack. Hence,  $N_{C2}$  is defined at a crack that has a strain of at least 1% over a length of about 2mm. This criterion is in line with the definition according to the Eurocode, since the cracks are also visually detectable. Since the cameras of the DIC system can also detect cracks smaller than 2mm, in addition to  $N_{C2}$ , the first visible crack at  $N_{C1}$  was documented. Hence,  $N_{C1}$  is defined at a crack of at least 1%, but with a length of smaller than 2mm.

It should be mentioned that higher DIC resolutions enable more accurate data on the displacement and strain during the fatigue test and thus could lead to a different ratio of crack initiation and crack propagation lifetime.

### 3.3.5 3D-scanning of specimen and reverse engineering method

**3D-scanning:** Before the fatigue test, the specimens were scanned with a high-resolution 3D measuring system Keyence VR-3000 (Figure 3-5).

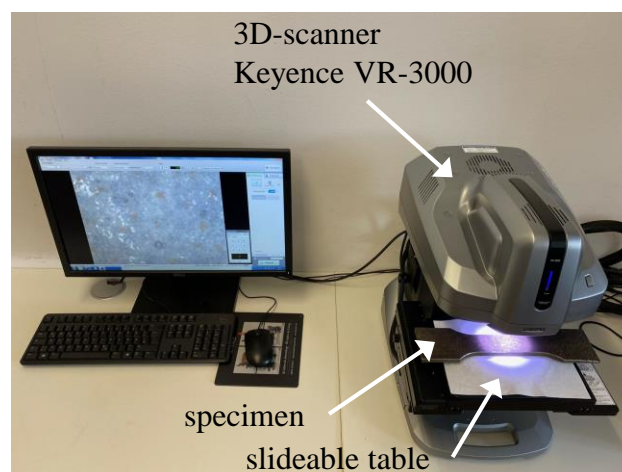


**Figure 3-5: 3D-scan with Keyence VR-3000**

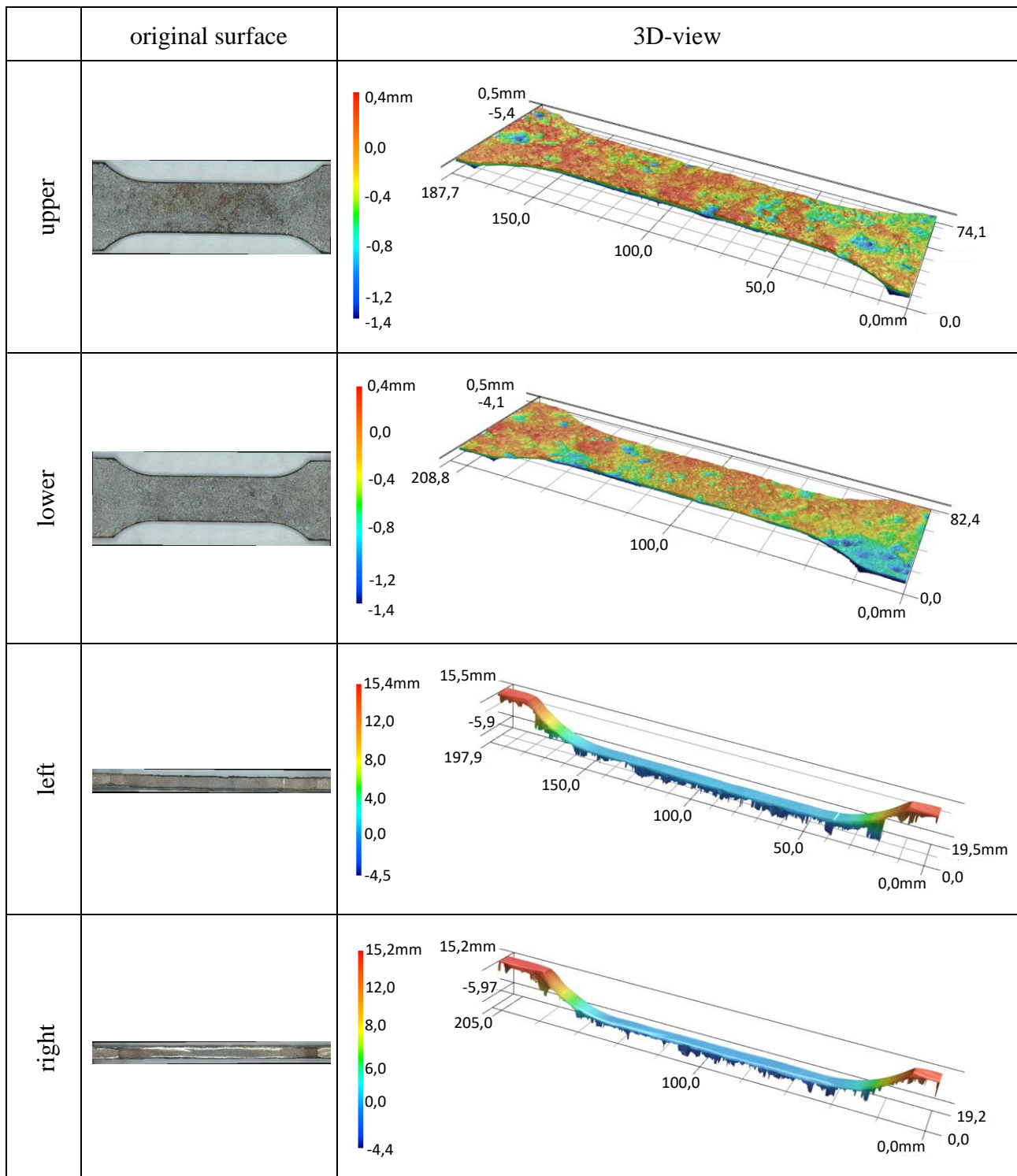


**Figure 3-6: High resolution shots of a corroded sample from all sides**

The scan and the assembling into a 3D-model requires several steps shown in Figure 3-7. The procedure starts with scanning the surface from all sides separately (see Figure 3-6) and exporting as STL-files. In the next step, the lateral surfaces are trimmed and all surface scans are pre-positioned in order to avoid complications in the assembling procedure. Hereafter, the surface scans are merged one after the other, with the best-fit command within the GOM Correlate software. The application of the best-



fit command requires the existence of a common area in each scan. This is ensured with the chamfered edges, which are captured from the upper and the lower as well as from the lateral scans. Beside this, the lateral scans ensure the exact caption of the specimen thickness. It should be noted that the quality of the scan depends on the grid size. Lower grid sizes lead to high amount of data and are very demanding to handle. However, in this research the scans were conducted with a grid size up to 0.02mm.

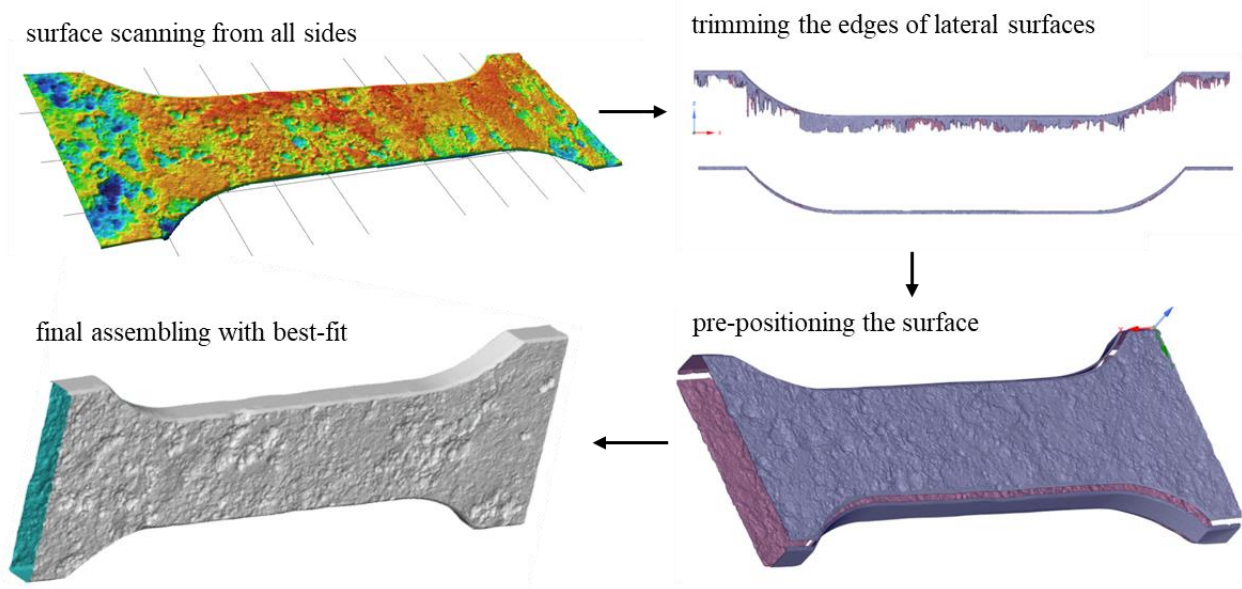


**Figure 3-7: Assembling the scans into a 3D-model as STL-data.**

Reverse Engineering: The reverse engineering method is used to create a solid model from the assembled 3D-model available in STL format. The transformation to a solid model is required due to following aspects:

1. The curvature of the surface in STL format is not continuous, because it consists of a series of individual facets that are connected to each other, see Figure 3-8 b). This would lead to singularities in the subsequent numerical analysis.
2. The faceted surfaces require too large amounts of data for illustration (high number of points, lines and facets).

The procedure of obtaining a solid model from STL-format is described in Shojai et. al. [46]. For this purpose, so called Non-Uniform Rational B-Spline (NURBS) surfaces are used. NURBS surfaces are described by two-dimensional, mathematically defined polynomial functions of higher order, which fit the shape of the faceted geometry. The advantage of NURBS surfaces are, that they need much less data for the description of the surface and have a continuous curvature. The quality of the fit depends on the number of polynomial functions per area. In the reverse engineering software Ansys SpaceClaim, this can be controlled through the number of the grids per area (grid rate), see Shojai et.al. [46]. Higher grid rates lead to better fitting of the facets and are thus more accurate. In [46] a grid rate of  $R=3$  [1/mm] (120 grids per 40mm length) was sufficient. Here a grid rate of  $R=7-8$  [1/mm]

(120 grids per 15mm length) was determined as sufficient. The difference is caused by the scan quality, which is higher with the VR-3000 scanner (0.1mm grid size in the 3D-scan). A scan with smaller grid size with higher scan quality, requires high grid rates for fitting the faceted surface. The impact of different scan qualities in the assessment of fatigue strength is an object of ongoing research and is not discussed here. However, it is not possible to create a solid model by transferring the entire surface in single NURBS surface. Hence, the surface is split into so-called NURBS-patches [11] [14] and merged into a solid model afterwards, see Figure 3-8 right. Up to 80 patches were required to assemble a solid model according to Figure 3-8.

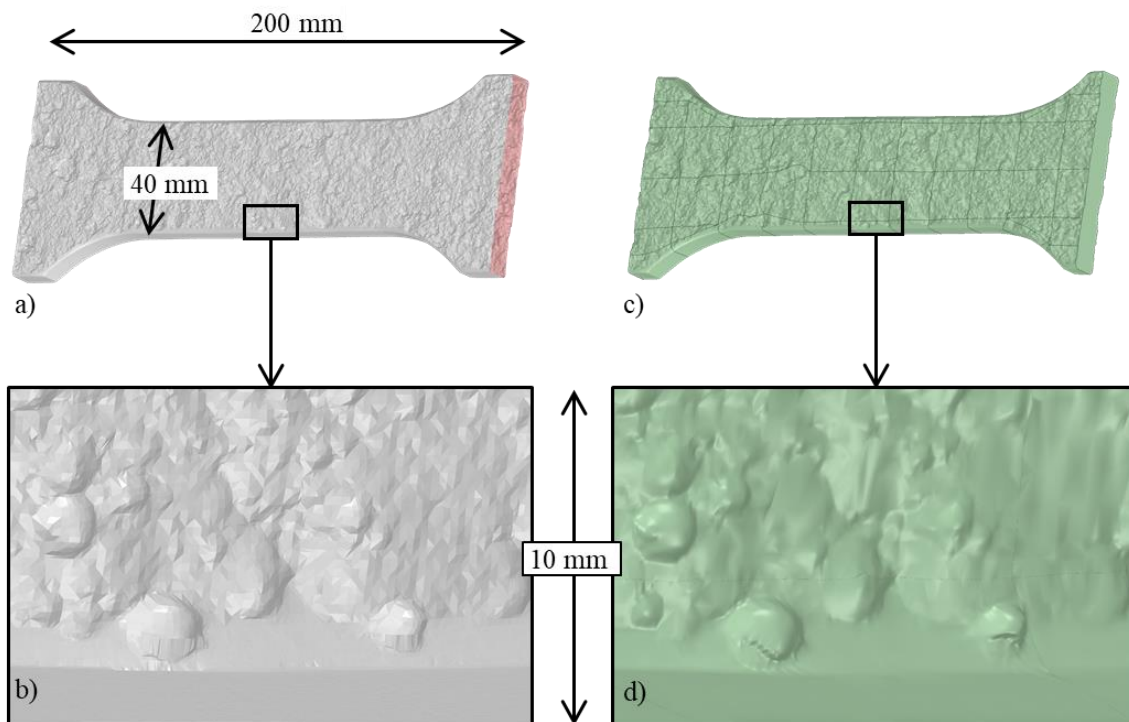


**Figure 3-8: Faceted 3D-model in STL-format with non-continuous surface in a) and b). Solid model with NURBS-patches with continuous surface in c) and d) - both for specimen P.01**

### 3.4 Numerical Analysis

#### 3.4.1 Numerical model

The numerical model with the boundary conditions for the analysis of the stress concentrations are shown in Figure 3-9 b). If the applied force is adjusted to the cross section, the stress results on the surface are equivalent to the stress concentrations. Since the cross section varies along the specimen, the cross-section area is determined by the mean of 5 different locations at an interval of approx. 20 mm in the region of the tapered area of the specimen. An example of the cross section is given in Figure 3-9 a). For the meshing quadratic tetrahedral elements were used in order to fit in the rugged surface and achieve a fast convergence. Studies on the element size have shown, that an element size of 0.3-0.4mm is required [46] to ensure, that the maximum stress concentration location doesn't change. After the maximum stress concentration location has been ensured, a convergence study only

for that area has been conducted. This reduced the number of elements and computing time significantly. The initial element size is shown in Figure 3-9 c).

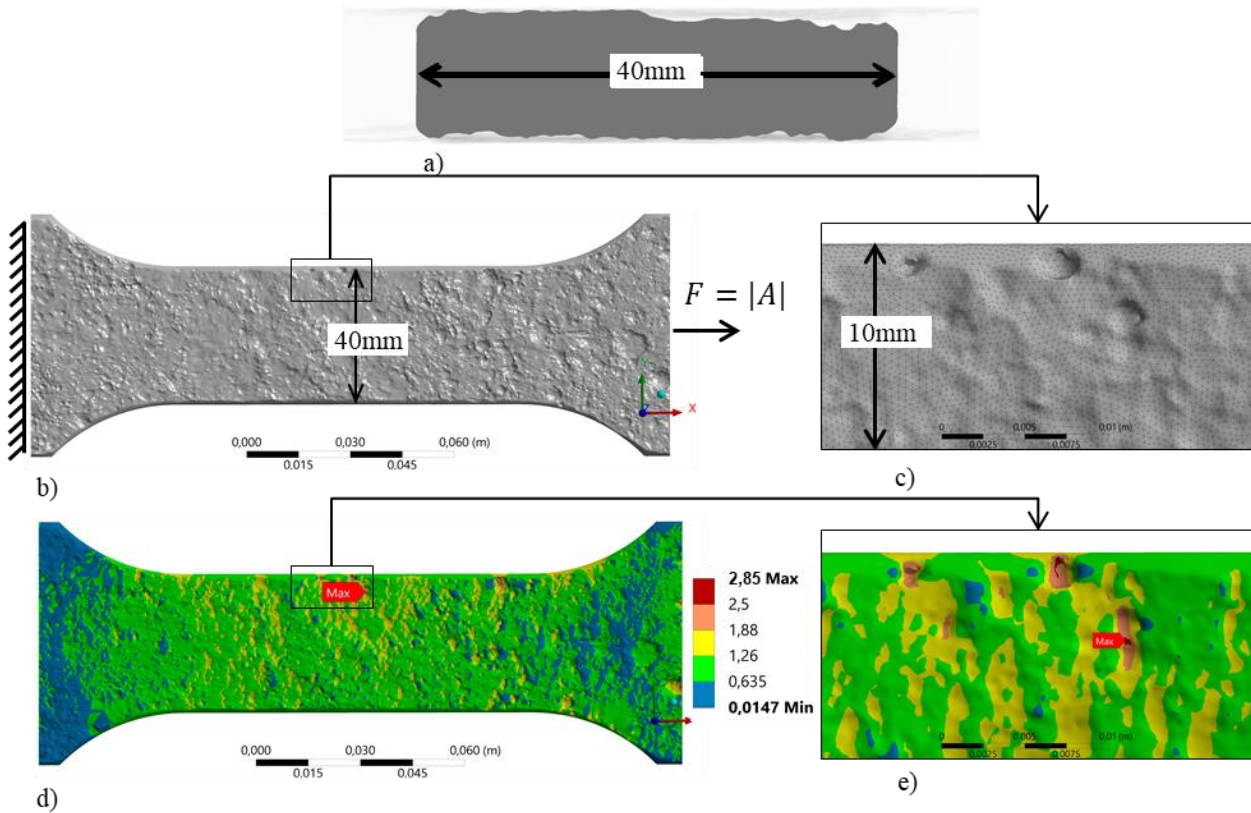


**Figure 3-9: Specimen P.01 a) cross section A at maximum stress concentration, b) solid 3D-model, c) initial surface mesh of solid model, d) results of numerical simulation, e) maximum stress concentration before convergence study**

### 3.4.2 Convergence study

The convergence study has been carried out in the area of the maximum stress concentration (see Figure 3-9 e). For this purpose, the adaptive convergence tool in Ansys Workbench has been used. The final mesh and the updated stress concentrations are shown Figure 3-10 on the left (a and b). The element size in the stress peak is 0.01mm. Around the stress peak the element size is 0.05 to 0.1mm. The change in the stress concentration due to refinement is not only caused by the FEM-dependent approximation of the real solution, but also on the rugged surface of the corroded specimen. The fine mesh shown in Figure 3-10 b) fits better into the surface of the solid model than the initial mesh shown in Figure 3-9 c). Finer meshes lead to more accurate description of the rugged surface and lead to higher stress concentrations. This is also shown in Figure 3-11, where an element size of 1.0mm (Figure 3-11, b) obviously can describe the rugged surface better than an element size of 1.8mm (Figure 3-11, c). This leads to the fact, that the surface geometry changes in every refinement step, which in return leads to higher initial slopes in the convergence study, see Figure 3-10 c). This behaviour is intensified by finer NURBS surfaces and can lead to very high stress concentrations.

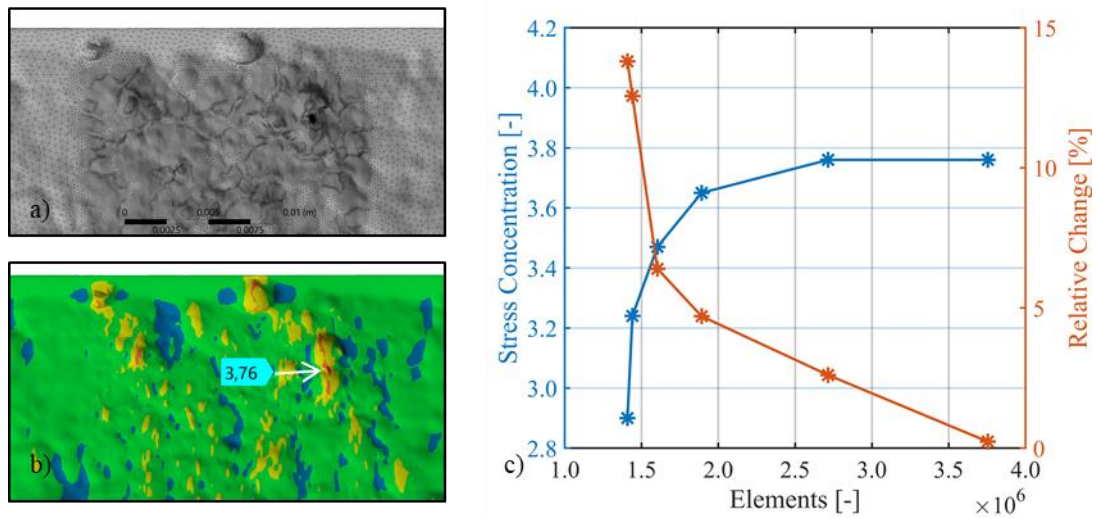


**Figure 3-10: Specimen P.01, adaptive convergence study applied on in the area of maximum stress concentrations. a) refined surface mesh at last stage, b) converged stress concentration c) convergence plot**

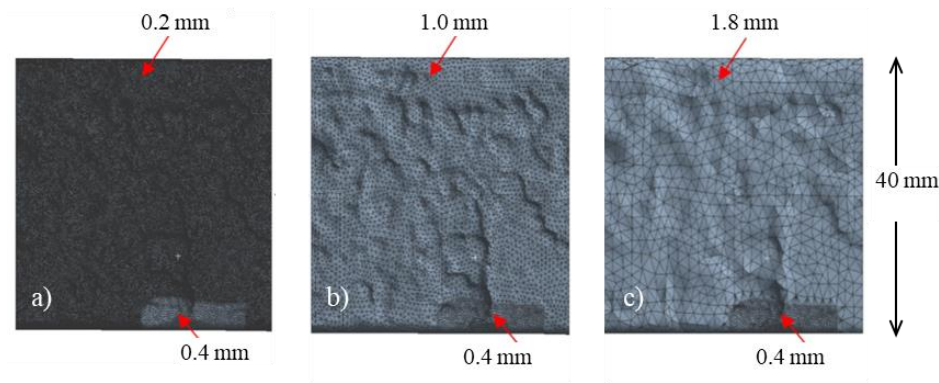


**Figure 3-11: Impact of mesh element size on surface description for 0.2mm (a), 1.0mm (b) and 1.8mm (c)**

However, for plausible results, a harmonization between the scanning grid size, the NURBS grid rate and the element size of in the numerical simulation is indispensable. In the case of the specimen shown in Figure 3-10, the stress concentrations converged to  $\alpha_k=3.76$  from the initial value of  $\alpha_k=2.85$  (see Figure 3-9) and can hence interpreted as a plausible result. All specimens were investigated in this manner. The results are presented in chapter 3.5.

## 3.5 Results and Discussion

### 3.5.1 Fatigue tests results

The fatigue test results with corresponding load values, load ratios, cross section areas and stress ranges for the specimens are summarized in Appendix A, Table 3-5. The cross-section area  $A_{ave}$  is determined according to chapter 3.4.1 with the mean of 5 different locations in the tailed area of the specimen. The results are statistically evaluated to obtain the SN-curve for the high cycle fatigue

(HCF) region, which is defined between  $N=10^4$  and  $N=7 \times 10^6$  in Eurocode 3 [21], DNV [22] and IIW [19]. The SN-curve is defined as

$$N = 2 \cdot 10^6 \cdot \left( \frac{\Delta\sigma_c}{\Delta\sigma} \right)^{m_1} \quad (3-1)$$

where  $N$  is the number of cycles to failure,  $\Delta\sigma_c$  is the characteristic stress range at  $N=2 \times 10^6$ ,  $\Delta\sigma$  is the stress range used as variable and  $m_1$  is the slope in the HCF region. Equation (3-1) can be transformed into the log scale and is then stated as a linear equation according to Basquin [47]:

$$\log N = \log a - m_1 \cdot \log \Delta\sigma \quad (3-2)$$

in accordance to:

$$y = b - m \cdot x \quad (3-3)$$

Here,  $\log a$  in equation (3-2) defines the axis intercept similar to  $b$  in equation (3-3) and is then used to calculate the characteristic stress range  $\Delta\sigma_c$ .

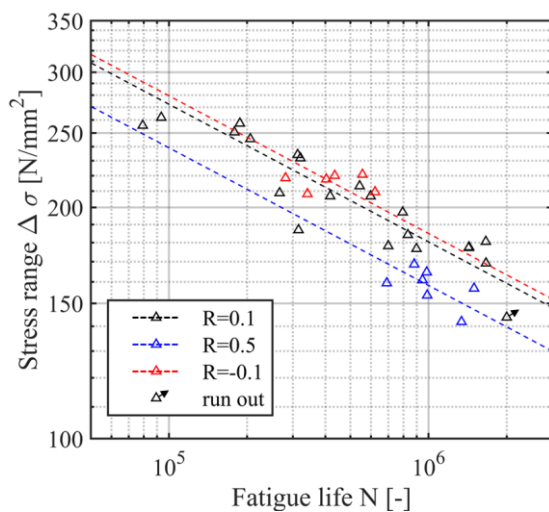
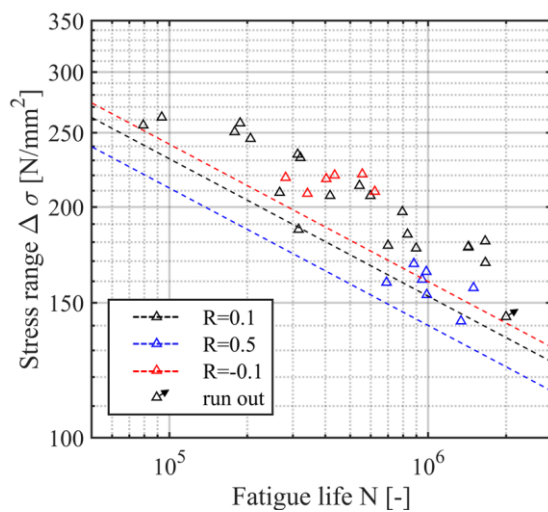
For the evaluation of the parameters  $\log a$  and  $m_1$  the pearl-string method according [48] is used. Therefore, a linear regression using the least squares method in the direction of the number of cycles is applied in the first step. In the second step, the statistical evaluation is carried out. For this purpose, all test results are projected onto an arbitrary load horizon on which the  $\log a$  value for the survival probabilities are calculated. This procedure allows the evaluation of test data with varying stress ranges, as listed in Table 3-5. It should be noted, that there are varying stress ranges, even though the applied loads are the same. This is caused by different cross section areas for each specimen (see Table 3-5, column 2 and 6) and rules out the application of the horizon-method.

The fatigue test results with the corresponding 50%-fractile curve are plotted in a S-N diagram in Figure 3-12. The slope  $m_1$  was determined based on the fatigue tests conducted with  $R=0.1$ . For the curves of  $R=-0.1$  and  $R=0.5$  the same slope is assumed, since there are not enough data to determine a slope reliably. The corresponding parameters for  $\log a$  and  $\Delta\sigma_c$  are listed in Table 3-3. For  $R=-0.1$  and  $R=0.1$  there is only little difference in the fatigue resistance, as illustrated in Figure 3-12. It should be noted, that due to the small difference and the small number of specimens, no clear statement about the influence of the mean stress can be made, when comparing  $R=-0.1$  and  $R=0.1$  results. However, compared to  $R=0.5$  the test results for  $R=0.1$  show clearly higher fatigue resistance. This is also illustrated in the Haigh-diagram shown in Figure 3-14, where the stress amplitudes and the corresponding mean stresses for the number of cycles of  $N=5 \times 10^5$  are plotted for different confidence levels. The number of cycles of  $N=5 \times 10^5$  selected for the Haigh-diagram evaluation is close to the test results for  $R=-0.1$  and  $R=0.5$ . This ensures that the effect from the assumption of equal slopes for all mean stress ratios is minimized. It becomes evident, that with higher mean stresses, the stress amplitude for reaching  $N=5 \times 10^5$  is getting smaller. This is in accordance to Eurocode 3 and DNV [15,16], where the stress range can be reduced up to 60% for mean stresses below  $R=0$ . For stress ratios above  $R=0$ , there are no distinctions made in Eurocode 3 and DNV. In the IIW recommendations [20] the reduction already starts at  $R=0.5$  and corresponds better to the test results in the range of  $R>0$ . Nevertheless, for the purpose of further comparisons the conducted S-N curves for  $R=0.1$  and  $R=0.5$  are used.



**Table 3-3: S-N curve parameters**

m1	R	50 %		95 %		97,7 %	
		$\Delta\sigma_c$ (FAT)	log a	$\Delta\sigma_c$ (FAT)	log a	$\Delta\sigma_c$ (FAT)	log a
5.58	-0.1	163.4	18.651	146.1	18.380	141.2	18.297
	0.1	159.3	18.590	139.3	18.264	135.1	18.191
	0.5	139.8	18.273	127.2	18.045	123.8	17.978

**Figure 3-12: Fatigue test results for different R-ratios and corresponding 50%-quantile S-N curves****Figure 3-13: Fatigue test results for different R-ratios and corresponding 97.7%-quantile S-N curves**

**Comparison with DNV rules:** In Figure 3-15, the conducted S-N curve for R=0.1 and R=0.5 with 97.7% probability of survival is plotted alongside of S-N curves for different detail categories according to DNV. The corresponding constructional details, environment conditions, slopes with  $\log a$  values and the stress range  $\Delta\sigma_c$  for the plotted curves are listed in Table 3-4.

According to DNV rolled and extruded plates corresponds to details category B1. In case of additional stress concentrations due to pitting corrosion on the plate surface, the use of curve C is recommended. Curves C1 and D are required for transversal butt welds. The slope of the conducted fatigue test with  $m_1=5.58$  is higher in all cases compared to the DNV curves. This leads to a flatter S-N curve and greater values of the stress range  $\Delta\sigma_c$  compared to all curves listed in Table 3-4, beside curve B1-Air. It is worth mentioning, that the test data with  $\Delta\sigma_c = 135.1$  N/mm<sup>2</sup> and  $\Delta\sigma_c = 123.8$  N/mm<sup>2</sup> (for R=0.1 and R=0.5 N/mm<sup>2</sup>) indicates higher stress ranges at  $N=2 \times 10^6$  than curve C1-Air and D-Air with  $\Delta\sigma_c = 112$  N/mm<sup>2</sup> and  $\Delta\sigma_c = 90$  N/mm<sup>2</sup>. This is a valuable finding, since it allows the implicit comparison of the pre-existing notch effects of butt welds to the notch effect of corroded base material.

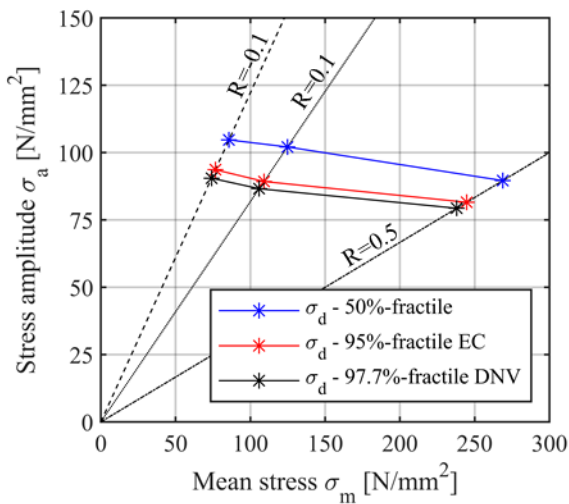


Figure 3-14: Haigh-diagram for fatigue life endurance  $N=5 \times 10^5$

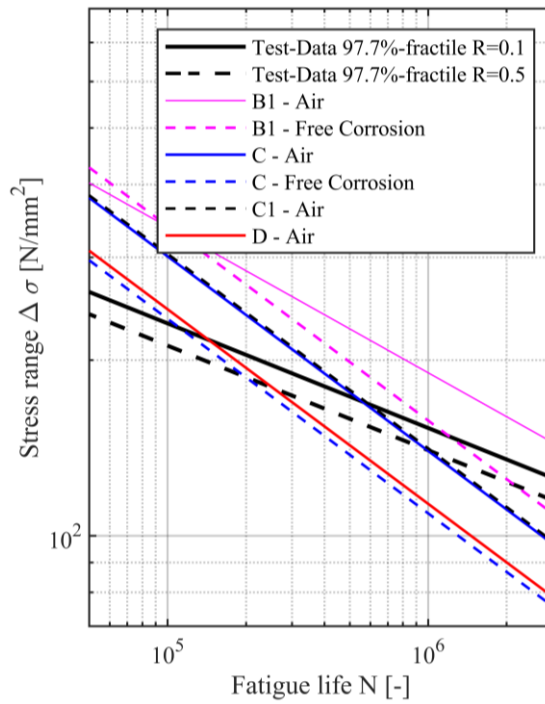


Figure 3-15: Comparison of test data to design S-N curves from DNV

Table 3-4: Detail categories according to DNV

Constructional detail	Detail category	Environmental condition	Slope $m_1$	Slope $m_2$	$\log a_1$	$\log a_2$	$\Delta\sigma_c$ (FAT)
rolled plates and flats	B1	Air	4	5	15.117	17.146	160.0
rolled plates and flats	B1	FC	3	5	12.436	12.436	110.9
rolled plates and flats + pitting corrosion	C	Air	3	5	12.592	16.081	125.0
rolled plates and flats + pitting corrosion	C	FC	3	3	12.115	12.115	86.7
butt welds + ground flush to plate surface	C1	Air	3	5	12.449	16.081	112.0
butt welds + convexity smaller than 10% of weld width	D	Air	3	5	12.164	15.606	90.0
test data – R=0.1	C	Air	5.58		18.191		135.1
test data – R=0.5	C	Air	5.58		17.978		123.8

### 3.5.2 Digital image correlation results

As mentioned, DIC was used to track strain and displacement as well as crack initiation. DIC was applied on all 36 specimens. In 21 cases, the crack was inside the DIC frame. The determination of

the crack initiation locations and the definition of the technical crack are described in chapter 3.3.4. Two values were documented accordingly, the fatigue lifetime  $N_{C1}$  and  $N_{C2}$ . The measured crack lengths for  $N_{C1}$  and the related fatigue lifetime is documented in Table 3-6 (Appendix B).

In Figure 3-16 the DIC shots (plot a) to d)) and the corresponding strains in [%] (plot e) to h)) are shown exemplary for specimen No. 07 at different number of cycles  $N_{C1}$ ,  $N_{C2}$  and  $N_T$ . The length of the first visible crack at  $N_{C1}$  is directly measured at the DIC shot (plot b)). The crack length at  $N_{C1}$  is smaller than 1mm and is only slightly visible in the strain plot, while it becomes clearer at  $N_{C2}$ . From  $N_{C2}$  the crack grows until fracture  $N_T$  (total fatigue life). It has to be noted, that dark blue and dark red colour in the strain plots are signal noise, which are also enhanced due to the very rugged surface, and hence can be ignored.

Moreover, the crack initiation ratios for  $N_{C1}$  and  $N_{C2}$  to the total fatigue life  $N_T$  were determined for all tests, where the crack was inside the DIC frame (see Table 3-6 (Appendix B)). The results are plotted in a frequency plot in Figure 3-17 (a). The mean ratio of  $r_{C1}=N_{C1}/N_T$  is  $\mu=0.82$ , while the standard deviation is  $\sigma=0.06$ . The mean ratio of  $r_{C2}=N_{C2}/N_T$  with  $\mu=0.86$  is slightly higher with a smaller deviation of  $\sigma=0.04$ . It can be concluded, that the crack initiation stage predominates the fatigue life of the tested specimens. This behaviour can be explained by the small thickness of the specimens and thus small capacity for crack propagation and the low notch acuity [41,49–51].

Specimen No. 07 – upper side

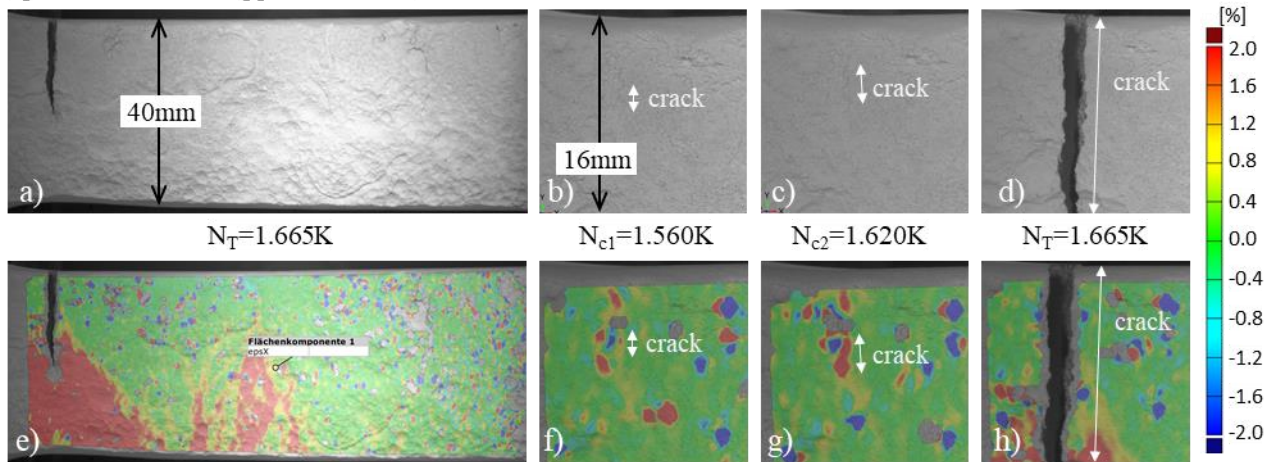


**Figure 3-16: DIC plot for crack initiation, crack propagation and fracture of Spec. No. 07**

The mean difference between  $N_{C1}$  and  $N_{C2}$  is  $\mu_{(1-2)}=0.05$ , see Table 3-6. It means that on average 5% of the total lifetime is needed to reach a crack length of 2mm, after the first visible crack initiation. It has to be noted, that the documentation of the first visible crack is highly dependent on the evaluator, because there is more room for interpretation, while it is clearly defined, when a crack length is given. Hence, for upcoming publication, which will deal with the evaluation of the fatigue resistance based on the notch strain concept and the subsequent comparison of the determined fatigue life, the fatigue life corresponding to an Initial crack length of 2mm crack will be used as reference.



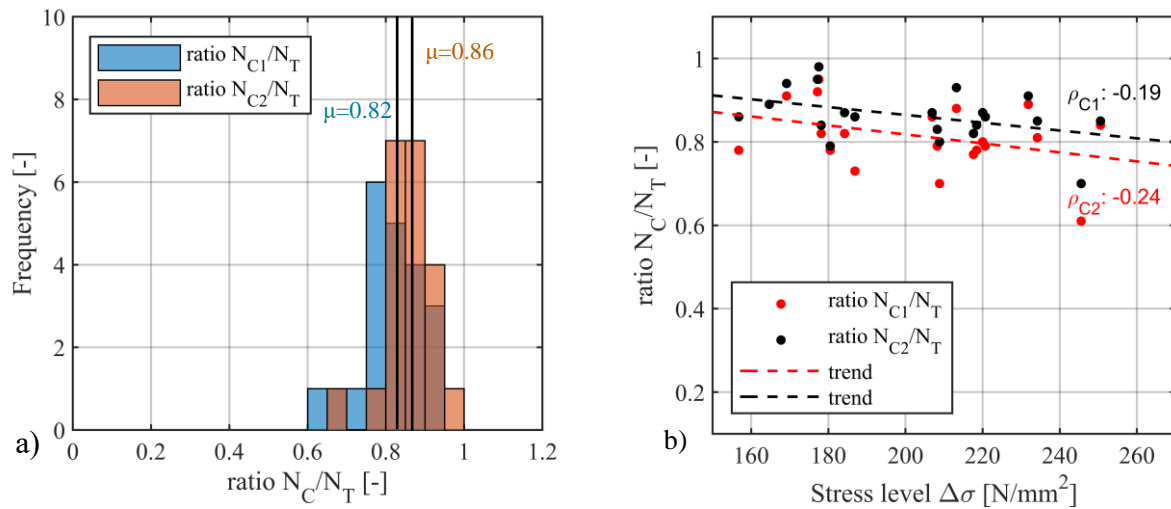


**Figure 3-17: Frequency plot for the ratio of cycles until crack initiation to total cycles (a) and relationship between crack initiation ratio and the corresponding stress level (b)**

In addition, the correlation between the load stress level and the crack initiation time, expressed by the ratio  $r_c = N_C/N_T$ , is investigated. According to [40] and [52] for welded components there is a dependency between stress level and crack initiation and crack propagation lifetime, where low stress levels lead to higher lifetime in the crack initiation stage while high stresses lead to higher lifetime at the crack propagation stage. For this reason, in Figure 3-17 (b) the crack initiation ratio is plotted over the corresponding stress level. It can be concluded, that for all specimens, which were inside the DIC frame (see Table 3-6 in Appendix B), there is only little correlation between the stress levels and the ratio. This is indicated by the trend line plotted Figure 3-17 (b) and the corresponding correlation values of  $\rho_{C1} = 0.19$  and  $\rho_{C2} = 0.24$ . This is assumed to be due to the fact that the nominal stress illustrated here does not reflect the local situation at the notch.

### 3.5.3 Numerical analysis results

The numerical analyses were carried out for all specimen listed in Table 3-6, according chapter 3.4. For each specimen, the crack location, the maximum resulting local notch stress as well as the notch stress at crack location were documented. Moreover, the coincidence of the numerically determined hotspot stress with the actual crack location was documented. For this purpose, three levels of conformity are introduced:

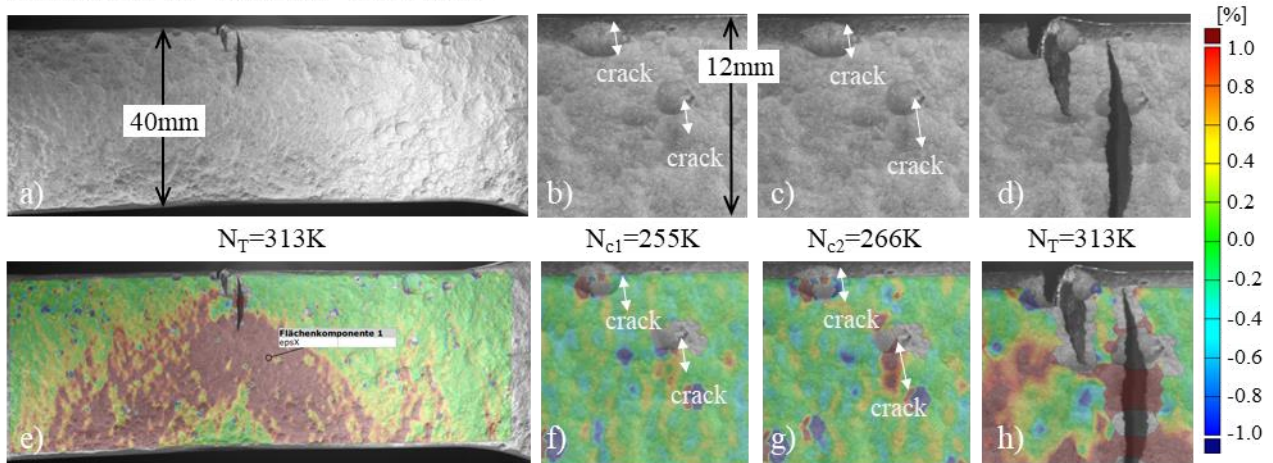
- Level 1: The max. stress concentration coincides with actual crack location and the crack path. The ratio between stress concentration at the crack location and the max. stress concentration is 1.0.
- Level 2: The 2<sup>nd</sup> max. stress concentration coincides with actual crack location and the crack path. The ratio between stress concentration at the crack location and the max. stress concentration is higher than 0.8.

- Level 3: The 2<sup>nd</sup>, 3<sup>rd</sup> or 4<sup>th</sup> max. stress concentration coincides with actual crack location and the crack path. The ratio between stress concentration at the crack location and the max. stress concentration is lower than 0.8.

The coincidence of the hotspots was investigated through the comparison of the DIC-shots with the numerical analyses results. For specimens, where the cracks occurred outside the DIC frame, the crack location was determined by inspection of the beach marks.

In Figure 3-18 the DIC results and the numerical simulation results are illustrated. As described in section 3.3.3, the DIC shots were taken from both sides (upper side and lower side). Here, only the side, at which the first crack initiated, is documented. For specimen No. 01 (Figure 3-18) the crack occurred at the lower side. The crack initiation as well as the propagation are shown in the DIC shots and in the corresponding strain plots (Figure 3-18 a) to h)).

Specimen No. 01 – lower side – DIC result:



Specimen No. 01 – lower side: numerical result

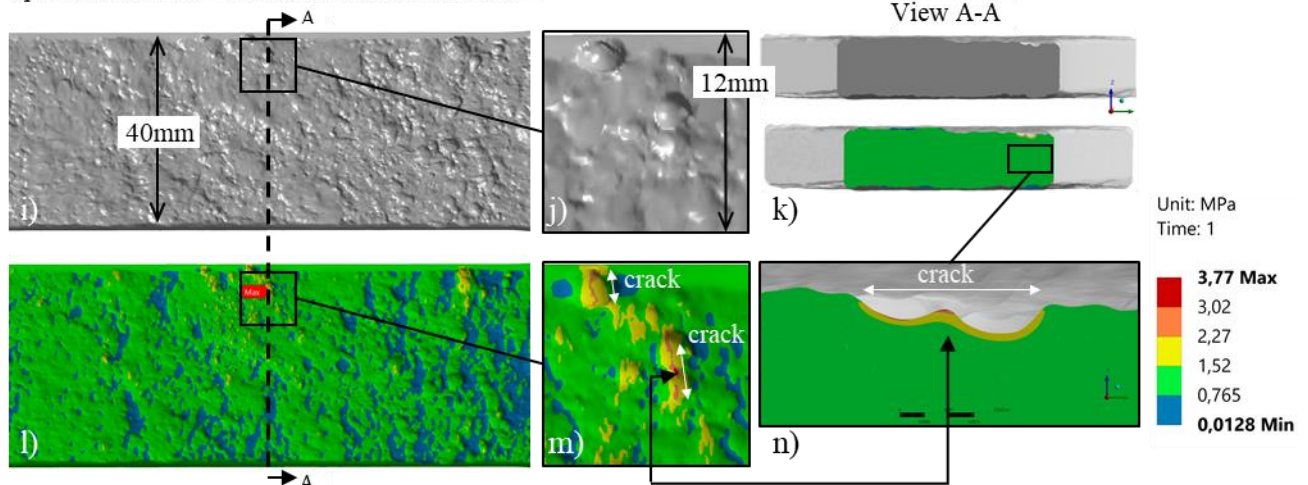
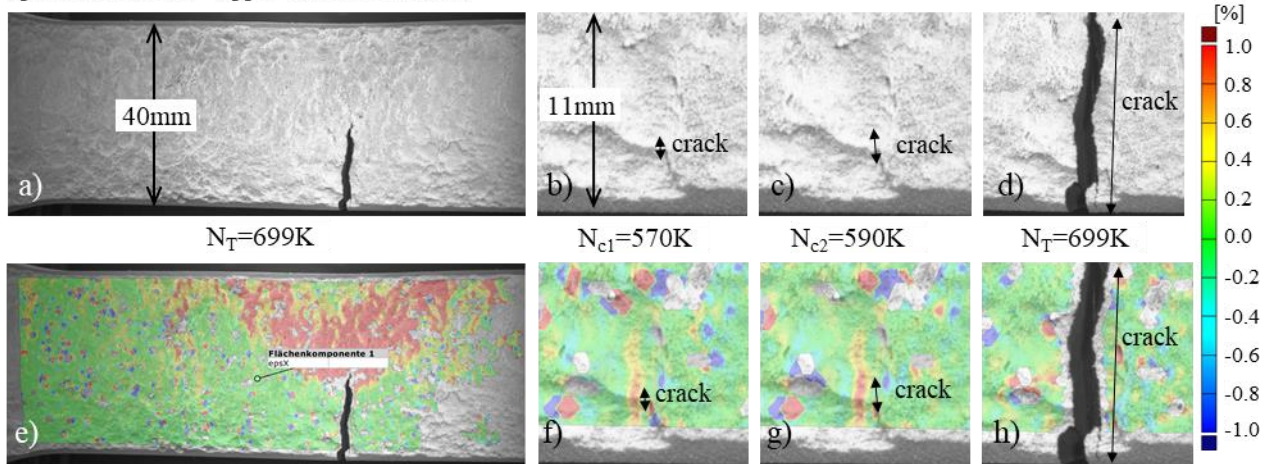


**Figure 3-18: Comparison of DIC results with numerical determined stress concentration results for specimen No. 01 – coincidence level 1**

In Figure 3-18 i) to n) the obtained stress concentrations from the numerical analysis are shown for the same locations. From the comparison of plot f) with m) it becomes evident, that the max. stress

concentration is in accordance to the crack initiation location. Moreover, the crack propagation follows fully the stress concentration path, which is an indication of the high impact of stress concentrations on the fatigue life. On plot k) and n) the cross section of the numerical model and the corresponding stress distribution is plotted. It shows, that the max. stress concentration is at the intersection of two overlapping pits. This is in line with Shojai et. al. [11], where a double pit model was introduced for the calculation of stress concentrations factors and the approach with a single pit model has been questioned. However, the numerical results of specimen No. 01 fully matches with the results of the fatigue test and is hence categorized in the coincidence level 1.

Specimen No. 05 – upper side: DIC results



Specimen No. 05 – upper side: numerical results

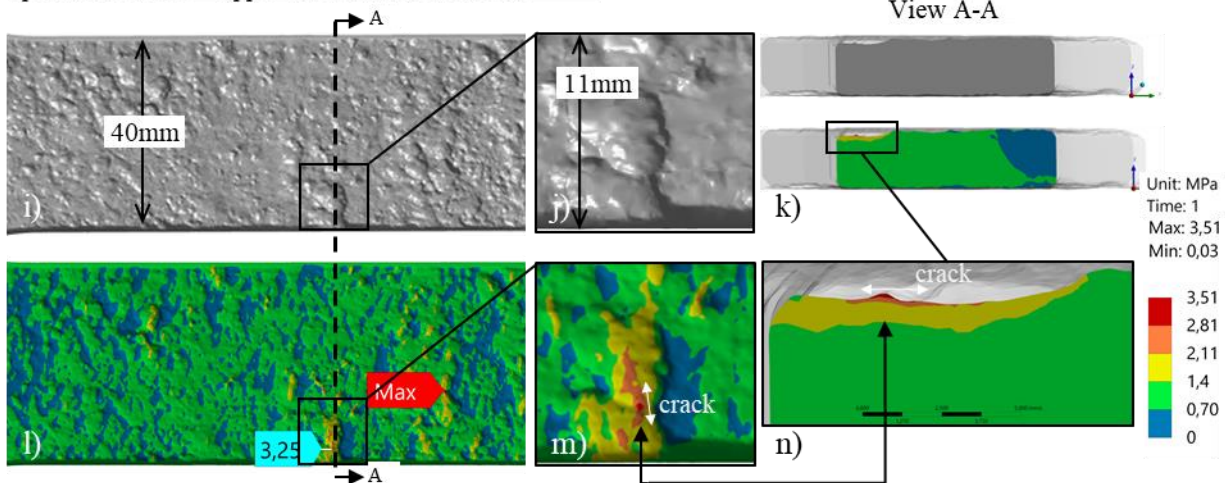


**Figure 3-19: Comparison of DIC results with numerical determined stress concentration result for specimen No. 05 – coincidence level 2**

In Figure 3-19, the result of specimen No. 05 is shown as an example of the coincidence level 2. The max. stress concentration from the numerical analysis is  $\alpha_{k,mx}=3.51$ , but it doesn't match with the crack location shown in plot a) to h). The actual crack is located inside the black frame (see Figure 3-19, l) and m)), where the local max. stress concentration is  $\alpha_{k,crack}=3.25$ . This is the second highest local value of the stress concentration and is only marginally lower than the absolute max. stress

concentration. The ratio defined as  $r_\alpha = \frac{\alpha_{k,crack}}{a_{k,max}}$  is  $r_\alpha=0.93$ . Nevertheless, the crack path fully agrees with the stress concentration, when plot f) and m) are compared. Besides this, the crack initiated here again at the intersection of two overlapping pits as shown in plot k) and n). In the coincidence level 3 the same pattern as in level 2 can be observed. The difference is only in the ratio  $r_\alpha$ , which is defined as lower than 0.80 in level 3.

However, in Figure 3-20 the crack initiation locations for all specimen (with cracks inside the DIC frame) at coincidence level 1 and the corresponding numerical results for the stress concentrations are shown. The max. stress concentration location is labelled with a red banner and matches with crack location. It follows, that for 13 out of 21 specimens the first crack initiated at the max. stress concentration location.

In Figure 3-21 the specimens of coincidence level 2 and 3 are plotted. The red banners show the max. stress concentrations location, while the blue banners indicate the crack location and the corresponding stress concentration. Only 8 of 21 specimens belong to that level. The max. stress concentrations and the stress concentration at the crack location are plotted in Figure 3-22 for all specimens. The related data are provided in Appendix C, Table 3-7. The values for both are, besides specimen No.15 and No.33 with  $\alpha k > 5.0$ , at a comparable level. This can be also observed in the frequency plot of the max. stress concentrations in Figure 3-23. The mean value for the max. stress concentrations is  $\mu=3.55$  and for the stress concentrations at the actual crack location  $\mu=3.30$ . The corresponding standard deviations are respectively  $\sigma=0.56$  and  $\sigma=0.61$ , which indicates a small scatter. Beside this, it becomes evident from Figure 3-22, that the difference between the max. stress concentration and the stress concentration at the crack is comparably small as well. This can be also observed in Figure 3-24, where the ratio  $r_\alpha$  are illustrated in a frequency plot. Only a few specimens have a ratio smaller than  $r_\alpha=0.8$ . For 31 of 34 specimens, the ratio is higher than  $r_\alpha=0.8$ . It should be noted, that in Figure 3-22, Figure 3-23 and Figure 3-24 all of the 34 specimens were considered in the evaluation, even though the crack was outside the DIC frame.



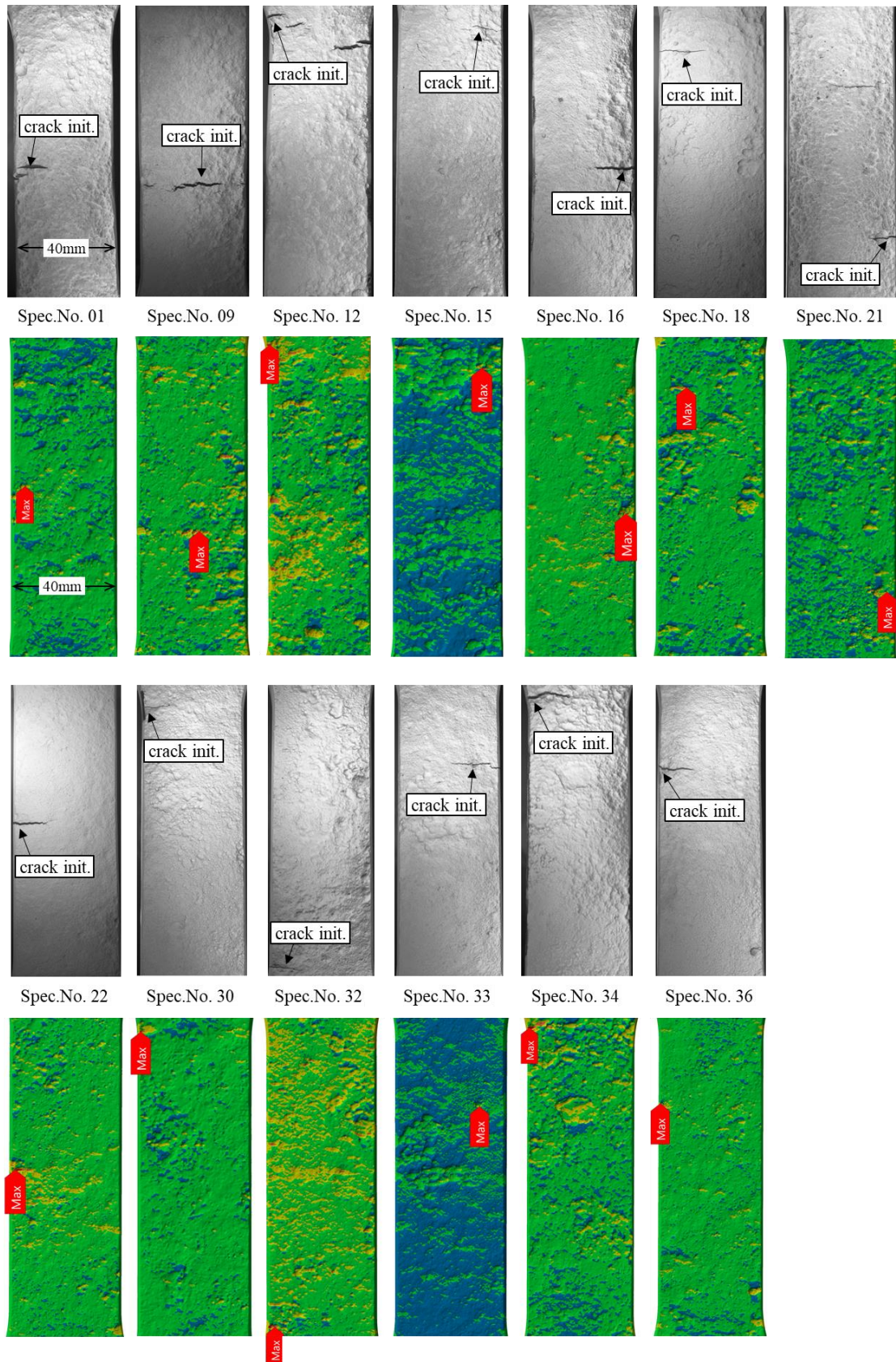
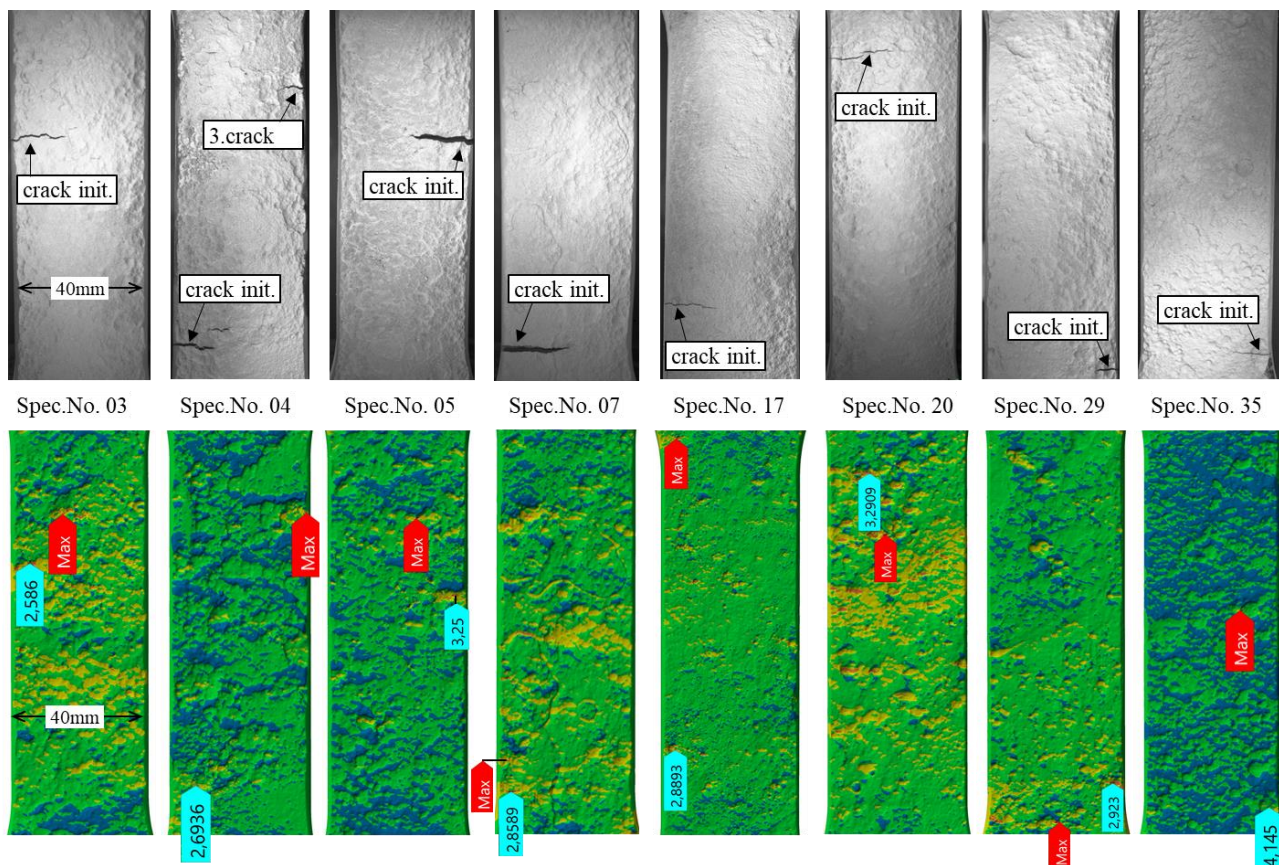


Figure 3-20: Specimens of coincidence level 1 with corresponding crack location and max. stress concentrations location (red banner)



**Figure 3-21: Specimens of coincidence level 2 with corresponding crack location (blue banner) and max. stress concentrations location (red banner)**

It is assumed that the difference between the predicted and the actual crack location is caused by various local structural support mechanism like micro and macro structural support. The here evaluated notch stress concentration is only depending on the geometry of the real corroded specimen and does not consider local plastification, although crack initiation is controlled by local strain [53,54]. Those plastification lead to lower fatigue-effective stresses, especially in mild steel. There are several methods in order to consider this effect like the stress gradient approach, the stress averaging approach [13,15], the theory of critical distances of Taylor [55] or the widespread approach of Neuber with an effective notch stress radius of  $r=1\text{mm}$ , which is established in relevant codes [19,22]. However, none of them are applied to corroded steel yet. Nevertheless, in Figure 3-25, the stress concentration of specimen No.5 is plotted for the max. stress concentration and the crack location along the thickness. The gradient at the max. stress location is slightly higher than at the crack location. At a distance of about 0.4mm from the surface the stresses at the crack location are getting higher than at the max. stress location. This is in accordance with the research of Skallerud et. al. [56], where a averaged stress over a certain distance was found out to be the crack initiation site of rough surfaces. This underlines the impact of micro and macro structural support, which is an object of further research.



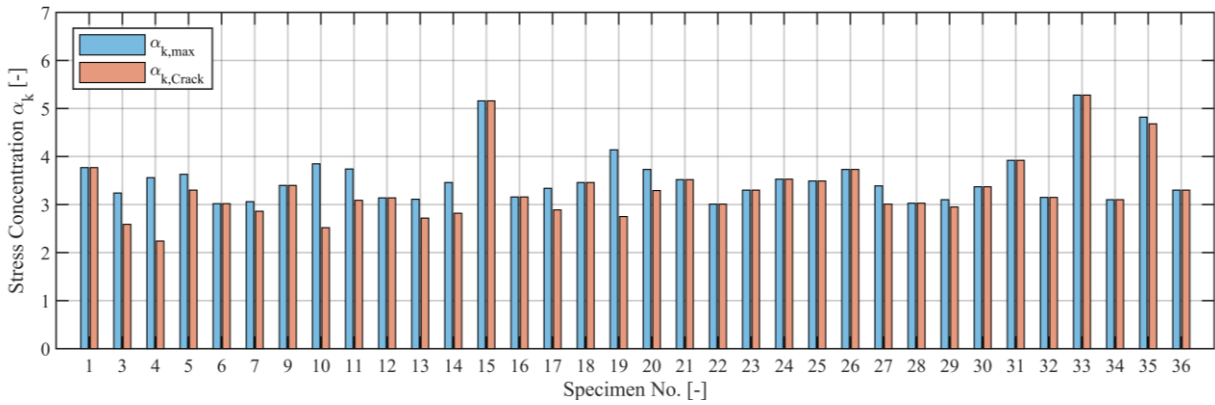


**Figure 3-22: Stress concentrations from numerical analysis of all specimens with corresponding stress concentrations at the crack location**

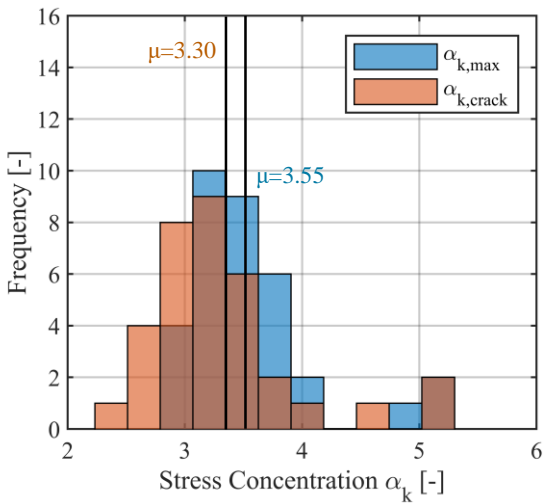


**Figure 3-23: Frequency plot of stress concentrations from numerical analyses of all specimens**

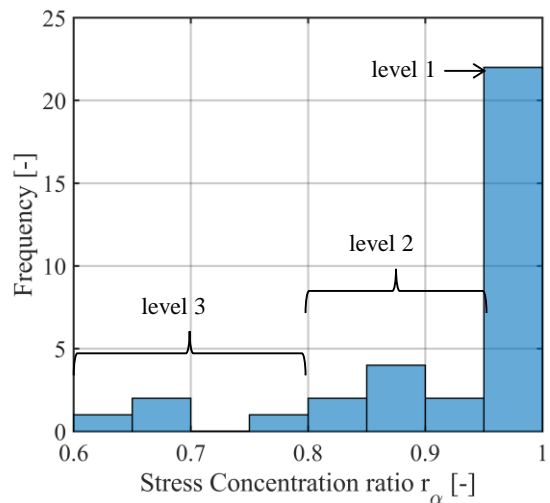


**Figure 3-24: Frequency plot of stress concentration ratio  $r_\alpha$**

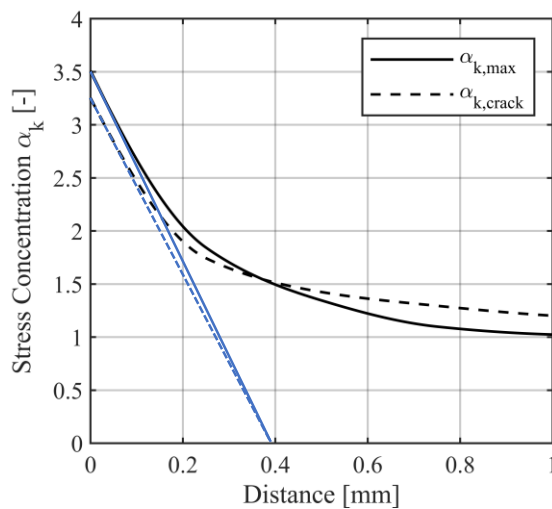


**Figure 3-25: Stress concentration along the thickness for max. stress concentration and crack location**

### 3.5.4 Findings

Following findings are described in this paper:

- The fatigue tests have shown a higher slope and higher fatigue life endurance compared to the corresponding DNV curve C-Air for rolled plates with pitting corrosion in Air
- The fatigue life endurance for plates with pitting are higher than that of butt welds (category C1 and D, whether ground flushed or not).
- The notch effects can be analysed by conversion of scan data into a numerical model with the aid of the reverse engineering method.
- The results of DIC enables the evaluation of the crack initiation life time. The average lifetime for steel plates with pitting corrosion is 88% of the total life time, based on a 2mm crack length. The crack length has only little correlation with the stress range.
- There is a good match of DIC with the numerical prediction. For 13 of 21 specimen the crack locations coincide with the hotspot from numerical simulation.
- The notch effect has a leading impact on the crack location and crack path. Based on this finding, it is assumed, that the value of the stress concentration factor has an influence on the fatigue life endurance as well.
- In cases the crack location did not match with the max. stress concentration it was found that the stress gradients along the thickness was higher, which indicates a possible micro or macro support effect.

### 3.6 Conclusion

The objective for this paper was to investigate the fatigue behaviour of steel plates with pitting corrosion and identify the impact of local stress concentrations due to pitting in order to enable local fatigue life approaches for corroded components of offshore wind energy support structures. With the aid of the reverse engineering method, it was shown that the stress concentration has a significant impact on the crack location and crack path. Nevertheless, in some specimens the max. stress concentrations were higher than at the actual crack location. This is assumed to be caused from the micro and macro structural support, which was not considered in the numerical simulation. The structural support has to be addressed in future research work. This becomes even more important, when calculating the fatigue life based on local approaches like e.g. the notch strain concept. For this purpose, the fatigue life data until crack initiation, conducted in this paper, can be used. Finally, with local fatigue approaches based on the reverses engineering method a differentiation between strongly notched components like tubular joints, which are not sensitive to stress concentration from pitting corrosion, and weakly notched components like welded plates can be made.

### 3.7 Acknowledgements

The project ISyMOO is funded by the Federal Ministry of Economic Affairs and Climate Action (BMWK) through the 6<sup>th</sup> National Energy Research Program under the funding number 0324254A.



Ms. Mengyan Peng has contributed to this work within her Master thesis. This contribution is much appreciated.

### 3.8 Appendix A: Fatigue test data

**Table 3-5: Fatigue test results**

Specimen No.	Max. load $F_{\max}$ [kN]	Min. load $F_{\min}$ [kN]	Load ratio R [-]	Cross section area $A_{\text{ave}}$ [mm <sup>2</sup> ]	Stress range $\Delta\sigma$ [N/mm <sup>2</sup> ]	Fatigue life $N_T$ [-]
P.01	105	10.5	0.1	403.5	234.2	313,070
P.02	40	4	0.1	364.5	98.8	2,000,000*
P.03	90	9	0.1	391.5	206.9	417,736
P.04	100	10	0.1	388.2	231.8	320,864
P.05	80	8	0.1	404.1	178.2	699,371
P.06	115	11.5	0.1	402.3	257.3	187,517
P.07	70	7	0.1	372.4	169.2	1,664,437
P.08	65	6.5	0.1	406.8	143.8	8,387,846*
P.09	115	11.5	0.1	421.5	245.6	205,740
P.10	115	11.5	0.1	404.8	255.7	79,200
P.11	115	11.5	0.1	395.3	261.8	93,357
P.12	90	9	0.1	379.9	213.2	542,572
P.13	90	9	0.1	391.6	206.8	597,934
P.14	90	9	0.1	411.0	197.1	795,004
P.15	75	7.5	0.1	361.2	186.9	315,444
P.16	80	8	0.1	398.9	180.5	1,661,456
P.17	80	8	0.1	405.5	177.5	1,432,112
P.18	80	8	0.1	406.4	177.2	1,427,084
P.19	80	8	0.1	407.5	176.7	898,498
P.20	80	8	0.1	390.9	184.2	832,000
P.21	115	11.5	0.1	413.1	250.6	178,651
P.22	90	9	0.1	387.9	208.8	266,790
P.23	115	57.5	0.5	405.1	141.9	1,339,331
P.24	125	62.5	0.5	406.8	153.7	988,000
P.25	130	65	0.5	407.8	159.4	690,454
P.26	130	65	0.5	414.3	156.9	1,497,211
P.27	130	65	0.5	404.1	160.8	947,958
P.28	130	65	0.5	385.4	168.6	880,362
P.29	130	65	0.5	394.7	164.7	983,877
P.30	130	65	0.5	414.6	156.8	411,240
P.31	80	-8	-0.1	420.1	209.5	622,036
P.32	80	-8	-0.1	400.0	220.0	435,103
P.33	80	-8	-0.1	422.6	208.2	341,448
P.34	80	-8	-0.1	404.4	217.6	403,782
P.35	80	-8	-0.1	402.9	218.4	281,212
P.36	80	-8	-0.1	398.7	220.7	556,415

\*run out

### 3.9 Appendix B: Results of DIC measurements

**Table 3-6: Results of DIC measurements**

Specimen No.	R [-]	Stress range $\Delta\sigma$ [N/mm <sup>2</sup> ]	Fatigue life total $N_T$	Fatigue life $N_{C1}$	Fatigue life $N_{C2}$	Ratio $r_{c1}$ $N_{C1}/N_T$	Ratio $r_{c2}$ $N_{C2}/N_T$	Difference $ N_{C1}-N_{C2} $	Crack length at $N_{C1}$ [mm]
P.01	0.1	234.2	313,070	255,000	266,000	0.81	0.85	0.04	0.61
P.02	0.1	98.8	2,000,000	run out					
P.03	0.1	206.9	417,736	358,000	365,000	0.86	0.87	0.02	1.00
P.04	0.1	231.8	320,864	286,000	291,200	0.89	0.91	0.02	0.39
P.05	0.1	178.2	699,371	570,000	590,000	0.82	0.84	0.03	0.56
P.06	0.1	257.3	187,517	crack outside DIC frame					
P.07	0.1	169.2	1,664,437	1,520,000	1,560,000	0.91	0.94	0.02	0.47
P.08	0.1	143.8	8,387,846	run out					
P.09	0.1	245.6	205,740	126,000	144,000	0.61	0.70	0.09	0.84
P.10	0.1	255.7	79,200	crack outside DIC frame					
P.11	0.1	261.8	93,357	crack outside DIC frame					
P.12	0.1	213.2	542,572	476,000	506,000	0.88	0.93	0.06	0.80
P.13	0.1	206.8	597,934	crack outside DIC frame					
P.14	0.1	197.1	795,004						
P.15	0.1	186.9	315,444	230,000	270,000	0.73	0.86	0.13	0.91
P.16	0.1	180.5	1,661,456	1,290,000	1,312,000	0.78	0.79	0.01	0.68
P.17	0.1	177.5	1,432,112	1,362,000	1,400,000	0.95	0.98	0.03	0.45
P.18	0.1	177.2	1,427,084	1,320,000	1,354,000	0.92	0.95	0.02	0.92
P.19	0.1	176.7	898,498	crack outside DIC frame					
P.20	0.1	184.2	832,000	684,000	722,000	0.82	0.87	0.05	0.62
P.21	0.1	250.6	178,651	150,000	152,000	0.84	0.85	0.01	0.45
P.22	0.1	208.8	266,790	186,000	213,000	0.70	0.80	0.10	0.41
P.23	0.5	141.9	1,339,331	crack outside DIC frame					
P.24	0.5	153.7	988,000	crack outside DIC frame					
P.25	0.5	159.4	690,454	crack outside DIC frame					
P.26	0.5	156.9	1,497,211	crack outside DIC frame					
P.27	0.5	160.8	947,958	crack outside DIC frame					
P.28	0.5	168.6	880,362	crack outside DIC frame					
P.29	0.5	164.7	983,877	874,000	880,000	0.89	0.89	0.01	0.83
P.30	0.5	156.8	411,240	320,000	352,000	0.78	0.86	0.08	0.68
P.31	-0.1	209.5	622,036	crack outside DIC frame					
P.32	-0.1	220.0	435,103	350,000	380,000	0.80	0.87	0.07	0.11
P.33	-0.1	208.2	341,448	269,000	283,000	0.79	0.83	0.04	0.71
P.34	-0.1	217.6	403,782	310,000	332,000	0.77	0.82	0.05	1.01
P.35	-0.1	218.4	281,212	218,000	236,000	0.78	0.84	0.06	0.80
P.36	-0.1	220.7	556,415	440,000	480,000	0.79	0.86	0.07	0.96
mean:						0.81	0.86	0.05	0.68
standard deviation:						0.06	0.04	0.03	0.19
5%-quantile						0.70	0.79	0.01	0.39
95%-quantile						0.92	0.95	0.10	1.00

## 3.10 Appendix C: Results of numerical analysis

Table 3-7: Stress concentrations from numerical analysis

Specimen No.	Load ratio R [-]	Stress range $\Delta\sigma$ [N/mm <sup>2</sup> ]	Stress concentration		Ratio $r_\alpha = \alpha_{k, crack} / \alpha_{k, max}$ [-]	Coincidence level [-]
			$\alpha_{k, max}$ [-]	$\alpha_{k, crack}$ [-]		
P.01	0.1	234.2	3.77	3.77	1.00	level 1
P.03	0.1	206.9	3.24	2.59	0.80	level 2
P.04	0.1	231.8	3.56	2.24	0.61	level 3
P.05	0.1	178.2	3.63	3.30	0.92	level 2
P.06	0.1	257.3	3.02	3.02	1.00	level 1
P.07	0.1	169.2	3.06	2.86	0.92	level 2
P.09	0.1	245.6	3.40	3.40	1.00	level 1
P.10	0.1	255.7	3.85	2.52	0.65	level 3
P.11	0.1	261.8	3.74	3.09	0.79	level 2
P.12	0.1	213.2	3.14	3.14	1.00	level 1
P.13	0.1	206.8	3.11	2.72	0.83	level 2
P.14	0.1	197.1	3.46	2.82	0.81	level 2
P.15	0.1	186.9	5.16	5.16	1.00	level 1
P.16	0.1	180.5	3.16	3.16	1.00	level 1
P.17	0.1	177.5	3.34	2.89	0.87	level 2
P.18	0.1	177.2	3.46	3.46	1.00	level 1
P.19	0.1	176.7	4.14	2.75	0.66	level 3
P.20	0.1	184.2	3.73	3.29	0.88	level 2
P.21	0.1	250.6	3.52	3.52	1.00	level 1
P.22	0.1	208.8	3.01	3.01	1.00	level 1
P.23	0.5	141.9	3.30	3.30	1.00	level 1
P.24	0.5	153.7	3.53	3.53	1.00	level 1
P.25	0.5	159.4	3.49	3.49	1.00	level 1
P.26	0.5	156.9	3.73	3.73	1.00	level 1
P.27	0.5	160.8	3.39	3.01	0.89	level 2
P.28	0.5	168.6	3.03	3.03	1.00	level 1
P.29	0.5	164.7	3.10	2.95	0.95	level 2
P.30	0.5	156.8	3.37	3.37	1.00	level 1
P.31	-0.1	209.5	3.92	3.92	1.00	level 1
P.32	-0.1	220.0	3.15	3.15	1.00	level 1
P.33	-0.1	208.2	5.28	5.28	1.00	level 1
P.34	-0.1	217.6	3.10	3.10	1.00	level 1
P.35	-0.1	218.4	4.82	4.68	0.97	level 2
P.36	-0.1	220.7	3.30	3.30	1.00	level 1

	Quantity
Level 1:	20
Level 2:	11
Level 3:	3

### 3.11 References

- [1] Det Norske Veritas. Corrosion protection for wind turbines(DNV-GL RP-0416); 2016.
- [2] Federal Maritime and Hydrographic Agency. Minimum requirements concerning the constructive design of offshore structures within the Exclusive Economic Zone (EEZ); 2015.
- [3] International Standards Organization. ISO 9233: Corrosion of metals and alloys — Corrosivity of atmospheres(ISO 9223); 2012.
- [4] Det Norske Veritas. Support structures for wind turbines(ST-0126); 2018.
- [5] Liang X, Sheng J, Wang K. Investigation of the mechanical properties of steel plates with artificial pitting and the effects of mutual pitting on the stress concentration factor. *Results in Physics* 2019;14:102520. <https://doi.org/10.1016/j.rinp.2019.102520>.
- [6] Xiang L, Pan J, Chen S. Analysis on the stress corrosion crack inception based on pit shape and size of the FV520B tensile specimen. *Results in Physics* 2018;9:463–70. <https://doi.org/10.1016/j.rinp.2018.03.005>.
- [7] Cerit M. Corrosion pit-induced stress concentration in spherical pressure vessel. *Thin-Walled Structures* 2019;136:106–12. <https://doi.org/10.1016/j.tws.2018.12.014>.
- [8] Huang Y, Wei C, Chen L, Li P. Quantitative correlation between geometric parameters and stress concentration of corrosion pits. *Engineering Failure Analysis* 2014;44:168–78. <https://doi.org/10.1016/j.engfailanal.2014.05.020>.
- [9] Hou J, Song L. Numerical Investigation on Stress Concentration of Tension Steel Bars with One or Two Corrosion Pits. *Advances in Materials Science and Engineering* 2015;2015:1–7. <https://doi.org/10.1155/2015/413737>.
- [10] Larrosa NO, Akid R, Ainsworth RA. Corrosion-fatigue: a review of damage tolerance models. *International Materials Reviews* 2018;63(5):283–308. <https://doi.org/10.1080/09506608.2017.1375644>.
- [11] Shojai S, Schaumann P, Brömer T. Probabilistic modelling of pitting corrosion and its impact on stress concentrations in steel structures in the offshore wind energy. *Marine Structures* 2022;84:103232. <https://doi.org/10.1016/j.marstruc.2022.103232>.
- [12] Braun M, Milaković A-S, Renken F, Fricke W, Ehlers S. Application of Local Approaches to the Assessment of Fatigue Test results obtained for Welded Joints at Sub-Zero Temperatures; 2020.
- [13] Radaj D, Vormwald M. *Advanced methods of fatigue assessment*. Heidelberg: Springer; 2013.
- [14] Ladinek M, Niederwanger A, Lang R, Schmid J, Timmers R, Lener G. The strain-life approach applied to welded joints: Considering the real weld geometry. *Journal of Constructional Steel Research* 2018;148:180–8. <https://doi.org/10.1016/j.jcsr.2018.04.024>.
- [15] Radaj D, Sonsino CM, Fricke W. *Fatigue assessment of welded joints by local approaches*. 2nd ed. Cambridge: Woodhead Publ. [u.a.]; 2006.

- [16] Sonsino CM, Fricke W, Bruyne F de, Hoppe A, Ahmadi A, Zhang G. Notch stress concepts for the fatigue assessment of welded joints – Background and applications. *International Journal of Fatigue* 2012;34(1):2–16. <https://doi.org/10.1016/j.ijfatigue.2010.04.011>.
- [17] Lener G, Lang R, Ladinek M, Timmers R. A numerical method for determining the fatigue strength of welded joints with a significant improvement in accuracy. *Procedia Engineering* 2018;213:359–73. <https://doi.org/10.1016/j.proeng.2018.02.036>.
- [18] Schaumann P, Schürmann K, Pittner A, Rethmeier M. Automatically Welded Tubular X-Joints for Jacket Substructures: Prediction of the Technical Fatigue Crack Location. *ce/papers* 2019;3(3-4):823–8. <https://doi.org/10.1002/cepa.1140>.
- [19] Hobbacher A. Recommendations for fatigue design of welded joints and components. IIW Document No. IIW-1823-07 International Institute of Welding; 2009.
- [20] Fricke W. IIW recommendations for the fatigue assessment of welded structures by notch stress analysis. Oxford: WP Woodhead Publ; 2012.
- [21] European Committee for Standardization. Eurocode 3 - Design of steel structures - Part 1-9: Fatigue(EN 1993-1-9); 2020.
- [22] Det Norske Veritas - Germanischer Lloyd. Fatigue design of offshore steel structures(DNV-GL RP-C203); 2019.
- [23] Deutsches Institut für Normung e.V. Structures for wind turbines and platforms - Part 3: Steel structures(DIN 18088-3); 2019.
- [24] Det Norske Veritas. Fatigue Assessment of Ship Structures(Classification Notes No. 30.7); 2014.
- [25] Health & Safety Executive. Background to new fatigue guidance for steel joints and connections in offshore structures(OTH 92 390); 1998.
- [26] Bundesanstalt für Wasserbau. Merkblatt: Bewertung der Tragfähigkeit bestehender Verschlüsse im Stahlwasserbau (TbVS); 2018.
- [27] British Standards Institution. Guide to fatigue design and assessment of steel products(BS 7608:2014+A1:2015); 2014.
- [28] Momber AW, Nattkemper TW, Langenkämper D, Möller T, Brün D, Schaumann P et al. A data-based model for condition monitoring and maintenance planning for protective coating systems for wind tower structures. *Renewable Energy* 2022;186:957–73. <https://doi.org/10.1016/j.renene.2022.01.022>.
- [29] Melchers R. A Review of Trends for Corrosion Loss and Pit Depth in Longer-Term Exposures. *Corros. Mater. Degrad.* 2018;1(1):42–58. <https://doi.org/10.3390/cmd1010004>.
- [30] Revie RW, Uhlig HH. Corrosion and corrosion control: An introduction to corrosion science and engineering. Hoboken, New Jersey: Wiley-Interscience a John Wiley & Sons Inc. Publication; 2008.

- [31] Marcus P. Corrosion mechanisms in theory and practice. 3rd ed. Boca Raton, Fla.: CRC Press; 2012.
- [32] Le Li, Mojtaba Mahmoodian, Chun-Qing Li, Dilan Robert. Effect of corrosion and hydrogen embrittlement on microstructure and mechanical properties of mild steel.
- [33] Mehmanparast A, Brennan F, Tavares I. Fatigue crack growth rates for offshore wind monopile weldments in air and seawater: SLIC inter-laboratory test results. *Materials & Design* 2017;114:494–504. <https://doi.org/10.1016/j.matdes.2016.10.070>.
- [34] Qvale P, Zarandi EP, Ås SK, Skallerud BH. Digital image correlation for continuous mapping of fatigue crack initiation sites on corroded surface from offshore mooring chain. *International Journal of Fatigue* 2021;151:106350. <https://doi.org/10.1016/j.ijfatigue.2021.106350>.
- [35] Neumann KM, Ehlers S. Power spectrum for surface description of corroded ship structure from laser scan. In: *Structures, safety, and reliability: Presented at ASME 2019 38th International Conference on Ocean, Offshore and Arctic Engineering, June 9-14, 2019, Glasgow, Scotland, UK*. New York, NY: The American Society of Mechanical Engineers; 2019.
- [36] Nugroho FA, Braun M, Ehlers S. Probability analysis of PIT distribution on corroded ballast tank. *Ocean Engineering* 2021;228:108958. <https://doi.org/10.1016/j.oceaneng.2021.108958>.
- [37] G01 Committee. Practice for Preparing, Cleaning, and Evaluating Corrosion Test Specimens. West Conshohocken, PA: ASTM International. <https://doi.org/10.1520/G0001-03R17E01>.
- [38] Biglu M. Doctoral Thesis - Effects of corrosion on the local behavior of steel structures under tensile loading. TU Hamburg; 2022.
- [39] Friedrich N, Ehlers S. Crack Monitoring in Resonance Fatigue Testing of Welded Specimens Using Digital Image Correlation. *Journal of visualized experiments JoVE* 2019(151). <https://doi.org/10.3791/60390>.
- [40] Radaj D, Vormwald M. Ermüdungsfestigkeit: Grundlagen für Ingenieure. 3rd ed. Berlin, Heidelberg: Springer-Verlag Berlin Heidelberg; 2007.
- [41] Braun M, Fischer C, Baumgartner J, Hecht M, Varfolomeev I. Fatigue Crack Initiation and Propagation Relation of Notched Specimens with Welded Joint Characteristics. *Metals* 2022;12(4):615. <https://doi.org/10.3390/met12040615>.
- [42] ECCS European Convention for Constructional Steelwork. Background information on fatigue design rules: Statistical evaluation. 2nd ed. Brussels: ECCS European Convention for Constructional Steelwork; 2018.
- [43] Friedrich N. Experimental investigation on the influence of welding residual stresses on fatigue for two different weld geometries. *Fatigue Fract Eng Mater Struct* 2020;65(3):128. <https://doi.org/10.1111/ffe.13339>.
- [44] Hutt T, Cawley P. Feasibility of digital image correlation for detection of cracks at fastener holes. *NDT & E International* 2009;42(2):141–9. <https://doi.org/10.1016/j.ndteint.2008.10.008>.

- 
- [45] Karsten Schürmann. Fatigue Behavior of Automatically Welded Tubular Joints for Offshore Wind Energy Substructures: Dissertation; 2021.
- [46] Shojai S, Schaumann P, Brömer T. Probabilistic modelling of pitting corrosion and its impact on stress concentrations in steel structures in the offshore wind energy. (under review) 2022.
- [47] BASQUIN OH. The exponential law of endurance tests. *Proc Am Soc Test Mater* 1910;10:625–30.
- [48] Deutsches Institut für Normung. DIN 50100: Load controlled fatigue testing – Execution and evaluation of cyclic tests at constant load amplitudes on metallic specimens and components. Berlin: Beuth; 2016.
- [49] Murakami Y. Metal fatigue: Effects of small defects and nonmetallic inclusions. Amsterdam, London, San Diego, CA: Academic Press an imprint of Elsevier; 2019.
- [50] Miller KJ. Initiation and growth rates of short fatigue cracks. *Fundamentals of Deformation and Fracture* 1984:477–500.
- [51] Suresh S, Ritchie RO. Propagation of short fatigue cracks. *International Metals Reviews* 1984;29(1):445–75. <https://doi.org/10.1179/imtr.1984.29.1.445>.
- [52] Collmann M. Ermüdungsfestigkeit von Stumpfnahftverbindungen größerer Blechdicke gefügt mit Hochleistungsschweißverfahren. Hannover Institutionelles Repositorium der Leibniz Universität Hannover; 2021.
- [53] Fatoba OO, Leiva-Garcia R, Lishchuk SV, Larrosa NO, Akid R. Simulation of stress-assisted localised corrosion using a cellular automaton finite element approach. *Corrosion Science* 2018;137:83–97. <https://doi.org/10.1016/j.corsci.2018.03.029>.
- [54] Turnbull A, Wright L, Crocker L. New insight into the pit-to-crack transition from finite element analysis of the stress and strain distribution around a corrosion pit. *Corrosion Science* 2010;52(4):1492–8. <https://doi.org/10.1016/j.corsci.2009.12.004>.
- [55] Taylor D. The theory of critical distances: A new perspective in fracture mechanics. Amsterdam, London: Elsevier; 2010.
- [56] Skallerud B, Ås SK, Ottosen NS. A gradient-based multiaxial criterion for fatigue crack initiation prediction in components with surface roughness. *International Journal of Fatigue* 2018;117:384–95. <https://doi.org/10.1016/j.ijfatigue.2018.08.020>.





## 4 Micro-support consideration of corroded steel (Paper III)

This section contains a reprint of the article: Shojai, Sulaiman; Schaumann, Peter; Ghafoori, Elyas (2024): Micro-support effect consideration in fatigue analysis of corroded steel based on real surface geometry. In: *Journal of Constructional Steel Research* 212, S. 108259. DOI: 10.1016/j.jcsr.2023.108259.

### Background

In the previous paper, fatigue tests on corroded specimens showed that the crack initiation locations coincided with the numerical predicted hotspots of stress concentrations for many specimens. Hence, it could be concluded that the notch effect has a decisive influence on the fatigue strength. However, predicting the fatigue strength on the basis of the calculated stress concentrations was not possible at this stage, since the stress concentrations were calculated based on a linear elastic material definition, without taking the micro-support effect into account. Furthermore, there were also specimens where the hotspots of the stress concentration did not coincide with the crack locations. For both, the prediction of fatigue strength and a higher coincidence of the hotspots with the crack locations, the influence of the micro-support effect has to be investigated.

With the point method (PM) and line method (LM), both methods of the theory of critical distances (TCD), as well as the implicit gradient model (IGM), different methods exist for the consideration of micro-support effect. The basic idea of both methods is, that the fatigue-driving (effective) stress is not the stress on the surface of a component, but a stress at a certain distance (PM) or the averaged stress over a certain length or volume (LM, IGM). The advantage of the IGM over the TCD methods is that the consideration of all notches of a model can be performed numerically in one step, whereas with TCD the stress paths in thickness direction of each notch have to be exported and evaluated individually.

### Overview

In this study, the PM and LM of the TCD approach, as well as the IGM approach were applied to the specimens of the fatigue tests from the previous paper to account for the micro-support effect. For all approaches, the magnitude of the above-mentioned distance, length and volume is required as an input parameter. This input parameter is a material parameter considering the brittleness of the material, which is not available in the literature for corroded specimens. Therefore, these parameters were calibrated for all methods based on the fatigue tests and compared with each other in respect to the resulting scatter in the notch stress-based SN-curve. A major focus was on the implementation of the IGM method and the investigation of the effect caused by the input parameter. Furthermore, it was investigated in this paper how the findings from this and the previous paper can be transferred to real structures using the so-called replica technique.

**Conclusion**

The consideration of the micro-support effect according to IGM could predict crack locations from the fatigue test with high accuracy for 25 out of 33 specimens. For some specimens the locations of the hotspots shifted towards the crack location because of the consideration of the micro-support effect. The calibration of the input parameters for PM, LM and IGM resulted in values of  $d^* = 0.04$  mm,  $\rho^* = 0.11$  mm and  $a = 0.0045$  mm<sup>2</sup>, whereby the lowest scatter in the associated notch stress SN-curve could be determined with the IGM. The resulting SN-curves were found to be FAT 236 with a slope of  $m = 4.63$ . The PM and LM resulted in similar FAT-classes. The replica technique showed that the fatigue-driving stress determination procedure can be transferred to corroded steel structures, as the replica is able to capture the corroded surfaces with sufficient accuracy. Moreover, the findings in this paper allow the probabilistically determined stress concentrations, presented in the first paper, to be transferred into effective stress concentrations. This in turn enables a probabilistic investigation of the fatigue life based on the double-pit model, which was shown to be accurate enough for the stress concentration analysis.

However, it should be noted that all investigations carried out to this stage are limited to plane base material. In real structures a high number of welds is present, which already have a notch effect from the weld seams, requiring further investigation regarding the interaction of welds and corrosion.

**Authors Contribution**

The experiments and numerical analysis as well as the paper conceptualization, methodology, validation, formal analysis, investigation, writing of the original draft and visualization were performed by the first author. Prof. Schaumann supervised the work presented in this paper and was responsible for the funding acquisition and project administration. Prof. Ghafouri supervised the work, commented, reviewed and edited the paper.

## Micro-support effect consideration in fatigue analysis of corroded steel based on real surface geometry<sup>1</sup>

### 4.1 Abstract

The service life of steel structures is significantly reduced by corrosion. In particular, pitting corrosion leads to high local stress concentrations and can reduce the expected fatigue strength. Previous studies on corroded specimens have shown that crack development in fatigue tests is correlated with stress concentrations. To consider stress concentrations in local fatigue concepts, the so-called micro-support effects must be quantified. This can be usually considered with the theory of critical distances, including the stress averaging approach by Neuber. For stress concentrations from pitting corrosion, the applicability of this method is limited because of the large number of notches in corroded surfaces. In this study, as an alternative approach, the implicit gradient model is presented, in which the influence of the micro-support effect is considered numerically on 3D FEM models by averaging the stresses over a defined volume around the notch. The consideration of the micro-support effect revealed for most of the specimens a coincidence of the crack location with the location of the maximum notch stress. For some of the specimens, where no coincidence could be observed before micro-support consideration, the maximum stress concentration shifted to the crack location after consideration of micro-support effect. Based on this, a notch stress SN-curve for pitted steel was derived.

**Keywords:** pitting corrosion; stress concentrations; local fatigue concept; micro-support effect

### 4.2 Introduction

Corrosion protection systems for steel structures have a limited lifetime, although significant improvements have been made in recent years. This is particularly true for steel structures such as bridges and offshore structures, which can be exposed to harsh environmental conditions. In addition, structures are simultaneously subjected to high dynamic loads due to wind, waves and operation. When corrosion protection (partially) fails, steel is exposed to corrosion. In some cases, a new coating is either not possible or not economically feasible. In these cases, a calculation of the (remaining) fatigue life under free corrosion is required to maintain the steel structure in service.

---

<sup>1</sup> [Shojai, S., Schaumann, P., Ghafoori, E., \*Journal of Constructional Steel Research\*, 2024, 212, S. 108259. DOI: 10.1016/j.jcsr.2023.108259.](https://doi.org/10.1016/j.jcsr.2023.108259)

Recent studies conducted by Quale et al. [1] and Shojai et al. [2] showed that crack initiation in fatigue tests on corroded specimens occurred at locations with high stress concentrations, resulting from pitting corrosion. With local concepts, which have so far been limited to the base material and weld seams [3–11], these stress concentrations can be considered in the fatigue analysis and enable a fatigue life evaluation based on the real surface geometry. In the context of maintenance of existing bridges and offshore structures there are novel efforts to capture the real surface geometry of corroded components with the so called replica technique, in which an imprint of the surface geometry is made [12]. The imprint can be digitized in the laboratory with a 3D-scanner and used to numerically analyse the stress concentrations due to pitting corrosion.

In the literature [13–16], notch stress concentrations from pitting corrosion are determined based on elasticity theory and do not consider local support mechanisms, such as the micro-support effect. The micro-support effect is related to the behaviour of micro cracks during cyclic loading. Particularly, in case of sharp notches, the yield stress in the surface crystallites can be exceeded and lead to micro cracks, which do not propagate with continued cyclic loading. This behaviour reduces the stress concentrations and supports the fatigue resistance [17,18].

Various micro-support effect hypotheses can be found in the literature for calculating the so-called effective fatigue notch stress. Peterson [19] proposed using the stress at a critical distance  $d^*$  from the stress peak as follows:

$$\sigma_f = \sigma_k(d^*) \quad (4-1)$$

where  $\sigma_f$  is the effective notch stress and the  $\sigma_k$  the elastic notch stress. Neuber assumed that the effective notch stress is a stress averaged over the width of a microstructure particle  $\rho^*$  in the notch base as follows [20]:

$$\sigma_f = \frac{1}{\rho^*} \int_0^{\rho^*} \sigma_k \, dx \quad (4-2)$$

The width of the micro-structure particle is called the equivalent length,  $\rho^*$ . It depends on the material type and yield point of the material. Taylor [21] unified both methods, into his theory of critical distances (TCD), in which Petersons approach is the point method (PM) and the Neuber approach is the line method (LM), see Figure 4-1 (a) and (b). According Taylor the critical distance for PM and the averaging length for LM can be related to the intrinsic material length  $L$ , which depends on the microstructure of the material and is derived on the basis of linear elastic fracture mechanics as

$$L = \frac{1}{\pi} \left( \frac{\Delta K_{th}}{\Delta \sigma_0} \right) \quad (4-3)$$

where  $\Delta K_{th}$  is the fatigue crack propagation threshold and  $\Delta \sigma_0$  is the fatigue limit. The intrinsic material length is related to the critical distance with  $d^* = L/2$ , while the equivalent averaging length is related to it with  $\rho^* = 2L$ . Further approaches are the area method (AM) defined by Sheppard [22], where the stress is averaged over a semicircular area with a radius of  $L$  and the volume method (VM) defined by Bellet [23], where the stress is averaged over a hemisphere with a radius of  $1.54L$ , respectively (see Figure 4-1 (c) and (d)). The TCD methods has been extensively checked on standard

notches [24,25] and also applied to weld seams (e.g., in [26–29]). The application to weld seams is possible because the potential crack locations are limited to the weld toe and weld root and thus only limited locations has to be evaluated.

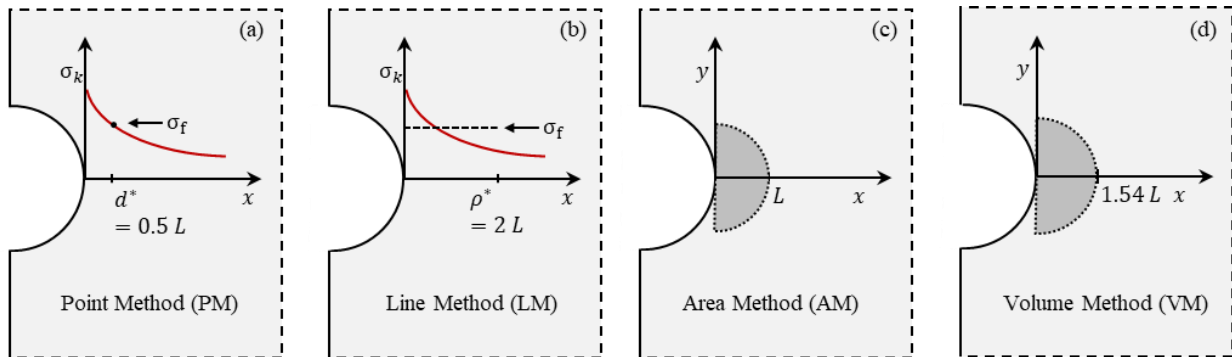


**Figure 4-1: Illustration of TCD-methods, (a) point method, (b) line method, (c) area method and (d) volume method**

However, in the case of corroded components analysed based on the real three-dimensional surface geometry, which includes several notches and potential crack locations, the application of the presented methods would require the evaluation of many more locations. Skallerud et al. [30] applied the LM on two-dimensional rough surfaces and evaluated the stresses separately for all possible notches, requiring an enormous effort in post processing. The application of TCD methods on corroded specimens, whether it is LM or one of the other mentioned approaches, is therefore assumed to be insufficient.

An alternative approach is the implicit gradient model (IGM) based on Peerlings [31,32], which allows the micro-support effect to be considered within the numerical analysis of the stress field for all notches of a corroded component. Analogous to the TCD methods, different approaches such as the PM, LM or VM can be considered by choosing appropriate weighting functions [33]. In the case of three-dimensional FE-models the VM approach is suitable. Similarly to TCD, the stresses are averaged over a volume, which is determined by a weighting factor considering the material properties (see section 4.3). However, it can be assumed that the material of corroded specimens no longer corresponds to that of the base material and that existing values from the literature cannot be applied directly. Hence, in this study, the weighting factor is calibrated based on the fatigue tests results.

Therefore, the theoretical background for IGM is explained first in section 4.3 and the fatigue test results are presented in Section 4.4. In Section 4.5, a numerical analysis based on the IGM approach and a parametric study of the weighting parameter  $a$  is carried out. The effective notch stress concentrations and weighting parameters are determined in Section 4.6. In section 4.7 finally, it is shown, how the results can contribute to the analysis of real structures using the replica technique.

The novelties in this paper can be summarized as follows:

- Consideration of micro-support effect of corroded structural steel based on real surface geometry with IGM and comparison with TCD.
- Derivation of a notch stress SN-curve and the weighting factor for application on corroded components made of structural steel.

- Application of the replica technique on corroded steel and analysis of the fatigue driving stress based on the IGM approach.

### 4.3 Theoretical background for the implicit gradient model (IGM)

The IGM approach applied in this study was derived by Peerlings [31,32,34] and already applied by Tovo and Livieri [33,35], Lang [36] and Schürmann [37] on standard notched specimen as well as on welded components. With the IGM all presented methods of TCD can be considered. This is done with the definition of a weighting function, which, if a Dirac function is assumed, can represent the PM of TCD. Also the LM as well as the AM and VM can be represented by appropriate weighting functions [35,38]. However, for the application it is important that the weighting functions are continuous in order to avoid boundary problems. Therefore, in the application of IGM, the VM has proven to be the most suitable, since it can be simply represented by a Gaussian equation. Analogous to the VM of TCD methods, the fatigue driving effective stress is assumed to be a stress averaged over a reference volume around the notch peak stress. The averaged stress  $\sigma_f(\mathbf{x})$  at the point  $\mathbf{x}=(x_1, x_2, x_3)$  can be described for the volume  $V$  using the weighting function  $G$ , that is dependent on the distance  $\|\mathbf{x} - \mathbf{y}\|$  between point  $\mathbf{x}$  and any point  $\mathbf{y}=(y_1, y_2, y_3)$ , and a reference volume  $V_r$  as follows:

$$\sigma_f(\mathbf{x}) = \frac{1}{V_r(\mathbf{x})} \int_V G(\mathbf{x}, \mathbf{y}) \sigma_k(\mathbf{y}) dV_y \quad (4-4)$$

There exist different weight functions, that can be used within this approach. According to Askes et al. [39] and Tovo et al. [40] the weighting function must fulfil some requirements: a) the maximum of the weighting function must occur at the point  $\mathbf{x}$  and b) tend to zero for greater distances from  $\mathbf{x}$ . With a Gaussian function according to Equation (4-5), both conditions can be met.

$$G(\mathbf{x}, \mathbf{y}) = \frac{1}{(4\pi a)^{3/2}} e^{-|\mathbf{x}-\mathbf{y}|^2/4a} \quad (4-5)$$

With a Gaussian function the reference volume turns out to be equal to  $V_r = 1$ , which simplifies the Equation (4-4) with consideration of Equation (4-5) to:

$$\sigma_f(\mathbf{x}) = \int_V \frac{1}{(4\pi a)^{3/2}} e^{-|\mathbf{x}-\mathbf{y}|^2/4a} \sigma_k(\mathbf{y}) dV_y \quad (4-6)$$

In the next step,  $\sigma_k(\mathbf{y})$  is developed in a Taylor series as

$$\sigma_k(\mathbf{y}) = \sigma_k(\mathbf{x}) + \nabla \sigma_k(\mathbf{x})(y_i - x_i) + \frac{1}{2!} \nabla^2 \sigma_k(\mathbf{x})(y_i - x_i)^2 + \frac{1}{3!} \nabla^3 \sigma_k(\mathbf{x})(y_i - x_i)^3 + \dots \quad (4-7)$$

Assuming isotropy of the weight function, the odd derivatives of (4-7) can be removed and then substituted into (4-6), which leads to

$$\sigma_f(\mathbf{x}) = \sigma_k(\mathbf{x}) + a_1 \nabla^2 \sigma_k(\mathbf{x}) + a_2 \nabla^4 \sigma_k(\mathbf{x}) \dots \quad (4-8)$$

where the coefficients  $a_1$  and  $a_2$  are given as:

$$a_1 = \frac{1}{2! G(x, y)} \int_V G(x, y) (y_i - x_i)^2 dV_y \quad (4-9)$$

$$a_2 = \frac{1}{4! G(x, y)} \int_V G(x, y) (y_i - x_i)^4 dV_y$$

Using a Gaussian weight function, the coefficients  $a_1$  and  $a_2$  turn out to be equal, so that the index can be dropped. By applying the Laplacian operator on both sides, in order to reduce the required boundary condition, and neglecting higher than the third-order derivatives of the Taylor-expansion, the following differential equation can be obtained:

$$\sigma_f(\vec{x}) - \sigma_k(\vec{x}) - a \nabla^2 \sigma_f(\vec{x}) = 0 \quad (4-10)$$

The parameter  $a > 0$  corresponds to the weighting scale of the surrounding volume at the notch and is linked to the intrinsic material length  $L$  defined in equation (4-3) with:

$$a = (\zeta \cdot L)^2 \quad (4-11)$$

Here,  $\zeta$  considers the stress criterion, which is equal to 0.545 for the maximum principal stress and 0.456 for the von Mises stress criterion [39]. With this, the impact of the material can be considered on the basis of linear elastic fracture mechanics, analogous to the TCD methods.

The total volume of the body is considered as the solution domain and the surface is defined as the boundary. Usually the Neumann boundary condition is used [31,41]:

$$\frac{\partial \sigma_f(\mathbf{x})}{\partial \mathbf{x}} \cdot \mathbf{n} = 0 \quad (4-12)$$

where  $\mathbf{n}$  is the normal to the surface of the solution domain.

In order to utilize commercial software for solving the differential equation, equation (4-10) is interpreted as a Helmholtz problem in form of  $\nabla^2 f \pm k^2 f = 0$ . According Lang et al. [42], for a negative sign, this problem can be considered as an initial value problem of the diffusion equation. If this equation is examined for a discrete time step, it results in:

$$\frac{f(t + \Delta t) - f(t)}{\Delta t} - a \nabla^2 f(t + \Delta t) = 0 \quad (4-13)$$

Transferred to equation (4-10), the Helmholtz problem can be described with the following:

$$\frac{\sigma_f(\vec{x}) - \sigma_k(\vec{x})}{\Delta t} - a \nabla^2 \sigma_f(\vec{x}) = 0 \quad (4-14)$$

Equation (4-14) can be solved numerically with commercial software. In practical applications, the notch stresses  $\sigma_k$  are calculated first. These are inserted as initial temperature conditions in a thermal-

transient heat conduction calculation and the heat conduction calculation is solved for the time  $\Delta t = 1$  s. The determined temperature is interpreted as the fatigue-driving effective stress,  $\sigma_f$ . Parameter  $a$  in the heat conduction calculation is a constant, which stands for the temperature conductivity. The parameter  $a$  can be linked to the thermal properties as:

$$a = \frac{\lambda}{\rho_d \cdot c_p} \text{ [mm}^2\text{/s]} \quad (4-15)$$

where  $\lambda$  is the thermal conductivity,  $c_p$  is the specific heat capacity and  $\rho_d$  is the material density.

## 4.4 Experiments

### 4.4.1 Material characterization tests

Specimens of corroded steel were extracted from approximately 11mm transverse floor plates of a ballast tank in a former bulk carrier. The exact exposure time to free corrosion environment and the environmental conditions are not recorded. In order to determine the mechanical properties of the corroded steel, tensile tests and hardness measurements were carried out.

**Tensile tests:** The tensile tests were conducted by Biglu [43] on 36 samples. In Table 3-1 the results for ultimate tensile stress  $R_m$ , yield stress  $R_{p0.2}$ , and the E-module are shown. The mean yield stress was 264 N/mm<sup>2</sup>, with a 95% quantile value of 250 N/mm<sup>2</sup>. For the ultimate tensile stress, a mean value of 414 N/mm<sup>2</sup> and a 95% quantile value of 371 N/mm<sup>2</sup> were obtained.

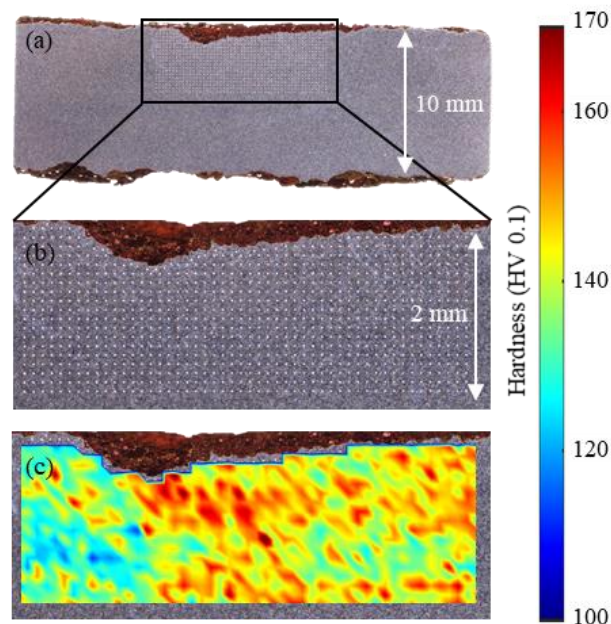


**Figure 4-2: Hardness measurement results, (a) cross section of tested specimen, (b) measured area, (c) hardness map**

**Hardness tests:** Hardness measurements were conducted using the QNess Q10A+ measuring device. Vickers hardness was measured according to ISO 6507-1 [44], considering sample preparation and



test procedure specifications. To account for the influence of corrosion near the specimen surface, the measurements were performed with HV 0.1 kN testing load, allowing measurements up to a distance of 75  $\mu\text{m}$  from the surface. For the hardness mapping, approximately 900 individual measurements were carried out on a 4x10 mm<sup>2</sup> area and an indentation distance of 200  $\mu\text{m}$ . The results in Figure 4-2 show values between HV 100 and HV 170 with a mean value of HV 140. Moreover, there is no noticeable difference between the values near the surface and the values located deeper inside the specimen.

Based on these tests, it is reasonable to assume a low alloy structural steel between S235 and S355.

#### 4.4.2 Fatigue tests

The specimen geometry is shown in Figure 4-3 (a). The specimens were made by waterjet cutting. The edges were chamfered manually with  $r = 1\text{mm}$  to avoid crack initiation on the sharp edges. The specimens were cleaned only with chemicals according to ASTM [45]. Thirty-six fatigue tests were performed in [2] with a test frequency of 10 Hz, and the stress ratios were  $R = 0.1$  (for 22 specimens),  $R = -0.1$  (for 6 specimens), and  $R = 0.5$  (for 8 specimens). In addition, the crack development was recorded using DIC. The results of the fatigue tests are summarized in Appendix A of [2]. Figure 4-3 shows the geometry of the specimen and fatigue test setup. For the sake of brevity, details regarding the test procedure and setup will not be discussed in this study and can be found in [2]. In Figure 4-4 the fatigue test results are illustrated based on nominal stress ranges, showing a characteristic strength of FAT 125 when all specimens with different R-ratios are considered. As this is greater than the recommended FAT 112 curve for pitting corrosion in air environment according to DNV [46], it is assumed that potentially existing damages from the load history are of minor magnitude and can be neglected in further investigations.

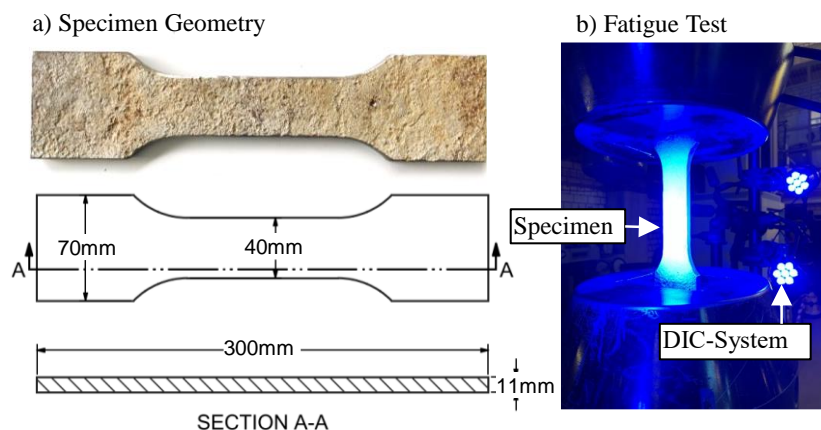


**Figure 4-3: (a) Tested specimen geometry and (b) fatigue test setup from [2]**

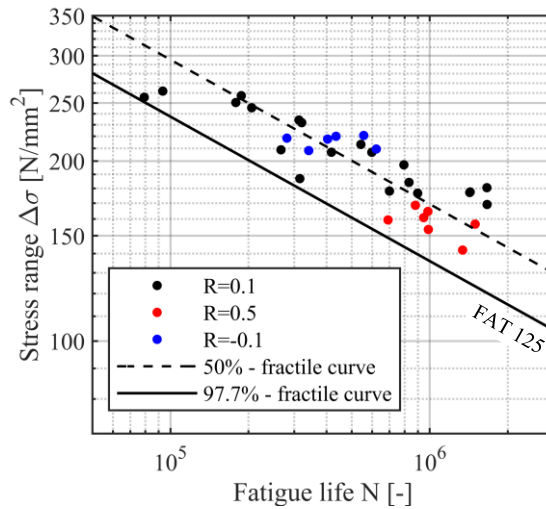


Figure 4-4: Fatigue test results from [2] for different R-ratios

#### 4.5 Numerical Analysis of effective notch stresses

Before fatigue tests, all specimens were scanned with a 3D-scanner, consisting of all relevant notches (pits) of the real surface geometry. These were used for numerical analysis of the stress concentrations based on the IGM approach. In Figure 4-5 a flowchart of the numerical analysis using the IGM approach is presented.

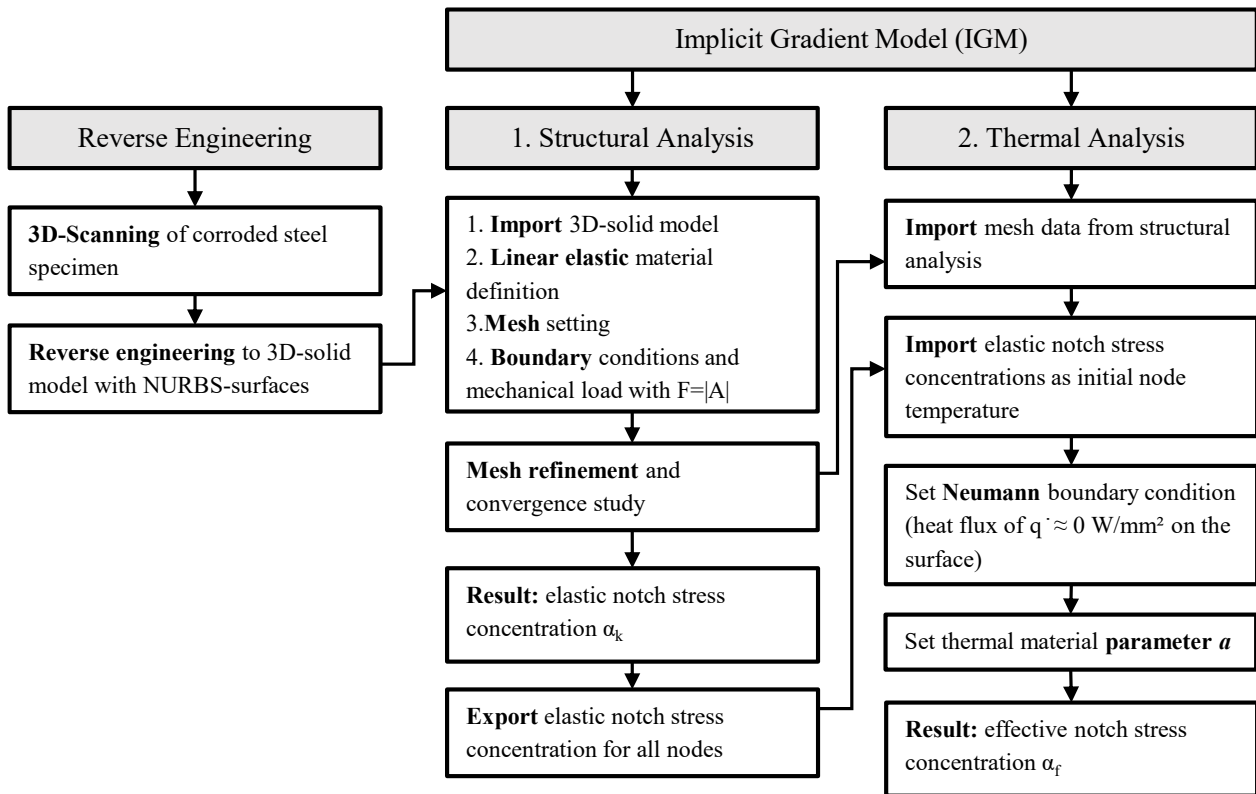


Figure 4-5: Flowchart of numerical analysis using the IGM approach

The stress concentrations analysis based on the real geometry consist of two steps: structural analysis and thermal analysis. The thermal analysis requires stress concentrations as the initial temperature. Therefore, the node numbers of the refined FE-mesh and the associated stress concentrations were exported and imported into the thermal analysis. The transfer of the stress concentrations as initial temperature requires identical numerical models for both analyses. Therefore, exporting the mesh-data and importing it into the thermal analysis is important.

#### 4.5.1 Reverse Engineering

For reverse engineering the corroded specimens were scanned with the high-resolution scanner Keyence VR-3000 (with a mean resolution of 20  $\mu\text{m}$ ) from all sides and then assembled into one 3D-model in STL-format. This was used to create a solid model for the numerical analysis. The transformation to a solid model is required due to following aspects:

- The curvature of the surface in STL format is not continuous, because it consists of a series of individual facets that are connected to each other. This would lead to singularities in the subsequent numerical analysis.
- The faceted surfaces require large amounts of data for illustration (high number of points, lines and facets).

To achieve this, Non-Uniform Rational B-Spline (NURBS) surfaces are utilized. These surfaces are mathematically defined polynomial functions of higher order that fit to the shape of the faceted geometry. NURBS surfaces require less data to describe the surface and provides a continuous curvature. The accuracy of the fit depends on the number of polynomial functions per area. In Ansys SpaceClaim, a software for reverse engineering, this can be adjusted by controlling the grid rate, which determines the number of grids per area. A grid rate of  $R = 7-8$  [1/mm] was determined to be sufficient. However, creating a solid model from a single NURBS surface is not feasible. Instead, the surface is divided into NURBS-patches [5] and then merged to form a solid model. The final solid model used for the numerical analysis is shown in Figure 4-6 (a). For more comprehensive information on the reverse engineering process, refer to the work of Shojai et al. [2,47].

#### 4.5.2 Structural Analysis

##### 4.5.2.1 Numerical model

The structural-mechanical analysis with the corresponding solid model and boundary condition is shown in Figure 4-6. The solid model has a fixed support on one side, whereas it is axially displaceable on the opposite side. The specimen was loaded with a centric tensile force corresponding to the cross-sectional area to achieve a nominal stress of  $\sigma_n = 1.0$  MPa. Thus, the results of the numerical analysis can be interpreted as stress concentrations. Since the cross-sectional area of the corroded specimen was not constant along its length, the average of five positions along the specimen was determined. Quadratic tetrahedral elements (SOLID187) with a linear elastic material definition (structural steel) were used for the calculation, with an initial element size of 0.3–0.4 mm.

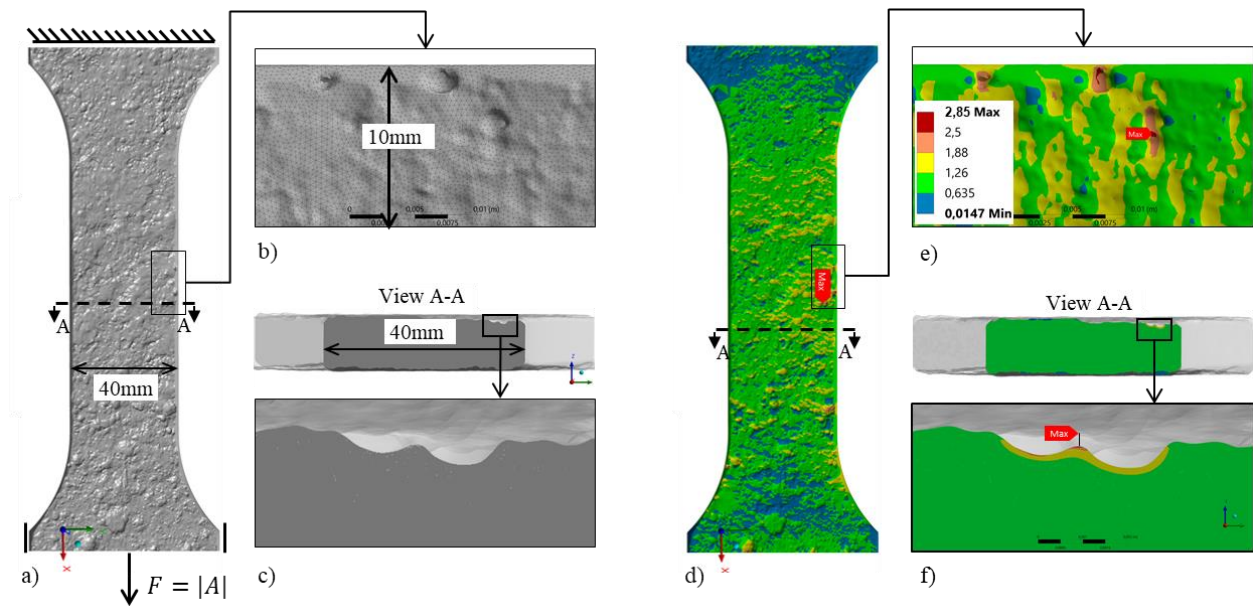


**Figure 4-6: Numerical model for structural-mechanical analysis of stress concentrations, a) solid 3D-model and boundary conditions, b) mesh before convergence study, c) cross section at crack location, d-f) elastic stress concentrations before convergence study**

#### 4.5.2.2 Convergence study

A convergence study was conducted using multiple approaches. In the first step, an adaptive convergence tool was applied to the entire specimen. In cases where the hotspot of the stress concentration did not coincide with the crack location (see Shojai et al. [2]), the adaptive convergence was separately applied at the crack location. When the convergence tool could not be applied due to mesh refinement problems caused by irregular NURBS surfaces, convergence was achieved manually by applying a pinball on the hotspot and crack location spot. For both approaches, element sizes of 0.01 to 0.05 mm were obtained at the stress peaks.

According to the studies by Lang et al. [36] on welded specimens, for the application of the IGM with quadratic elements, an element length of  $l_e < 2\sqrt{a}$  is recommended. However, this is only required in the region of examined notches. For parameter  $a$  in the range of 0.0001 to 0.3 mm<sup>2</sup>, element lengths of at least 0.02 to 1.1 mm are required, which can be achieved for all the specimens. According to investigations by Lang et al. [36], this can avoid errors occurring in the thermal-transient analysis due to poor mesh quality.

#### 4.5.2.3 Results of elastic notch stresses

The results of the elastic notch stress concentrations based on the von Mises stress criterion are shown in Figure 4-10 (b1) to (b4) for different specimens. For specimen No. 01, shown in Figure 4-10 (a1) to (c1), the maximum stress concentration location obtained from the numerical simulation matches

the crack location, while there is no match for specimen No. 03, Figure 4-10 (a2) to (c2). The maximum stress concentration for specimen No. 03 is  $\alpha_k = 3.24$ , whereas at the crack location, the stress concentration is  $\alpha_k = 2.58$ . The elastic stress concentrations were evaluated at the maximum stress and crack locations. In Figure 3-22 the corresponding stress concentrations for both locations are illustrated for all specimens. In cases, in which the maximum stress location matched the crack location, the values of both are equal. For half of the specimens of the cases, the maximum stress location matched the crack location, while for the other half no match could be observed.

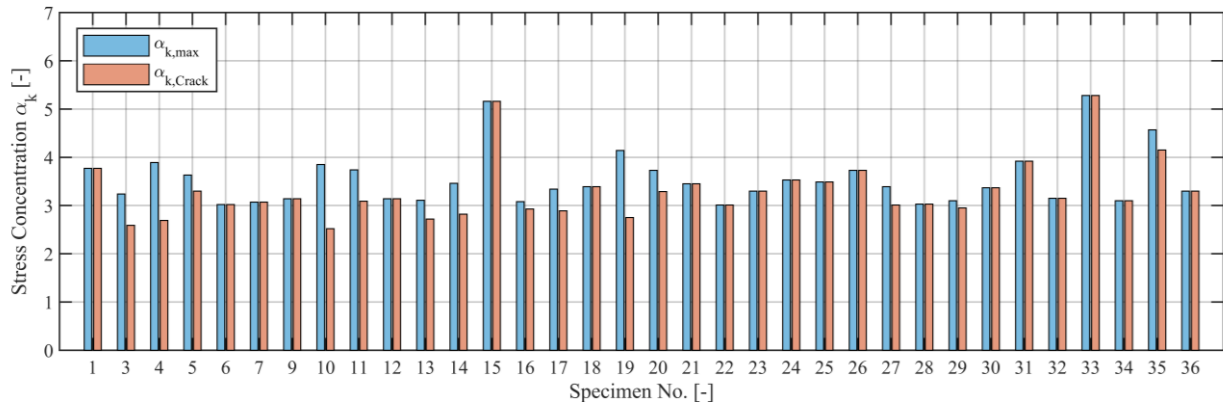


**Figure 4-7: Maximum stress concentrations from numerical analysis of all specimens with the corresponding stress concentrations at the crack location from Shojai et al. [2]**

### 4.5.3 Thermal analysis

For the thermal analysis, the material data, solid model and mesh-data must be identical to the data of the structural analysis. In the thermal steady-state analysis, the imported stress concentrations were defined as the temperature load. The results of this analysis were the same as those of the imported stress concentrations and were used as the initial temperature for the thermal transient analysis. To numerically solve the Helmholtz equation (4-14), the Neumann boundary condition must be considered. For this purpose, a heat flux of  $\dot{q} \approx 0 \text{ W/mm}^2$  was applied to the geometric surface ( $\dot{q} = 10^{-20} \text{ W/mm}^2$  in ANSYS Workbench). The results of the thermal transient analysis are driven by parameter  $a$ , which describes the thermal diffusivity in the thermal analysis but is in fact the weighting factor of the surrounding volume in the notch, as stated in section 4.3. To investigate the impact of parameter  $a$ , a parametric study was conducted. In the material definition, the specific heat capacity and density were set to  $c_p = 1.0$  and  $\rho_d = 1.0$ , respectively. This enabled control of parameter  $a$  solely through the thermal conductivity parameter  $\lambda$ .

#### 4.5.3.1 Parametric study for weighting parameter $a$

A parametric study was conducted for all specimens. Therefore, parameters in the range of 0.00001 and 1.0 were investigated. In Figure 4-8, the initial stress concentration  $\alpha_k$  ( $a = 0 \text{ mm}^2$ ) obtained from

the structural analysis is compared with the effective stress concentrations  $\alpha_f$  obtained from the thermal transient analysis. For values of  $a$  between 0.0001 and 0.01, high stress concentrations occurred at the individual notches and edges of the corroded surface. For  $a = 0.1 \text{ mm}^2$ , high stresses were no longer found locally at the notches and edges. Instead, high stresses are concentrated over a larger area. It is therefore assumed, that for a parameter  $a \geq 0.1 \text{ mm}^2$ , the crack initiation location does not match the cracks in the fatigue tests, since all cracks originated from an individual notch or edge of the corroded surface.

As It could be observed, that higher values of parameter  $a$ , led to lower effective stresses. Thus, greater weighting leads to an increased averaging of the maximum values, resulting in smaller effective stresses. This corresponds to the relationship shown in Equation (4-2), where a larger equivalent length  $\rho^*$  leads to a larger averaging and thus to smaller effective stresses.

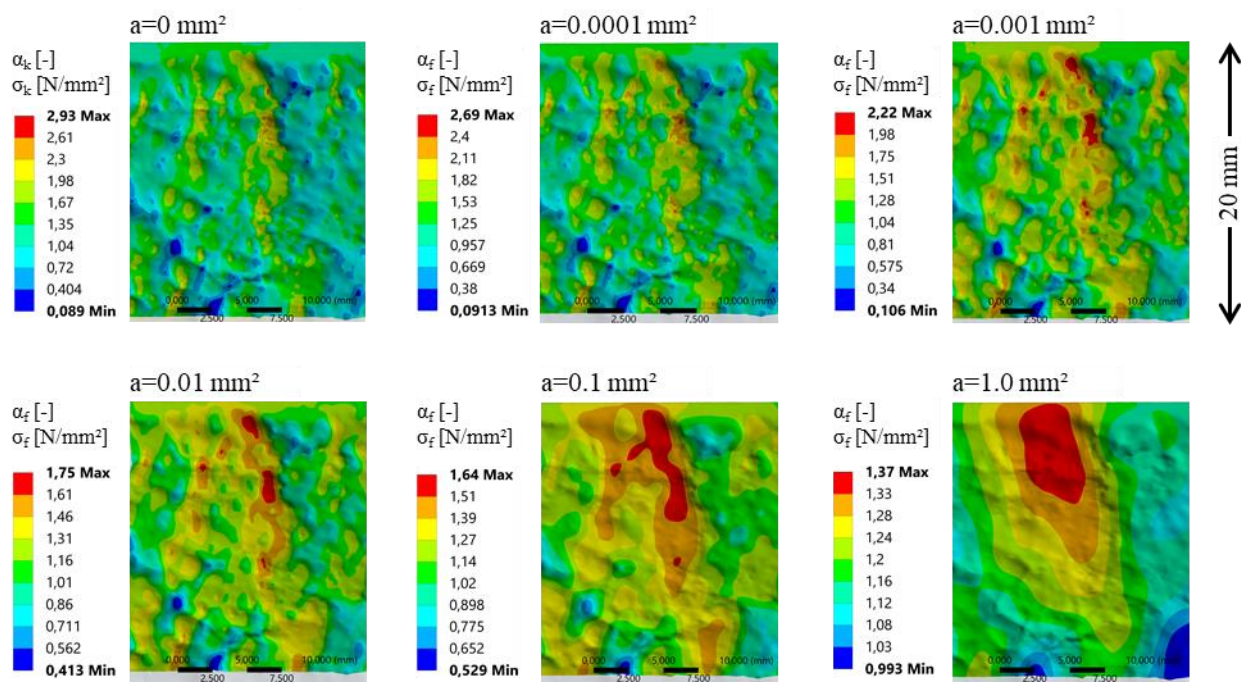


**Figure 4-8: Effective stress concentrations for different magnitudes of parameter  $a$  compared to initial stress concentrations from structural analysis**

In Figure 4-9 the effective stress concentrations are plotted against parameter  $a$  for specimen Nos. 03 and 11. The stress concentrations in both specimens were evaluated at two points: the maximum stress location from the structural analysis ( $\alpha_{f,\text{initial,max}}$ ) and crack location ( $\alpha_{f,\text{crack}}$ ). In both cases, the maximum stress concentrations are initially higher than at the crack location, hence, the crack location does not match the maximum stress location. This changes at the shifting point (see Figure 4-9) at  $a = 0.0012 \text{ mm}^2$  for specimen No. 03 and  $a = 0.00013 \text{ mm}^2$  for specimen No. 11. The effective stress concentration at the crack location is higher than that at the initial maximum stress location. This can be explained by the different stress gradients, since at different points of the specimen, the stress decreases at different rates. This can cause a change in the location of the maximum stress.



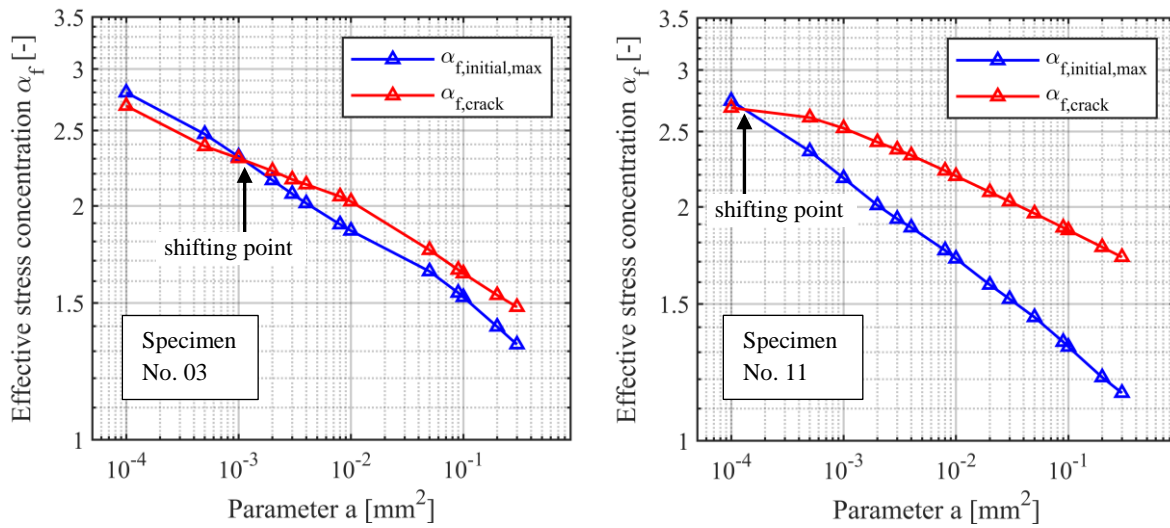


**Figure 4-9: Effective stress concentrations  $\alpha_f$  against parameter a for specimen Nos. 03 and 11 at different locations**

It can be concluded from the parameter study that with this method it is possible that the location of the maximum stress can change as a result of averaging the stresses. In addition, it was shown that physically meaningful results can only be obtained for values below 0.1 mm<sup>2</sup> as no clear crack location can be determined for larger values.

**4.5.3.2 Comparison of numerical and DIC hotspots**

For a comparison between the effective notch stresses and the actual cracks from the fatigue tests, a total of four conformity levels according Table 4-1 are suggested in this study.

The conformity levels are defined as follows:

- Level 1: The crack location from the fatigue tests matches the maximum stress location from the structural analysis, irrespective of micro-structural support.
- Level 2: The crack location from the fatigue tests does not match the maximum stress location without considering micro-structural support, but matches when it is considered.
- Level 3: The crack location from the fatigue tests matches the maximum stress location without considering the micro-structural support. However, it does not match when micro-structural support is considered.
- Level 4: The crack location from the fatigue tests does not match the maximum stress location, irrespective of micro-structural support.

**Table 4-1. Four different conformity levels suggested in this study.**

	Conformity with crack location			
	Before consideration of micro-structural support		After consideration of micro-structural support	
	yes	no	yes	no
Conformity level:	level 1	level 3	level 2	level 4

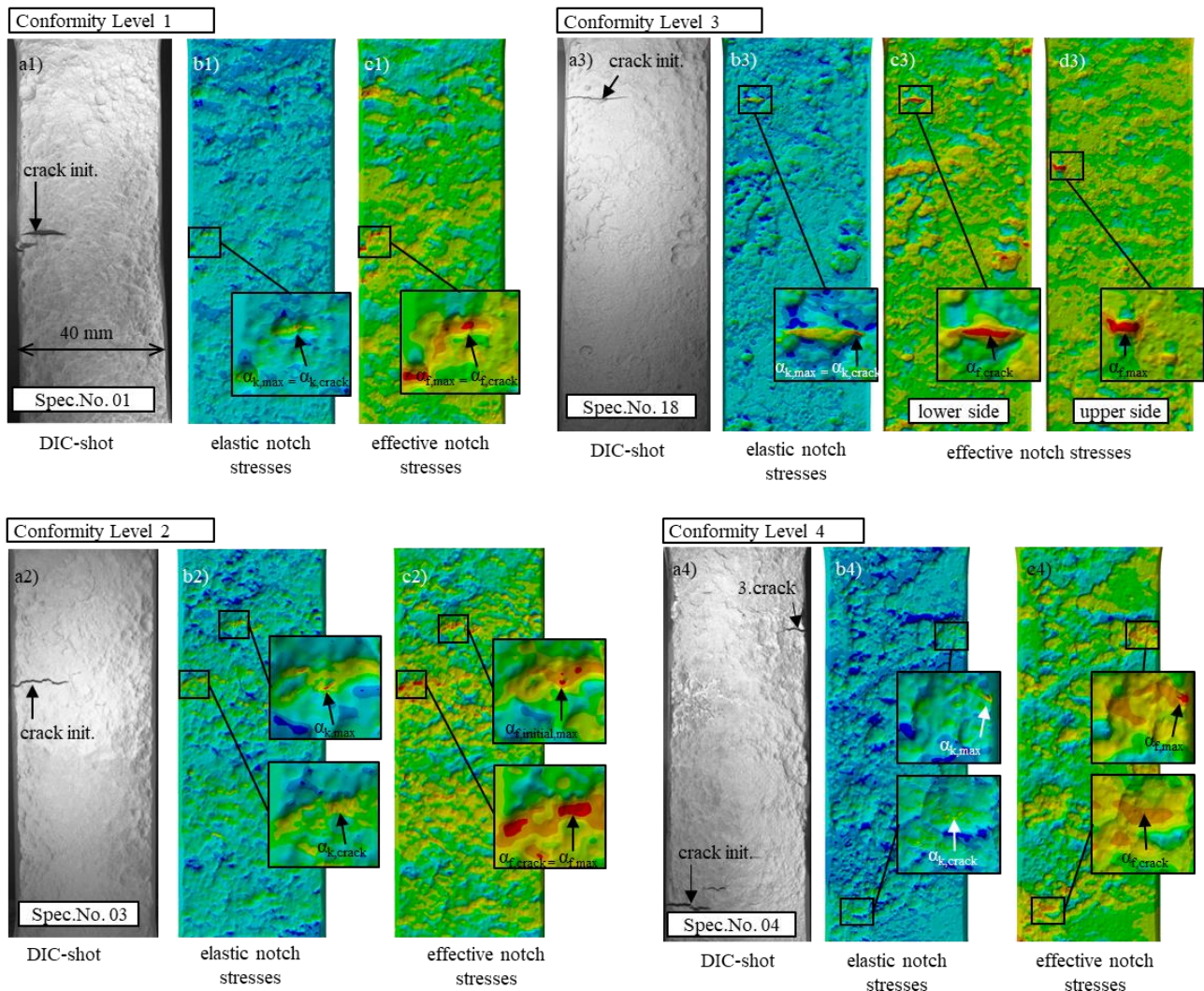


**Figure 4-10: Comparison of (a1-a4) DIC-shot with crack initiation, (b1-b4) elastic notch stresses (von Mises stress criterion) from structural analysis without consideration of micro-support effect, and (c1-c4, d4) effective notch stresses with consideration of micro-support-effect for  $a=0.01$  – Conformity Levels 1 to 4**

**Level 1:** Figure 4-10 shows the cracks from the fatigue test and results of the numerical analysis of the notch stresses in specimen No. 01 as an example of conformity level 1. Subfigure (a1) shows the DIC plot from the fatigue test, subfigure (b1) the result from the structural analysis (elastic notch stress  $\alpha_k$ ) and subfigure (c1) the result from the thermal analysis for parameter  $a = 0.01 \text{ mm}^2$  (effective notch stress  $\alpha_f$ ), with which the micro-support effect was considered. In the structural analysis, the locations of the crack initiation coincide with the locations of the maximum elastic notch stress  $\alpha_{k,max}$  (compare subfigures (a1) and (b1)). When the micro-support effect is considered, the location of the maximum stress remains unaffected (see subfigure (c1)). The micro-support effect leads only to a reduction in the notch stress and redistribution of the maximum notch stress over a larger area. However, conformity was not present for every investigated value of parameter  $a$  but only for a range of



values. This range of values was different for each specimen. Figure 4-11 illustrates the maximum effective notch stresses and effective notch stresses at the crack location versus parameter  $a$  for all conformity levels. For specimen No. 01, as an example for conformity level 1 (see subfigure a), an overlap of both notch stresses can be observed over a wide range of  $a$ , from 0.0001 to 0.03. However, for some specimens, only smaller overlap ranges for the same conformity level could be observed. Nevertheless, for Level 1 classification, an overlap between the two notch stresses for at least one value of  $a$  must be observed to indicate conformity between the crack location from the fatigue test and predicted crack location from the numerical analysis. The overlap can be represented by the ratio of the two notch stresses as  $r_{\alpha,f} = \alpha_{f,max} / \alpha_{f,crack}$ . Figure 4-12 (a) shows this ratio for all specimens with Level 1 conformity for different values of parameter  $a$ . For most samples and most values for parameter  $a$ , the ratio is  $r_{\alpha,f} = 1.0$ , which corresponds to an exact match. For individual specimens, such as specimen No. 28 or specimen No. 33, the notch stress ratio can reach a value of up to  $r_{\alpha,f} = 1.10$  for certain values of  $a$ . On average, the notch stress ratio is approximately  $r_{\alpha,f} = 1.01$  and is therefore relatively low.

**Level 2:** In Figure 4-10 (a2)–(c2), the results of specimen No. 03 as an example of conformity level 2 are illustrated. From a comparison between the DIC plot (a2) and the results for the elastic notch stresses in subfigure (b2), it becomes apparent that the crack location does not coincide with the location of the maximum notch stress. However, by considering the micro-support effect, the location of the maximum notch stresses shifts to the crack location from the fatigue test, as can be seen by comparing subfigures (a2) and (c2). The location of the maximum effective notch stress  $\alpha_{f,max}$ , shown in subfigure (c2), coincided with the crack location from the fatigue test. The conformity of the maximum notch stresses with the notch stress at the crack location is not ensured for every parameter  $a$ , analogous to conformity level 1. Figure 4-11(b) shows a match for values of  $a \geq 0.002$ . In fact, for most specimens, a match can be observed for values of  $a \geq 0.003$  (see Figure 4-12(b)).

**Level 3:** The results for specimen No. 18 as an example of conformity level 3 are presented in Figure 4-10 (a3) to (d3). Similar to level 1, the notch stress at the crack location is in accordance with the maximum notch stress from the structural analysis (see plots (a3) and (b3)). Plot (c3) shows the effective notch stresses with consideration of the micro-support effect for the lower and subfigure (d3) for the upper side of the specimen. Plot (c3) indicates that high notch stresses are present on the surface at the crack initiation location. Moreover, the notch stress pattern is consistent with the DIC plot in (a3). However, the effective notch stress at the crack location is lower than the maximum effective notch stress  $\alpha_{f,max}$ , which is located on the upper side of the specimen (see plot (d3)). In some cases,  $\alpha_{f,max}$  is even located on the same specimen side as the crack. However, for  $a = 0.01 \text{ mm}^2$ , there is only small deviation between maximum stress  $\alpha_{f,max} = 1.97$  and the stress at crack location,  $\alpha_{f,crack} = 1.92$  (see Figure 4-11 c). The difference between the values remains at the same level for smaller values of  $a$  and changes only for larger values of  $a$ . It can be concluded, that the notch stress factors are of similar magnitude at two locations for this specimen.

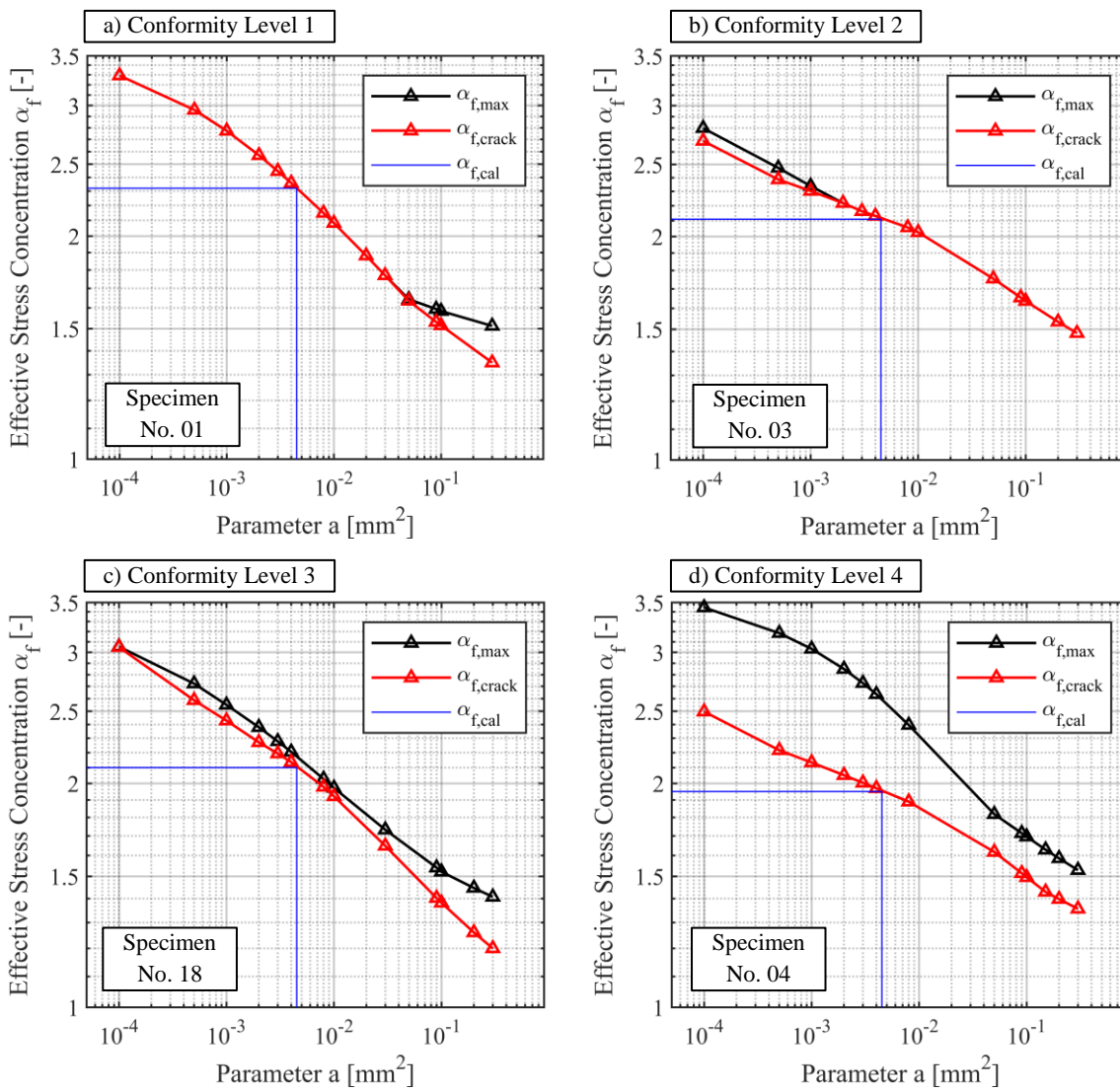
This can be related to the high number of individual competing notches on the specimen's surface, which are characteristic of pitting corrosion. As a result, parameters other than notch sharpness determine the exact crack initiation locations. The scattering material parameters on the specimen's surface are an example. This can result in deviations between the crack locations from the fatigue test

and numerical predictions. In addition, the stress determination resulting from the numerical analysis may be inaccurate due to the selected meshing methodology, which is not uniformly refined.

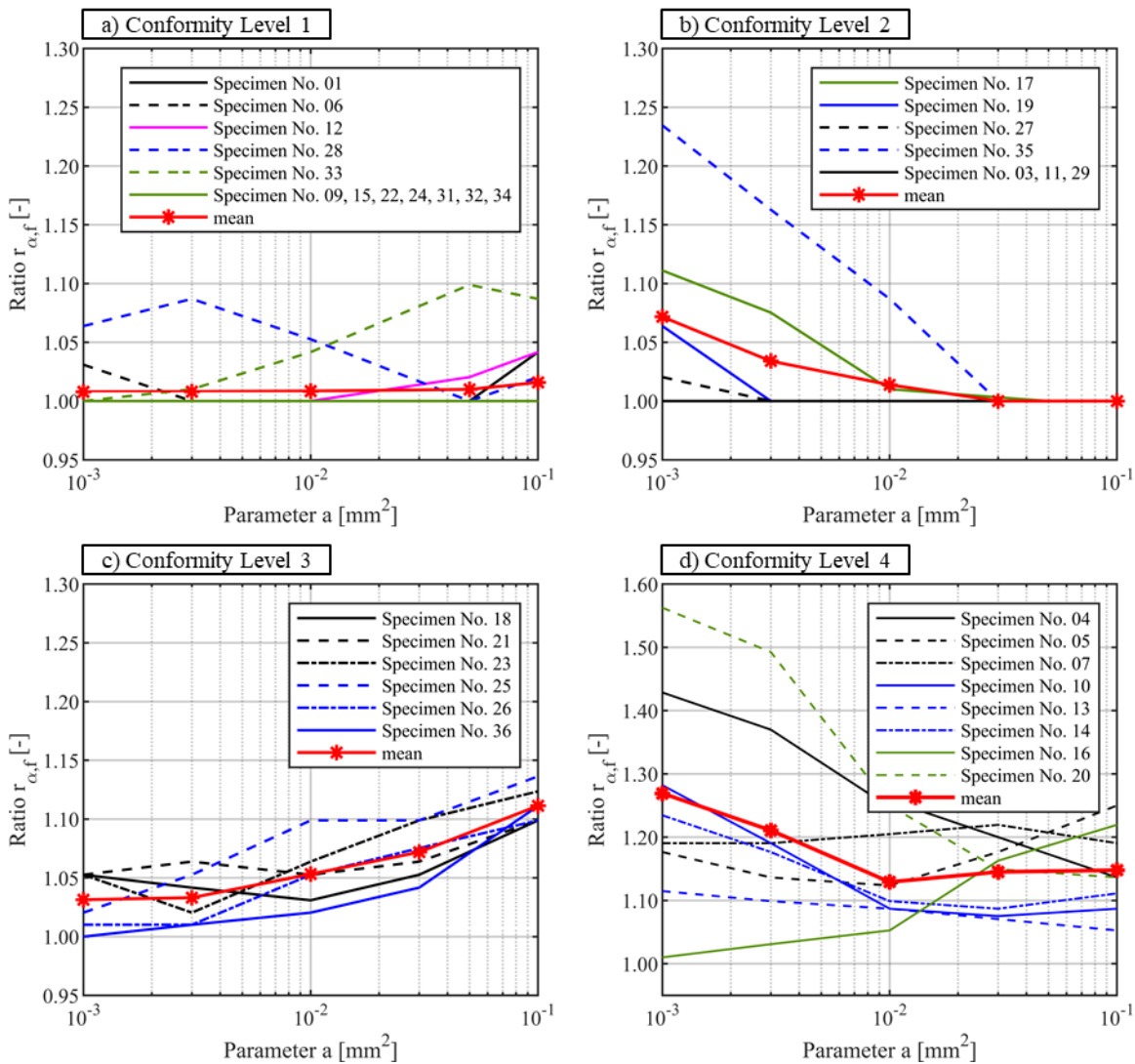
**Level 4:** The results for specimen No. 04 as an example of conformity level 4 are shown in Figure 4-10 (a4) to (c4). A comparison between plots (a4) and (b4) shows that the maximum elastic notch stresses from the structural analysis do not agree with the DIC plot. In this specimen, unlike most other specimens with level 4 conformities, several single cracks at different locations were present during the test. In this case, the third crack corresponded to the maximum elastic notch stress. Nevertheless, the classification is made at conformity level 4, since the stresses were redistributed after the first crack, which was not considered in the numerical analysis. A comparison of the DIC plot with plot (c3) shows, that the effective notch stresses do not agree with the DIC results even after micro-support consideration. The plot of the effective notch stress at the crack location (subfigure (c4)) shows a locally widespread stress concentration, which corresponds to the shape of the crack. However, the effective notch stress is lower than the maximum effective notch stress.

Figure 4-11(d) clearly shows, that the notch stresses do not coincide for any value of  $a$ . The effective notch stresses at the crack locations remains below their maximum values. However, the notch stresses converged as  $a$  increased. This can also be observed in Figure 4-12 (d). The mean line indicates with  $r_{a,f} = 1.13$  the smallest deviation for a value of  $a = 0.01 \text{ mm}^2$  (Figure 4-12 (d)).

Due to the high deviation between the effective notch stresses, it can be concluded that the crack locations from the fatigue test do not match the crack locations from the numerical calculation, even after considering the micro-support effect. This mismatch can be attributed to the fatigue test procedure, where secondary bending could have been generated at the clamping process, which is used to straighten partially curved specimens. This leads to additional stresses on the surface, which must be interpreted as constant mean stress. In numerical calculations, curved specimens led to higher notch stresses, which were not present in the test due to straightening. The straightening process cannot be reproduced numerically, as it requires the exact position of the specimen in the testing machine. In addition, deviations from the scattering material parameters within the corroded surfaces and inaccuracies in the entire reverse engineering process (from 3D recording to numerical calculation) may be involved, which ultimately cannot be investigated in detail. However, for 25 out of 33 specimens (levels 1–3), a good agreement between the locations of the maximum effective notch stresses and crack locations from the fatigue tests could be achieved.



**Figure 4-11: Comparison of maximum effective notch stresses and effective notch stresses at the crack location for conformity levels 1 to 4 with the governing effective stress concentration factors  $\alpha_{f,cal}$  from based on calibration of parameter a**



**Figure 4-12: Ratio  $r_{\alpha,f}$  of the effective notch stresses at the crack location and maximum effective notch stress for conformity levels 1 to 4**

## 4.6 Fatigue strength analysis

### 4.6.1 Determination of weighting factor for the implicit gradient model

The weighting factor  $a$  can be determined according to equation (4-11) by means of the intrinsic material length  $L$ , which depends on the material-specific fatigue crack propagation threshold  $\Delta K_{th}$  and the fatigue limit state  $\Delta\sigma_0$ . Due to the changed material at the surface of the corroded specimen, the values for  $\Delta K_{th}$  and  $\Delta\sigma_0$  cannot be taken from the literature. Besides the direct determination of the weighting factor, it is possible to determine the weighting factor using the scattering minimization technique [26,33,35]. Here, an iterative calculation is carried out for the weighting factor, with which the lowest scatter can be achieved, when the notch stresses determined with the weighting factor are plotted over the load cycles. Therefore, a mean stress correction is carried out first in order to consider

all fatigue tests. According the IIW guideline [5] for specimens with  $R = -0.1$ , the stress range is decreased by a factor of  $f = 1.26$ , specimens with  $R = 0.1$  by a factor of  $f = 1.14$ , while the stress range of specimens with  $R = 0.5$  was not further changed. Subsequently, the load cycles from the fatigue tests were plotted against the elastic notch stress ranges  $\Delta\sigma_k = \Delta\sigma_f$  ( $a = 0$ ), and the resulting scatter of the SN-curve was determined to  $T_\sigma = 1.89$ , see Figure 4-13 (a). The scatter  $T_\sigma$  was evaluated for varying effective notch stress concentrations, which in turn depend on the size of the parameter  $a$ . Figure 4-14 illustrates the resulting graph, which shows the scatter as a function of parameter  $a$ . It appears that there is a minimum point of scatter at about  $a = 0.0045 \text{ mm}^2$  with  $T_\sigma = 1.24$ , see Figure 4-13 (b). The corresponding fatigue resistance  $\Delta\sigma_c$  (FAT-class), which is defined by  $N = 2 \times 10^6$  cycles with a survival probability of 97.7%, is FAT 236 and the slope is  $m = 4.62$ .

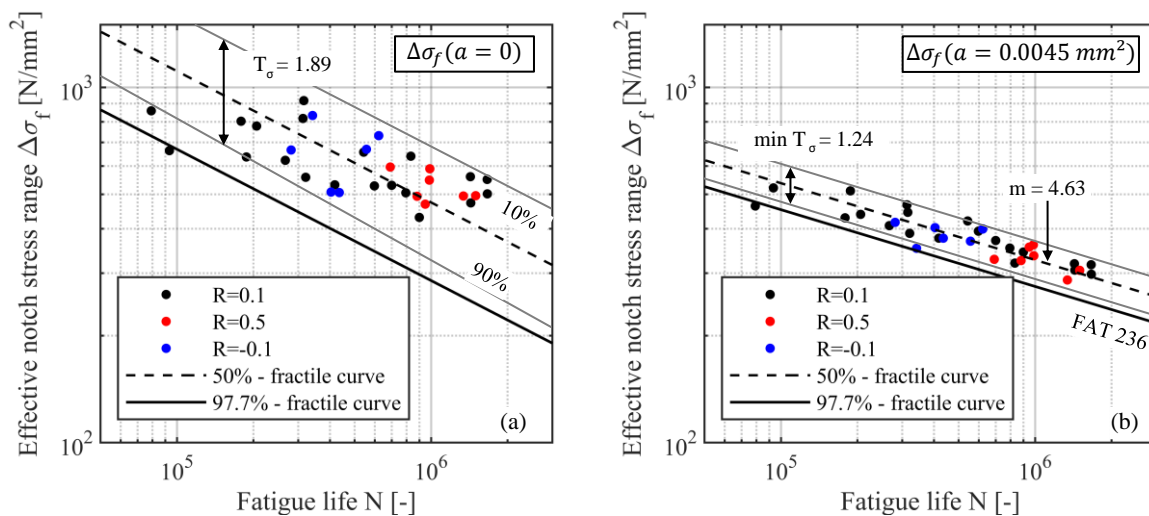


**Figure 4-13: Notch stress SN-curves, (a) SN-curve based on effective notch stress ranges without micro-support consideration, (c) SN-curve based on effective notch stress ranges with micro support consideration for  $a=0.0045$**

In addition, the conformity of crack locations from the fatigue tests with those predicted in the numerical investigation was investigated. For this purpose, the ratio  $r_{\alpha,f}$  (see Figure 4-12) was used. It was assumed that a ratio of  $r_{\alpha,f} \leq 1.05$ , i.e. a difference of 5% in the stress concentrations between crack location and the hotspot from the numerical analysis, still represents a good match. Depending on the parameter  $a$ , the number of specimens with good agreement is determined and divided by the total number of specimens. The resulting ratio for specimens with good conformity is shown in dependence of the parameter  $a$  in Figure 4-14. At the maximum,  $25/33 = 76\%$  of the specimens show good conformity between crack location and numerical prediction. It becomes apparent that the conformity increases with decreasing scatter  $T_\sigma$  of the SN curve and that the highest conformity is achieved at the lowest scatter point, which supports the procedure of calibrating the parameter  $a$  based on the lowest scatter. Figure 4-11 shows exemplary the corresponding effective notch stress concentration  $\alpha_{f,cal}$  for  $a = 0.0045 \text{ mm}^2$  for some specimens.

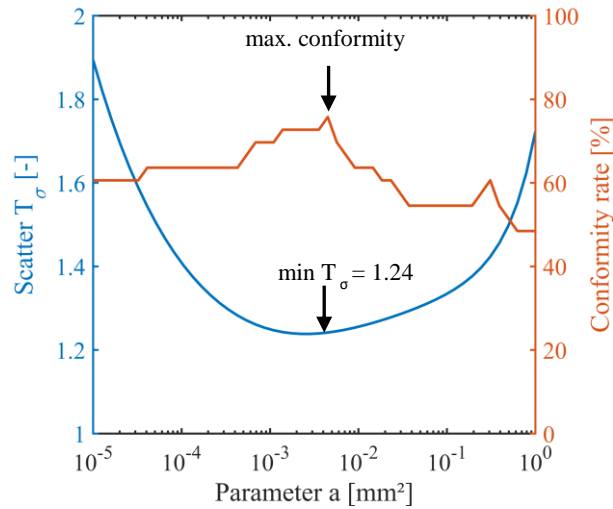


**Figure 4-14: Scatter  $T_{\sigma}$  and conformity rate in dependence of parameter  $a$**

#### 4.6.2 Comparison of TCD with IGM

For comparison of the IGM with the TCD, the fatigue results were evaluated using the point method and the line method. For this purpose, the elastic stress concentrations from the structural analysis were evaluated in the thickness direction. The evaluation was carried out for the crack location and for the maximum notch stress location using the formulas according to (4-1) for point method and (4-2) for line method. Analogous to the calibration of parameter  $a$ , the fatigue tests were first corrected with the mean stress correction factors. Then the load cycles were plotted against the notch stress range and the scatter  $T_{\sigma}$  was determined as a function of the distance  $d^*$  (for point method) and  $\rho^*$  (for line method). Based on the results in Figure 4-15 (a1) and (a2), the lowest scatter for the point method is at a distance of  $d^* = 0.04$  mm, while for the line method the lowest scatter is at an equivalent length of  $\rho^* = 0.11$  mm. The conformity rate at the point of the lowest scatter for all methods is about 75%, which is in the range of the IGM method. However, it appears that in both cases the maximum conformity lies outside the range of the smallest scatter. This is due to the circumstance that in the TCD method only two locations are evaluated and compared with each other, whereas in the IGM method the notch stress at the crack location is compared to the maximum stress from the whole specimen.

Figure 4-15 (b1) and (b2) presents the SN-curves based on notch stresses for the lowest scatter. It appears that the slope as well as the FAT-class of the SN-curves are similar for both TCD-methods. With FAT 233 for both TCD-methods, the value is very close to the value of FAT 236 predicted on the basis of IGM. From the comparison of the individual values, it can be seen that the TCD-methods and IGM-method show very similar results with low scatter in the range of higher cycles. Only at lower cycles the scatter becomes larger for the TCD-methods. Table 4-2 summarizes the resulting fatigue curve parameters for all methods.

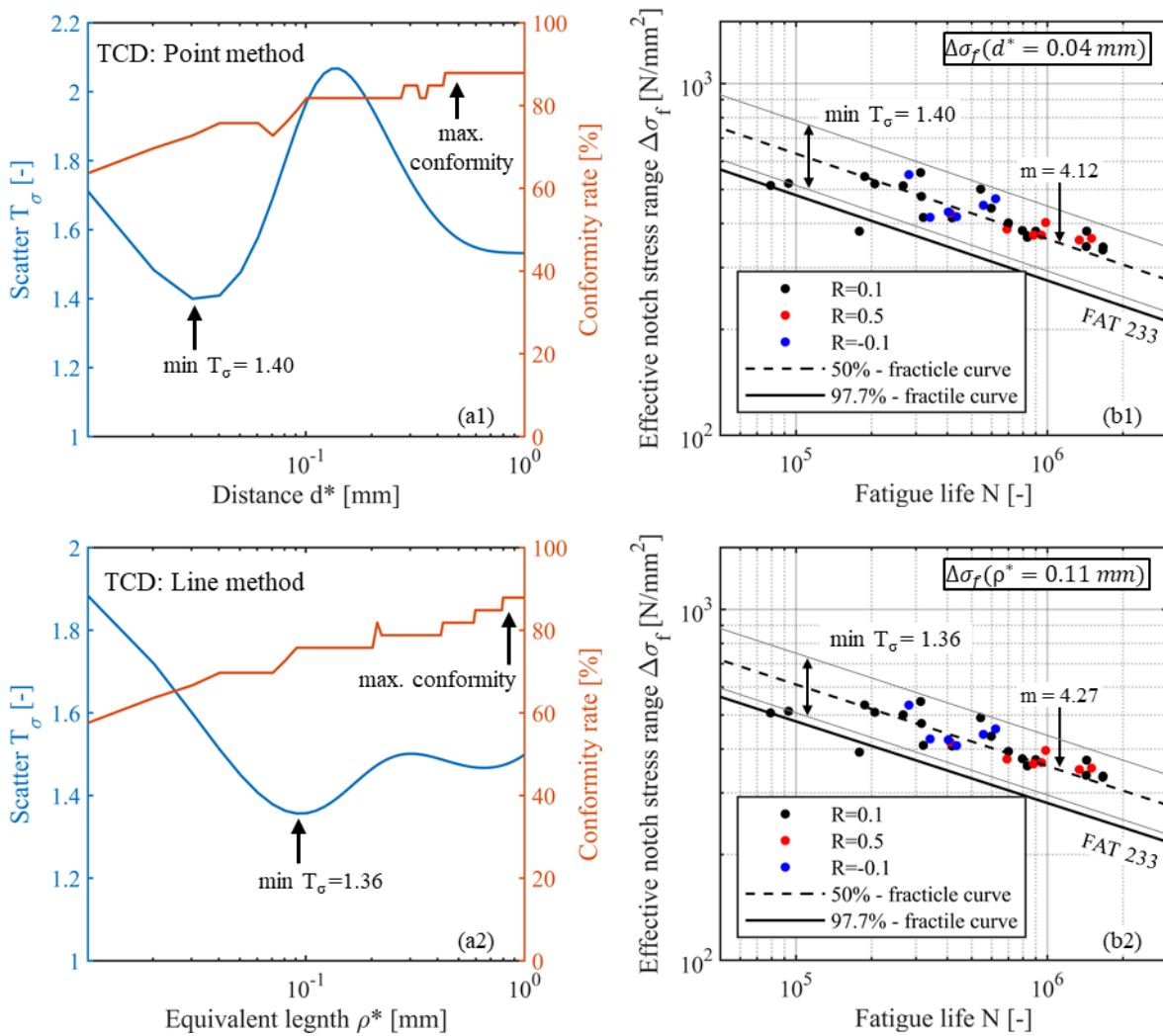


**Figure 4-15: Results for the point method and the line method, (a) Scatter of  $T_\sigma$  and conformity rate as a function of the distance  $d^*/$ equivalent length  $\rho^*$ , (b) SN-curve based on effective notch stress ranges with micro support consideration for  $d^* = 0.04$  mm and  $\rho^* = 0.11$  mm**

**Table 4-2: Fatigue curve parameter resulting from different methods for micro-support consideration**

Methods	Slope m	$\Delta\sigma_c$ [N/mm <sup>2</sup> ] / FAT-class	Scatter ratio $T_\sigma$ [-]
IGM	4.63	236	1.24
TCD – point method	4.12	233	1.40
TCD – line method	4.27	233	1.36

### 4.6.3 Discussion

In the literature, different weighting parameter for IGM analysis are proposed for mild steel based on the stress criterion and the stress ratio, see Table 4-3. Peerlings [34] assumed an estimated value of a

= 0.01 mm<sup>2</sup> for base material and the von Mises stress criterion. Askes et al. [39] have determined a = 0.027 mm<sup>2</sup> for R = 0 and a = 0.014 mm<sup>2</sup> for R = 0.4 for mild steels, based on the material parameters  $\Delta K_{th}$  and  $\Delta\sigma_0$  and with consideration of the maximum principal stress criterion. For weld seams, a value of a = 0.04 mm<sup>2</sup> is given by Tovo et al. [33] for R = 0 and the maximum principal stress criterion. This value is calibrated on the fatigue tests of welded joints based on the lowest scatter for all test specimens. Lang et al. [36] and Schürmann [37] calibrated the parameter *a* using Radaj's equivalent radius of  $\rho_f = 1.0$  mm according the IIW recommendation [10], which is based on the maximum principal stress criterion and a stress ratio of R = 0.5, and were able to determine values between a = 0.005 mm<sup>2</sup> and a = 0.008 mm<sup>2</sup> for welded joints.

**Table 4-3: Weighting parameter from literature for low alloy mild steel compared to result of this study**

Source	Geometry	Stress criterion	Stress ratio R [-]	Parameter a [mm <sup>2</sup> ]	Critical distance d* [mm]	Equivalent length $\rho^*$ [mm]
Peerlings [34]	Notched specimen	Von Mises	0.1	0.01		
Askes et al. [39]	Notched specimen	Max. principal	-1	0.063	0.23	0.92
Askes et al. [39]	Notched specimen	Max. principal	0	0.027	0.15	0.6
Askes et al. [39]	Notched specimen	Max. principal	0.4	0.014	0.109	0.436
Tovo et al. [33]	Weld seam	Max. principal	0	0.04	-	-
Lang et al. [36]	Weld seam	Max. principal	0.5	0.007	-	-
Schürmann [37]	Weld seam	Max. principal	0.5	0.005 – 0.008	-	-
Baumgartner [26]	Weld seam	Max. principal	0.5	-	0.1	0.4
Baumgartner [26]	Weld seam	Von Mises	0.5	-	0.05	0.2
This study:	Corroded specimen	Von Mises	0.5*	0.0045	0.04	0.11

\*mean stress corrected

The value of a = 0.0045 mm<sup>2</sup> determined in this study is based on the von Mises stress criterion and is related to a stress Ratio of R = 0.5, as the fatigue test results were corrected with mean stress correction factors according IIW recommendation [10] before calibration of the weighting parameter. Compared to the literature, the value from this study is lower than all given values. The first reason is that most of the values are given for the maximum principal stress rather than the von Mises stress. According equation (4-11) the different criteria can be considered with  $\zeta$ , where  $\zeta = 0.545$  is used for the maximum principal and  $\zeta = 0.456$  is used for the von Mises stress criterion. This, lead to a value of  $\frac{0.545}{0.456} a = 1.2a = 0.0054$  mm<sup>2</sup> for the maximum principal stress criterion, and thus would have only minor effect on the weighting parameter. According Table 4-3, the stress ratio R has a greater influence, since it affects the fatigue crack propagation threshold  $\Delta K_{th}$ , which in turn is linked to the



weighting parameter via the intrinsic material length  $L$ . This is supported by the British standard BS 7910 [48], where higher R-ratios lead to reduced crack propagation threshold  $\Delta K_{th}$  and thus result in smaller weighting parameters. For a comparison, the value given by Askes et al. [39] for  $R = 0.4$  is hence the most suitable, since it is closest to  $R = 0.5$  used in this study. It becomes evident that, despite taking into account the stress criterion and the R-ratio, the values with  $a = 0.014 \text{ mm}^2$  and  $a = 0.0054 \text{ mm}^2$  differ considerably.

Regarding TCD methods, for base material, predominantly values based on the maximum principal stress are given by Askes et al. [39] with  $d^* = 0.109 \text{ mm}$  and  $\rho^* = 0.436 \text{ mm}^2$  for  $R = 0.4$ . For welded joints, Baumgartner [26] suggests  $d^* = 0.1 \text{ mm}$  and  $\rho^* = 0.4 \text{ mm}^2$  for the maximum principal stress and  $d^* = 0.05 \text{ mm}$  and  $\rho^* = 0.2 \text{ mm}^2$  for the von Mises stress criterion, both for  $R = 0.5$ . The distance and the equivalent length are coupled via the intrinsic length scale  $L$ , so that  $\rho^* = 4 \cdot a$  [39]. Since the values obtained in this study are based on the von Mises stress criterion, a comparison with base material cannot be made directly. Instead, the values are compared to that for welded joints given by Baumgartner [26]. This is reasonable, since the values of Baumgartner [26] and Askes et al. [39] differ only slightly, although there are differences in the microstructure and material composition. The comparison shows that the value  $d^* = 0.04$  determined in this study agrees very well with the specified value of  $d^* = 0.05$ . However, the agreement for the equivalent length  $\rho^* = 0.11$  obtained in this study with the specified value of  $\rho^* = 0.2$  is lower.

By comparing IGM and TCD, it can be shown that both parameter  $a$  as well as distance  $d^*$  and equivalent length  $\rho^*$  are lower for the corroded specimens than the reported values for base material. It is reasonable to assume that corrosion changes the material near the surface and thus, at least on the surface, it no longer corresponds to the base material. However, based on the comparison between IGM and TCD, the IGM method can be attested a high accuracy.

It should be noted, that the simultaneous effects of corrosion and fatigue were not considered in this study. Corrosion leads to embrittlement of the material at the crack front and therefore to a lower fatigue crack propagation threshold  $\Delta K_{th}$ . This can be taken into account via the intrinsic material length  $L$ , which in turn is coupled to the parameter  $a$  via equation (4-11). Using the fatigue crack propagation thresholds for corrosive conditions, the method can be extended to simultaneous fatigue and corrosion.

## 4.7 Application to existing structures

With the replica technique, the findings can be transferred to real structures by taking impressions of corroded structures and examining it using the methods presented. In the following, a corroded specimen is therefore investigated using the replica technique and compared with the results from the original.

### 4.7.1 Replica imprint and 3D-scan

The replica technique involves creating a negative replica of the corroded surface using a fast-curing material with low viscosity. To achieve this, the corroded surface is initially cleaned of corrosion products following the guidelines of ISO 8407 [49]. The material is then applied to the surface and

once it has hardened, the impression is removed. Afterwards, the impression is scanned using a high-resolution 3D scanner.

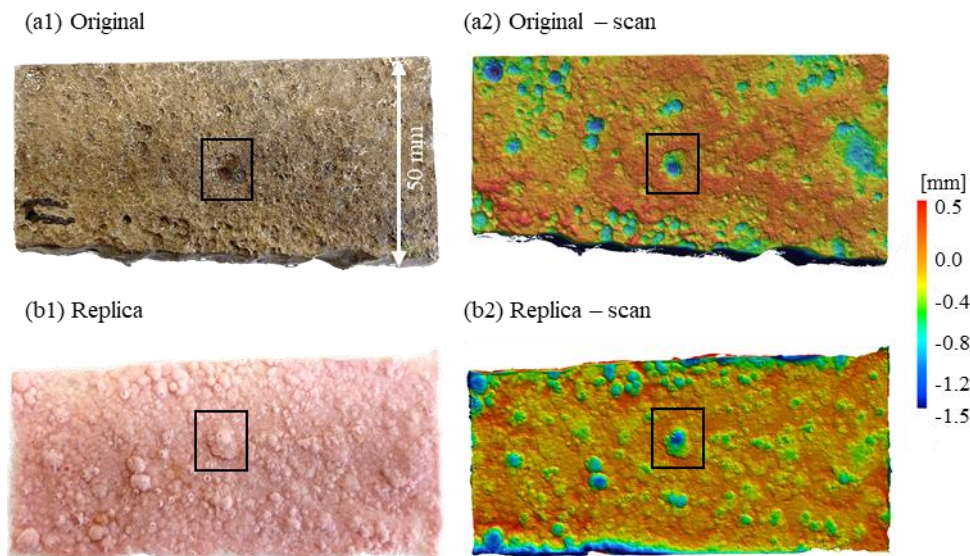


**Figure 4-16: Comparison between original specimen and replica with (a1) image of original specimen, (a2) 3D-scan of original specimen, (b1) image of replica and (b2) 3D-scan of replica**

Figure 4-16 shows a corroded steel specimen (subplot (a1)) and the corresponding replica impression (subplot (b1)). In subplot (a2) and (b2) the corresponding 3D-scans are shown illustrated. It is apparent, that the surfaces are similar. In particular, geometries of large pits are very well represented, as it can be observed in the framed area in Figure 4-16. Higher deviations occur at the edges of the specimen, which are attributed to the viscosity of the replica material in the non-hardened condition and thus are not relevant for an application on real structural components. In addition, small protrusions can be seen on the replica impression, which result from air inclusions.

#### 4.7.2 Reverse Engineering

The reverse engineering method is used to create a solid model from the 3D-scan. The 3D-scan data are first exported in STL format and then converted to a solid model with the help of NURBS-patches, as described in section 4.5.1. As the replica impression is only a single surface, a solid model cannot be generated directly by merging all the NURBS-patches into one solid model. Hence, a solid CAD-model with similar shape of the specimen is created in the first step. In the second step the surface of the created solid model is replaced with the NURBS-surface created from the replica scan. In Figure 4-17 the STL-data (plot a and d) as well as the resulting solid model (plot b,c,e and f) are illustrated.

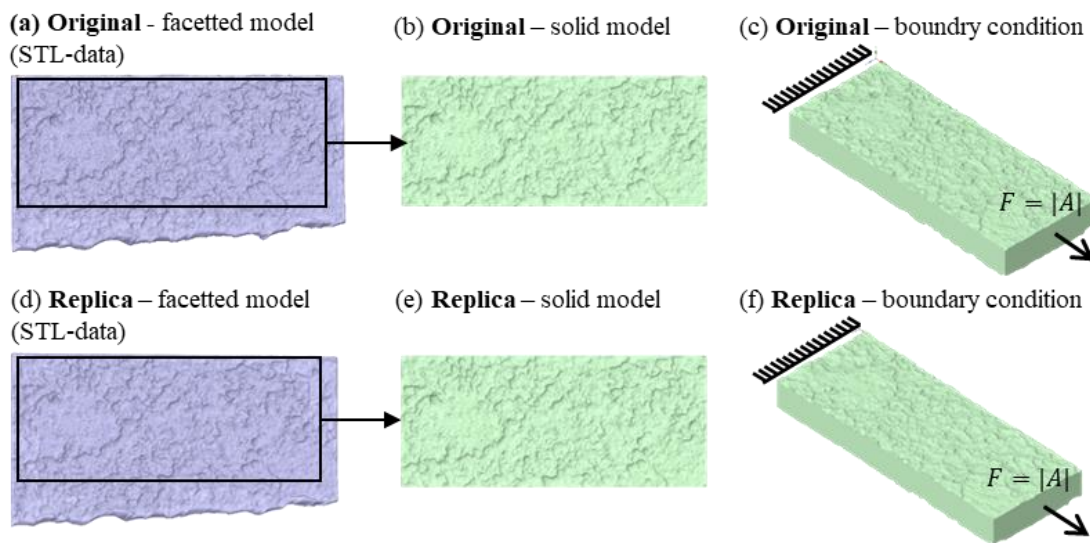


**Figure 4-17: Reverse Engineering from STL-data (a) and (d) to solid model (b) and (d) for the original specimen and the replica, with corresponding boundary condition in (c) and (f)**

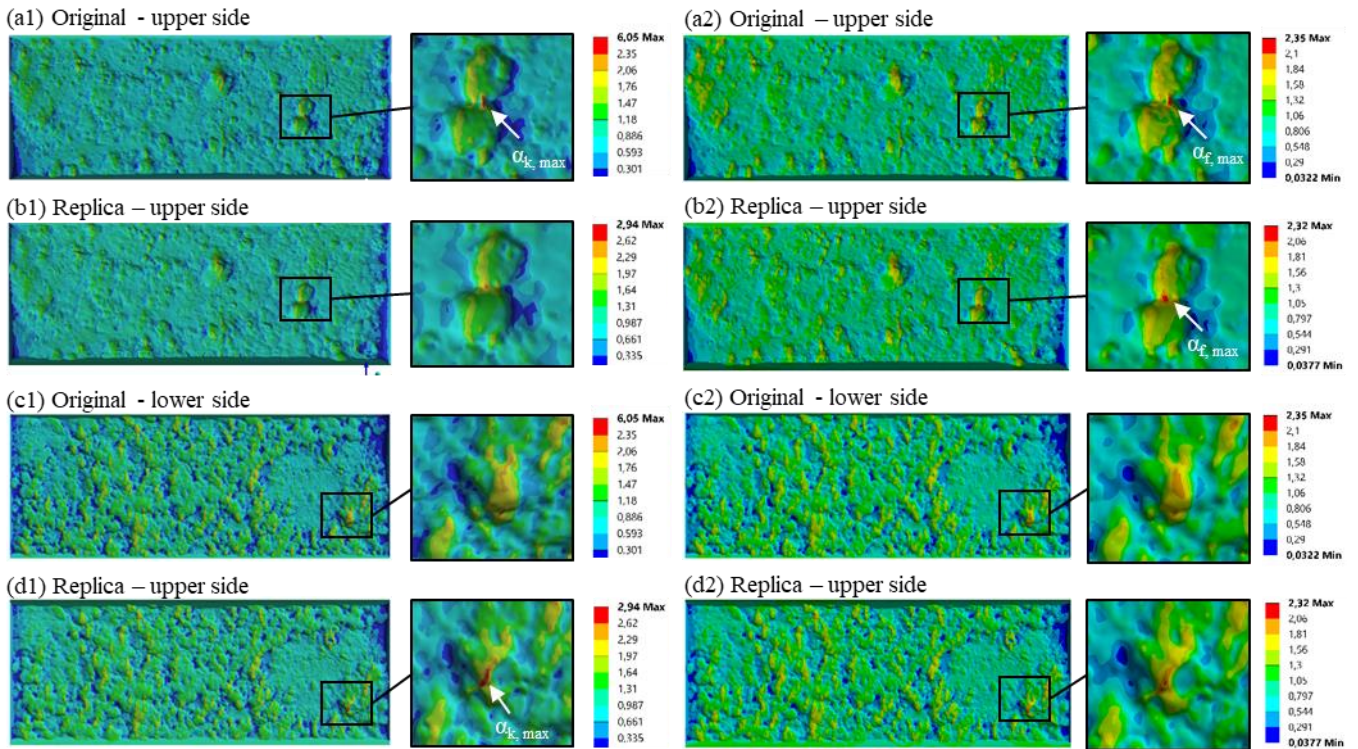
### 4.7.3 Results and discussion

Figure 4-18 (a1) to (d1) shows the stress concentrations for the original specimen and the replica impression over the entire surface for the upper as well as lower side. The course of the notch stresses is very similar, but the magnitudes of notch stresses are partly lower in the replica impression. For example, the maximum value for the original model is  $\alpha_k = 6.05$  (Figure 4-18 a1) and is found on the upper side, while for the replica model the maximum value is  $\alpha_k = 2.94$  (Figure 4-18 d1) and is found on the lower side. When comparing the results for the original model in Figure 4-18 (a1) with the corresponding replica in Figure 4-18 (b1) directly, it can be seen, that the notch stress at the same location in the replica is even lower than the maximum value of the replica. This results from the fact, that the replica imprint cannot properly reproduce extremely sharp notches, which, for example, occurs on double-pit edges.

Figure 4-18 (a2) to (d2) shows the stress concentrations after considering the micro-support effect with the recommended weighting factor of  $a = 0.0045 \text{ mm}^2$ . It is evident that both, the original model and the replica have their maximal stress on the same location. It can also be seen that the maximum values, with  $\alpha_{f,\max} = 2.35$  for the original model and with  $\alpha_{f,\max} = 2.32$  for the replica model, are very close to each other (see Figure 4-18 (a2) and (b2)). The notch stresses on the lower surface also show only small deviations between original and replica. It follows, that by taking the micro-support effect into account, the high stresses at the extremely sharp notches do not become decisive, as these are averaged over the range defined by parameter  $a$ .

It can be concluded, that although the surface geometry of the original surface cannot be reproduced to the full extent with the replica imprint, the influence on the stress concentration is not significant after consideration of the micro-support effect. In particular, the very sharp notches with high elastic stress concentrations, which cannot be reproduced by the replica with sufficient accuracy, are not

relevant when the micro-support effect is considered. Because of the micro-support effect, also the air inclusions occurring in the replica, do not have a great impact. This allows the replica technique to be applied on existing corroded structures, in order to calculate the (remaining-) fatigue life based on the real surface condition.



**Figure 4-18: (a1) to (d1) Elastic stress concentration based on von Mises stress criterion for the original and replica scan and for upper and lower side, and (a2) to (d2) effective stress concentration with consideration of the micro-support effect with a weighting factor  $a=0.0045 \text{ mm}^2$**

#### 4.8 Summary and Outlook

The purpose of this study was to investigate consideration of the micro-support effect, which so far had not been investigated for corroded specimens. The IGM-method was used to consider the micro-support effect since it allows all the notches to be accounted numerically based on FE-analysis. The results were compared to common TCD methods and a notch stress fatigue curve was derived. Subsequently, it was presented how these results can be applied to real steel structures. The following findings resulted from the study:

- The consideration of the micro-support effect according to the implicit gradient model could predict crack locations from the fatigue test with high accuracy for 25 out of 33 specimens. For 18 out of 25 specimens, the crack location matched well with the maximum notch stress location before and after the micro-support consideration. For 7 out of 25 specimens, the locations of the maximum notch stresses shifted towards the crack location because of the consideration of micro-support.



- For IGM a weighting factor of  $a = 0.0045 \text{ mm}^2$  was obtained based on the lowest scatter ( $T_\sigma = 1.24$ ) in the notch stress fatigue curve. The lowest scatter coincides with the highest conformity rate (76%) between the crack location from fatigue tests and the predicted maximum notch stress location.
- According to the TCD methods, a critical distance of  $d^* = 0.04 \text{ mm}$  and an equivalent length  $\rho^* = 0.11 \text{ mm}$  were determined based on the von Mises stress criterion.
- The comparison with the TCD methods reveals similar results for the point method and the line method as well as for the IGM method with respect to the notch stress fatigue curve, where the FAT-class for the TCD method is FAT 233 and for the IGM method FAT 236. In contrast to the IGM method, the highest conformity rate does not coincide with the lowest scatter of the notch stress fatigue curve.
- With the replica technique the surface geometry of corroded steel structures was recorded and transformed to a 3D solid model via reverse engineering, allowing numerical stress analysis of corroded structures based on real surface.
- By applying the recommended weighting factor of  $a = 0.0045 \text{ mm}^2$  in the numerical analysis the fatigue driving stress concentrations were calculated. In combination of the derived FAT-class FAT 236, the fatigue life of corroded steel structures can be estimated based on the calculated stress concentration.

These findings allow the micro-support effect to be considered for corroded structures, made of low alloy mild steel, based on real surface geometry. For structural components with welds or components made of high-strength materials, further investigations are necessary.

#### 4.9 Acknowledgements

The joint research project ISyMOO was funded by the German Federal Ministry of Economic Affairs and Climate Action (BMWK) through the 6<sup>th</sup> National Energy Research Program under funding number 0324254A. The authors would like to express their sincere thanks for the support of the Ministry, PT Jülich, and research partners.

#### 4.10 References

- [1] Qvale P, Zarandi EP, Ås SK, Skallerud BH. Digital image correlation for continuous mapping of fatigue crack initiation sites on corroded surface from offshore mooring chain. *International Journal of Fatigue* 2021;151:106350. <https://doi.org/10.1016/j.ijfatigue.2021.106350>.
- [2] Shojai S, Schaumann P, Braun M, Ehlers S. Influence of pitting corrosion on the fatigue strength of offshore steel structures based on 3D surface scans. *International Journal of Fatigue* 2022;164:107128. <https://doi.org/10.1016/j.ijfatigue.2022.107128>.
- [3] Braun M, Milaković A-S, Renken F, Fricke W, Ehlers S. Application of Local Approaches to the Assessment of Fatigue Test results obtained for Welded Joints at Sub-Zero Temperatures; 2020.

- 
- [4] Radaj D, Vormwald M. *Advanced methods of fatigue assessment*. Heidelberg: Springer; 2013.
- [5] Ladinek M, Niederwanger A, Lang R, Schmid J, Timmers R, Lener G. The strain-life approach applied to welded joints: Considering the real weld geometry. *Journal of Constructional Steel Research* 2018;148:180–8. <https://doi.org/10.1016/j.jcsr.2018.04.024>.
- [6] Radaj D, Sonsino CM, Fricke W. *Fatigue assessment of welded joints by local approaches*. 2nd ed. Cambridge: Woodhead Publ. [u.a.]; 2006.
- [7] Sonsino CM, Fricke W, Bruyne F de, Hoppe A, Ahmadi A, Zhang G. Notch stress concepts for the fatigue assessment of welded joints – Background and applications. *International Journal of Fatigue* 2012;34(1):2–16. <https://doi.org/10.1016/j.ijfatigue.2010.04.011>.
- [8] Lener G, Lang R, Ladinek M, Timmers R. A numerical method for determining the fatigue strength of welded joints with a significant improvement in accuracy. *Procedia Engineering* 2018;213:359–73. <https://doi.org/10.1016/j.proeng.2018.02.036>.
- [9] Schaumann P, Schürmann K, Pittner A, Rethmeier M. Automatically Welded Tubular X-Joints for Jacket Substructures: Prediction of the Technical Fatigue Crack Location. *ce/papers* 2019;3(3-4):823–8. <https://doi.org/10.1002/cepa.1140>.
- [10] Hobbacher A. Recommendations for fatigue design of welded joints and components. IIW Document No. IIW-1823-07 International Institute of Welding; 2009.
- [11] Fricke W. IIW recommendations for the fatigue assessment of welded structures by notch stress analysis. Oxford: WP Woodhead Publ; 2012.
- [12] Momber AW, Nattkemper TW, Langenkämper D, Möller T, Brün D, Schaumann P et al. A data-based model for condition monitoring and maintenance planning for protective coating systems for wind tower structures. *Renewable Energy* 2022;186:957–73. <https://doi.org/10.1016/j.renene.2022.01.022>.
- [13] Xiang L, Pan J, Chen S. Analysis on the stress corrosion crack inception based on pit shape and size of the FV520B tensile specimen. *Results in Physics* 2018;9:463–70. <https://doi.org/10.1016/j.rinp.2018.03.005>.
- [14] Cerit M. Corrosion pit-induced stress concentration in spherical pressure vessel. *Thin-Walled Structures* 2019;136:106–12. <https://doi.org/10.1016/j.tws.2018.12.014>.
- [15] Huang Y, Wei C, Chen L, Li P. Quantitative correlation between geometric parameters and stress concentration of corrosion pits. *Engineering Failure Analysis* 2014;44:168–78. <https://doi.org/10.1016/j.engfailanal.2014.05.020>.
- [16] Hou J, Song L. Numerical Investigation on Stress Concentration of Tension Steel Bars with One or Two Corrosion Pits. *Advances in Materials Science and Engineering* 2015;2015:1–7. <https://doi.org/10.1155/2015/413737>.
- [17] Radaj D, Vormwald M. *Ermüdungsfestigkeit: Grundlagen für Ingenieure*. 3rd ed. Berlin, Heidelberg: Springer-Verlag Berlin Heidelberg; 2007.

- [18] Neuber H. Kerbspannungslehre: Grundlagen für genaue Festigkeitsberechnung mit Berücksichtigung von Konstruktionsform und Werkstoff. Berlin, Heidelberg, s.l.: Springer Berlin Heidelberg; 1958. <https://doi.org/10.1007/978-3-642-53069-2>.
- [19] Peterson R. Notch sensitivity. *Metal Fatigue* 1959;293–306.
- [20] Neuber H. Über die Berücksichtigung der spannungskonzentration bei festigkeitsberechnungen; 1968.
- [21] Taylor D. The theory of critical distances: A new perspective in fracture mechanics. Amsterdam, London: Elsevier; 2010.
- [22] Sheppard SD. Field Effects in Fatigue Crack Initiation: Long Life Fatigue Strength. *J. Mech. Des* 1991;113(2):188–94. <https://doi.org/10.1115/1.2912768>.
- [23] Bellett D, Taylor D, Marco S, Mazzeo E, Guillois J, Pircher T. The fatigue behaviour of three-dimensional stress concentrations. *International Journal of Fatigue* 2005;27(3):207–21. <https://doi.org/10.1016/j.ijfatigue.2004.07.006>.
- [24] Taylor, Wang. The validation of some methods of notch fatigue analysis. *Fatigue & Fracture of Engineering Materials & Structures* 2000;23(5):387–94. <https://doi.org/10.1046/j.1460-2695.2000.00302.x>.
- [25] Susmel L, Taylor D. Fatigue design in the presence of stress concentrations. *The Journal of Strain Analysis for Engineering Design* 2003;38(5):443–52. <https://doi.org/10.1243/03093240360713496>.
- [26] Baumgartner J, Schmidt H, Ince E, Melz T, Dilger K. Fatigue assessment of welded joints using stress averaging and critical distance approaches. *Weld World* 2015;59(5):731–42. <https://doi.org/10.1007/s40194-015-0248-x>.
- [27] Ahola A, Lipiäinen K, Afkhami S, Lilja H, Björk T. Fatigue performance of the welded details of an old, demolished steel railway bridge. *Engineering Structures* 2022;256:113966. <https://doi.org/10.1016/j.engstruct.2022.113966>.
- [28] Braun M, Müller AM, Milaković A-S, Fricke W, Ehlers S. Requirements for stress gradient-based fatigue assessment of notched structures according to theory of critical distance. *Fatigue & Fracture of Engineering Materials & Structures* 2020;43(7):1541–54. <https://doi.org/10.1111/ffe.13232>.
- [29] Braun M, Grimm J-H, Milaković A-S, Hoffmeister H, Canaletti A, Ehlers S et al. Bewertung der Schwingfestigkeit ausgeschliffener Schweißnähte aus hochfesten Stählen und Vergleich mit gekerbten Grundmaterialproben. In:
- [30] Skallerud B, Ås SK, Ottosen NS. A gradient-based multiaxial criterion for fatigue crack initiation prediction in components with surface roughness. *International Journal of Fatigue* 2018;117:384–95. <https://doi.org/10.1016/j.ijfatigue.2018.08.020>.
- [31] Peerlings RH, Borst R de, Brekelmans WAM, Vree JHP de. Computational Modelling of Gradient-Enhanced Damage for Fracture and Fatigue Problems. In: Owen DRJ, Oñate E, editors.

Computational plasticity: Fundamentals and applications ; proceedings of the fourth international conference held in Barcelona, Spain, 3th - 6th April, 1995 ; [a book in memoriam of Juan Carlos Simo. Swansea: Pineridge Press; 1995, p. 975–986.

- [32] Peerlings RHJ, Brekelmans WAM, Borst R de, Geers MGD. Gradient-enhanced damage modelling of high-cycle fatigue. *Int. J. Numer. Meth. Engng.* 2000;49(12):1547–69.
- [33] Tovo R, Livieri P. An implicit gradient application to fatigue of sharp notches and weldments. *Engineering Fracture Mechanics* 2007;74(4):515–26. <https://doi.org/10.1016/j.engfrac-mech.2006.06.009>.
- [34] Peerlings R. Enhanced damage modelling for fracture and fatigue. Technische Universiteit Eindhoven; 1999.
- [35] Tovo R, Livieri P. An implicit gradient application to fatigue of complex structures; 2008.
- [36] Lang R, Ladinek M, Lener G. Über die Anpassung eines fortschrittlichen Stützwirkungsansatzes für das Kerbspannungskonzept. *Stahlbau* 2017;86(6):470–82. <https://doi.org/10.1002/stab.201710494>.
- [37] Karsten Schürmann. Fatigue Behavior of Automatically Welded Tubular Joints for Offshore Wind Energy Substructures: Dissertation; 2021.
- [38] Zhang G. Method of effective stress for fatigue: Part I – A general theory. *International Journal of Fatigue* 2012;37:17–23. <https://doi.org/10.1016/j.ijfatigue.2011.09.018>.
- [39] Askes H, Livieri P, Susmel L, Taylor D, Tovo R. Intrinsic material length, Theory of Critical Distances and Gradient Mechanics: analogies and differences in processing linear-elastic crack tip stress fields. *Fatigue Fract Engng Mater Struct* 2013;36(1):39–55. <https://doi.org/10.1111/j.1460-2695.2012.01687.x>.
- [40] Tovo R, Livieri P, Benvenuti E. An implicit gradient type of static failure criterion for mixed-mode loading. *Int J Fract* 2006;141(3-4):497–511. <https://doi.org/10.1007/s10704-006-9011-z>.
- [41] Borst R de, Pamin J, Peerlings RHJ, Sluys LJ. On gradient-enhanced damage and plasticity models for failure in quasi-brittle and frictional materials. *Computational Mechanics* 1995;17(1-2):130–41. <https://doi.org/10.1007/s004660050098>.
- [42] Lang R. Ein Beitrag zur Bestimmung der Anrisslebensdauer geschweißter Bauteile. Universität Innsbruck; 2015.
- [43] Biglu M. Doctoral Thesis - Effects of corrosion on the local behavior of steel structures under tensile loading. TU Hamburg; 2022.
- [44] International Standards Organization. ISO 6507-1, Metallic materials — Vickers hardness test — Part 1: Test method;2022.
- [45] G01 Committee. Practice for Preparing, Cleaning, and Evaluating Corrosion Test Specimens. West Conshohocken, PA: ASTM International. <https://doi.org/10.1520/G0001-03R17E01>.



- 
- [46] Det Norske Veritas - Germanischer Lloyd. Fatigue design of offshore steel structures(DNV-GL RP-C203); 2019.
- [47] Shojai S, Schaumann P, Brömer T. Probabilistic modelling of pitting corrosion and its impact on stress concentrations in steel structures in the offshore wind energy. *Marine Structures* 2022;84:103232. <https://doi.org/10.1016/j.marstruc.2022.103232>.
- [48] British Standards Institution. BS 7910: Guide to methods for assessing the acceptability of flaws in metallic structures; 2019.
- [49] ISO 8407: Corrosion of metals and alloys – Removal of corrosion products from corrosion test specimens. Berlin: Beuth; 2021.



## 5 Assessment of corrosion fatigue in welded joints (Paper IV)

This section contains a reprint of the article: Shojai, Sulaiman; Brömer, Tim; Ghafoori, Elyas; Woitzik, Christian; Braun, Moritz; Köhler, Markus; Schaumann, Peter (2023): Assessment of corrosion fatigue in welded joints using 3D surface scans, digital image correlation, hardness measurements, and residual stress analysis. In: *International Journal of Fatigue* 176, S. 107866. DOI: 10.1016/j.ijfatigue.2023.107866.

### Background

In the previous papers, the influence of pitting corrosion on the fatigue strength of plane steel was investigated by experimental and numerical investigation. In real offshore steel structures, however, there are a large number of welds that significantly influence the fatigue resistance of the whole structure due to their notch effect. The interaction between the welds and corrosion on the fatigue strength is considered in the DNV guidelines with a general reduction of the SN curves. However, this reduction is a rough estimate, as the corrosion process and fatigue mechanics were superimposed in the underlying fatigue tests. Consequently, this method cannot account for notch stresses resulting from localized changes in surface geometry due to corrosive exposure, nor does it differentiate between moderately and strongly notched structural components. Moreover, particularly in the case of offshore support structures, where components undergo clean blasting before the application of corrosion coatings, the beneficial impact of clean blasting has to be considered as well. Both, with regard to the utilization of this positive effect and in view of calculating the (remaining) lifetime of existing support structures with local fatigue approaches, it is important to quantify the individual fatigue driving factors in order to include them in the calculations.

### Overview

In this study fatigue tests were carried out on base material, butt-welded and fillet-welded specimen with different conditions, such as as-welded, clean blasted - uncorroded, and clean blasted - corroded. The corrosion process was carried out in a salt spray chamber for about one month. The fatigue tests were accompanied with DIC in order to capture the crack initiation locations and the crack development. Moreover, the specimens were investigated regarding changes in weld geometry based on 3D-surface scans of the whole specimen. Additionally, material hardness and residual stress measurements were carried out for all geometries and surface conditions.

### Conclusion

The 3D-surface scans showed, that material removal can occur in the area of the base metal and directly at the weld toe, indication pitting corrosion on the welds. The fatigue tests have shown that the as-welded specimens have the lowest fatigue strength, which is increased by clean blasting and subsequently decreased due to corrosion exposure. For both, butt and fillet welds, it could be shown that the geometrical parameters change due to clean blasting and corrosion. Clean blasting resulted in lower SCF, while corrosion increased the SCF to the previous level of the as-welded condition. As the fatigue strength was not the same for as-welded and corroded specimens, despite similar SCF, the

SCF cannot be considered as the sole fatigue-driving parameter. Residual stress measurements indicated that the as-welded specimen has the highest tensile residual stresses in the loading direction, whereas the clean blasted specimen displays compressive residual stresses. The removal of material due to corrosive exposure reduced the initially introduced compressive stresses on the surface, leading tensile residual stresses near the weld toe. Nonetheless, these residual tensile stresses are considerably lower compared to those found in the as-welded specimens, providing a clear relation to the different fatigue strengths from the tests.

The findings and the data obtained from the investigations can be integrated in the local fatigue approach (see paper V) and enable a more precise prediction of the service life.

### **Authors Contribution**

Most of the experiments as well as the paper conceptualization, methodology, validation, formal analysis, investigation, writing of the original draft and visualization were carried out by the first author. Moreover, the first author was responsible for funding acquisition and project administration. Tim Brömer performed the analysis and the documentation of the stress concentration factors as well as commented, reviewed, and edited the paper. Prof. Ghafoori, Dr. Woitzik, Dr. Braun commented, reviewed, and edited the paper. Markus Köhler performed the residual stress measurements and commented, reviewed, and edited the paper. Prof. Schaumann supervised the work and was responsible for the funding acquisition and project administration.

## Assessment of corrosion fatigue in welded joints using 3D surface scans, digital image correlation, hardness measurements, and residual stress analysis<sup>1</sup>

### 5.1 Abstract

Corrosion can significantly reduce fatigue resistance of steel constructions including offshore support structures. This can be attributed to either localized stress concentration caused by pitting corrosion or to embrittlement of the material during the corrosion process. In addition to the stress concentrations that can arise from pitting corrosion, offshore steel structures are characterized by a significant number of notches at weld seams, which may also cause stress concentrations. Therefore, it is of great importance to study the interaction between the pre-existing notches from welds and the notches from corrosion. Thus, reference material specimens as well as butt- and fillet-welded specimens from a mild steel S355 were investigated in this study. Before being stored in a salt spray chamber, the specimens were clean blasted as usually carried out for offshore support structures. After one month of exposure, the specimens were tested against fatigue and monitored by digital image correlation (DIC). The specimens were scanned with high-resolution 3D-scanners before and after corrosion exposure. In addition, material hardness and residual stresses were investigated to quantify the influence of corrosion on the material side and the influence from the welding process. It is shown that corrosion strongly influences the weld geometry. Both, individual pits and uniform corrosion are observed at the weld toe, which is relevant for fatigue. It was also shown that the fatigue strength of welded specimens depends not only on the geometry and its degradation by corrosion, but to a greater extent on the residual stresses present after corrosion. The residual compressive stresses applied by clean blasting were partly relieved by corrosion. The fatigue tests have shown increased fatigue strength after clean blasting and subsequent reduction due to corrosion. The fatigue strength of fillet welded specimen, for example, were increased from 74 N/mm<sup>2</sup> in its as-welded condition to 158 N/mm<sup>2</sup> through clean blasting. However, due to corrosion, fatigue strength decreases to 98 N/mm<sup>2</sup>.

**Keywords:** offshore-wind; digital scans; digital image correlation; corrosion fatigue; stress concentrations; welds; residual stress, hardness.

---

<sup>1</sup> [Shojai, S., Brömer, T., Ghafoori, E., Woitzik, C., Braun, M., Köhler, M., Schaumann, P., International Journal of Fatigue, 2022, 164, S. 107866. DOI: 10.1016/j.ijfatigue.2023.107866.](#)

## 5.2 Introduction

Although notable advancements have been made in recent years, the lifespan of corrosion protection systems for steel support structures of offshore wind turbines and platforms remains limited. These structures experience high dynamic loads from wind, waves, and operation. If the corrosion protection fails (e.g., damage during transportation, installation or operation), the steel becomes susceptible to corrosion. For structural components protected by coating, there exist situations where a new coating is not a viable option, either technically or financially. In these situations, it is necessary to perform a calculation of the remaining fatigue life under the conditions of free corrosion to ensure a continued operation of the offshore wind turbine.

Corrosion can occur in form of uniform as well as pitting corrosion. Especially pitting corrosion leads to high stress concentrations arising from changes in the surface geometry and can thus significantly reduce the fatigue strength of the support structures. Regardless of corrosion behaviour, offshore support structures have a large number of welded components where high stress concentrations are present by default. In the literature, the geometrical changes from pitting corrosion are investigated mainly on plane steel plates [1–4]. The influence of corrosion on weld geometry and the related change in stress concentration has not been explicitly investigated yet.

In case of welded structures, current research focuses mainly on the fatigue behaviour itself [5] or additionally on the change in roughness [6]. Normative, the influence of free corrosion can be considered with the stress-life (SN) curves of the DNV guideline [7]. These were derived from investigations of the Safety Executive UK [8], in which fatigue tests were carried out in artificial seawater and in air. Based on this, the Environment Reduction Factor (ERF) was introduced, which represents the ratio of load cycles without corrosion influence ( $N_{\text{air}}$ ) to load cycles under free corrosion ( $N_{\text{FC}}$ ):  $\text{ERF} = N_{\text{air}}/N_{\text{FC}}$ . For free corrosion, a constant design value of  $\text{ERF} = 3.0$  was defined, with which all existing SN curves from DNV were reduced. However, this is a rough estimate with scientific and mechanistic lacks, as the corrosion process and fatigue physics were convoluted in these tests. With this method, a consideration of notch stresses caused by local changes in the surface geometry, as a result of corrosive exposure, is not possible. Neither a differentiation is made between welded and non-welded, nor between moderately and strongly notched structural components. However, for an economic assessment of existing corrosion damage and calculation of the (residual) service life in the case of free corrosion exposure, a differentiated consideration is necessary. This can be done by local methods like the notch stress or notch strain approach.

Beside the influence of stress concentrations, corrosion has an influence on the material itself. As noted by Melchers et al. [9], the presence of acidic conditions beneath the rust layer can lead to the generation of hydrogen, which may permeate the surface of the steel. Corrosion, as explained by Revie and Uhlig [10], and Marcus [11], involves both an oxygen reaction and the evolution of hydrogen, which is subsequently released. This leads to a strong increase in crack propagation, which has already been reported in several studies [12–14].

Furthermore, especially in case of offshore support structures, where the components are clean blasted in preparation for the application of corrosion coatings, the influence of clean blasting must be taken into account as well. Investigations by Gericke et al. [15] have shown increased fatigue strengths after

clean blasting by inducing compressive residual stresses at surfaces. Both, with regard to the utilization of this positive effect and in view of calculating the (residual) lifetime of existing support structures with local fatigue approaches, it is important to quantify the individual fatigue driving factors in order to include them in the calculations. Thus, in this study, not only fatigue tests were carried out on different specimen geometries and surface conditions, but also investigations regarding changes in weld geometry, material hardness and residual stresses were carried out.

The novelties of this study can be summarized as follows:

- Investigation of weld geometry and stress concentration changes based on digital scans
- Fatigue tests accompanied by digital image correlation (DIC) to investigate crack initiation and crack propagation lifetime
- Change in hardness and residual stress near the surface due to corrosion

These novelties allow a more accurate fatigue life prediction of steel constructions by incorporating the results into local fatigue approaches.

## 5.3 Experiments

### 5.3.1 Specimens geometry and surface preparation

In the framework of this study, both base material specimens (G) and welded specimens made of low-alloy structural steel S355 ML were investigated. For the welded specimens, double V-shaped butt welds (S) and fillet welds (K) were examined. Specimens with fillet welds included non-load carrying transverse stiffeners, which were welded on a continuous plate with a throat thickness of 4 mm. Fillet welds were produced using the gas metal arc welding (GMAW) process and the butt welds using the submerged arc welding (SAW) process. In both cases, the limits for irregularities are in line with the evaluation group B according to ISO 5817 [16].

After welding, the specimens were cut in 70mm stripes from a metal sheet of 1000 mm length and 300 mm width by water jet. Then, the specimens were clean blasted according to the requirements of DNV RP-0416 [17] for real offshore support structures, in order to clean and roughen the surface for the subsequent application of the corrosion protection. Grit was used as the blasting medium. The cleanliness grades according ISO 8501-1 [18] and the roughness are documented. For the investigated specimens, cleanliness grades of Sa 2 ½ to 3 according to ISO 8501-1 were achieved (see Figure 5-2 (a)). The achieved roughness values are documented in section 5.4.1. In Table 5-1 the test matrix with the number of specimens for each test-series for the three different geometries (G, S and K) and the different surface conditions (00, 0 and 1) are illustrated. The number 00 refers to the as-welded condition, 0 refers to clean blasted and uncorroded condition, while 1 refers to one-month corrosion exposure after clean blasting.

After surface preparation, corrosion protection was applied in the clamping area of the specimen, in order to ensure an even surface and a uniform loading of the specimen, which can reduce secondary bending moments during the fatigue test. In the area of the welds, no corrosion protection was applied. After the corrosion process, the specimens were cut into the typical shape shown in Figure , in order

to get clean edges. Moreover, the edges were chamfered to avoid crack initiation from the side. In Figure 5-2 (a), the blasted specimen with the applied corrosion protection is illustrated.

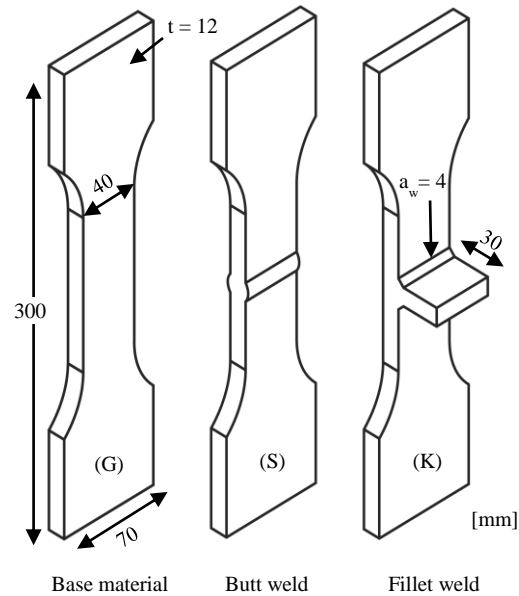


**Figure 5-1: Specimen geometries for base material (G), butt weld (S), and fillet weld (K)**

**Table 5-1: Test matrix including different surface conditions and weld types**

Specimen geometry:	Base material (series)	Butt weld (series)	Fillet welds (series)
Surface condition:			
As-welded	-	7 (00-S)	10 (00-K)
Clean blasted - uncorroded	12 (0-G)	12 (0-S)	12 (0-K)
Clean blasted – corroded (for 1 month according ISO 9227:2017)	12 (1-G)	12 (1-S)	12 (1-K)

Due to the fabrication of the specimens, angular and linear misalignments occurred. According to ISO 6520 [19], angular misalignment describes the deviation between welded steel surfaces whose surfaces are not parallel or at a specified angle to each other. Linear misalignment describes the distance between the parallel surfaces of welded steel plates. The equations are given in appendix A. The value for both were evaluated based on the 3D-scans described in section 5.3.4 and are presented in Appendix A, Table 3-5.

### 5.3.2 Accelerated corrosion experiment

Corrosion experiment: After preparation, the specimens were subjected to the standardized neutral salt spray (NSS) test with a 5% sodium-chloride solution according to ISO 9227 [20]. The NSS test



is mainly used in corrosion protection testing to evaluate the resistance of corrosion protection. In this study, the NSS test is used for accelerated corrosion development. Therefore, the steel specimens were placed at an angle between  $15^\circ$  and  $20^\circ$  from the vertical so that the surfaces were fully exposed to the salt spray. In addition, it was ensured that the steel specimens did not touch the chamber walls. For the preparation of the spray medium, sodium-chloride was dissolved in distilled and deionized water. In the salt spray chamber, the spray medium is sprayed to the chamber roof for a uniform distribution on the steel specimens. The pH value of the spray medium was between 6.5 and 7.2 at  $(25 \pm 2)^\circ\text{C}$  and was continuously checked and adjusted if necessary. At least 12 specimens for each geometry (see Table 5-1)) were exposed to free corrosion in the salt spray chamber with a duration of one month. In Figure 5-2 (b), a specimen after the NSS test is shown.

**Rust removal:** The rust on the specimens were removed according ISO 8407-1 [21] in a hydrochloric acid bath, which is prepared in the ratio of 1000 ml hydrochloric acid (HCl), 20 g antimony trioxide ( $\text{Sb}_2\text{O}_3$ ) and 50 g tin(II)chloride ( $\text{SnCl}_2$ ). Before storing the specimens in the hydrochloric acid bath, the specimens were mechanically cleaned with a wire brush until large and loose pieces of the corrosion products were removed. The storage time in the hydrochloric acid bath was between 5-20 minutes. In Figure 5-2 (c), the specimen after rust removal is shown.

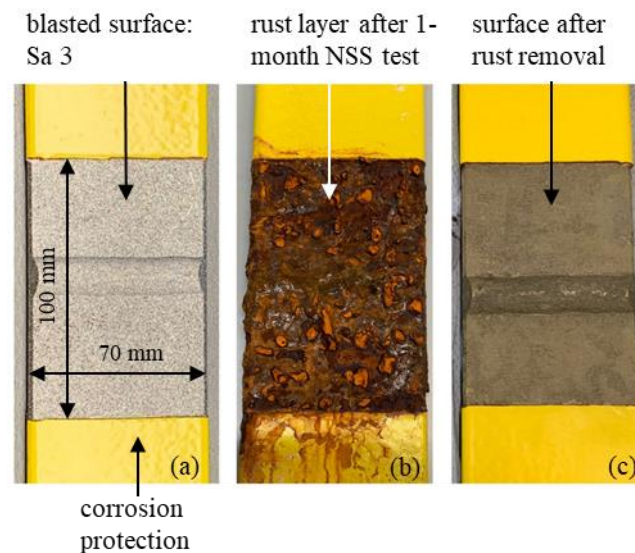


**Figure 5-2: Surface conditions of the specimen, (a) blasted surface with cleanliness grade Sa 3, (b) specimen after 1 month of NSS test, (c) specimen after rust removal**

### 5.3.3 Surface characterization measurements

In order to evaluate the influence of corrosion, surface measurements were conducted before and after the NSS test. The measurements were carried out with non-contact 3D-optical profilometer, Keyence VR-3000, which allows scanning of larger areas (in this case  $70 \times 30$  mm) with high-resolution ( $20 \mu\text{m}$ ). The scanned surface can be described by different surface components according to ISO 21920-2 [22]: roughness and waviness.

The primary profiles can be extracted from the scanned surface. The primary profile consists of different wavelength components, which can be detected by Fourier transformation. The removal of short wavelength components from the primary profile leads to the waviness profile, which also represents the centreline for the roughness profile. The removal of long wave components leads to the roughness profile. For the evaluation of the primary profiles, it is therefore important to define the short and long wave components. This is possible with a cut-off wavelength  $\lambda_c$ . Generally, a cut-off wavelength of  $\lambda_c = l_e/5$  according ISO 21920-3 [23] is recommended, where  $l_e$  corresponds to the measurement length. However, the cut-off wavelength can also be chosen depending on the surface geometry to be investigated. In this work, the cut-off wavelength is set to  $\lambda_c = 2$  mm, since the widths for pitting corrosion are in this range. Thus, a possibly existing surface change due to pitting corrosion can be visualized in the roughness profile. For the removal of wave components, a Gaussian filter is utilized. Both profile components can be described with different parameters, such as  $R_a$ ,  $R_z$ , and  $W_a$ ,  $W_z$ , according ISO 21920-2 [22], with  $R$  referring to roughness and  $W$  to waviness.

$$\text{Maximum roughness and waviness:} \quad R_z, W_z = Z_{max}(x) + Z_{min}(x) \quad (5-1)$$

$$\text{Mean arithmetic height:} \quad R_a, W_a = \frac{1}{l_e} \int_0^{l_e} |Z(x)| dx \quad (5-2)$$

#### 5.3.4 3D-scans of specimens

The 3D-scans were carried out with the optical 3D-scanner ATOS Core 5M from GOM with a resolution of 0.12 mm. In Figure 5-3 (a) the setup for the scan is shown. The 3D-scanner is positioned in a distance of 500 mm from the specimen. The specimen is placed on a rotatable plate in order to take images from different perspectives. The GOM Suite software is capable to automatically merge the taken scan images, if there are enough reference points in each scan. Therefore, several reference points are attached on the rotatable plate. In most cases, 4 scans were enough to scan each side of the specimen. In order to merge both sides of the specimen into one model, additional reference points were placed on the sides of the specimens. With 8 reference points it is possible to scan the whole specimen, as illustrated in Figure 5-3 (b) and (c). All specimens from Table 5-1 were scanned in this way, whereas specimen with corrosion were scanned twice, before and after corrosion. The result of the scan is a STL-file, which is a closed surface generated from a point cloud via triangulation. The STL-file is used for measurement of linear and angular misalignment and for digital surface comparison.

The digital surface comparison is carried out in the GOM Suite software only for the corroded specimen. Therefore, both specimens are inserted in one project and prepositioned over each other manually. After pre-positioning, the scans are overlaid with the best-fit command based on the least square approximation. To achieve high accuracy with the best-fit command, it is necessary that the specimens before and after corrosion have as many surface elements in common as possible. This is ensured with the area of the corrosion protection, which remains the same after corrosion exposure.

Hence, the scans for the specimens were performed with corrosion protection, see Figure 5-3 (b) and (c).

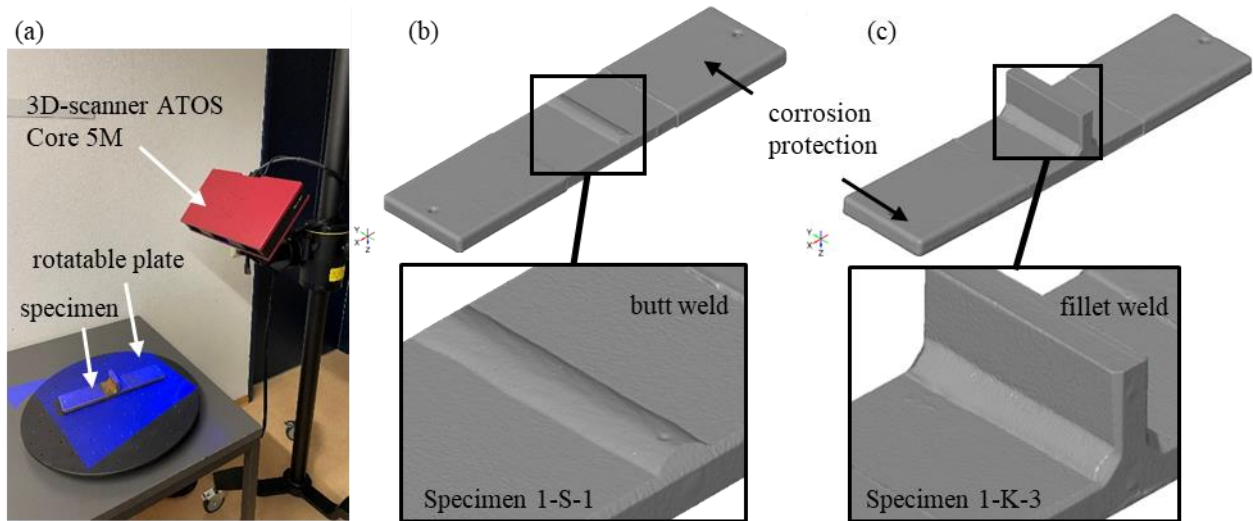


**Figure 5-3: 3D-surface scans with ATOS Core 5M: (a) test setup, (b) scan of butt-welded specimen and (c) scan of fillet-welded specimen.**

### 5.3.5 Geometrical weld parameters

The weld geometry has an important role in the fatigue analysis, as it is linked to the stress concentration, which is a driving parameter in fatigue strength. The weld geometry of each specimen can be described with the weld toe radius  $r$  and flank angle  $\theta$  according to ISO 5817 [16] (see Figure 5-4 (a)). Based on the geometrical parameters, the elastic stress concentration factor (notch factor  $\alpha_k$ ) can be determined with different analytical formula for welded components that have been summarized in Radaj et al. [24], as for example equation (5-3) proposed by Anthes et al. [25]:

$$\alpha_k = 1 + 0.728(\sin(180^\circ - \theta))^{0.932} \left(\frac{t}{r}\right)^{0.382} \quad (5-3)$$

where the notch factor  $\alpha_k$  depends on the weld toe radius  $r$ , the flank angle  $\theta$  and the component thickness  $t$ . It increases with greater flank angles, greater notch radius and smaller thicknesses. In order to quantify the influence of corrosion on fatigue, it is therefore important to analyse the geometrical parameters and the change due to corrosion. First methods for fully digital evaluation of real geometry parameters of welded components have been developed and applied by Renken et al. [26] and Schubnell et al. [27]. In this study, the geometrical parameters are analysed with a MATLAB tool that was developed specifically for this application. The basis for that are the high-resolution scans from Keyence 3000 VR, which are evaluated in the form of point clouds in ASCII format. The surface is evaluated in longitudinal direction over all recorded points, which results in a series of longitudinal cross sections. For each cross section, the derivatives of the height coordinates are calculated in the first step. With those derivatives the point of the maximum slope in the weld seam (point A) as well as the notch toe (point B) can be derived. These points are needed to calculate the

balance lines of the surface - one line for the steel surface and one line for the weld seam (see Figure 5-4 (b)). Thus, the flank angle is the angle between the balance lines. The intersection of these two lines serves as the starting point for the approximation of a circle, which fits best into the real data of the notch radius based on the minimum sum of squared deviations. For the fillet-welded specimens, the geometrical parameters of two welds were evaluated (left and right), while for butt-welded specimen the weld is evaluated on four locations (2 x upper and 2 x lower location). The geometrical parameters were analysed for all surface conditions.

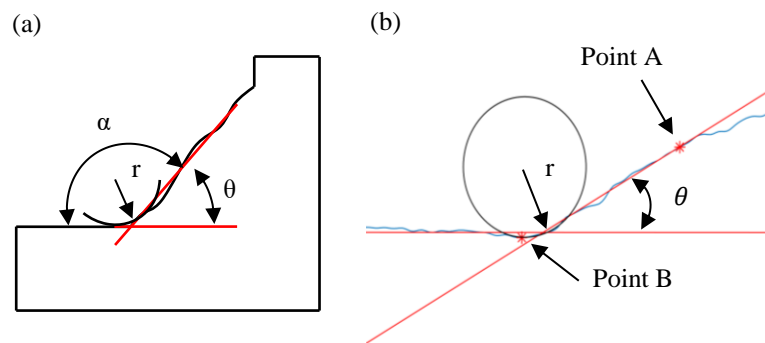


**Figure 5-4: (a) Geometrical weld parameters according ISO 5817 [16] and (b) Implementation in the MATLAB tool**

### 5.3.6 Hardness and residual stress measurements

In addition to the 3D scans, which can only record changes in the topography, hardness and residual stress measurements were carried out. This allows the influence on the material side to be measured in more detail. Both measurements were performed for one specimen of each surface condition and only for the fillet-welded joint.

**Hardness measurement:** The hardness measurements were carried out on cross-sections of the respective welded joints using a QNess Q10A+ measuring device. The measuring device enables automated hardness mapping of a given surface, as both the indenter and the microscope for measuring the impression are integrated in the measuring device. The Vickers hardness was measured according to ISO 6507-1 [28], taking into account all specifications for sample preparation and test procedure. Given that both the influence of clean blasting and the influence of corrosion are greatest near the specimen surface, the hardness measurement was performed with a testing load of approximately 1.0 N according to HV 0.1. On average, indentation diagonals of  $d = 30 \mu\text{m}$  were achieved. According to the standard, the required edge distance is given in relation to the impression diagonal with  $2.5 \cdot d$  for steel. With HV 0.1, the hardness could be determined up to a distance of  $75 \mu\text{m}$  from the surface. The distance between the indentations was set at  $100 \mu\text{m}$ .

**Residual stress measurements:** The residual stress was measured on the surface of the specimens using X-ray diffraction (XRD) according to the  $\sin^2\psi$  technique with copper radiation. The diffraction patterns were obtained at 11 angles between  $\Psi = 159^\circ$  and  $161^\circ$  using a collimator diameter of 2 mm.

The setup results in a measurement spot of approximately 2.0 - 2.5 mm in diameter, depending on the angle settings. Thereby, the diffraction information is averaged over the measurement spot. The depth of the diffraction information is approx. 5  $\mu\text{m}$ . The measurements were conducted along a measuring path perpendicular to the weld seam, starting at the weld toe. In order to represent the expected stress gradients with sufficient accuracy, the distances of the individual measuring points were chosen smaller than the spot diameter. For each measurement, stress components in longitudinal and transverse direction with regard to the weld path were determined, i.e., transverse stress components are in test loading direction of the specimen.

### 5.3.7 Fatigue tests

Fatigue tests were carried out on a servo-hydraulic fatigue testing machine MFL HUS 60 with a frequency between 8-10 Hz and a mean stress ratio of  $R = 0.1$ . The specimens were clamped on both sides, which introduced additional mean stresses due to misalignments of the specimens, resulting in a higher effective R-ratio. Before clamping, the corrosion protection on the clamping area was removed in order to avoid slippage of the specimens. The fatigue tests were monitored with DIC in order to capture the crack initiation location and the corresponding fatigue life  $N_C$ . In Figure 5-5 (a), the fatigue test setup with the DIC-system GOM ARAMIS 12M (lens with 75 mm focal length) is shown for the butt-welded specimens.

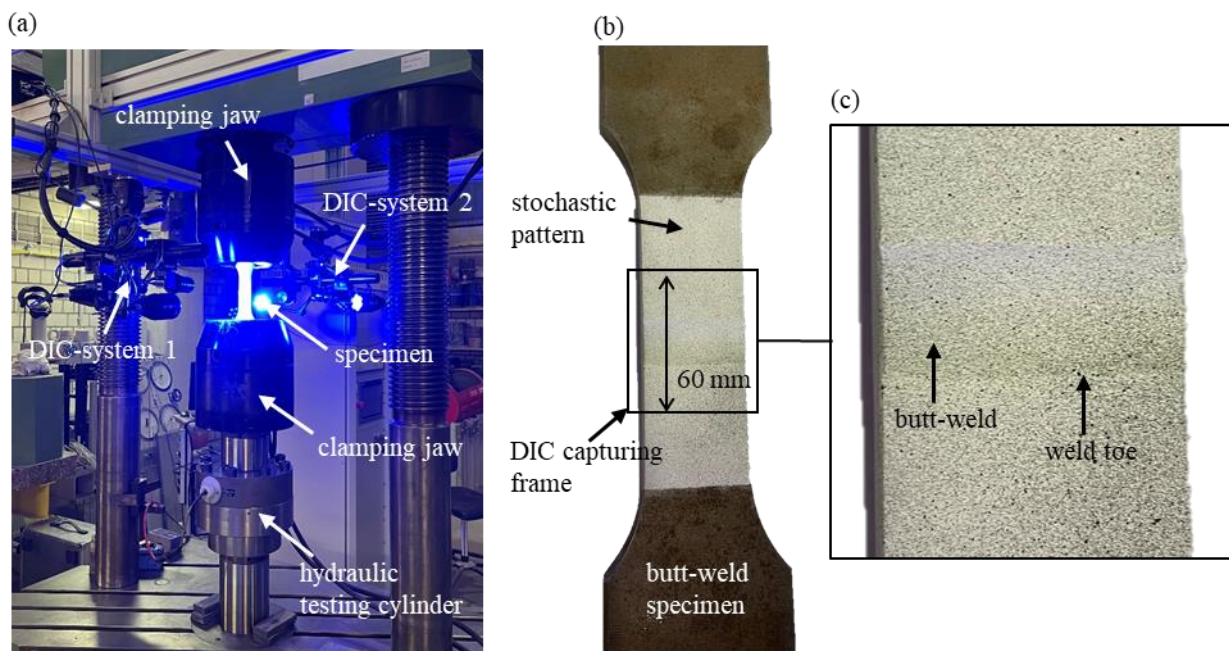


**Figure 5-5: Fatigue test setup, (a) test setup for butt-welded specimen, (b) butt-welded specimen with stochastic pattern, (c) DIC capturing frame**

The DIC-system was positioned on both sides, since the crack initiation could occur on any side of the butt-welded specimens. For fillet-welded specimens, both DIC-systems were positioned on one side, above each other, in order to capture both fillet welds. Each DIC-system consists of two cameras, which enables 3D-strain measurements. The measuring distance was 425 mm with a corresponding



measuring volume of 80x60 mm, see plot (b) and (c). For every specimen, a stochastic black and white pattern was applied on the relevant surface (plot (c)). The stochastic pattern is important for the DIC-software to correlate the images with high accuracy. During the fatigue tests, an image was taken every 500 to 2000 load cycle, depending on the expected fatigue life. The trigger for the image shot was set on approximately 85% of the load peak [29] due to the delay between the trigger signal and actual image shot.

### 5.3.8 Crack detection with digital image correlation

For the crack detection, a MATLAB-tool was developed based on the crack definition of Radaj in [24] and Radaj and Vormwald [30], where the technical crack is defined as a crack between 0.5-2 mm length and 0.5 mm depth. The implemented methodology in the MATLAB-tool is based on Hutt and Cawley [31] and Schürmann [32], where the location of the crack is defined by a gap in the axial displacement plot.

In Figure 5-6, the definition of the technical crack is presented. In Figure 5-6 (a), the high-resolution image taken during the fatigue test of a fillet-welded specimen is shown, while in Figure 5-6 (b) and (c) the corresponding strain is presented. For the evaluation of the strain, the captured images are compared with a reference image. The reference image should be chosen as the one in which any possible hardening or softening of the material has already been completed. By comparing the strains at several points on the surface, in most cases material softening could be observed. However, the softening process was completed after approximately 1,000 to 6,000 load cycles. For each specimen, the reference image has been determined in this way. As a result, the displacements used for crack detection are not superimposed by other displacement components, ensuring an increased accuracy. In Figure 5-6 (c), the strain plot at the crack initiation location and in Figure 5-6 (d) the displacement and corresponding gradient along the intersection line Y are shown. At the crack initiation location, the displacement curve has a significant jump of about 0.002 mm and, leading to a significant peak in corresponding gradient curve (strain curve). Along the whole specimen, intersection lines are defined analogous to plot (c) at a distance of 0.1 mm and checked for a jump in the displacement according to plot (d). Only if the jump can be found at a total of 20 consecutive intersection lines, the technical crack of 2 mm is reached. This also avoids finding non-existent cracks due to signal noise. In Figure 5-6 (e1), the location of the greatest jump along the intersection lines are shown over width (X-axis). Between  $X = 2.8$  to  $X = 4.9$ , the crack is about 2.1 mm and has reached the technical crack size. Additionally, in Figure 5-6 (e2) the crack is illustrated in a propagated state. The crack has grown along the width in both directions, while the crack pattern between  $X = 2.8$  and  $X = 4.9$  remained the same. This confirms the stability of the proposed procedure for crack detection.

A different criterion for crack detection is proposed by Friedrich and Ehlers [33]. Here, the technical crack is reached, when a strain of 1% over a length of 2 mm is detected. In Figure 5-6 (c) of, the resulting strain at the technical crack is about 0.4 to 0.5% and is less than proposed by Friedrich and Ehlers [33]. A stricter criterion is given by Qvale et. al. [34], where a macroscopic crack at an inter-node displacement of 0.002 mm is defined as crack initiation. This would lead to lower fatigue life in the crack propagation state for the specimens in this study. Both criteria would lead to different

results than obtained in this study. However, the purpose of comparing different specimen geometries and surface conditions is not affected by the choice of the technical crack criterion.

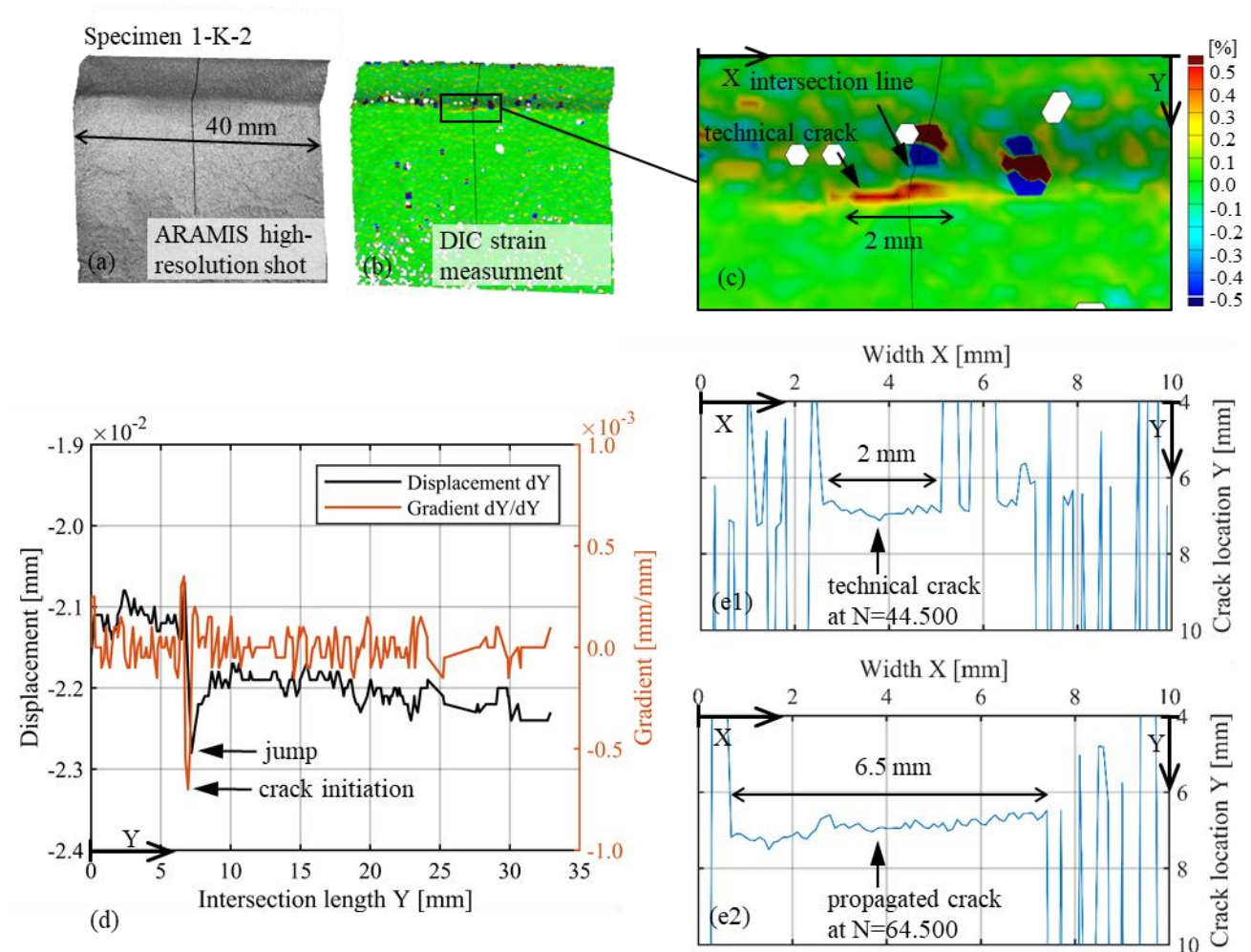


**Figure 5-6: Technical crack definition in DIC: (a) high-resolution shot during fatigue testing of fillet-welded specimen with ARAMIS, (b) and (c) corresponding DIC strain plot, (d) displacement in axial direction, (e1) illustration of crack detection at technical crack stage, (e2) illustration of crack detection at propagated stage**

## 5.4 Experimental results and discussion

### 5.4.1 Surface measurement results

The surface characterization measurements were performed on butt-welded specimens, which were scanned in the as-welded condition, as well as after clean blasting and after one month of corrosive exposure in the NSS chamber. Figure 5-7 (a1) to (c1) presents the corresponding 3D-optical profilometer scans for the same specimen in different conditions. To evaluate the surface change, a profile parallel to the weld was considered, which is shown in Figure 5-7 (a2) to (c2) for the corresponding surface conditions. The waviness profile between as-welded and the uncorroded blasted specimen differ only slightly ( $W_z = 198 \mu\text{m}$  and  $W_z = 180 \mu\text{m}$ ) while the roughness increases ( $R_z = 16 \mu\text{m}$  and

$R_z = 49 \mu\text{m}$ ). Comparing the uncorroded and corroded sample, it appears that the roughness profile remains almost unchanged ( $R_z = 49 \mu\text{m}$  and  $R_z = 50 \mu\text{m}$ ), while the waviness profile changes more.

In addition to the direct comparison of the surfaces, further measurements were carried out parallel to the weld seam. The resulting average values for roughness and waviness are shown in Table 5-2. The increase in roughness due to blasting and the unchanged roughness after corrosion are confirmed. For the waviness, however, the highest values are obtained for the as-welded specimen. These are due to the rolling process during manufacture, which can be confirmed by the long wavelengths. In comparison, the corroded samples have a higher number of small wavelengths, as can be seen in Figure 5-7 (c2).

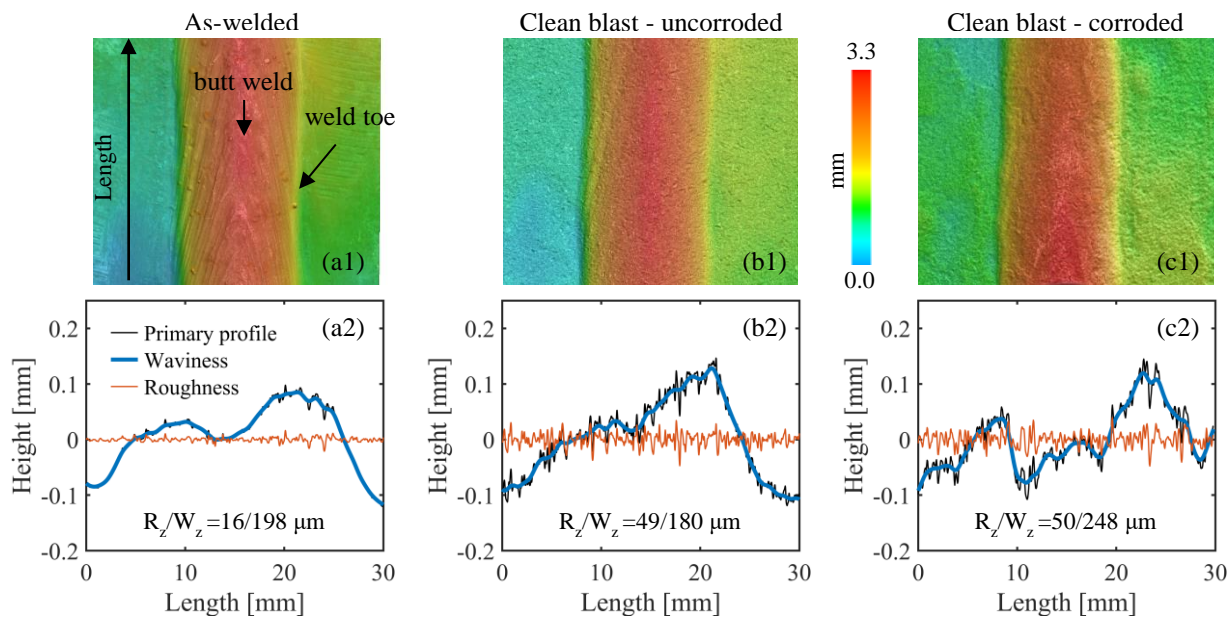


**Figure 5-7: Surface measurement results for (a) as-welded specimen, (b) clean blasted – uncorroded specimen and (c) clean blasted – corroded specimen**

**Table 5-2: Mean values for surface measurements**

Surface condition:	Roughness		Waviness	
	Ra [ $\mu\text{m}$ ]	Rz [ $\mu\text{m}$ ]	Wa [ $\mu\text{m}$ ]	Wz [ $\mu\text{m}$ ]
as-welded	4	20	36	171
Clean blasted - uncorroded	9	52	27	131
Clean blasted - corroded	11	54	31	148

#### 5.4.2 Digital surface comparison

The results of the surface scan are presented in Figure 5-8 and Figure 5-9. In subplots (a1) and (a2), the clean-blasted uncorroded specimen and in (b1) and (b2) the scan after one-month corrosion exposure are illustrated. It should be noted, that the specimen shown in (b1) is slimmer than in (a1), as the specimen has already been cut to the fatigue test geometry according Figure . It appears that the



surface topography has changed compared to the plots in (a). Both, the base material as well as the welds are affected from corrosion. This is underlined, when both surfaces are compared to each other in the deviation plot (c1), (c2) and (d). Especially for the butt welds in Figure 5-9 plot (c2), high differences appear in the weld toe, which is the fatigue driving area. Also for the fillet-weld, comparatively high differences can be observed at the weld toe (Figure 8 c2). The lower material removal at the weld toe in the fillet-weld compared to the butt-weld is related to the scatter within the corrosion process and cannot be observed systematically for other specimens. Based on the assumption, that high differences on a small area can be considered as pitting corrosion, while low differences on a greater area are considered as uniform corrosion, in Figure 5-9 plot (c2), pitting corrosion with a maximum pitting depth of 0.405 mm on the weld seam can be observed. However, most of the specimen surface is uniformly corroded, which is in line with the findings from the surface measurements in section 5.4.1. In addition, positive values can be observed in plot (d), which indicates an increase of the surface plane, resulting from undermining of corrosion protection. In the area of corrosion protection, the surface has no difference, see green area in plot (d).

It should be noted that due to the comparatively low resolution of 0.12 mm of the ATOS Core system, only values at a distance of 0.12 mm could be measured. In case of significant height gradients within the distance of 0.12 mm, the results could be corrupted. With regard to the intention of this investigation to make mainly qualitative statements, this resolution is sufficient.

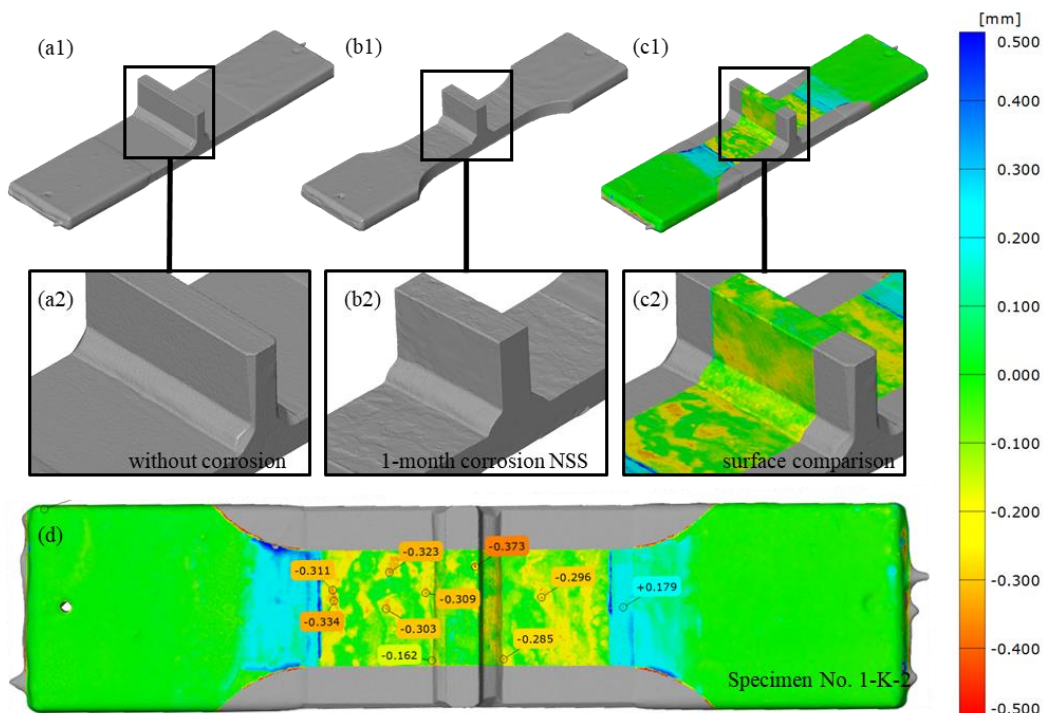


**Figure 5-8: Results of surface scans for fillet welds, (a) scan without corrosion, (b) scan after one-month corrosion, (c) deviation plot of the surface scans, (d) deviation plot with deviation banners**

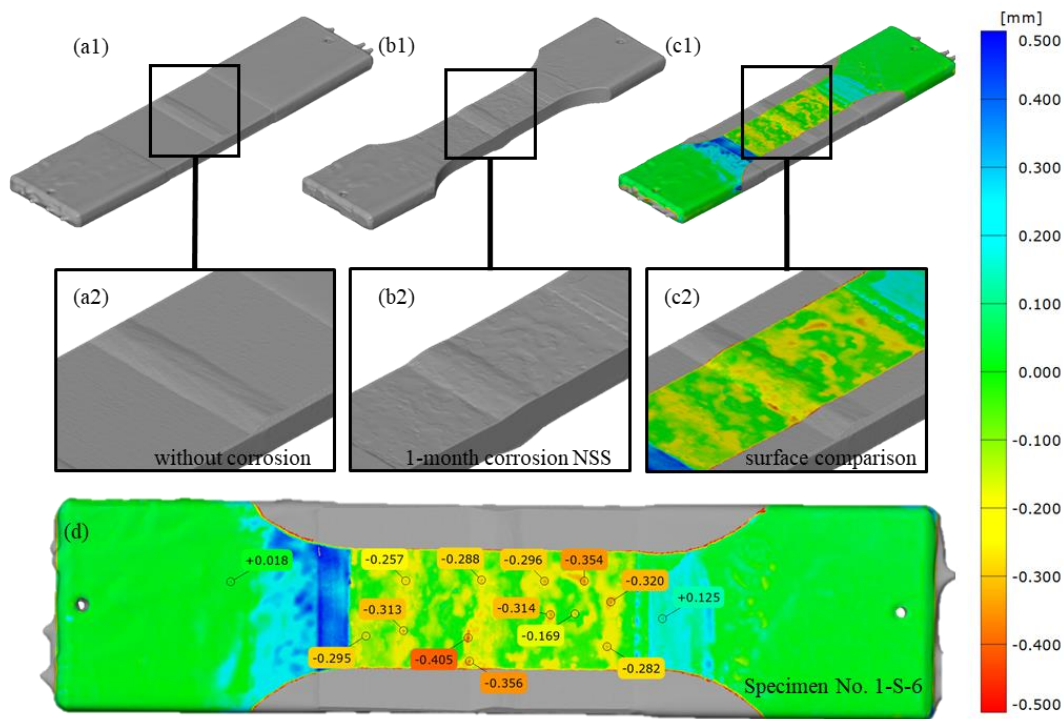


**Figure 5-9: Results of surface scans for butt welds, (a) scan without corrosion, (b) scan after one-month corrosion, (c) deviation plot of the surface scans, (d) deviation plot with deviation banners**

### 5.4.3 Results of geometrical parameter evaluations

In order to evaluate the geometrical parameters of weld toe radius  $r$  and flank angle  $\theta$ , the self-developed MATLAB tool was utilized. A total of four representative specimens with two different weld geometries, butt welds and fillet welds, were investigated, each specimen in two different conditions: as-welded / clean blasted – uncorroded; clean blasted uncorroded / clean blasted - corroded. The geometrical parameters and the resulting SCF for the different conditions are compared on the same specimen and summarized in Appendix A, Table 5-4. Here, in addition to the mean value and the standard deviations, the associated 5% and 95% quantile values were evaluated as well.

The results for the weld toe radii are illustrated in Figure 5-10 (a). In the first and second frequency plot (butt weld 1 and fillet weld 1), the weld toe radii are plotted in the as-welded and clean blasted - uncorroded condition. Generally, the radii of the specimens with butt welds are greater than those of the fillet-welded specimens. Comparing the mean values of the as-welded and the clean blasted – uncorroded condition reveals greater values for the clean blasted – uncorroded condition than in the as-welded condition for both specimen geometries. The mean radius for the butt-welded specimen in the as-welded condition is 1.19 mm and increases due to clean blasting to 1.55 mm, while for the fillet-welded specimen the mean radius is 0.92 mm and increases slightly to 0.96 mm. Regarding the scatter of the radii, no general statement can be made, as it increases for butt welds and decreases for fillet welds after clean blasting. The frequency plots for butt weld 2 and fillet weld 2 illustrate the radii for clean blasted – uncorroded in comparison to the clean blasted - corroded condition. For the

butt weld, the mean radius is reduced only marginally from 1.62 mm to 1.57 mm, while there is no reduction for the fillet weld.

The weld toe radii are related to the flank angles of the weld; these are compared in the same way as the radii. Great radii of the weld notch lead to a small flank angles and vice versa (see Figure 5-4). Accordingly, the frequency plot, see Figure 5-10 (b), for butt weld 1 shows a decrease of the flank angle from 23.2° to 19.4° after clean blasting, while for fillet weld 1 no changes can be observed. Comparing the specimens in uncorroded and corroded condition, an increase of the flank angle from 20.7° to 27.1° and from 42.4° to 48.6° can be seen for butt weld 2 and fillet weld 2, respectively. The scatter is not subjected to any significant change in all examined cases.

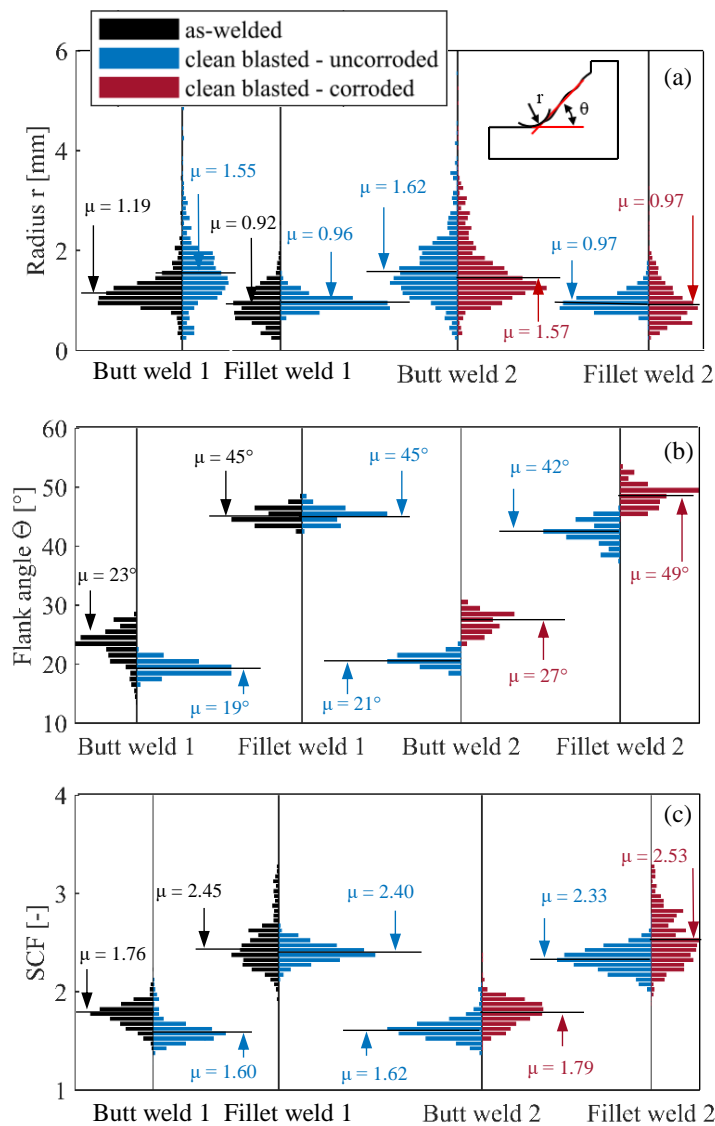


**Figure 5-10: Frequency plots for (a) radius, (b) the flank angle, and (c) the SCF for different specimen geometry and surface conditions**

Moreover, in Figure 5-10 (c) the resulting stress concentration factors (SCF) based on equation (5-3) are shown for the examined specimens. For butt welds, the mean stress concentrations decrease from 1.76 to 1.60 significantly after clean blasting (see butt weld 1), but increase after corrosion exposure

to the level of the as-welded condition. This is obviously mainly driven by the change in the flank angle. This is true for the mean SCF as well as the 5% and the 95%-quantile values. For the fillet weld the mean SCF decreases from 2.47 to 2.40 only slightly after clean blasting, but differs greatly for the 95%-quantile value than in the as-welded condition, resulting from a smaller scatter band (see fillet weld 1). After corrosion exposure (fillet weld 2), the mean SCF changes from 2.33 to 2.53. Additionally, the scatter increases and leads to a significant change in the 95%-quantile values from 2.52 to 2.97.

Overall, the evaluation of the geometry parameters showed that both, the weld toe radius and the flank angle of the weld, can change when steel is clean blasted or under the influence of corrosion. The comparison for different surface conditions shown in Figure 5-10 revealed greater radii accompanied with smaller flank angles due to the clean blasting process, while due to the corrosion process smaller radii accompanied with greater flank angles were detected. This led to a reduction of the SCF after clean blasting and to an increase after corrosion exposure.

#### 5.4.4 Hardness measurements

For the hardness mapping, approximately 400 individual measurements were carried out per specimen. A minimum length of 1 mm in thickness direction was measured along the weld toe. The results of the hardness measurements for all surface conditions are shown in Figure 5-11. Subplots (c1) to (c3) show macro images of the cross sections. In subplot (b1) to (b3) and (d1) to (d3), macro images of the weld toe with the impressions resulting from the hardness measurement are shown. The different zones such as weld material, heat affected zone (HAZ) and base material are clearly visible. The higher roughness of the blasted specimens is visible for both the uncorroded (b2, d2) and corroded (b3, d3) states. In subplots (a1) to (a3) and (e1) to (e3), the hardness values for all specimens are shown for the left and the right sight of the specimens, respectively. The as-welded specimen has the lowest hardness across all zones. Especially around the weld toe (framed area), where the fatigue fracture originated in almost all tests, the mean hardness for both (left and right) measurements are with HV 225 lower than the blasted specimen, with HV 240 for the uncorroded and HV 250 for the corroded condition. Usually, higher hardness values from blasting are only visible at a distance of up to 100  $\mu\text{m}$  from the surface. Here (a1 and e2), the higher hardness values are present to a depth of at least 1 mm. Hence, the higher hardness values compared to the as-welded specimens cannot be entirely attributed to the clean blasting and is rather attributed to the welding process. However, the highest values throughout all zones can be observed for the corroded specimen. This could on the one hand be attributed to the scattering in the welding process and on the other hand to hydrogen embrittlement resulting from the corrosion process [10,11]. There are partly contradictory reports on the influence of hydrogen on material hardness, where both hardening [35] and softening [36] of the material could be observed. In [37], these opposing behaviours are attributed to the absorbed amount of hydrogen during charging and the hydrogen concentration gradient. Since no experiments were carried out on the presence of hydrogen, no clear statement can be made about the origin of the higher hardness. Irrespective of this, the hardness values after corrosion in the relevant weld toe area indicate only little difference. Therefore, only a minor role is attributed to the hardness.

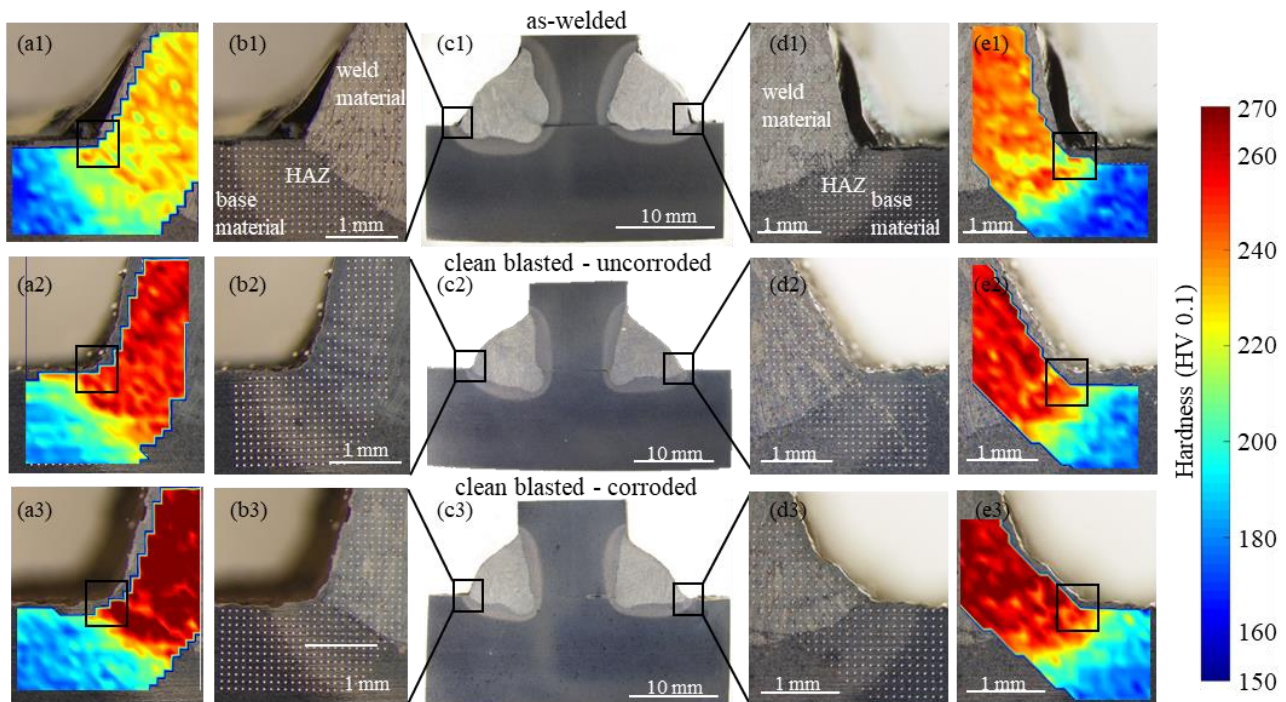


**Figure 5-11: Macrographs and hardness values HV 0.1 for different surface conditions, (a1) to (c1) for as-welded specimen, (a2) to (c2) for clean blasted – uncorroded specimen, (a3) to (c3) for clean blasted – corroded specimen**

#### 5.4.5 Residual stress results

The residual stress measurement results are shown in Figure 5-12 (a) for the transversal stresses and in Figure 5-12 (b) for the longitudinal stresses as a function of distance  $X$  from the weld toe. The first measurement at  $X = 0$  mm was performed directly on the weld toe. The transverse residual stresses are decisive for the assessment of the fatigue strength, as they correspond to the load direction from the fatigue test. According Figure 5-12 (a), for all three surface conditions, the highest transversal residual stress is located directly at the weld toe and decreases with increasing distance. The highest tensile residual stress at the weld toe is found in the as-welded specimen. In the clean blasted - uncorroded specimen, the residual stress is below zero and thus in the compression range. As the distance to the weld toe increases, the residual stress decreases and, from approximately  $X = 3$  mm, it resembles that of the as-welded specimen. The clean blasted - corroded specimen shows a low magnitude of tensile residual stresses at the weld toe, which are, however, lower than those of the as-welded specimen. The progression at higher distances from the weld toe is similar to that of the other specimens, with slightly higher compressive residual stresses. Based on the values directly at the weld toe, it can be concluded that clean blasting introduces considerable compressive residual stresses through plastic deformation of the surface. This causes the residual stresses to fall from the tensile to the compressive region. The corrosion process removes the near-surface material layer introduced with compressive residual stresses. In the new and initially deeper material layer, the influence of the



blasting is smaller, but still present. As a result, tensile residual stresses are present after the corrosion process, which are lower than in the as-welded condition.

It should be noted that rust removal of the specimens with a wire brush can partially influence the results of X-ray diffraction. Due to the fact, that the brush could not reach the weld toe and that the results are only of qualitative character, the effect from rust removal is considered to be negligible.

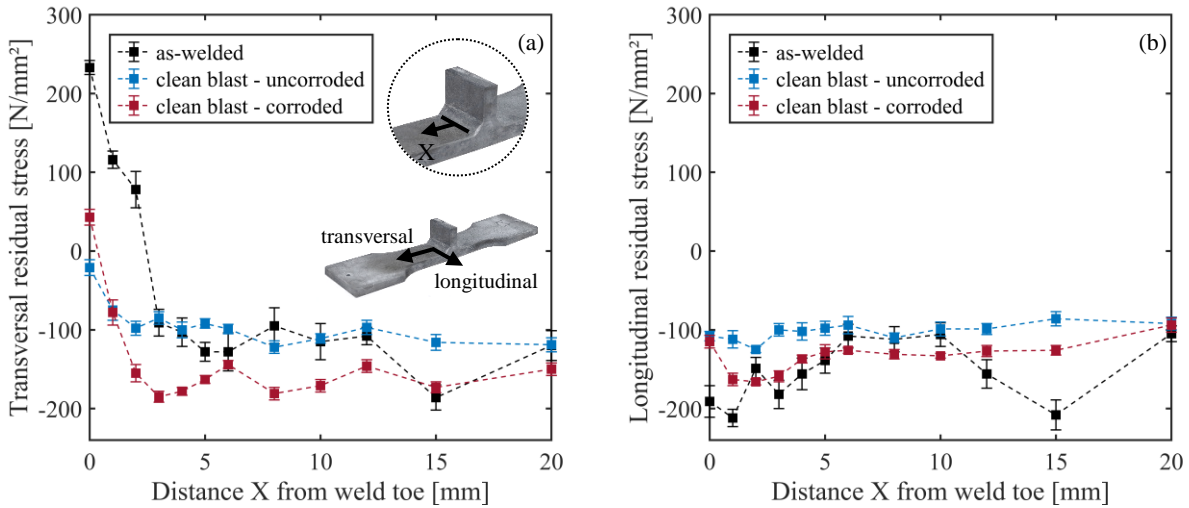


**Figure 5-12: Residual stress measurement with results for (a) transversal stresses and (b) for longitudinal stresses**

#### 5.4.6 Fatigue tests results

The results of the fatigue tests and the corresponding load values, load ratios, cross-section areas, stress ranges as well as the values for angular and linear misalignment are shown Appendix A, Table 3-5. The cross-section area corresponds to the original cross-section and does not consider the reduction due to corrosion. The results are statistically evaluated to obtain the SN-curve for the high cycle fatigue (HCF) region, which is defined between  $N = 10^4$  cycles and  $N = 7 \times 10^6$  cycles in Eurocode 3 [38], DNV [7], and IIW [39]. The SN-curve is defined as

$$N = 2 \cdot 10^6 \cdot \left( \frac{\Delta\sigma_c}{\Delta\sigma} \right)^{m_1} \quad (5-4)$$

where  $N$  is the number of cycles to failure,  $\Delta\sigma$  is the stress range used as variable,  $m$  is the slope and  $\Delta\sigma_c$  is the characteristic stress range at  $N = 2 \times 10^6$  cycles, which can be compared to the FAT-classes defined in Eurocode 3 [38] and IIW [39]. For the evaluation of  $\Delta\sigma_c$  and  $m$ , the pearl-string method according DIN 50100 [40] is used. Therefore, a linear regression using the least squares method in the direction of the number of cycles is applied in the first step and a statistical evaluation is carried out in the second step. According Eurocode 3 [38], the FAT-classes are defined for a survival probability  $P_s = 95\%$ . The sample size for each test series is considered with the Student's t-distribution. For smaller sample sizes, a higher scatter is considered, which leads to lower values for the 95% survival probability in comparison with a normal distribution.

In Figure 5-13 (a1) to (a3), the raw data of the fatigue test presented in Table 4, and the corresponding 50% survival curve are plotted in a SN-curve for all specimen geometries and surface conditions. In subplots (b1) to (b3), the stress range is corrected with the stress magnification factor ( $k_m$ ) due to linear and angular misalignment based on the analytical formula from IIW [39]. According to the IIW [39], in the fatigue design curve for butt-welded joints a magnification factor of  $k_m = 1.15$  is already considered. For non-load carrying attachments joined with fillet welds, a magnification factor of  $k_m = 1.25$  is already covered. In order to compare the fatigue results with existing design-curves, the stress range is corrected with

$$k_{m,eff} = \frac{k_{m,calculated}}{k_{m,alreadycovered}} \quad (5-5)$$

where  $k_{m,eff}$  is the ratio between the calculated  $k_m$  of the fatigue-test specimen and the already covered  $k_m$  in the design-curve. In contrast to the common practice according to IIW [39], the correction was also performed when  $k_{m,eff}$  was less than 1.0, in order to have the same basis for all specimens. Run-outs and failures outside welds, for welded specimen, were not considered in the evaluation. The evaluation results are shown in Table 5-3 for the data without and with misalignment consideration. Without the consideration of misalignment, the characteristic stress range is higher for most of the series. This is due to the  $k_m$ -values of the tested specimen, which for fillet welds for example, is in average  $k_m = 1.16$  (see Table 3, Appendix A) and hence lower than the already covered SCF in the fatigue curves. However, for the purpose of comparison, the characteristic stress range including misalignment are considered.

The test results show the highest fatigue resistance for the base material. For the clean-blasted and uncorroded condition, a  $\Delta\sigma_c = 282 \text{ N/mm}^2$  is achieved, which is lowered to  $\Delta\sigma_c = 250 \text{ N/mm}^2$  by subsequent corrosion. The slopes are  $m = 14.8$  and  $14.5$ , respectively. According to the IIW and EC3, there is no comparable SN curve, therefore the SN curve of category C according to DNV is applied. Curve C primarily considers thermally cut edges, but according to DNV it can also be applied to surfaces with pitting corrosion. Curve C corresponds to the curve for FAT 125 according to IIW and EC3. The comparison with FAT 125 indicates high fatigue strength for the corroded base material. Since there is no characterization of the pit geometry in DNV on which the curve C / FAT 125 is based, it is difficult to make a direct comparison. However, it can be stated that the clean blasted specimens have higher fatigue strength, even after corrosion, compared to the design fatigue strength of FAT 160 (base material without corrosion).

For the butt-welded and fillet-welded specimens, additional tests were carried out in the as-welded condition. The as-welded curve for butt welds shows a fatigue strength of  $\Delta\sigma_c = 96 \text{ N/mm}^2$ , which is slightly higher than the standards (FAT 80 according to EC3 and IIW), although the slope  $m = 4.4$  is flatter than  $m = 3.0$  from the standard. Clean blasting increases the fatigue strength to  $\Delta\sigma_c = 195 \text{ N/mm}^2$  with a slope of  $m = 6.9$ . Corrosion reduces the fatigue strength to  $\Delta\sigma_c = 122 \text{ N/mm}^2$ , yet remains above the as-welded curve. A similar behaviour is observed for the fillet welds. The fatigue strength of the as-welded specimens is with  $\Delta\sigma_c = 74 \text{ N/mm}^2$  slightly below the FAT 80 from EC3 and IIW. Clean blasting initially increases this to  $\Delta\sigma_c = 158 \text{ N/mm}^2$ , and then corrosion reduces it to

$\Delta\sigma_c = 98 \text{ N/mm}^2$ , again resulting in a higher fatigue strength than the as-welded condition. The relative fatigue strength increase due to clean blasting is higher for the butt welds than for the fillet weld. The relative reduction in fatigue strength from uncorroded to corroded condition (for fillet welds  $158 \text{ N/mm}^2 / 98 \text{ N/mm}^2 = 1.60$ ) is of similar magnitude for butt welds and fillet welds. Similar observations can be made with regard to the scatter ratio ( $T_\sigma$ ) between the fatigue strength for  $P_s = 10\%$  and  $90\%$  (see Table 5-3). In the as-welded state, the scatter is relatively high and is reduced by clean blasting. The scatter increases due to corrosion, and in the case of fillet welds, the scatter after corrosion is even greater than in the as-welded condition. However, the consideration of misalignment has only minor effect on the scatter ratio.

It should be noted that the FAT-classes from EC3 and IIW are design curves related to an R-ratio of  $R = 0.5$ . For a comparison with these curves, the fatigue tests performed here, which were carried out at  $R = 0.1$ , must be corrected with a mean stress correction factor corresponding to IIW. However, due to the controversial accuracy, this is not carried out. Nevertheless, it can be assumed that the characteristic fatigue strengths determined here would be slightly smaller. For the comparison within the specimen series this is not relevant in any case.

**Table 5-3: Fatigue curve parameter**

Geometry	Surface condition	Without misalignment			With misalignment		
		Slope	$\Delta\sigma_c$ [N/mm <sup>2</sup> ]/	Scatter	Slope	$\Delta\sigma_c$ [N/mm <sup>2</sup> ]/	Scatter
Base material	Clean blasted - uncorroded	-14.8	282	1.09	-14.8	282	1.09
	Clean blasted - corroded	-14.5	251	1.17	-14.5	251	1.17
Butt weld	As-welded	-3.9	88	2.31	-4.4	96	2.11
	Clean blasted - uncorroded	-9.4	214	1.32	-6.9	195	1.44
	Clean blasted - corroded	-6.7	160	1.42	-3.9	122	1.60
Fillet weld	As-welded	-3.2	79	1.51	-3.2	74	1.46
	Clean blasted - uncorroded	-6.7	168	1.29	-6.7	158	1.24
	Clean blasted - corroded	-3.8	109	1.43	-3.9	98	1.55



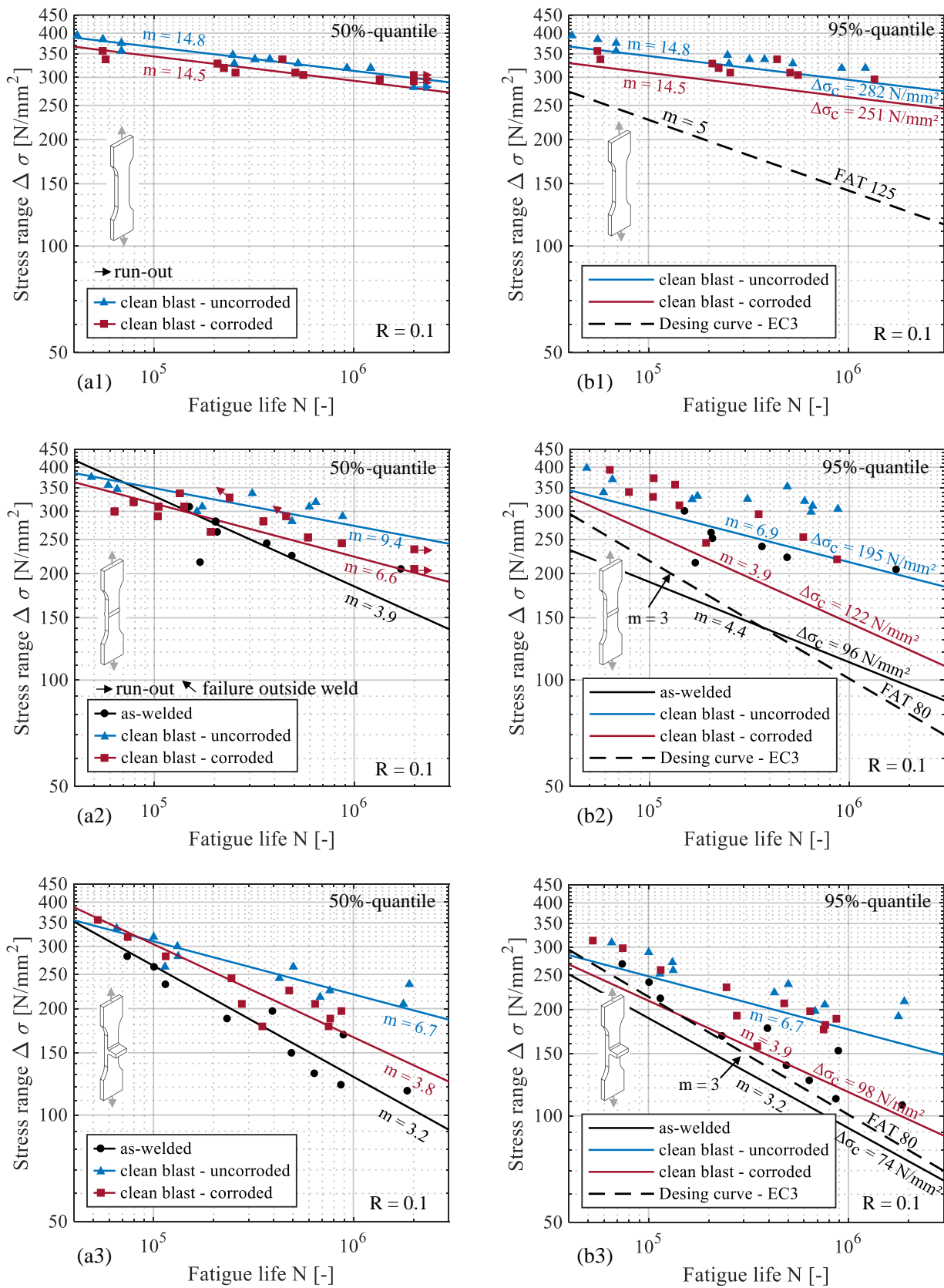


**Figure 5-13: Fatigue test results: (a1) to (a3) without consideration of misalignment and (b1) to (b3) with consideration of misalignment**

### 5.4.7 Crack detection with digital image correlation

In Appendix A Table 3-5, the results of the crack initiation lifetime  $N_C$  analysed with DIC are presented for every specimen, where the crack development could be measured. Moreover, the results of crack initiation lifetime are presented in Figure 5-14 (a), and the crack propagation lifetime is illustrated in (b) in a SN-diagram. The SN-curves for the crack initiation stage differ significantly from each other, while the SN-curves for the crack propagation stage show only little difference, except for the uncorroded butt welds. This is especially true for the fillet-welded specimens, where the notches on the weld toe are a priori sharper. In addition, it can be noted that for the corroded specimens there is no difference between the fillet and butt welds in the crack propagation stage. This can be explained by the crack growth after initiation of the first crack. On the one hand, new cracks appear along the weld toe, merging into one long crack as the cycles progress. On the other hand, the crack also grows in depth. The influence of the surface finish vanishes in depth direction, which means that the specimens behave similarly to each other in the crack propagation stage. However, it should be noted that the influence from the surface condition cannot be completely excluded, since the crack also grows on the surface.

Beside this, the ratio of the crack initiation and total lifetime defined as  $r_c = N_C/N_T$  is evaluated for every specimen. The ratio  $r_c$  ranges between 0.23 and 0.95 with a mean value of 0.57, indicating a high degree of scatter. In order to find dependencies between the fatigue test data, the data in Table 3-5 were analysed regarding their correlation to each other. It was found, that the crack initiation ratio is negatively correlated to the stress range. In Figure 5-14 (c), the crack ratio is plotted against the stress range for butt- and fillet welds for all three surface conditions. It appears, that for the uncorroded and corroded clean blasted specimens, higher stress ranges lead to lower crack initiation ratio and thus to lower fatigue life in the crack initiation stage for lower stress ranges, which is in line with findings of Braun et al. [41]. On the other hand, no correlation can be observed for the as-welded specimens.

Comparing butt and fillet welds reveals, that the ratio  $r_c$  is lower for fillet welds than for butt welds, for all three surface conditions. This can be attributed to the sharper notches for fillet welds already shown by the analysis of the geometrical parameters. Sharper notches lead to an earlier crack, since the stress concentrations are higher. Beside this, it can be observed, that the ratios for the corroded specimens are lower than the uncorroded specimens, but higher than in the as-welded condition. Crack initiation starts earlier for the corroded specimens than for the uncorroded specimens. Especially for low stress ranges, corresponding to the high-cycle fatigue region, the difference between the as-welded and the clean blasted condition is significant. This is true for the uncorroded as well as for the corroded condition. For a fillet-welded specimen and a stress range of  $\Delta\sigma = 230 \text{ N/mm}^2$ , for example, the ratios according the trend lines in Figure 5-14 (c) are  $r_c = 0.76$  and  $0.58$  for the clean blasted - uncorroded and corroded specimen, respectively, while for the as-welded specimen the ratio is  $r_c = 0.23$ .

Nevertheless, these observations lead to the assumption, that the higher fatigue life is mainly driven by the difference in the crack initiation stage.

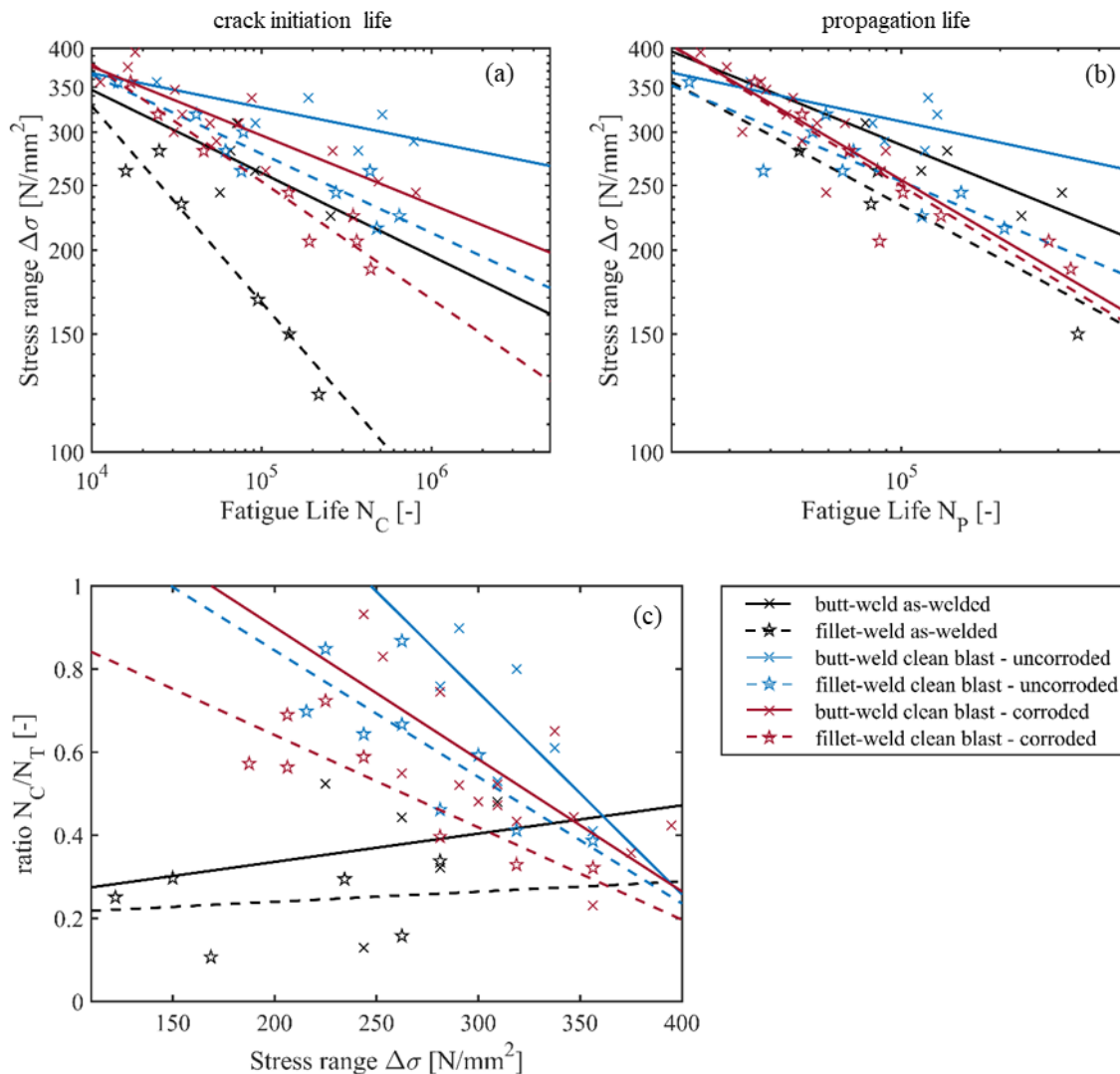


**Figure 5-14: DIC results for butt and fillet welds with different surface conditions, (a) crack initiation lifetime, (b) crack propagation lifetime and (c) crack initiation ratio  $r_c$  as a function of the stress range.**

#### 5.4.8 Discussion

The fatigue tests showed that the as-welded specimens had the lowest fatigue strength. The fatigue strength was greatly increased by clean blasting. The effect of one-month corrosion in the salt spray chamber reduced the fatigue strength for all specimen geometries, but not below the level of the as-welded condition. It was shown by DIC that the decrease in fatigue strength is predominantly coupled with the decrease in fatigue life at the crack initiation stage and that the crack propagation stage has a smaller influence on it. The crack initiation stage is in turn dependent on notch sharpness and the resulting SCF.

To investigate the SCF, geometrical parameters such as the weld toe radius and the flank angle were examined. It was shown that the relatively high SCF in the as-welded condition were initially reduced by clean blasting and increased by the corrosion process. In the case of butt welds, this was mainly driven by the change in the flank angle, while in the case of fillet welds, it was mainly the radii

that changed. The increase due to corrosion resulted in SCF similar to the as-welded condition. As, despite similar SCF values, the fatigue strength in the as-welded condition was lower than in the clean blasted-corroded condition, the SCF cannot be considered as the only relevant parameter. The hardness measurements have shown that the mean hardness at the weld toe for the clean blasted - uncorroded specimen are lower than for the corroded specimen. Regardless, whether this results from material embrittlement or is because of the scattering in the material process, the difference is only minor. However, although higher hardness can delay crack initiation, it also leads to higher notch sensitivity [42]. A higher notch sensitivity leads to faster crack growth, which reverses the positive effect of a higher hardness, especially in the case of strongly notched components, such as the specimens tested here. In view of this, the influence is rated as low.

A clearer picture can only be drawn if the influence of residual stresses is taken into account. The residual stress measurements showed that the as-welded specimens at the weld toe exhibit the highest tensile residual stresses in loading direction, while the clean blasted - uncorroded specimens at the weld toe are subjected to compressive residual stresses beneficial to fatigue strength. Corrosion removes the near-surface material induced with compressive stress. The residual stress present on the new corroded surface is in the tensile range, but much lower than in the as-welded specimen. Consequently, the residual stresses play a significant role in the fatigue strength of welded specimens subjected to corrosive environments. This is also true for the additional mean stresses from the clamping process caused by misalignments. Both can influence the effective R-ratio and must be considered in the fatigue analysis. However, in this study residual stress was only considered in the initial stage before testing. Possible stress relaxation under cyclic loading was not determined. In this respect, literature results show that residual stress stability tends to decrease with increasing local notch stress depending on the welded detail [43]. Therefore, the effects of residual stress relaxation under combined cyclic and corrosion stress should be within the scope of further research.

The evaluated SCFs can be incorporated in the notch stress approach based on IIW [39], where the SCFs are calculated with the fictitious radius of  $\rho_f = \rho + 1$  mm, where  $\rho$  is the real notch radius. For fatigue analysis the SCF have to be calculated with the modified radii and multiplied by the nominal stresses, which subsequently can be compared to the FAT 225 curve recommended for the fatigue resistance for structural steel in IIW [39]. The residual stresses can be considered as additional mean stresses or by new local fatigue approaches as the 4R-method [44,45]. In this way, the major fatigue driving parameters (SCF and the residual stresses) can be considered for the different surface conditions (as-welded, clean blasted – uncorroded, and clean blast – corroded). However, it should be noted as the FAT 225 curve is derived by fatigue tests conducted without consideration of potential embrittlement from the corrosion process, which requires further investigation in the future.

## 5.5 Summary and Outlook

The motivation of the study was to investigate the influence of corrosion on the fatigue strength of welded components including those in offshore support structures. The investigations were intended to contribute to the prediction of the remaining service life of existing support structures with local

concepts, as this can lead to higher utilization of the existing structures. For this purpose, welded and unwelded specimens were exposed to free corrosion for one month in a salt spray chamber and subsequently fatigue tested while being monitored using DIC. In addition, the geometrical properties of the specimens were recorded with a 3D-scanner before and after corrosion in order to investigate changes in surface texture and in the governing geometrical parameters at the weld. Furthermore, hardness and residual stress measurements provided a comprehensive understanding on the effect of corrosion. The following findings can be drawn from this study for one-month corrosion exposure in the salt spray chamber from this study:

- Surface measurement: clean blasting increased the surface roughness, but the surface did not experience any further increase in roughness due to corrosion. The visible changes in the surface scans can be attributed to the changes in waviness, as the changes are caused by longer wavelengths.
- Digital surface comparison before and after corrosion based on 3D-scans: this showed that material removal can take place both in the area of the base metal and directly at the weld toe, which is the critical location for fatigue. The removal can occur over a large area, but also locally in form of pitting.
- Fatigue tests: the fatigue tests have shown that the as-welded specimens have the lowest fatigue strength, but still are within the existing guidelines and standards. Clean blasting increased the fatigue strength; however, subsequent corrosion decreased the fatigue strength. For fillet weld, for example, the characteristic fatigue strength could be increased from  $\Delta\sigma_c = 74 \text{ N/mm}^2$  in the as-welded condition to  $\Delta\sigma_c = 158 \text{ N/mm}^2$  and was reduced to  $\Delta\sigma_c = 98 \text{ N/mm}^2$  as a result of corrosion.
- Crack detection with DIC: this showed that the differences in fatigue strength are mainly associated with the crack initiation stage, whereas the fatigue life in the crack propagation stage differs only slightly. This is particularly clear in the case of fillet welds.
- Geometrical parameters: for both, butt and fillet welds, it could be shown that the geometrical parameters change due to clean blasting and corrosion. Clean blasting resulted in lower SCF, while corrosion increased the SCF to the previous level of the as-welded condition. As the fatigue strength was not the same despite similar SCF, it is not representative as the sole fatigue driving parameter.
- Residual stress results: the residual stress measurements have shown that the highest tensile residual stresses in loading direction are present in the as-welded specimen, while the clean blasted specimen exhibits compressive residual stresses. The removal of material because of corrosive exposure decreases the introduced compressive stresses on the surface, resulting in enhanced tensile residual stresses of low magnitude at the weld toe. However, these residual tensile stresses are much lower than in the as-welded specimens, which provides a clear relation to the different fatigue strengths.

Based on these findings, it can be concluded that there are several influencing factors that can act simultaneously. Both the geometrical parameters as well as the residual stresses can have an influence on the fatigue strength. The fatigue strength calculations with local concepts can consider the listed

influences separately and thus open up the possibility for differentiated estimation of the (residual) service life of existing offshore support structures.

## 5.6 Acknowledgements

The research project “Influence of corrosive media on the fatigue strength of offshore wind turbines (CorroFAT)”, grant number 37 LN/1, of the Research Association for Steel Applications (FOSTA) e. V. was funded by the German Federal Ministry of Economics and Climate Action (BMWK) via the German Federation of Industrial Research Associations "Otto von Guericke" (AiF) e. V. as part of the program "Leittechnologien für die Energiewende" and as part of the joint project "Offshore Wind Energy Systems for Hydrogen Supply" to promote joint industrial research (IGF) on the basis of a resolution of the German Bundestag. The authors would like to express their sincere gratitude for the experienced financial support.

In addition, special recognition is given to the project partners involved in the production of the specimens: Salzgitter AG, Muehlhan AG, Fraunhofer IGP.

## 5.7 Appendix A

### Equations for angular and linear misalignment:

$$\text{Angular misalignment: } \omega = |\omega_1 + \omega_2| = \left| \frac{h_2 - h_1 + h_3 - h_4}{f} \right| \quad (5-6)$$

$$\text{Linear misalignment: } e = \left| (h_2 - h_3) + (h_2 - h_3 + h_4 - h_1) * \frac{g}{f} + \frac{d_2 - d_1}{2} \right| \quad (5-7)$$

**Table 5-4: Statistical results of radius, flank angle, and corresponding stress concentrations for different surface conditions**

		Radius r [mm]				Flank angle $\theta$ [°]				Stress concentration SCF [-]			
		Mean	95%	5%	Std.	Mean	95%	5%	Std.	Mean	95%	5%	Std.
Butt weld 1	as - welded	1.19	1.89	0.78	0.39	23.2	27.3	17.9	2.7	1.76	1.92	1.55	0.12
	clean blasted - uncorroded	1.55	2.72	0.50	0.68	19.4	21.4	17.6	1.1	1.60	1.85	1.45	0.12
Fillet weld 1	as - welded	0.92	1.55	0.35	0.37	45.0	47.2	43.2	1.3	2.47	3.02	2.17	0.25
	clean blasted - uncorroded	0.96	1.25	0.76	0.15	45.3	47.5	43.3	1.2	2.40	2.56	2.26	0.09
Butt weld 2	clean blasted - uncorroded	1.62	2.85	0.73	0.66	20.7	22.3	18.9	1.0	1.62	1.79	1.46	0.10
	clean blasted - corroded	1.57	2.95	0.85	0.68	27.1	29.7	24.3	1.7	1.79	1.98	1.57	0.13
Fillet weld 2	clean blasted - uncorroded	0.97	1.33	0.72	0.19	42.4	45.5	38.6	1.9	2.33	2.52	2.14	0.12
	clean blasted - corroded	0.97	1.71	0.45	0.41	48.6	52.2	45.5	1.9	2.53	2.97	2.16	0.26

Table 5-5: Fatigue test data and DIC results

Specimen No.	Max. load $F_{max}$ [kN]	Min. load $F_{min}$ [kN]	Cross section area [mm <sup>2</sup> ]	Stress range $\Delta\sigma$ [N/mm <sup>2</sup> ]	Fatigue life total $N_T$ [-]	Fatigue life crack initiation $N_C$ [-]	Ratio $r_{c1}$ $N_C/N_T$ [-]	Angular misalignment $\omega$ [°]	Linear misalignment $e$ [mm]	Stress magnification factor $k_{m,eff}$ [-]	Note:
00-K-01	150	15	480.0	281.3	73,875	24,958	0.34	1.50	0.00	0.93	
00-K-02	140	14	480.0	262.5	100,595	15,857	0.16	1.54	0.00	0.93	
00-K-03	100	10	480.0	187.5	233,185	-	-	1.60	0.00	0.93	
00-K-04	125	12.5	480.0	234.4	114,617	33,740	0.29	1.59	0.00	0.93	
00-K-05	80	8	480.0	150.0	489,701	145,318	0.30	1.61	0.00	0.94	
00-K-06	70	7	480.0	131.3	637,374	-	-	1.85	0.00	0.96	
00-K-07	65	6.5	480.0	121.9	865,935	216,984	0.25	1.88	0.00	0.96	
00-K-08	62.5	6.25	480.0	117.2	1,858,787	-	-	1.66	0.00	0.94	
00-K-09	90	9	480.0	168.8	890,591	94,996	0.11	0.55	0.00	0.85	
00-K-10	105	10.5	480.0	196.9	393,415	-	-	0.47	0.00	0.84	
00-S-01	115	11.5	480.0	215.6	169,360	-	-	1.36	0.01	1.00	
00-S-05	110	11	480.0	206.3	1,711,744	-	-	1.19	0.09	1.00	
00-S-06	120	12	480.0	225.0	487,616	255,468	0.52	1.09	0.09	0.99	
00-S-07	130	13	480.0	243.8	365,274	56,847	0.16	0.93	0.12	0.98	
00-S-08	165	16.5	480.0	309.4	149,586	71,841	0.48	0.80	0.15	0.97	
00-S-09	140	14	480.0	262.5	206,491	91,446	0.44	0.68	0.13	0.96	
00-S-10	150	15	480.0	281.3	203,244	65,468	0.32	0.52	0.06	0.93	
0-G-01	150	15	480	281.3	2,000,000	-	-	0.00	0.00	1.00	
0-G-02	210	21	480	393.8	41,400	-	-	0.00	0.00	1.00	
0-G-03	205	20.5	480	384.4	55,662	-	-	0.00	0.00	1.00	
0-G-04	200	20	480	375.0	68,901	-	-	0.00	0.00	1.00	
0-G-05	190	19	480	356.3	68,901	-	-	0.00	0.00	1.00	
0-G-06	180	18	480	337.5	320,527	-	-	0.00	0.00	1.00	
0-G-09	170	17	480	318.8	1,217,401	-	-	0.00	0.00	1.00	
0-G-10	185	18.5	480	346.9	248,618	-	-	0.00	0.00	1.00	
0-G-11	175	17.5	480	328.1	252,820	-	-	0.00	0.00	1.00	
0-G-12	180	18	480	337.5	380,895	-	-	0.00	0.00	1.00	
0-G-14	170	17	480	318.8	926,367	-	-	0.00	0.00	1.00	
0-G-15	175	17.5	480	328.1	527,174	-	-	0.00	0.00	1.00	
0-K-01	190	19	480	356.3	36,882	14,261	0.39	1.92	0.00	0.96	
0-K-04	170	17	480	318.8	100,221	41,267	0.41	1.34	0.00	0.91	
0-K-05	140	14	480	262.5	500,597	434,342	0.87	1.18	0.00	0.90	
0-K-06	150	15	480	281.3	132,842	61,312	0.46	1.42	0.00	0.92	
0-K-07	110	11	480	206.3	1,780,057	-	-	1.51	0.00	0.93	
0-K-08	140	14	480	262.5	114,107	76,071	0.67	1.93	0.00	0.96	
0-K-09	115	11.5	480	215.6	682,191	476,340	0.70	1.40	0.00	0.92	
0-K-10	180	18	480	337.5	65,416	-	-	1.41	0.00	0.92	
0-K-11	160	16	480	300.0	131,754	78,076	0.59	1.29	0.00	0.91	
0-K-12	125	12.5	480	234.4	1,905,485	-	-	1.19	0.00	0.90	
0-K-13	130	13	480	243.8	426,269	274,243	0.64	1.39	0.00	0.92	
0-K-15	120	12	480	225.0	762,191	646,768	0.85	1.40	0.00	0.92	
0-S-01	185	18.5	480	346.9	65,190	-	-	1.12	0.44	1.07	
0-S-02	370	37	840	396.4	26,663	-	-	1.80	1.12	1.26	
0-S-03	180	18	480	337.5	309,172	188,520	0.61	0.50	0.23	0.96	
0-S-04	160	16	480	300.0	163,429	-	-	1.21	0.48	1.08	
0-S-06	175	17.5	480	328.1	654,726	-	-	0.38	0.21	0.95	
0-S-07	165	16.5	480	309.4	596,704	-	-	1.02	0.35	1.04	

0-S-09	155	15.5	480	290.6	875,797	787,007	0.90	1.39	0.25	1.05	
0-S-10	165	16.5	480	309.4	173,803	92,013	0.53	1.10	0.48	1.07	
0-S-11	190	19	480	356.3	58,887	24,127	0.41	0.49	0.19	0.95	
0-S-12	150	15	480	281.3	488,798	370,878	0.76	1.78	1.03	1.25	
0-S-13	200	20	480	375.0	48,482	-	-	1.22	0.39	1.06	
0-S-15	170	17	480	318.8	643,000	514,400	0.80	0.33	0.18	0.94	
1-G-03	165	16.5	480	309.4	256,454	-	-	0.00	0.00	1.00	
1-G-04	162.5	16.25	480	304.7	2,000,000	-	-	0.00	0.00	1.00	run out
1-G-07	156	15.6	480	292.5	2,000,000	-	-	0.00	0.00	1.00	run out
1-G-07_2	180	18	480	337.5	57,459	-	-	0.00	0.00	1.00	
1-G-08	180	18	480	337.5	440,003	-	-	0.00	0.00	1.00	
1-G-09	190	19	480	356.3	55,522	-	-	0.00	0.00	1.00	
1-G-1	165	16.5	480	309.4	511,310	-	-	0.00	0.00	1.00	
1-G-10	175	17.5	480	328.1	208,537	-	-	0.00	0.00	1.00	
1-G-11	162.5	16.25	480	304.7	559,680	-	-	0.00	0.00	1.00	
1-G-12	170	17	480	318.8	224,454	-	-	0.00	0.00	1.00	
1-G-12	158	15.8	480	296.3	1,350,833	-	-	0.00	0.00	1.00	
1-G-13	160	16	480	300.0	2,174,200	-	-	0.00	0.00	1.00	run out
1-K-01	95	9.5	480	178.1	350,243	-	-	0.99	0.00	0.88	
1-K-02	150	15	480	281.3	115,061	45,636	0.40	1.44	0.00	0.92	
1-K-03	100	10	480	187.5	766,305	438,596	0.57	1.96	0.00	0.96	
1-K-04	105	10.5	480	196.9	871,277	-	-	1.86	0.00	0.96	
1-K-05	170	17	480	318.8	74,331	24,457	0.33	1.64	0.00	0.93	
1-K-06	130	13	480	243.8	245,647	144,527	0.59	1.78	0.00	0.95	
1-K-07	110	11	480	206.3	276,735	190,903	0.69	1.56	0.00	0.93	
1-K-08	95	9.5	480	178.1	752,251	-	-	2.20	0.00	0.99	
1-K-09_1	90	9	480	168.8	2,000,000	-	-				run out
1-K-09_2	110	11	480	206.3	643,713	362,892	0.56	1.88	0.00	0.96	run out specimen, tested on new load level
1-K-10	190	19	480	356.3	52,686	16,935	0.32	0.96	0.00	0.88	
1-K-12	85	8.5	480	159.4	2,000,000	-	-	1.83	0.00	0.95	run out
1-K-13_1	95	9.5	480	178.1	2,000,000	-	-				
1-K-13_2	120	12	480	225.0	477,532	345,589	0.72	1.49	0.00	0.92	run out specimen, tested on new load level
1-S-02	180	18	480	337.5	134,190	87,345	0.65	1.17	0.39	1.06	
1-S-03	175	17.5	480	328.1	238,106	-	-	0.56	0.04	0.93	crack outside weld
1-S-07	160	16	480	300.0	63,260	30,441	0.48	2.17	1.13	1.31	
1-S-08	170	17	480	318.8	78,843	34,133	0.43	1.33	0.37	1.07	
1-S-09	165	16.5	480	309.4	141,045	73,695	0.52	0.80	0.31	1.01	
1-S-10	150	15	480	281.3	351,572	261,946	0.75	1.83	0.06	1.05	
1-S-11	155	15.5	480	290.6	457,078	-	-	0.22	0.03	0.90	crack outside weld
1-S-12	165	16.5	480	309.4	104,948	49,559	0.47	2.13	0.66	1.20	
1-S-13	155	15.5	480	290.6	104,099	54,228	0.52	1.00	0.81	1.13	
1-S-14	130	13	480	243.8	867,632	808,609	0.93	1.00	0.14	0.90	
1-S-15_1	125	12.5	480	234.4	2,000,000	-	-				run out
1-S-15_2	140	14	480	262.5	191,836	105,322	0.55	0.44	0.28	0.93	run out specimen, tested on new load level
1-S-16_1	110	11	480	206.3	2,000,000	-	-				Run out
1-S-16_2	135	13.5	480	253.1	587,737	487,822	0.83	0.55	0.61	1.00	run out specimen, tested on new load level



## 5.8 References

- [1] Xiang L, Pan J, Chen S. Analysis on the stress corrosion crack inception based on pit shape and size of the FV520B tensile specimen. *Results in Physics* 2018;9:463–70. <https://doi.org/10.1016/j.rinp.2018.03.005>.
- [2] Cerit M. Corrosion pit-induced stress concentration in spherical pressure vessel. *Thin-Walled Structures* 2019;136:106–12. <https://doi.org/10.1016/j.tws.2018.12.014>.
- [3] Huang Y, Wei C, Chen L, Li P. Quantitative correlation between geometric parameters and stress concentration of corrosion pits. *Engineering Failure Analysis* 2014;44:168–78. <https://doi.org/10.1016/j.engfailanal.2014.05.020>.
- [4] Hou J, Song L. Numerical Investigation on Stress Concentration of Tension Steel Bars with One or Two Corrosion Pits. *Advances in Materials Science and Engineering* 2015;2015:1–7. <https://doi.org/10.1155/2015/413737>.
- [5] Weinert J, Gkatzogiannis S, Engelhardt I, Knoedel P, Ummenhofer T. Application of high frequency mechanical impact treatment to improve the fatigue strength of corroding welded joints. *Weld World* 2021;65(11):2157–67. <https://doi.org/10.1007/s40194-021-01171-7>.
- [6] Gkatzogiannis S, Weinert J, Engelhardt I, Knoedel P, Ummenhofer T. Correlation of laboratory and real marine corrosion for the investigation of corrosion fatigue behaviour of steel components. *International Journal of Fatigue* 2019;126:90–102. <https://doi.org/10.1016/j.ijfatigue.2019.04.041>.
- [7] Det Norske Veritas - Germanischer Lloyd. Fatigue design of offshore steel structures(DNV-GL RP-C203); 2019.
- [8] Health & Safety Executive. Background to new fatigue guidance for steel joints and connections in offshore structures(OTH 92 390); 1998.
- [9] Melchers R. A Review of Trends for Corrosion Loss and Pit Depth in Longer-Term Exposures. *Corros. Mater. Degrad.* 2018;1(1):42–58. <https://doi.org/10.3390/cmd1010004>.
- [10] Revie RW, Uhlig HH. Corrosion and corrosion control: An introduction to corrosion science and engineering. Hoboken, New Jersey: Wiley-Interscience a John Wiley & Sons Inc. Publication; 2008.
- [11] Marcus P. Corrosion mechanisms in theory and practice. 3rd ed. Boca Raton, Fla.: CRC Press; 2012.
- [12] Mehmanparast A, Brennan F, Tavares I. Fatigue crack growth rates for offshore wind monopile weldments in air and seawater: SLIC inter-laboratory test results. *Materials & Design* 2017;114:494–504. <https://doi.org/10.1016/j.matdes.2016.10.070>.
- [13] Vosikovskiy O. Fatigue-Crack Growth in an X-65 Line-Pipe Steel at Low Cyclic Frequencies in Aqueous Environments. *J. Eng. Mater. Technol* 1975;97(4):298–304. <https://doi.org/10.1115/1.3443302>.

- [14] Thorpe TW, Scott PM, Rance A, Silvester D. Corrosion fatigue of BS 4360:50D structural steel in seawater. *International Journal of Fatigue* 1983;5(3):123–33. [https://doi.org/10.1016/0142-1123\(83\)90025-7](https://doi.org/10.1016/0142-1123(83)90025-7).
- [15] Gericke A, Glienke R. Untersuchung des Reinigungsstrahlens als Nahtnachbehandlungsmethode zur Verbesserung der Schwingfestigkeit geschweißter Strukturen. DVS;2018.
- [16] International Standards Organization. ISO 5817: Welding – Fusion-welded joints in steel, nickel, titanium and their alloys (beam welding excluded) – Quality levels for imperfections; 2014.
- [17] Det Norske Veritas. Corrosion protection for wind turbines(DNV-GL RP-0416); 2016.
- [18] International Standards Organization. ISO 8501-1:2007-12; Preparation of steel substrates before application of paints and related products - Visual assessment of surface cleanliness - Part 1: Rust grades and preparation grades of uncoated steel substrates and of steel substrates after overall removal of previous coatings (ISO 8501-1:2007).
- [19] International Standards Organization. ISO 6520-1: Welding and allied processes – Classification of geometric imperfections in metallic materials – Part 1: Fusion welding(DIN 2007); 2007.
- [20] International Standards Organization. ISO 9227: Corrosion tests in artificial atmospheres – Salt spray tests. Berlin: Beuth; 2017.
- [21] ISO 8407: Corrosion of metals and alloys – Removal of corrosion products from corrosion test specimens. Berlin: Beuth; 2021.
- [22] International Standards Organization. ISO 21920-2: Geometrical product specifications (GPS) – Surface texture: Profile – Part 2: Terms, definitions and surface texture parameters; 2022.
- [23] International Standards Organization. ISO 21920-3: Geometrical product specifications (GPS) – Surface texture: Profile – Part 3: Specification operators; 2021.
- [24] Radaj D, Sonsino CM, Fricke W. Fatigue assessment of welded joints by local approaches. 2nd ed. Cambridge: Woodhead Publ. [u.a.]; 2006.
- [25] Anthes RJ, Köttgen VB, SEEGER T. Kerbformzahlen von Stumpfstößen und Doppel-T-Stößen. *Schweißen und Schneiden* 1993(45 (12)):685–8.
- [26] Renken F, Bock und Polach RUF von, Schubnell J, Jung M, Oswald M, Rother K et al. An algorithm for statistical evaluation of weld toe geometries using laser triangulation. *International Journal of Fatigue* 2021;149:106293. <https://doi.org/10.1016/j.ijfatigue.2021.106293>.
- [27] Schubnell J, Jung M, Hieu Le C, Majid F, Braun M, Ehlers S et al. Influence of the optical measurement technique and evaluation approach on the determination of local weld geometry parameters for different weld types. *Weld World* 2020;64(2):301–16. <https://doi.org/10.1007/s40194-019-00830-0>.

- [28] International Standards Organization. ISO 6507-1, Metallic materials — Vickers hardness test — Part 1: Test method;2022.
- [29] Shojai S, Schaumann P, Braun M, Ehlers S. Influence of pitting corrosion on the fatigue strength of offshore steel structures based on 3D surface scans. *International Journal of Fatigue* 2022;164:107128. <https://doi.org/10.1016/j.ijfatigue.2022.107128>.
- [30] Radaj D, Vormwald M. *Ermüdungsfestigkeit: Grundlagen für Ingenieure*. 3rd ed. Berlin, Heidelberg: Springer-Verlag Berlin Heidelberg; 2007.
- [31] Hutt T, Cawley P. Feasibility of digital image correlation for detection of cracks at fastener holes. *NDT & E International* 2009;42(2):141–9. <https://doi.org/10.1016/j.ndteint.2008.10.008>.
- [32] Karsten Schürmann. *Fatigue Behavior of Automatically Welded Tubular Joints for Offshore Wind Energy Substructures: Dissertation*; 2021.
- [33] Friedrich N, Ehlers S. Crack Monitoring in Resonance Fatigue Testing of Welded Specimens Using Digital Image Correlation. *Journal of visualized experiments JoVE* 2019(151). <https://doi.org/10.3791/60390>.
- [34] Qvale P, Zarandi EP, Ås SK, Skallerud BH. Digital image correlation for continuous mapping of fatigue crack initiation sites on corroded surface from offshore mooring chain. *International Journal of Fatigue* 2021;151:106350. <https://doi.org/10.1016/j.ijfatigue.2021.106350>.
- [35] VAUGHAN HG, MORTON ME de. Change of Hardness in Steel due to Hydrogen. *Nature* 1956;177(4522):1225. <https://doi.org/10.1038/1771225a0>.
- [36] Wasim M, Djukic MB. Hydrogen embrittlement of low carbon structural steel at macro-, micro- and nano-levels. *International Journal of Hydrogen Energy* 2020;45(3):2145–56. <https://doi.org/10.1016/j.ijhydene.2019.11.070>.
- [37] Zhao Y, Seok M-Y, Choi I-C, Lee Y-H, Park S-J, Ramamurty U et al. The role of hydrogen in hardening/softening steel: Influence of the charging process. *Scripta Materialia* 2015;107:46–9. <https://doi.org/10.1016/j.scriptamat.2015.05.017>.
- [38] European Committee for Standardization. *Eurocode 3 - Design of steel structures - Part 1-9: Fatigue(EN 1993-1-9)*; 2020.
- [39] Hobbacher AF. *Recommendations for Fatigue Design of Welded Joints and Components*. Cham: Springer International Publishing; 2016.
- [40] Deutsches Institut für Normung. *DIN 50100: Load controlled fatigue testing – Execution and evaluation of cyclic tests at constant load amplitudes on metallic specimens and components*. Berlin: Beuth; 2016.
- [41] Braun M, Fischer C, Baumgartner J, Hecht M, Varfolomeev I. Fatigue Crack Initiation and Propagation Relation of Notched Specimens with Welded Joint Characteristics. *Metals* 2022;12(4):615. <https://doi.org/10.3390/met12040615>.
- [42] Radaj D, Vormwald M. *Advanced methods of fatigue assessment*. Heidelberg: Springer; 2013.

- [43] Farajian M, Nitschke-Pagel T. Residual stress relaxation in welded large components. *Materials Testing* 2015;57(9):750–4. <https://doi.org/10.3139/120.110773>.
- [44] Nykänen T, Björk T. Assessment of fatigue strength of steel butt-welded joints in as-welded condition – Alternative approaches for curve fitting and mean stress effect analysis. *Marine Structures* 2015;44:288–310. <https://doi.org/10.1016/j.marstruc.2015.09.005>.
- [45] Ahola A, Muikku A, Braun M, Björk T. Fatigue strength assessment of ground fillet-welded joints using 4R method. *International Journal of Fatigue* 2021;142:105916. <https://doi.org/10.1016/j.ijfatigue.2020.105916>.

## 6 Fatigue analysis of corroded welded joints with local approaches (Paper V)

This section contains a reprint of the article: Shojai, Sulaiman; Brömer, Tim; Ghafoori, Elyas; Schau-mann, Peter (2024): Application of local fatigue approaches on corroded welded joints with considera-tion of weld geometry and residual stresses. In: *Theoretical and Applied Fracture Mechanics*, S. 104215. DOI: 10.1016/j.tafmec.2023.104215.

### Background

In the last paper it was shown that corrosion can influence the geometry and the residual stresses of welded specimens. In addition, there are other factors such as the additional bending moments result-ing from angular and linear misalignment of the specimens. With local fatigue approaches, all afore-mentioned factors can be considered in the stress analysis. The material effects, such as embrittlement of the near-surface material, can be considered separately within the micro-support effect considera-tion via the intrinsic material length.

### Overview

In this study, the specimens investigated in the previous paper were captured digitally using 3D-scanners in order to consider both the misalignments and the real weld geometry in the calculation of stresses. By means of reverse engineering, the 3D-scans are transformed into numerical 3D-models and used to compute the additional bending stresses from misalignments as well as the effective notch stress concentrations for axial loads. The micro-support effect was considered for the entire specimen using IGM. The residual stresses and the bending stresses were acknowledged using the mean stress correction factor according to Smith, Watson and Topper (SWT), which considers the local R-ratio of the notch. To verify the calculation, the numerically predicted crack locations were compared with the crack locations from the fatigue tests obtained with DIC. In addition, the resulting scatter in the SN-curves was used as a measure of the reliability of the method.

### Conclusion

Based on the comparisons between the numerical results and the DIC measurements, it could be shown that the predicted crack locations matched the actual crack locations in most cases. Moreover, by contemplating the notch stress concentrations, it was possible to significantly reduce the scatter in the SN-curve. A further reduction of the scatter was possible by considering the residual stresses and the bending stresses from the clamping process. However, the obtained SN-curve showed further potential for scatter reduction resulting from different behaviour of the near-surface material for as-welded, clean blasted, and corroded specimens. By introducing an enhancement/deterioration param-eter for each of the mentioned surface conditions, a further reduction of the scatter and thus a higher reliability of the prediction could be achieved. Alternatively, it is possible to consider the material effect by the corresponding intrinsic material length, which have to be determined in future research activities for the respective surface conditions.

**Authors Contribution**

The experimental work and numerical analysis as well as the paper conceptualization, methodology, validation, formal analysis, investigation, writing of the original draft and visualization were carried out by the first author. Moreover, the first author was responsible for funding acquisition and project administration. Tim Brömer built the 3D-numerical models as part of his master's thesis, under the supervision of the first author, reviewed, and edited the paper. Prof. Ghafoori reviewed and edited the paper. Prof. Schaumann supervised the work, reviewed and edited the paper, and was responsible for the funding acquisition and project administration.

## Application of local fatigue approaches on fatigue test results obtained for corroded welded joints<sup>5</sup>

### 6.1 Abstract

Corrosion can significantly affect the fatigue strength of steel structures. On the one hand, it can cause stress concentrations by changing the surface geometry, and on the other hand, it can lead to embrittlement of the material. In welded steel components, sharp notches are already present due to the weld geometry, which may interact with the notches from corrosion. In addition, residual stresses exist in the fatigue-relevant area, which can also be partially modified by surface preparation methods such as clean blasting. In the current standards, all the mentioned effects are considered by reducing the design stress-life (SN) curves, in which all aforementioned effects are superimposed. One possibility to consider the effects separately is the application of local concepts, with which the influence of the geometry, here obtained from 3D-scans, the influence of measured residual stresses and the influence of material can be considered individually. For butt and fillet welds investigated in this study, it could be shown that by considering the real geometry via a reverse engineered 3D-solid model, the location of crack initiations in the fatigue test, measured by digital image correlation (DIC), matched with the numerically predicted locations in most cases. Moreover, it was shown that by taking into account the real geometry and residual stresses, the use of local approaches can result in a substantial reduction of the scatter in SN-curves from  $T_{\sigma} = 2.17$  to  $T_{\sigma} = 1.26$ , demonstrating the great reliability of the applied method.

**Keywords:** corrosion fatigue; notch stress approach; welds geometry; stress concentrations; residual stresses

---

<sup>5</sup>[Shojai, S., Brömer, T., Ghafoori, E., Schaumann, P., Theoretical and Applied Fracture Mechanics, 2024, S. 104215. DOI: 10.1016/j.tafmec.2023.104215.](#)

## Nomenclature

ERF	Environment Reduction Factor	NSS	Neutral Salt Spray
CSS	Cyclic Stress-Strain	NURBS	Non-Uniform Rational B-Spline
DIC	Digital Image Correlation	PM	Point Method
HFMI	High Frequency Mechanical Impact	R-O	Ramberg and Osgood
IGM	Implicit Gradient Model	SWT	Smith, Watson and Topper
LM	Line Method	VM	Volume Method
$a$	Weighting scale factor (parameter)	$\Delta K_{th}$	Fatigue crack propagation threshold
$A_{nom}$	Cross section area	$\Delta \bar{\sigma}$	Elastic-plastic stress range
$c_p$	Specific heat capacity	$\Delta \sigma_0$	Fatigue limit
$d^*$	Critical distance	$\Delta \sigma_c$	Characteristic fatigue strength for nominal stresses
$f(R)$	Mean stress correction factor	$\Delta \sigma_{c,ref}$	Characteristic fatigue strength for $\Delta \sigma_{f,ref}$
$G$	Weighting function	$\Delta \sigma_{el}$	Elastic stress range
$K'$	Cyclic strain hardening coefficient	$\Delta \sigma_f$	Effective notch stress range
$L$	Intrinsic material length	$\Delta \sigma_{f,ref}$	Mean stress corrected notch stress
$m$	Slope of SN-curve	$\Delta \sigma_n$	Nominal stress range
$n'$	Cyclic strain hardening exponent	$\varepsilon_a$	Local strain amplitude
$P_s$	Failure probability	$\lambda$	Conductivity parameter
$\dot{q}$	Heat flux	$\rho^*$	Length of a microstructure particle
$R$	Mean stress ratio	$\rho_d$	Specific heat density
$r_f$	Fictitious notch radius	$\sigma_b$	Bending stress from clamping
$R_{local}$	Local mean stress ratio	$\sigma_f$	Effective notch stresses
$R_m$	Tensile strength	$\sigma_k$	Elastic notch stresses
$r_{real}$	Existing notch radius	$\sigma_{max}$	Maximum elastic-plastic stress according IIW
$T_\sigma$	Scatter coefficient	$\sigma_{max,el}$	Maximum elastic stress
$V_f$	Reference volume	$\sigma_{min}$	Minimum local stress
$\alpha_f$ (also $K_f$ )	Effective notch stress concentrations	$\sigma_n$	Nominal stress
$\alpha_{f,crack}$	Stress concentration at crack location	$\sigma_{o,el}$	Elastic stress from fatigue test load with consideration of micro-support effect
$\alpha_{f,initial,max}$	Maximum stress concentration before micro-support consideration	$\sigma_{res}$	Residual stress
$\alpha_k$ (also $K_t$ )	Elastic notch stress concentration	$\sigma_S$	Structural stress

## 6.2 Introduction

The aging of steel support structures is a major problem for both onshore and offshore structures. In view of the high replacement costs and the associated additional environmental emissions, the focus has shifted to service life extension and retrofitting. For steel structures such as bridges or offshore support structures, which are exposed to dynamic loads as well as extreme environments, the service life is determined by material fatigue and corrosion process.

The design of offshore support structures against fatigue is carried out according to the guidelines of DNV [1] under the assumption of an existing corrosion protection system. If this is no longer present



due to damage or degradation, the influence of corrosion is taken into account by the environment reduction factor (ERF), which is used to reduce the design SN-curves. The reduction is equal for all existing SN curves, although it is known from other guidelines such as the German BAW Standard [2] that the influence of corrosion varies depending on the already existing notch effect from the welds (expressed in FAT classes). This is on the safe side for strongly notched welded structures and opens up the possibility of utilizing potential load-bearing reserves for existing structures and extending the service life. To exploit these load-bearing reserves, the remaining service life of structures must be evaluated on the basis of the actual condition of the weld geometry, including potentially changes due to corrosion. With the existing guidelines, utilization of these reserves is not possible. Nor is it possible to consider the separate influence of the corrosion process, which consist of changes in the surface geometry as well as embrittlement of the material [3,4]. Moreover, in the case of welded components, residual stresses and their relaxation effect has to be considered [5,6]. In particular, clean blasting, which is used to prepare the surface for the application of corrosion protection, induces beneficial residual compressive stresses [7–9]. This has to be considered in order to exploit the beneficial effect and accurately predict the remaining service life of existing support structures.

To thoroughly account for the aforementioned influencing factors in a nuanced manner, local fatigue concepts, such as the notch stress approach anchored in the IIW [10] and summarized in Radaj et al. [11], can be used, in which the fatigue strength is calculated based on the notch stresses. This allows all stress increases, whether from geometric imperfections due to misalignments, from weld geometry, or from geometry change due to corrosion, to be expressed using the notch stresses, provided that the appropriate data is available. The influence of residual stresses has been studied mainly in the context of weld improvement techniques such as high frequency mechanical impact (HFMI), among other, by Yildirim et al. [12] and Nykänen et al. [13]. Nykänen et al. [13] consider the influence of residual stress by means of a mean stress correction based on the local mean stress ratio  $R_{local}$ , which is obtained based on the Ramberg and Osgood (R-O) [14] cyclic stress-strain behaviour. For HFMI treated butt and fillets welds with different residual stress levels, already good results could be obtained [13,15].

In this study, the notch stress approach considering residual stresses according to the method of Nykänen et al. [13] is applied to corroded butt and fillet welds from a previous study [16], which were exposed to corrosion for one month in a neutral salt spray chamber according to ISO 9227 [17] and tested under cyclic loading. The notch stresses are determined on the basis of 3D scans, which take into account the misalignments of the specimens as well as the weld geometry and the corroded surface geometry. In addition to this, the bending stresses resulting from the clamping process of the specimens, which superpose with the residual stresses, are also considered.

The novelties of this study can be summarized as follows:

- Consideration of the effective notch stresses, for the first time, on the basis of 3D scans of the specimens.
- Validation of the method by comparison of the notch stress hot-spots with the locations of crack initiation observed during the experiments using digital image correlation (DIC).
- Consideration of residual and bending stresses and validation by determining the scatter of the resulting notch stress curve, for the first time for corroded welded specimens.

Combined with the so called replica technique [18], in which an impression of the welds can be made during the inspection of the structure, these novelties are supposed to provide a more accurate fatigue life prediction of existing steel structures exposed to corrosion and fatigue.

### 6.3 Background of the notch stress methods

#### 6.3.1 Notch stress analysis methods

With local fatigue methods, like the notch stress method, it is possible to consider the stress concentrations arising from the geometry, the residual stresses from welding process, surface treatments or from the clamping process, and also the local material behaviour at the notch base.

In the notch stress method, the analysis of the notch stresses concentration is based on the notch geometry and on linear elastic material behaviour, leading to the elastic notch stress  $\sigma_k$ . In case of sharp notches, the yield stress in the surface crystallites can be exceeded and lead to micro cracks, which do not propagate with continued cyclic loading. This behaviour is called micro-support effect, which reduces the stress concentrations and supports the fatigue resistance [19,20]. Various hypotheses related to micro-support effects exist in the literature for calculating the effective fatigue notch stress, here denoted as  $\sigma_f$ . Among these methods are the point method (PM) by Peterson [21], the line method (LM) by Neuber [22], the volume method (VM) by Bellet [23], and the fictitious notch stress approach by Radaj [24].

In the PM, the effective notch stress  $\sigma_f$  is considered as the stress at a critical distance  $d^*$  (equation (6-1), Figure 6-1a), while in the LM the effective notch stress is considered to be the stress averaged over the length of a microstructure particle  $\rho^*$  in the notch base (equation (6-1)), Figure 6-1b). Analogously, in VM the stresses are averaged over a hemisphere defined by a radius of  $1.54L$  (Figure 6-1c). With the critical distance  $d^* = L/2$  and the equivalent averaging length  $\rho^* = 2L$ , PM, LM, and VM can be related to the intrinsic material length  $L$ , derived from linear elastic fracture mechanics [25] and defined in equation (6-3). Here  $\Delta K_{th}$  is the fatigue crack propagation threshold and  $\Delta\sigma_0$  is the fatigue limit.

In the fictitious notch stress approach by Radaj, the notch stresses are calculated based on fictitious notch radius  $r_f$ . Therefore, the existing notch radius  $r_{real}$  is increased by 1 mm (equation(6-4), Figure 6-1d). Assuming a worst-case scenario with  $r_{real} = 0$  for welded components, this leads to a fictitious radius of  $r_f = 1$  mm as recommended in various standards including the IIW recommendations [10]. The fictitious radius varies depending on material behaviour and the nominal plate thickness between 0.05 mm to 1.0 mm as reported in [26,27].

$$\sigma_f = \sigma_k(d^*) \quad (6-1)$$

$$\sigma_f = \frac{1}{\rho^*} \int_0^{\rho^*} \sigma_k dx \quad (6-2)$$

$$L = \frac{1}{\pi} \left( \frac{\Delta K_{th}}{\Delta\sigma_0} \right) \quad (6-3)$$

$$r_f = r_{real} + 1 \quad (6-4)$$

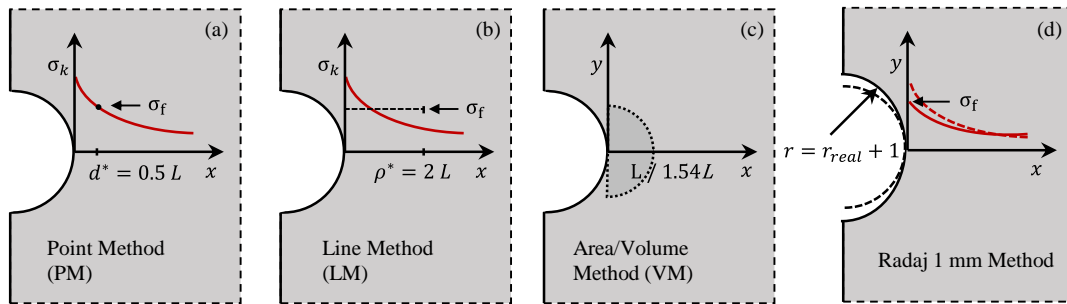


Figure 6-1: Notch stress analysis methods (a) point method, (b) line method, (c) area/volume method, summarized in [28] and (d) Radaj 1 mm method [24]. However, all presented methods show deficiencies when the effective stresses shall be investigated on the basis of a real 3D geometry. The application of 1 mm approach of Radaj requires a change of geometry, which is not possible for 3D-models. The analysis with PM, LM, and VM is possible, but requires a lot of post processing because of the great number of notches in real corroded geometries, requiring all the stress paths to be evaluated individually.

### 6.3.2 Implicit gradient model (IGM) approach

An alternative approach is the implicit gradient model (IGM) introduced by Peerlings [29,30]. The IGM allows considering the micro-support effect for all notches of a component in a single analysis. Different approaches like PM, LM, or VM can be used by selecting appropriate weighting functions [28]. In the case of three-dimensional FE-models, the VM approach is suitable, as it can be implemented in commercial numerical software. Considering this, the effective stress  $\sigma_f(\mathbf{x})$  at the point  $\mathbf{x} = (x_1, x_2, x_3)$  can be described as the integral over the volume  $V$  of the weighting function  $G$ , that is dependent on the distance  $\|\mathbf{x} - \mathbf{y}\|$  between point  $\mathbf{x}$  and any point  $\mathbf{y} = (y_1, y_2, y_3)$ , and a reference volume  $V_r$  as follows:

$$\sigma_f(\mathbf{x}) = \frac{1}{V_r(\mathbf{x})} \int_V G(\mathbf{x}, \mathbf{y}) \sigma_k(\mathbf{y}) dV_y \quad (6-5)$$

Assuming a Gaussian function for the weighting function  $G$ , that approximates the hemisphere in Figure 6-1c, this leads to the following differential equation:

$$\sigma_f(\vec{\mathbf{x}}) - \sigma_k(\vec{\mathbf{x}}) - a \nabla^2 \sigma_f(\vec{\mathbf{x}}) = 0 \quad (6-6)$$

The total volume of the body is considered as the solution domain and the surface is defined as the boundary. Usually the Neumann boundary condition is used [29,31]:

$$\frac{\partial \sigma_f(\mathbf{x})}{\partial \mathbf{x}} \cdot \mathbf{n} = 0 \quad (6-7)$$

where  $\mathbf{n}$  is the normal to the surface of the solution domain.

Considering this, the differential equation (6-6) can be solved to  $\sigma_f$  for any given stress  $\sigma_k$  under specification of the weighting scale factor  $a$ . The weighting scale corresponds to the surrounding volume at the notch and is linked to the intrinsic material length  $L$  defined in equation (6-3) with:

$$a = (\zeta \cdot L)^2 \quad (6-8)$$

where  $\zeta$  considers the stress criterion, which is equal to 0.545 for the maximum principal stress as well as for the Tresca stress criterion and 0.456 for the von Mises stress criterion [32]. With this, the impact of the material can be considered on the basis of linear elastic fracture mechanics. A detailed derivation of the method is provided in the literature [28–30,33,34] and is not discussed here. The application of this method on the examined specimens is described in section 6.5.4.

It should be noted, that for the IGM approach there is no recommendation for choosing a specific stress criterion. However, as the stress analysis is based on 3D-models, which leads to multiaxial stress conditions, the von Mises stress criterion was used in this study. According to Sonsino [35] and Radaj and Vormwald [19] the application of the von Mises criterion for consideration of multiaxial stresses leads to reliable results, if it is applied to ductile materials and in-phase loading.

### 6.3.3 Consideration of residual stresses and mean stress correction

Residual stresses can have an impact on the local mean stress ratio, which in turn can affect the fatigue resistance. In the recommendation of IIW [10] this is considered with the mean stress correction factors  $f(R)$ , which are different for low, medium and high residual stresses.

An alternative approach is the mean stress correction according to Smith, Watson and Topper (SWT) [36], where the fatigue life is assumed to depend on the product of  $\sigma_{max} \cdot \varepsilon_a$ , where  $\sigma_{max}$  is the maximum local stress and  $\varepsilon_a$  is the local strain amplitude. Karakas [37] applied the SWT-criterion on welded magnesium joints. Nykänen and Björk [13,38] employed this correction factor and introduced the mean stress corrected notch stress range as:

$$\Delta\sigma_{f,ref} = \frac{\Delta\sigma_f}{\sqrt{1 - R_{local}}} \quad (6-9)$$

where,  $R_{local}$  is the local mean stress ratio defined as

$$R_{local} = \frac{\sigma_{min}}{\sigma_{max}} \quad (6-10)$$

and  $\Delta\sigma_f$  is the effective notch stress range, considering the notch stress concentration factor  $\alpha_f$  and the nominal stress range  $\Delta\sigma_n$  from the fatigue test:

$$\Delta\sigma_f = \alpha_f \cdot \Delta\sigma_n \quad (6-11)$$

The residual stresses, the secondary bending stresses from the clamping process as well as the mean stresses and the stress amplitudes at the notch base have to be considered in the local mean stress ratio  $R_{local}$ . Figure 6-2 shows the procedure for determining  $R_{local}$ . For this purpose,  $\sigma_{max}$  is first calculated

on the basis of nonlinear material behaviour according to the cyclic stress-strain (CSS) curve by R-O [14] with

$$\varepsilon_{max} = \frac{\sigma_{max}}{E} + \left(\frac{\sigma_{max}}{K'}\right)^{\frac{1}{n'}} \tag{6-12}$$

taking into account all previously mentioned stress components (first branch, load step 1, Figure 6-2). For low-alloyed structural steel, the cyclic strain hardening coefficient is  $K' = 1.65 R_m$ , and the cyclic strain hardening exponent is  $n' = 0.15$  [11,39]. Subsequently,  $\sigma_{min}$  is calculated using the modification of the cyclic-stress-strain curve according to the Masing-hypothesis [40]

$$\frac{\Delta\varepsilon}{2} = \frac{\Delta\sigma}{2E} + \left(\frac{\Delta\sigma}{2K'}\right)^{\frac{1}{n'}} \tag{6-13}$$

where only the variable part of the stress, the stress range  $\Delta\bar{\sigma}$ , is taken into account (second branch, load step 2, Figure 6-2). Any further load and unload branches are performed according to the Masing hypothesis, as long as the external load remains unchanged.

The calculation of the stresses can be performed numerically if the nonlinear CSS-curve is defined with kinematic hardening. Kinematic hardening causes the unloading and reloading branches to be consistent with the Masing-hypothesis, which overcomes the need for separate consideration of the branches. Alternatively, the stresses can be approximated by projecting the elastic response curve (see elastic response curve, Figure 6-2b) on the CSS-curve by means of the Neuber hyperbola [41]. Neuber's approach is based on the assumption that the elastic and elastic-plastic stresses perform the same incremental work [42]:

$$\sigma_{max,el} \varepsilon_{max,el} = \sigma_{max} \varepsilon_{max} \tag{6-14}$$

Incorporating equation (6-12) into equation (6-14) and solving the resulting nonlinear equation leads to local elastic-plastic stress  $\sigma_{max}$ . This is calculated separately for the initial load branch (load step 1, for  $\sigma_{max}$ ) with the R-O curve and for the unloading and reloading branches (load step 2, for  $\sigma_{min}$ ) with the Masing curve. More details regarding application of the method is provided in section 6.5.6.

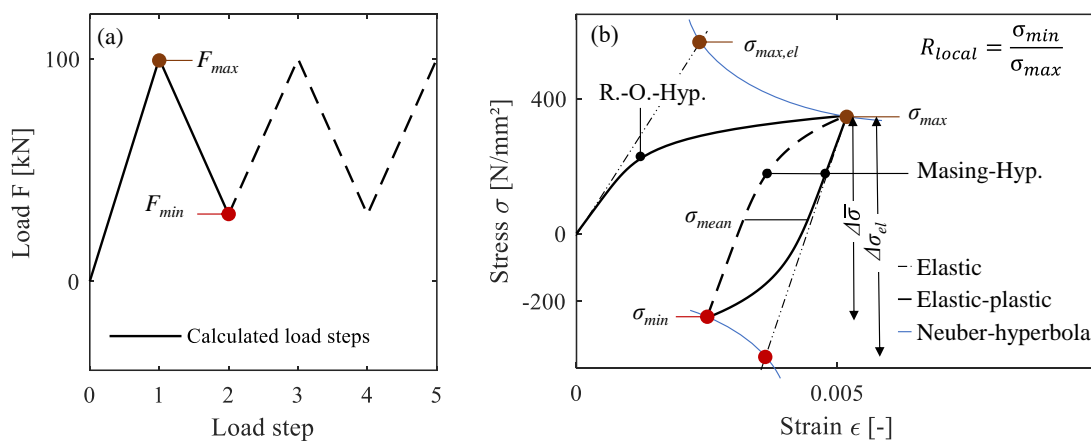


**Figure 6-2: Procedure of calculating the local mean stress ratio  $R_{local}$  (a) illustration of load steps in fatigue tests and (b) resulting stress-strain behaviour at the notch base with typical hysteresis**

## 6.4 Experiments

### 6.4.1 Fatigue tests

Fatigue test were conducted on butt-welded (S) and fillet welded specimen (K), including non-load carrying transverse stiffeners (see Figure 6-3a). The fillet welds were produced by gas metal arc welding (GMAW) and had a thickness of 4 mm. The butt welds were produced by submerged arc welding (SAW). Both specimen series were made of S 355 ML structural steel. The material properties are summarized in Table 6-1.

**Table 6-1: Material properties S 355 ML**

Chemical composition [%]								
C	Si	Mn	P	S	N	Al	Cu	Cr
0.06	0.27	1.37	0.012	0.001	0.005	0.036	0.02	0.03
Mechanical properties:								
Yield stress $R_{p0.2}$ [N/mm <sup>2</sup> ]			Ultimate strength $R_m$ [N/mm <sup>2</sup> ]			Elongation $A_5$ [%]		
421			493			35		

Part of the specimens were clean blasted after production and subsequently, a part of the clean blasted specimens were subjected for one month to the standardized neutral salt spray (NSS) test according to ISO 9227 [17]. Hence, three different surface conditions were tested: as-welded, clean blasted – uncorroded, and clean blasted corroded. All specimens were tested in a servo-hydraulic fatigue testing machine on a mean stress ratio  $R = 0.1$  and a test frequency of 8-10 Hz. The DIC-system GOM ARAMIS 12M was employed to observe the crack initiation formation during the fatigue tests. Figure 6-3 (b) illustrates the fatigue test configuration including the DIC system for the butt-welded specimens. For the fatigue tests, the specimens were clamped on both sides, resulting in additional bending stresses due to the presence of linear and angular misalignments in the specimens. For more details on the specimens, fatigue test, and DIC-measurements, it is referred to [16].

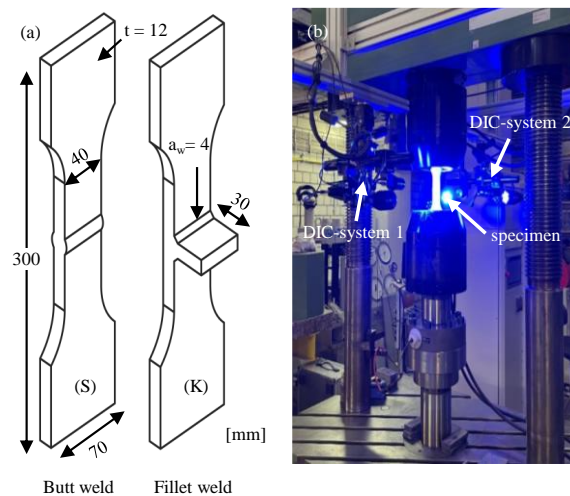


**Figure 6-3: (a) Specimen geometries for butt weld (S) and fillet weld (K), (b) Fatigue test and DIC-system setup**

### 6.4.2 Fatigue test results

In Figure 6-4 (a) the obtained results are shown for butt welds and in Figure 6-4 (b) for fillet welds, for each surface condition, in a stress-life (SN) diagram based on the nominal stresses. The results are used to derive the corresponding SN-curves, which are defined as:

$$N = 2 \cdot 10^6 \cdot \left( \frac{\Delta\sigma_c}{\Delta\sigma_n} \right)^m \tag{6-15}$$

In the equation,  $N$  represents the number of cycles to failure,  $\Delta\sigma_n$  is the variable nominal stress range,  $m$  is the slope, and  $\Delta\sigma_c$  is the characteristic stress range at  $N = 2 \cdot 10^6$  cycles. Furthermore, the scatter coefficient  $T_\sigma$  was evaluated for both geometries. This is defined as

$$T_\sigma = \frac{\Delta\sigma_{c,10\%}}{\Delta\sigma_{c,90\%}} \tag{6-16}$$

where  $\Delta\sigma_{c,10\%}$  and  $\Delta\sigma_{c,90\%}$  are the characteristic fatigue strengths derived from the SN-curve for 10 % and 90 % survival probability at  $N = 2 \cdot 10^6$  cycles. For both geometries it is visible that the fatigue strength is lowest for the as-welded situation. Clean - blasting leads to increased fatigue strength, while subsequently corrosion exposure leads to reduction. With  $T_\sigma = 1.75$  for butt welds and  $T_\sigma = 2.01$  for fillet welds, high scattering of the data can be observed, as a result of different surface conditions.

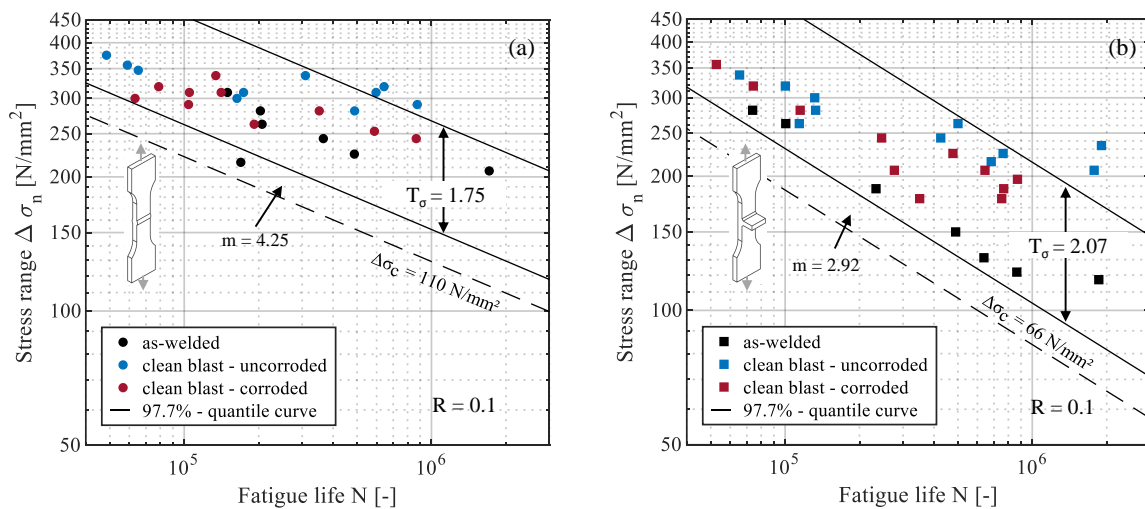


**Figure 6-4: Fatigue test results for as-welded, clean blasted – uncorroded and clean blasted – corroded specimens with corresponding scattering of the SN-curve for (a) butt welds and (b) fillet welds**

## **6.5 Numerical analysis and fatigue strength assessment**

### **6.5.1 Reverse engineering and numerical model**

The reverse engineering process for the examined specimens in this study included several steps, see Figure 6-5. The procedure started with scanning the whole specimen with the optical 3D-scanner ATOS Core 300 5M from GOM with a resolution of 0.12 mm. Here, the specimen was positioned at a distance of 500 mm, scanned from different angles and subsequently merged into one 3D-model in STL-format (Figure 6-5a). In order to ensure a high accuracy at the weld seams, which are most critical regarding fatigue strength, additional measurements were performed using the 3D-profilometer Keyence VR-3000 with a resolution of 0.02 mm (Figure 6-5b and d). In the next step, the welded area was cut off from the global STL-model (Figure 6-5c) and replaced with the high-resolution scan of the profilometer utilizing the best fit algorithm of the software GOM Correlate (Figure 6-5e).

For the numerical analysis the final STL-model was converted into a solid model. This transformation is necessary for two major reasons. Firstly, the STL-format consists of discrete facets that are connected to each other, resulting in non-continuous curvature of the surface leading to singularities in the following numerical analysis. Secondly, the surfaces in the STL-format require a large amount of data to represent the model accurately, as it is built of a high number of points, lines, and facets.

The method for obtaining a solid model from the STL format is described in the work of Shojai et al. [16]. It involves utilizing Non-Uniform Rational B-Spline (NURBS) surfaces, which are two-dimensional, mathematically defined polynomial functions of higher order that can fit the shape of the faceted geometry. NURBS surfaces offer several advantages, including the need for less data to describe the surface and continuous curvature.



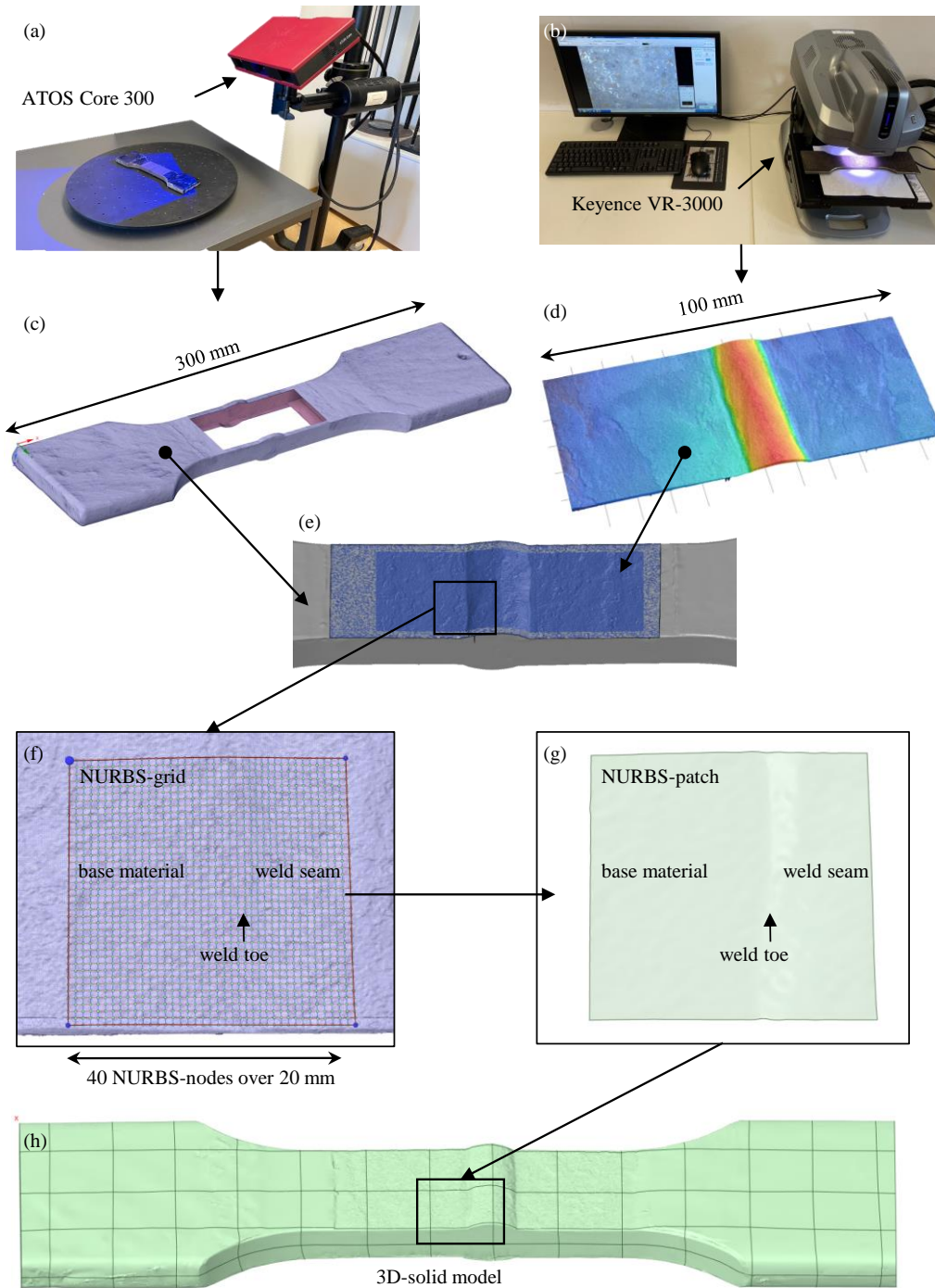


**Figure 6-5: Reverse engineering procedure shown exemplarily for a corroded butt-welded specimen , (a) scanning of the whole specimen with ATOS Core 300, (b) scanning of the welded area with Keyence VR-3000 with higher resolution than in (a), (c) STL-geometry as result of ATOS Core 300, (d) result of the welded area from Keyence VR-3000, (e) assembled STL- model from (c) and (d), (f) generation of a NURBS-patch based on the STL-model, (g) generated NURBS-patch, (h) 3D-solid model assembled from individual NURBS-patches**

However, it is not possible to create a solid model by transferring the entire STL-model into a single NURBS surface. Instead, the surface is divided into NURBS-patches [3] [4], which are then merged

to form the final solid model. In Figure 6-5 (f) the generation of a single NURBS-patch from the STL-model is illustrated. Therefore, the reverse engineering module of ANSYS SpaceClaim is utilized.

The quality of the fit depends on the number of polynomial functions per area, which can be controlled through the grid rate, as discussed in Shojai et al. [16]. In Figure 6-5 (f), for example, a NURBS-grid with 40 nodes on a length of 20 mm, resulting in a grid rate of 2 [1/mm], is illustrated. Based on investigation with different grid rates, a grid rate of 7-8 [1/mm] has been determined as sufficient and was used for all specimens.

The solid model resulting from the reverse engineering process is illustrated in Figure 6-6 (a1) to (a3) for fillet welded specimen after one-month corrosion exposure in the NSS. It can be seen, that the solid model is very precise at the weld toe, as the surface irregularities due to corrosion, such as pitting corrosion, are also captured in the model (see, Figure 6-6a1). For the mesh, quadratic tetrahedral elements (SOLID187 in ANSYS) with an initial element size of 0.4 mm at the weld area and 2.0 mm at all other areas were used. An adaptive convergence study led to element sizes of 0.05 mm at the weld toe and  $10^6$  to  $10^7$  nodes for each specimen, see Figure 6-6 (b3).

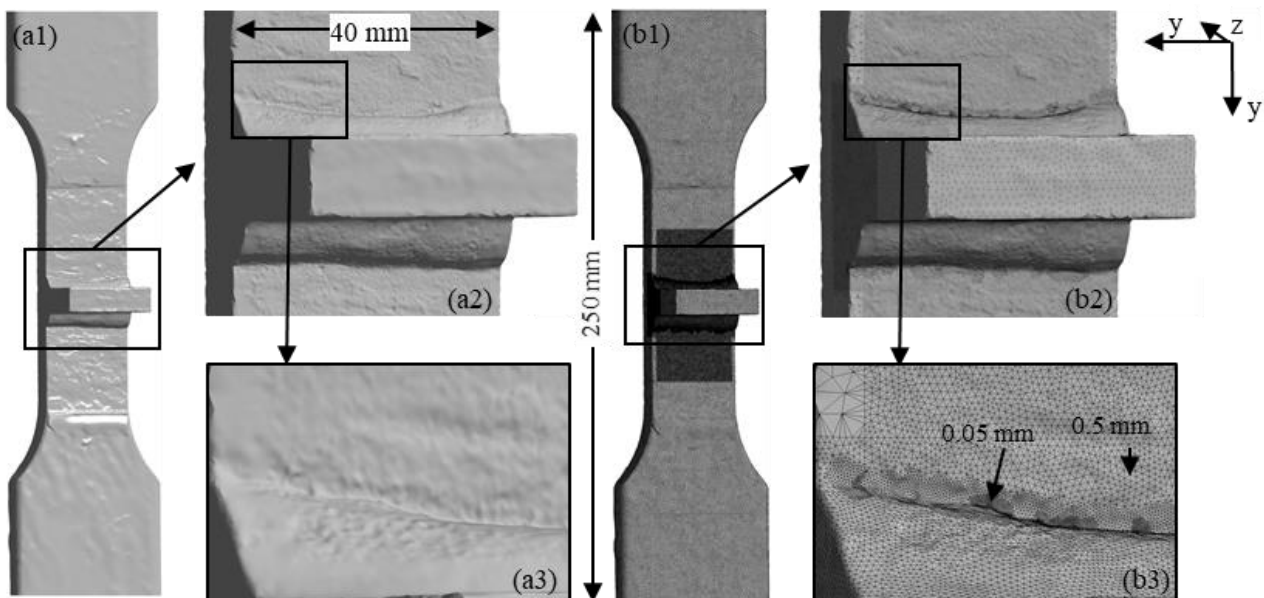


**Figure 6-6: Numerical 3D-model of a fillet welded specimen in corroded condition , (a1-a3) 3D-solid model after reverse engineering process and generation of NURBS-patches, (b1-b3) discretization of the solid model with different element lengths for weld toe and base material area**

### 6.5.2 Analysis of bending stresses

As already mentioned, the specimen included linear and angular misalignment after the fabrication. In the clamping process, where one side of the specimen (here the upper side) is clamped first, this results in an offset between the ends of the specimen. While the existing offset between the ends is

eliminated by clamping the lower side, it leads to additional secondary bending stresses, which increase the effective R-ratio. Figure 6-7 shows the numerical simulation of this process.

For the numerical simulation, the model and the mesh from Figure 6-6 were used. The consideration of the S355 structural steel is achieved via a nonlinear material definition with a yield strength of  $R_m = 355 \text{ N/mm}^2$ . The boundary conditions are applied according to the experimental tests, see Figure 6-7 (a). The offset is calculated for each specimen separately with a MATLAB-tool based on the scanned data of the whole specimen and applied as a displacement in z-direction. From comparison of the plain line illustrated in Figure 6-7 (a) and (b), it becomes evident that the offset is eliminated after application of the deformation. Moreover, from Figure 6-7 (c) – (e) it appears, that the resulting von Mises stresses reach the yield strength at the weld toe. The magnitude of the stresses depends on the magnitude of the offset and on the notch sharpness. For nearly all fillet-welded specimens the stresses reached the yields strength. For butt-welded specimens the offset and the notch sharpness at the weld toe are lower than in fillet-welded specimen, resulting in lower stresses respectively. In Table 3-5 the offset and the resulting stresses for all examined specimens are listed. It should be noted, that the listed stresses were evaluated at the real crack location, which not always coincided with the maximum stress location. This is especially true for butt-welded specimen, where the clamping process induced tensile stresses on one side of the weld, and compressive stresses on the opposite side of the weld. In some cases, the crack occurred on the compression side of the specimen. This occurred, when the weld notch was sharper on the compression side and at the same time the stresses from clamping were low. Under these circumstances, the sharp notch led to higher stresses under axial fatigue loading, which in total with the compressive stresses were higher than on the side with tensile stresses. For these cases, the normal stresses are documented instead of the von Mises stress (see specimens 00-S-10 and 0-S-11, Table 3-5).

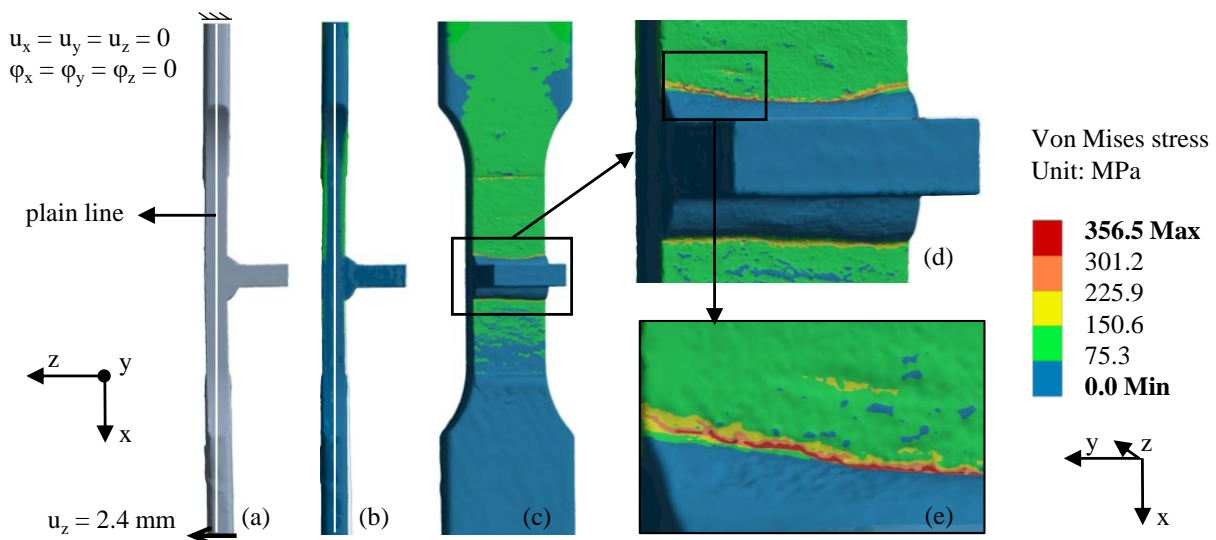


**Figure 6-7: Numerical analysis of the clamping process, (a) 3D-model with angular misalignment and the resulting offset at the lower side of the specimen (compared to the plain line), (b) straightened 3D-model after application of the offset  $u_z$ , (c-e) resulting von Mises stresses from the clamping process with nonlinear material definition for the whole specimen and the weld area**

### 6.5.3 Numerical analysis of stress concentration

The stress concentrations are calculated based on linear elastic material formulation. Therefore, the deformed model from the clamping process is utilized for the analysis. Analogous to the fatigue test, the model is fixed on both sides, allowing only axial deformation, see Figure 6-8 (a). The applied force equals the magnitude of the cross section in the tailed area with  $F = |A_{nom}| = 480 \text{ N}$ , which leads to a nominal stress  $\sigma_n = 1 \text{ N/mm}^2$  and allows the resulting notch stresses to be interpreted as notch stress concentrations ( $\sigma_k = \alpha_k$ ). It should be noted, that for all specimens, the initial cross section before clean blasting and corrosion was considered.

The results of the numerical analysis are shown in Figure 6-8 (b) – (e). The highest stress concentrations are occurring, as expected, at the weld toe and are resulting from the notch geometry. From the stress distribution in Figure 6-8 (b), it can be seen that there is a stress gradient from the upper to the lower surface of the specimens, especially at the welded area of the specimen. This is considered as a structural stress  $\sigma_S$  resulting from the global curvature of the specimen. The curvature remains although the offset of the specimen shown in Figure 6-7 (a) was eliminated during the clamping process. The high stress concentrations are hence a result from the interaction of global structural geometry and local notch geometry.

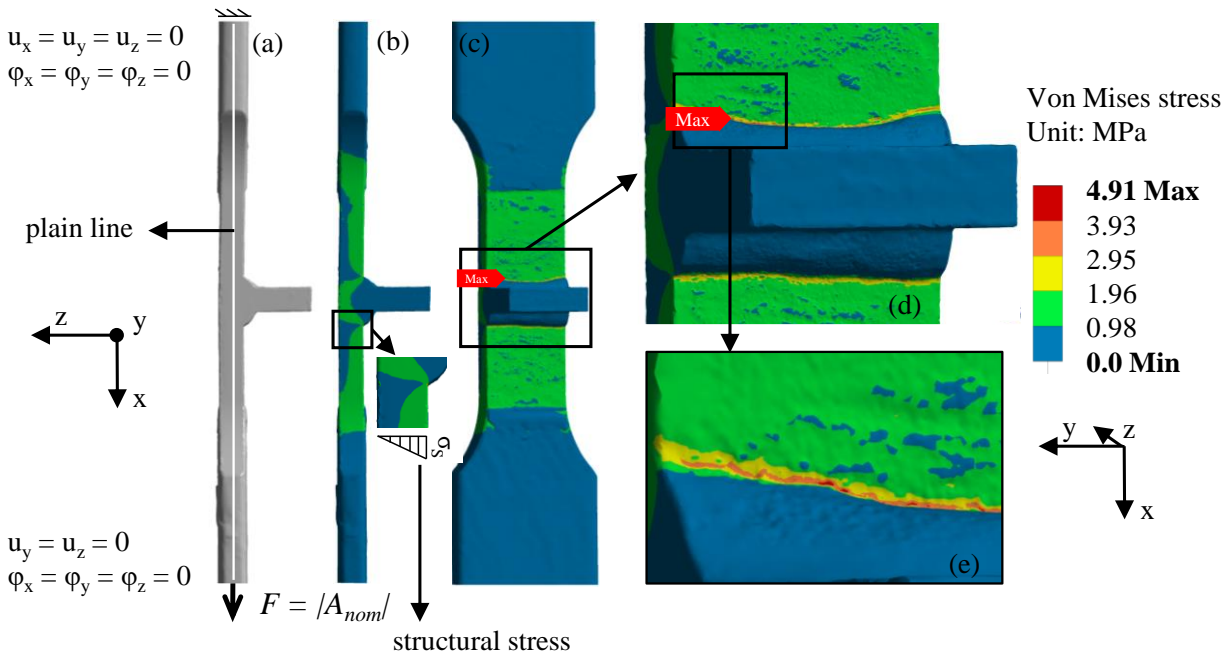


**Figure 6-8: Numerical analysis of stress concentrations based on linear elastic material definition, (a) straightened 3D-model from clamping process with corresponding boundary conditions, (b-c) resulting von Mises stresses for the whole specimen and (d-e) at the weld area**

### 6.5.4 Consideration of micro-support effect with IGM

For consideration of the micro-support effect with IGM the differential equation (6-6) has to be solved to  $\sigma_f$ . For one- or two-dimensional problems, the equation can be solved by implementation in

MATLAB. For three-dimensional problems, it is recommended to use the solvers of commercial FE-software. According Lang et al. [43] and Lener et al. [44] it can be solved with the thermal analysis module of commercial FE-software, as equation (6-6) is similar to the differential equation of the thermal diffusion problem. For more information on the numerical implementation, it is referred to Shojai et al. [45].

In this study, the thermal analysis module of ANSYS Workbench is used to solve equation (6-6). For this purpose, the elastic notch stresses  $\sigma_k (= \alpha_k)$  are used as input values for the diffusion analysis for each individual node of the numerical model from Figure 6-6 (b1). The Neumann boundary condition according equation (6-7) is considered with a ‘heat flux’ boundary condition of  $\dot{q} \approx 0$  applied to the surface of the specimen ( $\dot{q} = 10^{-20}$  in ANSYS Workbench). The weighting parameter  $a$  is linked to the thermal properties with  $a = \frac{\lambda}{\rho_d \cdot c_p}$  and is considered with the thermal conductivity parameter  $\lambda$ , as the specific heat capacity and density were set to  $c_p = 1.0$  and  $\rho_d = 1.0$ .

**Results:** In Figure 6-9 the calculated effective notch stress concentrations  $\alpha_f$  are shown in dependence of the weighting parameter  $a$  for two different locations. In black, the location of the maximum stress concentration before micro-support consideration (indexed with ‘initial, max’) and in red, the actual crack location from fatigue test (indexed with ‘crack’) is illustrated. For very small weighting parameters, for example  $a = 0.0001 \text{ mm}^2$  the value of  $\alpha_{f,initial,max}$  is higher than  $\alpha_{f,crack}$ . With greater weighting parameters, the stresses are averaged over a greater volume, leading to lower effective stress concentrations. Moreover, it can result in a change of the maximum stress location, as it is the case for  $a \geq 0.003 \text{ mm}^2$  in Figure 6-9.

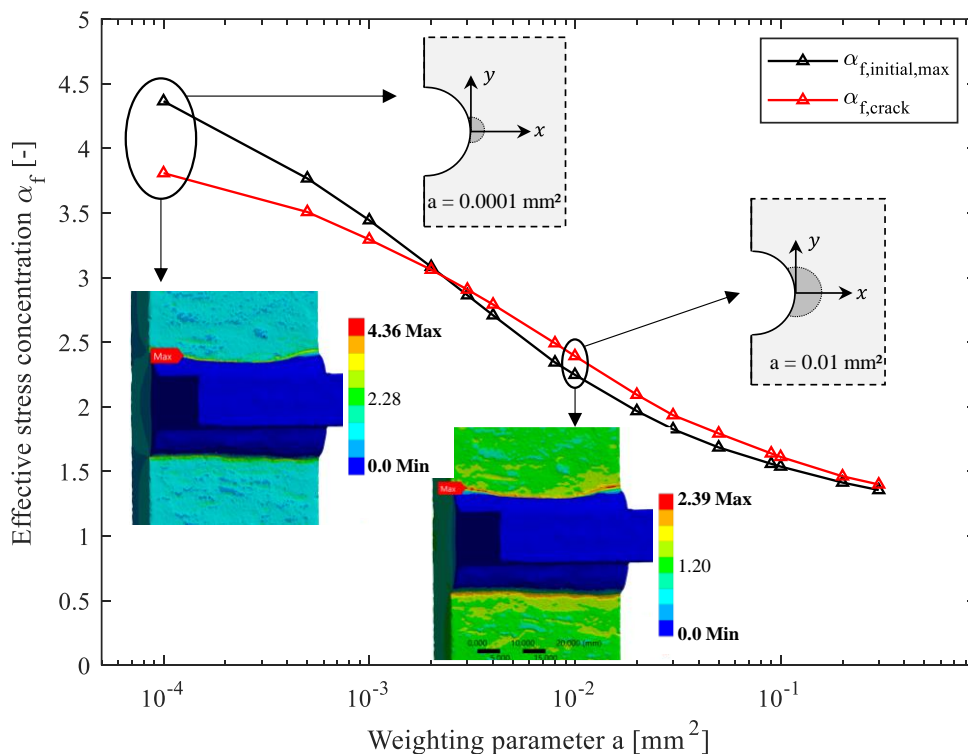


**Figure 6-9: Effective stress concentrations  $\alpha_f$  in dependence of the weighting factor  $a$  for specimen No. 1-K-1**

Various weighting parameters for IGM analysis have been proposed in the literature for mild steel, depending on the chosen stress criterion and the R-ratio. Askes et al. [28] considered  $a = 0.027 \text{ mm}^2$  for  $R = 0$  and  $a = 0.014 \text{ mm}^2$  for  $R = 0.4$  for mild steels, based on the material parameters  $\Delta K_{th}$  and  $\Delta\sigma_0$  and taking into consideration the maximum principal stress criterion. Tovo et al. [33] used  $a = 0.04 \text{ mm}^2$  for weld seams and  $R = 0$ . Beside this, the micro-structure at the surface itself, which is different for all studied surface conditions, can have a role on the weighting parameter. Although in this study the fatigue tests were conducted with  $R = 0.1$ , the effective R-ratio due to additional bending moments from the clamping process are in the range of  $R_{eff} = 0.3$  to  $R_{eff} = 0.5$ . Assuming an effective R-ratio of  $R_{eff} = 0.4$  for all specimen and considering, that the stress concentrations are based on the von Mises stress criterion, which with  $\zeta = 0.456$  (compare equation (6-8)) leads to smaller weighting factors than for the maximum principal stress criterion, it is reasonable to assume  $a = 0.01 \text{ mm}^2$  for all specimen in this study.

### 6.5.5 Comparison of DIC and effective stress concentrations

The DIC measurements were performed during the fatigue tests with the GOM ARAMIS 12M system. Depending on the load level, an image was taken after 500-2000 load cycles in order to monitor the crack initiation and crack development. For more details on the measurement and the crack definition it is referred to [16].

In Figure 6-10 (a1)-(f1) the results of DIC measurements are illustrated for a fillet-welded specimen in the corroded condition. It is shown, how the crack initiates at the weld toe (d1) and propagates (e1) until final rupture (f1). In Figure 6-10 (a2)-(g2) the results of the effective stress concentrations  $\alpha_f$  are illustrated for the same specimen. The comparison of crack initiation location from DIC-results (d1) with the hot-spot location from the numerical analysis (d2) reveals a good match.

Also, the comparison of the butt-welded joints shows a good agreement between the crack locations from DIC and the effective stress concentrations (see Figure 6-11 d1 and d2). It should be noted that for butt-welded joints the hot-spot from numerical analysis is not as expected at the location of the minimum weld toe radius or maximum flank angle (see Figure 6-11 e2-g2). This is because the local stress concentrations from the weld geometry are superposed with the global stress magnification due to misalignments. In the case of butt-welded joints, this leads in many cases to the effect that the stress concentrations on the side of mild weld toe notches are increased with additional tensile stresses, while on the side of sharp weld toe notches the stress concentrations are reduced by compressive stresses.

Up to 27 butt-welded and 30 fillet-welded specimens were analysed in this way. A match between crack location from fatigue test and the hot-spot from numerical analysis is present, when the stress concentrations ratio at crack location and the hot-spot is higher than 0.95. With this, inaccuracies in the entire modelling process can be considered. The percentage of the match are summarized in Table 6-2. For butt-welded specimens a match occurs for 80-90% of the specimens, regardless of the surface condition. For fillet-welded specimen there is a 100% match for the clean blasted – uncorroded and clean blasted – corroded specimen, while for the as-welded specimen there is only little match. This

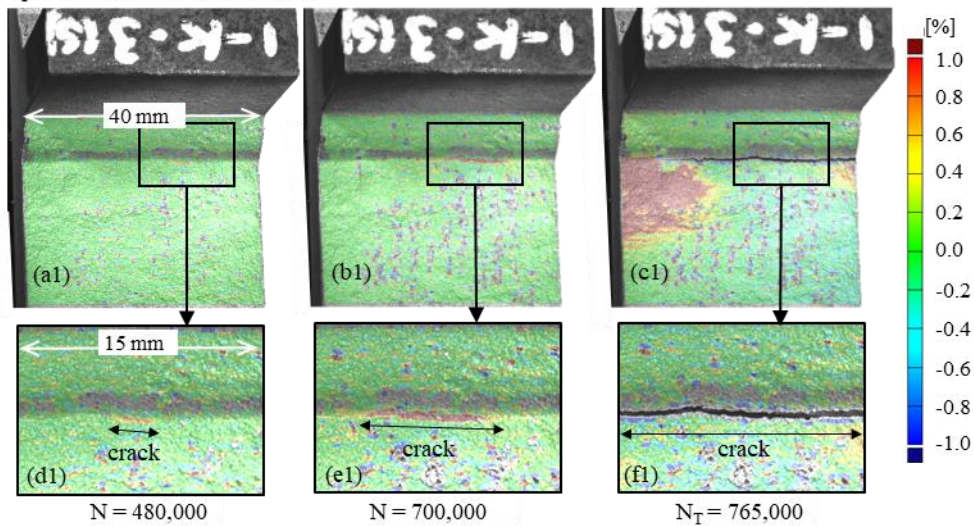


can be attributed to the weld process causing slag which was not removed in the area of the weld toe. This affects the scanned weld geometry and leads to an incorrect prediction of the crack location. However, the high agreement of the crack location with the numerical hot-spot justifies the modelling process and supports the assumption made regarding the weighting parameter.

**Table 6-2: Match of crack location and numerical prediction**

Geometry:	Butt-welds joints			Fillet-welded joints		
Surface condition:	As-welded	Clean blasted – uncorroded	Clean blasted – corroded	As-welded	Clean blasted – uncorroded	Clean blasted – corroded
Number of matched specimen / Number of considered specimen:	6/7 = 85%	8/10 = 80%	9/10 = 90%	4/7 = 57%	12/12 = 100%	11/11 = 100%

Specimen 1-K-03 – DIC results



Specimen 1-K-03 – Numerical analysis

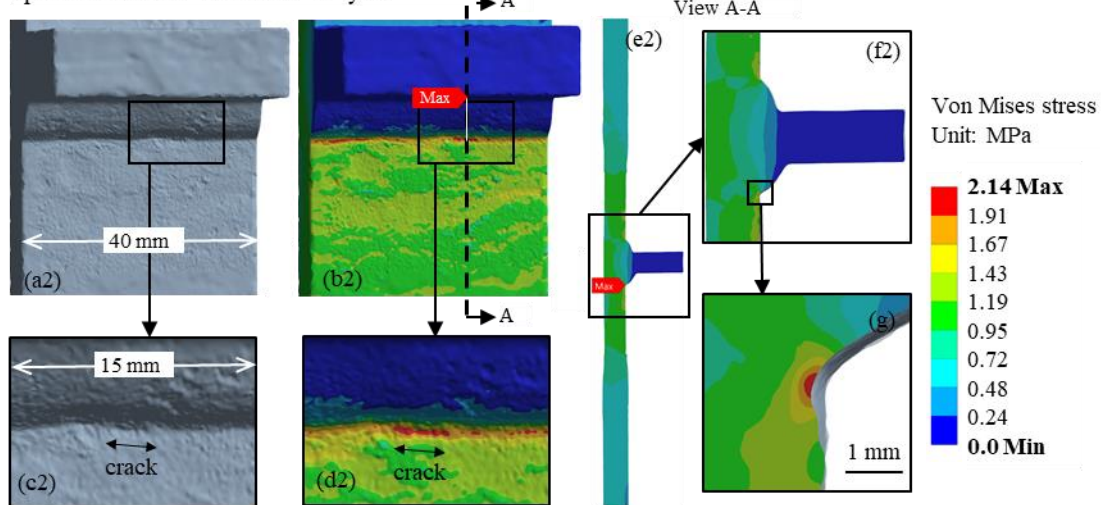


**Figure 6-10: Comparison of DIC results for different load cycles (a1-f1) with numerical determined stress concentration (a2-g2) for corroded fillet weld specimen no. 1-K-03**

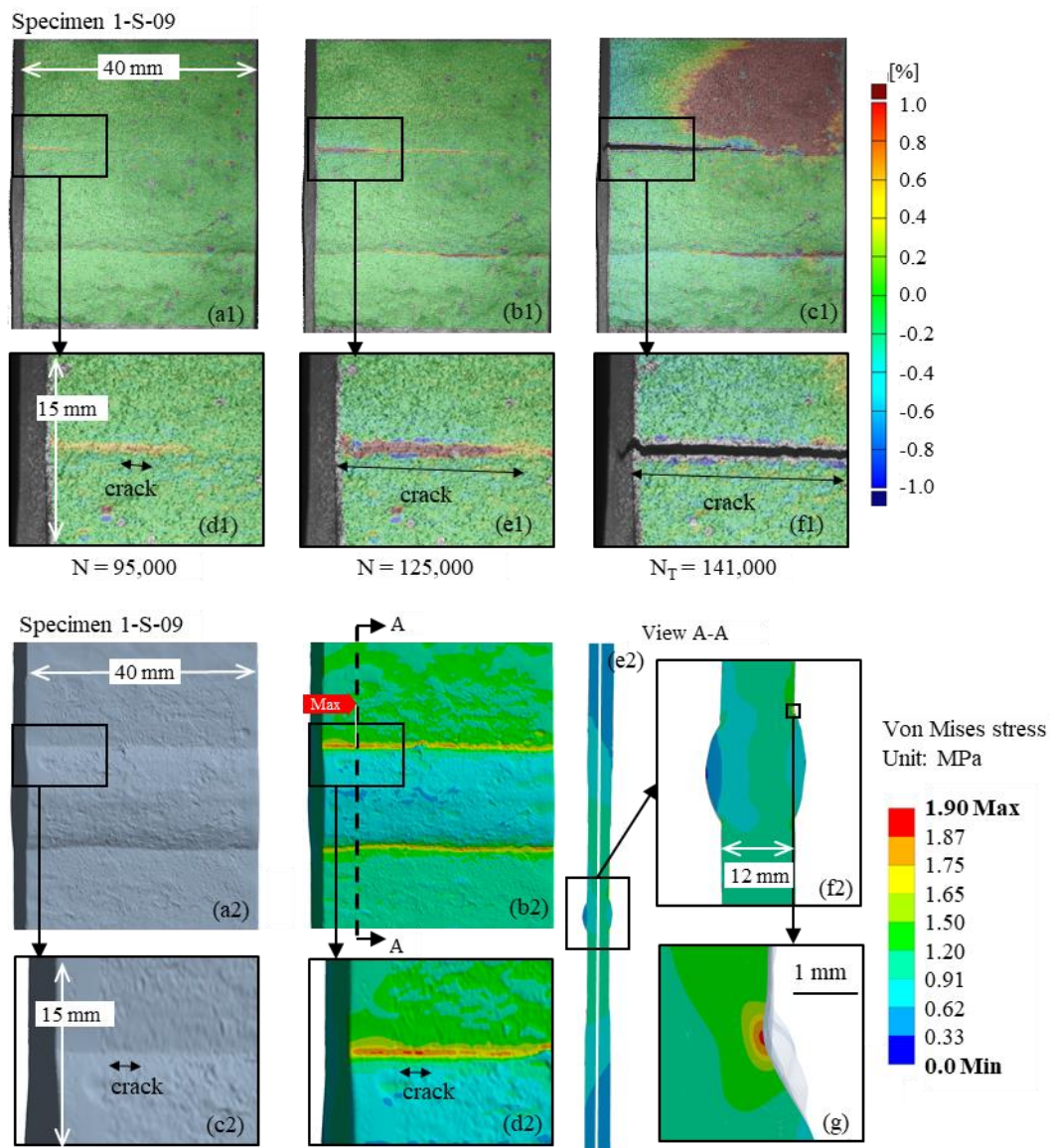


Figure 6-11: Comparison of DIC results for different load cycles (a1-f1) with numerical determined stress concentration (a2-g2) for corroded butt weld specimen no. 1-S-09

### 6.5.6 Fatigue strength assessment

For the fatigue strength assessment all relevant stress components, such as the bending stresses from clamping  $\sigma_b$ , (section 6.5.2), stresses from fatigue test loads with consideration of the micro-support effects  $\sigma_{o,el} = \alpha_f F_{max}/A$  (section 6.5.3) and the residual stresses  $\sigma_{res}$  superposed to the following for each specimen:

$$\sigma_{max,el} = \sigma_{res} + \sigma_b + \sigma_{o,el} \quad (6-17)$$



For  $\sigma_b$  and  $\alpha_f$  the results at the crack location were used. The residual stresses were set based on measurements on fillet-welded specimen from [16]:

- $\sigma_{res} = 230 \text{ N/mm}^2$  for as-welded specimen
- $\sigma_{res} = -20 \text{ N/mm}^2$  for clean blasted – uncorroded
- $\sigma_{res} = 40 \text{ N/mm}^2$  for clean blasted – corroded

The values were applied on fillet- as well as butt-welded specimen. The ultimate strength was set to  $R_m = 491 \text{ N/mm}^2$  based on tensile strength test conducted in [46]. The R-O equation (6-12) and the Neuber-hyperbola (6-14) are utilized to calculate the elastic-plastic stress  $\sigma_{max}$  from the elastic stress  $\sigma_{max,el}$ . In the second step, the elastic-plastic stress range  $\Delta\bar{\sigma}$  is calculated from the elastic stress range  $\Delta\sigma_{el}$  accordingly, but on basis of the Masing equation (6-13). The elastic stress range considers only the variable loads from fatigue test and is defined with  $\Delta\sigma_{el} = \alpha_f (F_{max} - F_{min})/A$ . The minimum elastic-plastic stress can then be derived with  $\sigma_{min} = \sigma_{max} - \Delta\bar{\sigma}$  and be utilized to calculate  $R_{local}$ , which in turn is used for the mean stress correction of the notch stress ranges  $\Delta\sigma_f$  according equation (6-9).

The mean stress corrected notch stresses  $\Delta\sigma_{f,ref}$  and their corresponding fatigue life from fatigue tests are plotted for both specimen geometries and each surface condition separately in Figure 6-12. The statistical evaluation is performed following Deming regression, which is based on the least squares method but, in contrast to the proposed method of Eurocode [47] and IIW [10], includes the uncertainties of both, the x- and the y-axis. This has the advantage that the results can be well approximated even in the high cycle regime. For further information about this regression type, it is referred to [38]. On this basis, the slope  $m$ , the 95%-quantile curve and the characteristic fatigue strength  $\Delta\sigma_{c,ref}$ , defined at  $N = 2 \times 10^6$ , were determined for each specimen series. In addition, the scatter ratio  $T_\sigma$  was determined. From Figure 6-12 it becomes apparent, that the scatter is very low, in particular, for the fillet-welded specimens. This becomes clearer, when the scatter from the notch stress method is compared with that from the nominal stress method, summarized in Table 6-3.

**Table 6-3: Comparison of nominal stress curves with mean stress corrected notch stress curves**

Geometry	Surface condition	Nominal stress curves			Notch stress curves		
		Slope m	$\Delta\sigma_c$ [N/mm <sup>2</sup> ]/ $P_s = 97.7\%$	Scatter $T_\sigma$	Slope m	$\Delta\sigma_{c,ref}$ [N/mm <sup>2</sup> ]/ $P_s = 97.7\%$	Scatter $T_\sigma$
Butt weld	As-welded	-3.9	75	2.31	-11.7	326	1.20
	Clean blasted - uncorroded	-9.4	206	1.32	-15.3	369	1.29
	Clean blasted - corroded	-6.7	150	1.42	-7.6	343	1.11
Fillet weld	As-welded	-3.2	73	1.51	-6.2	280	1.12
	Clean blasted - uncorroded	-6.7	161	1.29	-8.9	372	1.12
	Clean blasted - corroded	-3.8	103	1.43	-6.1	306	1.11

For every series the scatter is narrower with the notch stress method, while the slope is shallower. Comparing the characteristic fatigue strengths  $\Delta\sigma_{c,ref}$ , it becomes evident that for both specimen geometries the as-welded series has the lowest values, while the clean blasted – uncorroded has the highest, and the as welded – corroded is in between of both. However, compared to the evaluation based on the nominal stresses, the relative difference is much lower (206 N/mm<sup>2</sup> : 75 N/mm<sup>2</sup> compared to 369 N/mm<sup>2</sup> : 326 N/mm<sup>2</sup> for clean blasted – uncorroded : as-welded butt welds). This shows that the differences in the SN-curves can be greatly reduced by taking the notch geometry and residual stresses into account.

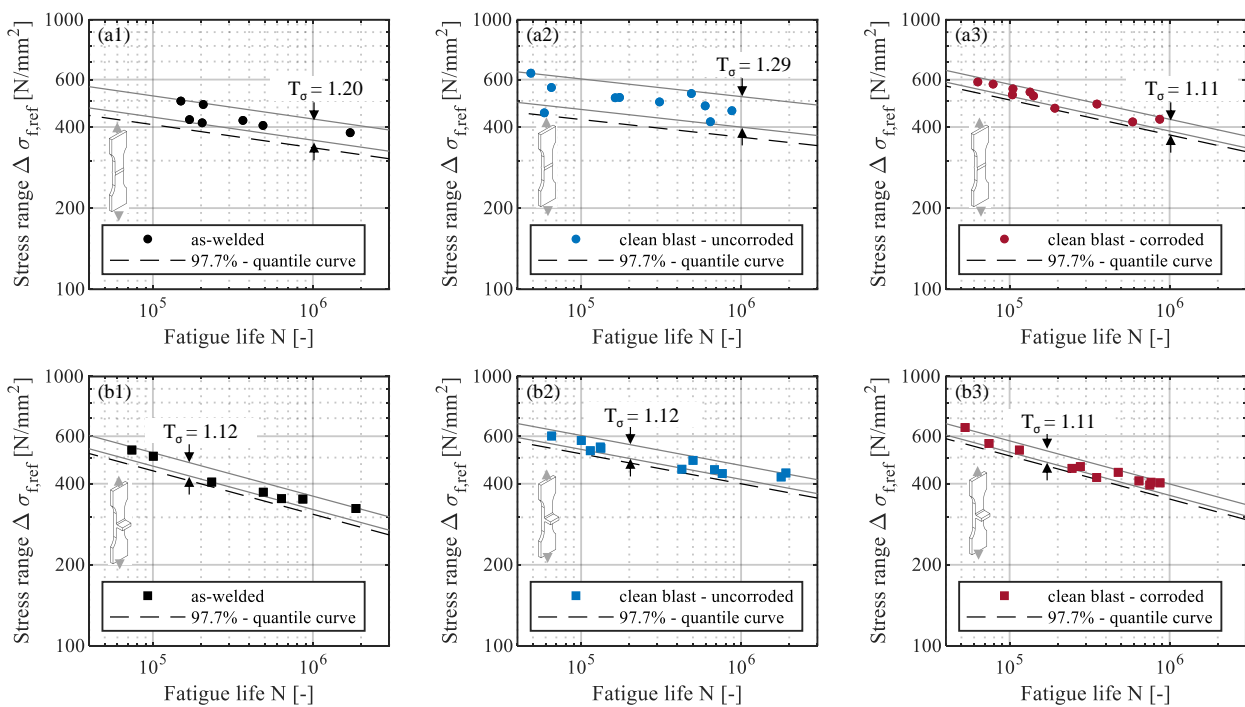


**Figure 6-12: SN-curves based on 4R-method for (a1-a3) butt welded joints, and (b1-b3) for fillet welded joints**

In Figure 6-13 (a) all fatigue test data are plotted in one SN-diagram based on the nominal stresses with  $\Delta\sigma_n$ , indicating a scatter of  $T_\sigma = 2.17$ . In Figure 6-13 (b) all fatigue test data are plotted based on the notch stresses  $\Delta\sigma_f$ , showing a reduced scatter of  $T_\sigma = 1.43$ . Here, only the determined effective notch stress concentrations for every specimen were taken into account, without consideration of bending stresses from clamping process and residual stresses. In Figure 6-13 (c) all fatigue test data are plotted based on the mean stress corrected notch stresses  $\Delta\sigma_{f,ref}$ , considering the bending stresses and the residual stress, leading to a further reduced scatter of  $T_\sigma = 1.26$ . The scatter in the range of low cycles is lower than for high cycles and results mainly from the differences between surface conditions such as the as-welded, clean blasted or corroded specimens. The relatively high scatter from the individual investigations for the butt welds (Figure 6-12 a,b) are within the overall scatter range and therefore do not stand out. It can be seen that for the clean blasted - uncorroded and clean blasted corroded specimens, there are only minor differences between fillet and butt welds. However, for the as-welded specimens, a difference between fillet and butt welds can be observed, which can

be attributed to the previously mentioned issue with the presence of slag during the scan of the fillet welds. In addition, the master curves of Nykänen and Björk [38] for butt-welded joints with FAT 305 and  $m = 5.85$  as well as from Ahola et al. [48] for fillet-welded joints with FAT 288 and  $m = 4.86$  are shown in Figure 6-13 (d). The here determined curve has a much shallower slope with  $m = 7.82$ , but has a comparable fatigue strength of FAT 303 ( $\Delta\sigma_{c,f,ref}$ ). However, it should be noted, that the master curves in [38,48] were derived based on the maximum principal stress criterion, which normally results in higher FAT classes than the evaluation based on von Mises stresses. Thus, the derived curve from this study should only be applied in combination with von Mises stresses.

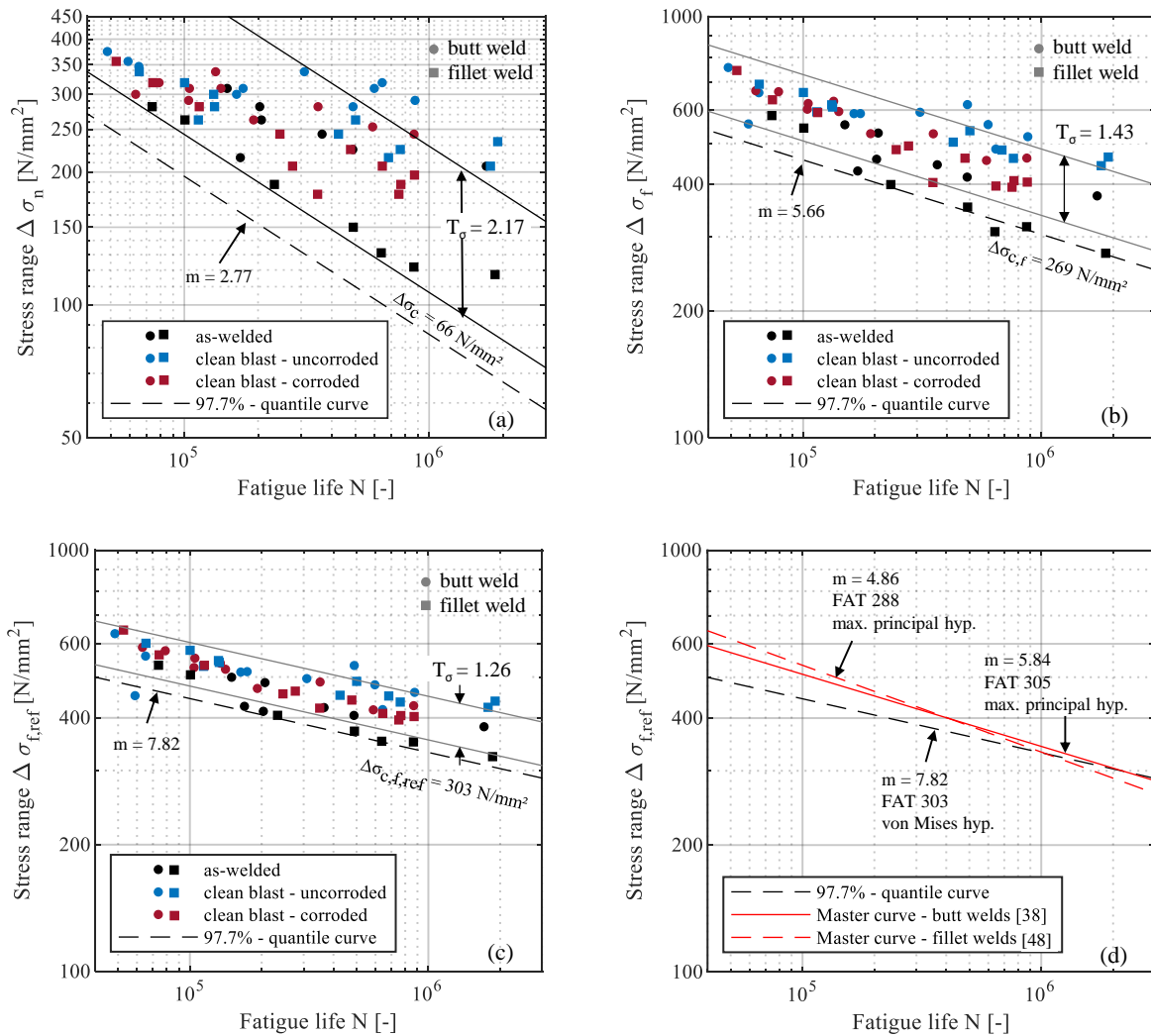


**Figure 6-13: Evaluation of all data based on (a) nominal stresses, (b) notch stresses without consideration of bending and residual stresses, (c) mean stress corrected notch stresses with consideration of bending and residual stresses, and (d) comparison of obtained SN-curve from this study to existing master curves for butt and fillet welds.**

### 6.5.7 Discussion

The fatigue tests have shown that there are differences in fatigue strength between the fillet- and butt-welded as well as between the surface conditions as-welded, clean blasted - corroded and clean blasted - uncorroded, which can be attributed to the notch effect as well as to the residual stresses in the welds. Investigating the effective notch stress concentrations based on the real component and notch geometry led to a reduction of the scatter in the fatigue strength from  $T_\sigma = 2.17$  to  $T_\sigma = 1.26$ . A key factor in determining the effective notch stress concentrations was that the component geometry and the weld geometry were taken into account, as both quantify different stress components. The component geometry takes into account the global stress magnification caused by misalignments of specimens, while the weld geometry quantifies the influence of the weld notch. In the case of butt-welded specimens, it was shown that the stress components partly have a contrary effect and that focusing solely on the weld geometry is therefore not sufficient.

Consequently, a reduced scatter could already be achieved on the basis of  $\Delta\sigma_f$ , where bending stresses and residual stresses were not yet considered, compared to the curve according to the nominal stresses. By taking into account the bending and residual stresses with mean stress corrected notch stresses  $\Delta\sigma_{f,ref}$ , the scatter could be further reduced. However, differences between the individual surface conditions were still visible.

For the as-welded specimens, this difference may to some extent be due to the inaccurate scan of the fillet welds, where residual slag was present. However, since the difference is also observed for the as-welded butt welds, and seen between the clean blasted uncorroded and corroded specimens, another influencing parameter has to be suspected.

In addition, it should be mentioned that the measurements of the residual stresses were only carried out on reference specimens (only fillet welded specimens) in the unloaded condition. Especially for the corroded specimens, there is a high probability that the residual stresses are very scattered due to the different corrosion rates along the weld and therefore a single measurement is not sufficient. Moreover, possible influences from residual stress relaxation and its superposition with the bending stresses from clamping are not sufficiently investigated. This also applies to the consideration of the micro-support effect for the stress components from bending and residual stresses, which can lead to reduction of the stresses and were not considered here. All mentioned uncertainties regarding the residual stresses can eventually reduce the scatter, however, it cannot be excluded that the scatter can also be increased.

Another aspect is the material behaviour in the notch, which may theoretically be included in the calculation via a correlation of the HV hardness and the tensile strength  $R_m$  [49]. The HV values measured in [16] on the weld toes of HV 225, HV 240, and HV 250 (as-welded, clean blasted uncorroded, clean blasted corroded) did not lead to a reduction of the scatter by comparative calculations. However, these HV values were determined at a distance of 0.075 mm from the surface. Since crack initiation occurs directly on the surface, the measured hardness values are probably insufficient. Nevertheless, from the results of the mean stress corrected notch stress approach, it can be assumed that clean blasting improves the material behaviour at the surface, while corrosion deteriorates it. The deterioration may be due to removal of the hardened material, to embrittlement, or to a combination

of both. However, the deterioration in the specimens studied here with one month of exposure in the NSS is not as significant that the material condition is poorer than that of the as-welded specimens.

In addition to the tensile strength  $R_m$ , the material behaviour can implicitly be considered via the intrinsic material length  $L$  according equation (6-3), which among other factors depends on the fatigue crack propagation threshold  $\Delta K_{th}$ . The embrittlement at the crack front caused by corrosion leads to a reduction of the threshold [50] and thus to a reduced value for the intrinsic material length and consequently to a reduced weighting parameter  $a$ . This applies also to the hardening effect from clean blasting, which can increase the  $\Delta K_{th}$  and thus the weighting parameter.

However, the assumption of  $a = 0.01 \text{ mm}^2$  for the weighting parameter does not apply to hardened or corroded steel, even though according to Figure 6-12 very low scattering of the notch stress curves and a high agreement between the crack locations and the hot-spots from simulation of the effective notch stress concentrations could be achieved. Additional investigations have shown that for smaller as well as for larger values than  $a = 0.01 \text{ mm}^2$ , the scatter in the notch stress curves and the agreement of crack location with the hot-spots remains at the same order of magnitude, meaning that also other values for the weighting parameter would fulfil the criterion of low scatter in the fatigue curves and the high agreement of the crack location with the hot-spot.

Based on these results, it is proposed to either consider different weighting parameters, resulting from different  $\Delta K_{th}$  for each surface condition, or introduce a parameter to account for material enhancement by clean blasting and material deterioration through corrosion. In order to consider this issue more precisely in the context of local approaches, both proposals should be defined as future research tasks.

## 6.6 Engineering application

The methods and findings derived from this study can be applied to existing steel structures by means of the so-called replica technique. In the replica technique, a low viscous and fast curing material is used to create an imprint of the inspected weld seam, including the geometrical changes that have occurred on the surface due to corrosion. The imprint is then scanned and converted to a 3D-solid model using the reverse engineering process shown in Figure 6-5. Figure 6-14 presents the application of the replica technique exemplarily on a corroded fillet-welded specimen. Figure 6-14 (c) and (d) shows the original specimen and the corresponding scan (carried out with Keyence VR 3000). Compared with the scan of the replica, it can be seen that areas with very fine notches/pits on the base material cannot be reproduced well. However, it can be seen that the weld toe, which is the decisive area, is well reproduced.

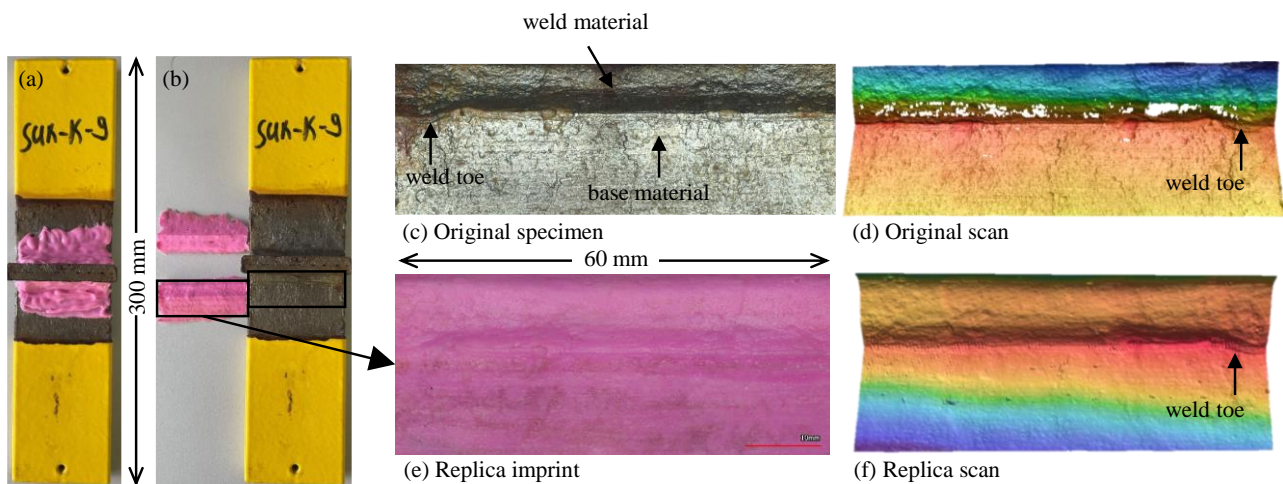


**Figure 6-14: Replica technique applied on corroded fillet-welded specimen, (a,b) corroded welded specimen, (c) original specimen, (d) original scan, (e) replica imprint, (f) replica scan**

Previous studies using the replica technique on corroded base material [18,45] have shown that the replica technique could not capture the pits in the magnitude of the roughness, but due to the micro-support, which has to be taken into account, they did not become relevant. Thus, the procedure provides a possibility to transfer the findings from this study to real structures.

## 6.7 Summary and Outlook

The aim of this work was to apply local fatigue methods in order to investigate the influence of corrosion on welded details, typically used in bridges or offshore support structures. The goal was to consider the fatigue driving factors separately and to quantify their influence.

The relevant factors of the welded specimens are the geometrical imperfections resulting from misalignments in the specimens, the weld geometry and the residual stresses. All data for this were already obtained experimentally for as-welded, for clean blasted – uncorroded, and for clean blasted – corroded specimens in a previous study [16].

For consideration of the geometrical imperfections and the weld geometry, the 3D scan data were transferred into a numerical model. With this model, both the notch effect and the bending stresses from the clamping process could be investigated. The residual stresses were taken into account together with the bending stresses via the mean stress correction factor according to SWT. The following findings could be drawn from this study:

- The influence of global stress magnification, here due to misalignments in the specimens, and the stress concentrations from the weld geometry must be taken into account as a whole, as they can have a contrary effect. Here, particularly in butt-welded specimens, the tensile stresses from the bending moment, resulting from the clamping process, occur at the points where the notch radius is greater than on the side with compressive stresses. Hence, a separate consideration and subsequent superposition will lead to over- or underestimation of the actual stress and thus increase the scatter in the SN-curves.

- The analysis of bending stress as a result of the clamping process showed for fillet welded specimen stresses up to the yield stress of 355 N/mm<sup>2</sup>, while for the butt welds the stresses were lower. Compared to the residual stresses of 220 N/mm<sup>2</sup> considered for the as-welded condition, this is a great value and must therefore be considered in the fatigue analysis.
- It was observed that by consideration of both the residual stresses and the bending stresses from clamping, SN-curves shows a narrower scatter of  $T_\sigma = 1.26$ .
- Despite the narrow scatter of  $T_\sigma = 1.26$ , a difference is still noticeable between the as-welded, clean blasted uncorroded, and clean blasted corroded specimens. This difference is attributed to the material behaviour on the surface, which is different for each specimen series, and can be taken into account by introducing an enhancement/deterioration parameter.
- The comparison between the location of crack initiation determined by DIC and the hot-spot from the numerical calculation have shown a good agreement for the majority of the specimens and thus underline the approach.

From the results of this study, it can be concluded that on one hand the fatigue behaviour of corroded weld de-tails can be reduced to a few relevant parameters and on the other hand that it is possible to consider them using local concepts. The presented methods can also be used for a probabilistic calculation if an extensive amount of data on stress concentrations and residual stresses are available. This would enable a reliability-based calculation of the remaining service life of existing structures. However, before extending the methodology towards probabilistic applications, the consideration of local material changes due to clean blasting and corrosion should be explored in more detail in further research activities. In particular with regard to the components that experience a different corrosion exposure than one-month NSS as investigated here.

## 6.8 Acknowledgements

The authors express their sincere gratitude for the financial support of the research project “Influence of corrosive media on the fatigue strength of offshore wind turbines (CorroFAT)”, grant number 37 LN/1, of the Research Association for Steel Applications (FOSTA) e. V. funded by the German Federal Ministry of Economics and Climate Action (BMWK) via the German Federation of Industrial Research Associations "Otto von Guericke" (AiF) e. V on the basis of a resolution of the German Bundestag.

## 6.9 Appendix A

### Angular and linear misalignments and resulting bending stresses from clamping process

$$\text{Angular misalignment:} \quad \omega = |\omega_1 + \omega_2| = \left| \frac{h_2 - h_1 + h_3 - h_4}{f} \right| \quad (\text{A.1})$$

$$\text{Linear misalignment:} \quad e = \left| (h_2 - h_3) + (h_2 - h_3 + h_4 - h_1) * \frac{g}{f} + \frac{d_2 - d_1}{2} \right| \quad (\text{A.2})$$

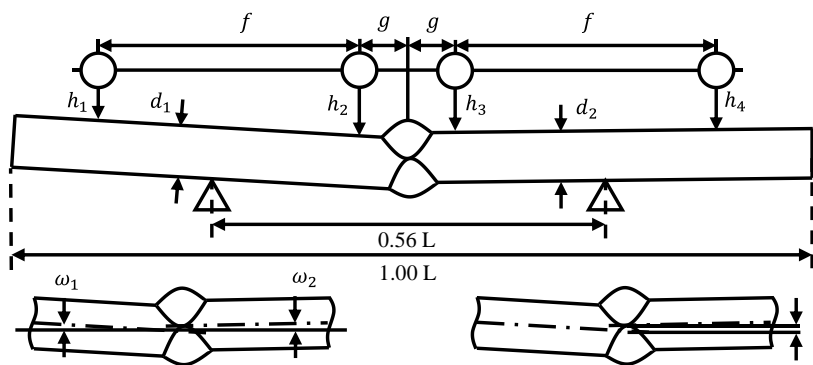


Figure 6-15: Misalignment equations according IIW [10]:

Table 6-4: Bending stresses from clamping process

Specimen No.	Offset w [mm]	Angular misalignment $\omega$ [°]	Linear misalignment e [mm]	Von Mises Stress [N/mm <sup>2</sup> ]
00-K-01	3.81	1.5	0	268
00-K-02	3.36	1.54	0	270
00-K-03	4.30	1.6	0	256
00-K-05	3.79	1.61	0	208
00-K-06	4.55	1.85	0	355
00-K-07	4.08	1.88	0	244
00-K-08	4.32	1.66	0	265
0-K-01	5.21	1.92	0	355
0-K-04	3.97	1.34	0	355
0-K-05	3.12	1.18	0	355
0-K-06	3.67	1.42	0	355
0-K-07	3.65	1.51	0	355
0-K-08	5.14	1.93	0	355
0-K-09	3.65	1.4	0	355
0-K-10	3.69	1.41	0	355
0-K-11	3.29	1.29	0	355
0-K-12	2.86	1.19	0	355
0-K-13	3.58	1.39	0	207
0-K-15	3.58	1.4	0	355
1-K-01	2.40	0.99	0	355
1-K-02	3.92	1.44	0	355
1-K-03	4.22	1.96	0	355
1-K-04	4.39	1.86	0	355
1-K-05	4.43	1.64	0	355
1-K-06	4.85	1.78	0	355
1-K-07	3.89	1.56	0	355
1-K-08	5.92	2.2	0	355
1-K-09	3.20	1.88	0	355
1-K-10	3.58	0.96	0	355
1-K-13	4.15	1.49	0	355

Specimen No.	Offset w [mm]	Angular misalignment $\omega$ [°]	Linear misalignment e [mm]	Von Mises Stress (Normal stress) [N/mm <sup>2</sup> ]
00-S-01	3.33	1.36	0.01	265
00-S-05	3.35	1.19	0.09	143
00-S-06	2.76	1.09	0.09	111
00-S-07	2.46	0.93	0.12	89
00-S-08	2.19	0.8	0.15	95
00-S-09	1.83	0.68	0.13	132
00-S-10	1.40	0.52	0.06	(-98)
0-S-01	3.14	1.12	0.44	158
0-S-03	0.36	0.5	0.23	16
0-S-04	3.48	1.21	0.48	212
0-S-07	2.09	1.02	0.35	115
0-S-09	3.67	1.39	0.25	171
0-S-10	3.18	1.1	0.48	225
0-S-11	1.31	0.49	0.19	(-35)
0-S-12	3.52	1.78	1.03	181
0-S-13	1.86	1.22	0.39	160
0-S-15	0.38	0.33	0.18	25
1-S-02	1.79	1.17	0.39	105
1-S-07	5.26	2.17	1.13	355
1-S-08	2.62	1.33	0.37	250
1-S-09	2.29	0.8	0.31	185
1-S-10	4.55	1.83	0.06	355
1-S-12	4.96	2.13	0.66	345
1-S-13	1.85	1	0.81	180
1-S-14	1.53	1	0.14	189
1-S-15	1.19	0.44	0.28	150
1-S-16	1.55	0.55	0.61	132



## 6.10 References

- [1] Det Norske Veritas - Germanischer Lloyd. Fatigue design of offshore steel structures(DNV-GL RP-C203); 2019.
- [2] Bundesanstalt für Wasserbau. Merkblatt: Bewertung der Tragfähigkeit bestehender Verschlüsse im Stahlwasserbau (TbVS); 2018.
- [3] Revie RW, Uhlig HH. Corrosion and corrosion control: An introduction to corrosion science and engineering. Hoboken, New Jersey: Wiley-Interscience a John Wiley & Sons Inc. Publication; 2008.
- [4] Marcus P. Corrosion mechanisms in theory and practice. 3rd ed. Boca Raton, Fla.: CRC Press; 2012.
- [5] Farajian M, Nitschke-Pagel T. Residual stress relaxation in welded large components. *Materials Testing* 2015;57(9):750–4. <https://doi.org/10.3139/120.110773>.
- [6] McClung RC. A literature survey on the stability and significance of residual stresses during fatigue. *Fatigue & Fracture of Engineering Materials & Structures* 2007;30(3):173–205. <https://doi.org/10.1111/j.1460-2695.2007.01102.x>.
- [7] Hensel J, Eslami H, Nitschke-Pagel T, Dilger K. Fatigue Strength Enhancement of Butt Welds by Means of Shot Peening and Clean Blasting. *Metals* 2019;9(7):744. <https://doi.org/10.3390/met9070744>.
- [8] Guilemany JM, Llorca-Isern N, Szabo PJ. Residual stress characterisation of grit blasted steel surfaces. *Surface Engineering* 1996;12(1):77–9. <https://doi.org/10.1179/sur.1996.12.1.77>.
- [9] Gericke A, Glienke R. Untersuchung des Reinigungsstrahlens als Nahtnachbehandlungsmethode zur Verbesserung der Schwingfestigkeit geschweißter Strukturen. *DVS*;2018.
- [10] Hobbacher AF. Recommendations for Fatigue Design of Welded Joints and Components. Cham: Springer International Publishing; 2016.
- [11] Radaj D, Sonsino CM, Fricke W. Fatigue assessment of welded joints by local approaches. 2nd ed. Cambridge: Woodhead Publ. [u.a.]; 2006.
- [12] Yildirim HC, Marquis GB, Barsoum Z. Fatigue assessment of high frequency mechanical impact (HFMI)-improved fillet welds by local approaches. *International Journal of Fatigue* 2013;52:57–67. <https://doi.org/10.1016/j.ijfatigue.2013.02.014>.
- [13] T. Nykänen and T. Björk. A new proposal for assessment of the fatigue strength of steel butt-welded joints improved by peening (HFMI) under constant amplitude tensile loading.
- [14] Ramberg W, Osgood WR. Description of stress-strain curves by three parameters. Washington D.C.: National Advisory Committee for Aeronautics; 1943.
- [15] Ahola A, Lipiäinen K, Afkhami S, Lilja H, Björk T. Fatigue performance of the welded details of an old, demolished steel railway bridge. *Engineering Structures* 2022;256:113966. <https://doi.org/10.1016/j.engstruct.2022.113966>.

- [16] Shojai S, Brömer T, Ghafoori E, Woitzik C, Braun M, Köhler M et al. Assessment of corrosion fatigue in welded joints using 3D surface scans, digital image correlation, hardness measurements, and residual stress analysis. *International Journal of Fatigue* 2023;176:107866. <https://doi.org/10.1016/j.ijfatigue.2023.107866>.
- [17] International Standards Organization. ISO 9227: Corrosion tests in artificial atmospheres – Salt spray tests. Berlin: Beuth; 2017.
- [18] Shojai S, Schaumann P, Momber A, Ghafoori E. Fatigue stress concentrations analysis of real corroded steel structures based on replica imprints. *ce papers* 2023;6(3-4):2527–33. <https://doi.org/10.1002/cepa.2568>.
- [19] Radaj D, Vormwald M. Ermüdungsfestigkeit: Grundlagen für Ingenieure. 3rd ed. Berlin, Heidelberg: Springer-Verlag Berlin Heidelberg; 2007.
- [20] Neuber H. Kerbspannungslehre: Grundlagen für genaue Festigkeitsberechnung mit Berücksichtigung von Konstruktionsform und Werkstoff. Berlin, Heidelberg, s.l.: Springer Berlin Heidelberg; 1958. <https://doi.org/10.1007/978-3-642-53069-2>.
- [21] Peterson R. Notch sensitivity. *Metal Fatigue* 1959:293–306.
- [22] Neuber H. Über die Berücksichtigung der spannungskonzentration bei festigkeitsberechnungen; 1968.
- [23] Bellett D, Taylor D, Marco S, Mazzeo E, Guillois J, Pircher T. The fatigue behaviour of three-dimensional stress concentrations. *International Journal of Fatigue* 2005;27(3):207–21. <https://doi.org/10.1016/j.ijfatigue.2004.07.006>.
- [24] Radaj D, Lazzarin P, Berto F. Generalised Neuber concept of fictitious notch rounding. *International Journal of Fatigue* 2013;51:105–15. <https://doi.org/10.1016/j.ijfatigue.2013.01.005>.
- [25] Taylor D. The theory of critical distances: A new perspective in fracture mechanics. Amsterdam, London: Elsevier; 2010.
- [26] Karakas Ö, Morgenstern C, Sonsino CM. Fatigue design of welded joints from the wrought magnesium alloy AZ31 by the local stress concept with the fictitious notch radii of  $r_f = 1.0$  and 0.05 mm. *International Journal of Fatigue* 2008;30(12):2210–9. <https://doi.org/10.1016/j.ijfatigue.2008.05.017>.
- [27] Karakaş Ö, Baumgartner J, Susmel L. On the use of a fictitious notch radius equal to 0.3 mm to design against fatigue welded joints made of wrought magnesium alloy AZ31. *International Journal of Fatigue* 2020;139:105747. <https://doi.org/10.1016/j.ijfatigue.2020.105747>.
- [28] Askes H, Livieri P, Susmel L, Taylor D, Tovo R. Intrinsic material length, Theory of Critical Distances and Gradient Mechanics: analogies and differences in processing linear-elastic crack tip stress fields. *Fatigue Fract Engng Mater Struct* 2013;36(1):39–55. <https://doi.org/10.1111/j.1460-2695.2012.01687.x>.
- [29] Peerlings RH, Borst R de, Brekelmans WAM, Vree JHP de. Computational Modelling of Gradient-Enhanced Damage for Fracture and Fatigue Problems. In: Owen DRJ, Oñate E, editors.

Computational plasticity: Fundamentals and applications ; proceedings of the fourth international conference held in Barcelona, Spain, 3th - 6th April, 1995 ; [a book in memoriam of Juan Carlos Simo. Swansea: Pineridge Press; 1995, p. 975–986.

- [30] Peerlings RHJ, Brekelmans WAM, Borst R de, Geers MGD. Gradient-enhanced damage modelling of high-cycle fatigue. *Int. J. Numer. Meth. Engng.* 2000;49(12):1547–69.
- [31] Borst R de, Pamin J, Peerlings RHJ, Sluys LJ. On gradient-enhanced damage and plasticity models for failure in quasi-brittle and frictional materials. *Computational Mechanics* 1995;17(1-2):130–41. <https://doi.org/10.1007/s004660050098>.
- [32] Tovo R, Livieri P, Benvenuti E. An implicit gradient type of static failure criterion for mixed-mode loading. *Int J Fract* 2006;141(3-4):497–511. <https://doi.org/10.1007/s10704-006-9011-z>.
- [33] Tovo R, Livieri P. An implicit gradient application to fatigue of sharp notches and weldments. *Engineering Fracture Mechanics* 2007;74(4):515–26. <https://doi.org/10.1016/j.engfrac-mech.2006.06.009>.
- [34] Tovo R, Livieri P. An implicit gradient application to fatigue of complex structures; 2008.
- [35] Sonsino CM. Multiaxial fatigue of welded joints under in-phase and out-of-phase local strains and stresses. *International Journal of Fatigue* 1995;17(1):55–70. [https://doi.org/10.1016/0142-1123\(95\)93051-3](https://doi.org/10.1016/0142-1123(95)93051-3).
- [36] Smith K, Watson P, Topper T. A stress–strain function for the fatigue of metals (stress-strain function for metal fatigue including mean stress effect)-1970. *Journal of Materials* 1970;1970.
- [37] Karakas Ö. Consideration of mean-stress effects on fatigue life of welded magnesium joints by the application of the Smith–Watson–Topper and reference radius concepts. *International Journal of Fatigue* 2013;49:1–17. <https://doi.org/10.1016/j.ijfatigue.2012.11.007>.
- [38] Nykänen T, Björk T. Assessment of fatigue strength of steel butt-welded joints in as-welded condition – Alternative approaches for curve fitting and mean stress effect analysis. *Marine Structures* 2015;44:288–310. <https://doi.org/10.1016/j.marstruc.2015.09.005>.
- [39] Bäumel A, Seeger T. *Materials data for cyclic loading: Supplement 1*. Amsterdam: Elsevier; 1990.
- [40] G. Masing. *Eigenspannungen und Verfestigung beim Messing*.
- [41] Haibach E. *Betriebsfestigkeit: Verfahren und Daten zur Bauteilberechnung*. 3rd ed. Berlin: Springer; 2006.
- [42] Neuber H. *Kerbspannungslehre: Theorie der Spannungskonzentration ; genaue Berechnung der Festigkeit*. 4th ed. Berlin: Springer; 2001.
- [43] Lener G, Lang R, Ladinek M, Timmers R. A numerical method for determining the fatigue strength of welded joints with a significant improvement in accuracy. *Procedia Engineering* 2018;213:359–73. <https://doi.org/10.1016/j.proeng.2018.02.036>.

- [44] Lang R, Ladinek M, Lener G. Über die Anpassung eines fortschrittlichen Stützwirkungsansatzes für das Kerbspannungskonzept. *Stahlbau* 2017;86(6):470–82. <https://doi.org/10.1002/stab.201710494>.
- [45] Shojai S, Schaumann P, Ghafoori E. Micro-support effect consideration of corroded steel in fatigue analysis based on real surface geometry. (under review) 2023.
- [46] Woitzik C, Braun M, Ehlers S, Shojai S, Schaumann P. Fatigue assessment of offshore wind turbine support structures subjected to seawater. In: W. Ringsberg J, Guedes Soares C, editors. *Advances in the Analysis and Design of Marine Structures*. London: CRC Press; 2023, p. 521–528.
- [47] European Committee for Standardization. Eurocode 3 - Design of steel structures - Part 1-9: Fatigue(EN 1993-1-9); 2020.
- [48] Ahola A, Muikku A, Braun M, Björk T. Fatigue strength assessment of ground fillet-welded joints using 4R method. *International Journal of Fatigue* 2021;142:105916. <https://doi.org/10.1016/j.ijfatigue.2020.105916>.
- [49] Pavlina EJ, van Tyne CJ. Correlation of Yield Strength and Tensile Strength with Hardness for Steels. *J. of Materi Eng and Perform* 2008;17(6):888–93. <https://doi.org/10.1007/s11665-008-9225-5>.
- [50] Mehmanparast A, Brennan F, Tavares I. Fatigue crack growth rates for offshore wind monopile weldments in air and seawater: SLIC inter-laboratory test results. *Materials & Design* 2017;114:494–504. <https://doi.org/10.1016/j.matdes.2016.10.070>.

## 7 Conclusions and Outlook

The motivation for this work was to investigate the influence of corrosion on the fatigue strength of steel components in order to quantify the remaining service life of existing corroded structures and to potentially extend the service life, if the load-bearing reserves are not exploited. The utilization of the load-bearing reserves is only possible if sophisticated local fatigue approaches are applied, in which, in contrast to the global approaches, various fatigue-relevant effects can be investigated separately.

The investigations in this thesis can be divided between the investigations on steel plates made of base material, which were carried out within the framework of papers I-III, and the investigations on weld seams, carried out in the papers IV and V.

### 7.1 Investigations on corroded steel plates

The surface geometry has a significant influence on fatigue, especially in the case of pitting corrosion this can result in high stress concentrations. For this reason, in the first paper various methods of modelling the stress concentrations were investigated.

1. It was found that a double-pit model, in which two interacting pits are modelled, can describe the stress concentration on the steel surface with sufficient accuracy.
2. In addition, a 3D numerical model was established for the first time, using 3D scans of corroded steel by means of reverse engineering and investigated regarding their stress concentrations. The comparison with the double-pit model showed good agreement between both models.
3. Probabilistic distributions of stress concentrations could be established for both models, which allow a reliability-based analysis of fatigue strength.

In order to establish a relationship between the stress concentrations modelled in the first paper and the actual fatigue behaviour, fatigue tests were carried out on corroded specimens in the second paper. In addition, the specimens were previously transformed into a 3D-solid model using the reverse engineering procedure developed in the first paper and investigated numerically.

4. The fatigue tests have shown a higher slope and higher fatigue life endurance compared to the corresponding DNV curve C-Air for rolled plates with pitting corrosion in air. Moreover, the fatigue strength for the tested specimen were higher compared to butt welds according DNV, category C1 and D.
5. For the majority of specimens, the stress hotspots from numerical calculation matched with the actual crack location measured by digital image correlation (DIC), showing a leading impact of the notch effect on the fatigue resistance. In many cases the crack initiated from two overlapping pits, underlining the double-pit model proposed in the first paper.
6. In cases the crack location did not match with the stress concentration hotspot, the stress gradients along the thickness were greater, indicating an influence of the micro-support effect.

Although a qualitative correlation between high stress concentrations and crack initiation sites could be established from the fatigue tests, the micro-support effect had to be considered in order to establish a quantitative correlation between the notch stress concentration and the expected fatigue life. For this purpose, the implicit gradient model (IGM) approach was applied in the third paper, which allowed the micro-support effect to be considered for the entire specimen. In addition, the replica technique was investigated for the practical application.

7. The consideration of the micro-support effect according to IGM could predict crack locations from the fatigue test with high accuracy for a large number of specimens. For many specimens, where no match between numerical prediction and actual crack location existed, the location of the maximum notch stress shifted towards the crack location because of micro-support consideration.
8. A weighting factor was calibrated for IGM on the basis of the fatigue test results of the second paper. It could be shown, that for this weighting factor, the lowest scatter in the resulting notch stress fatigue curve and the highest conformity rate between the actual crack locations and the numerical predicted locations can be achieved.
9. A comparison with other methods for the micro-support consideration, such as theory of critical distance (TCD) methods, shows similar results for the fatigue strength as for IGM. But, unlike the IGM method, the highest conformity rate does not coincide with the lowest scatter of the notch stress fatigue curve.
10. The application of the widely used TCD-methods is not recommended for corroded specimens, as they have a high number of notches, which has to be exported and evaluated separately for each notch and are hence associated with much effort in the postprocessing.
11. The replica method was successfully applied to capture the surface geometry of corroded steel structures and converted into a 3D-solid model using reverse engineering. By applying the recommended weighting factor for micro-support consideration, the results showed a good match between the stress concentrations of the original and the replica. These results allow the above findings to be applied on real structures and calculate the fatigue driving stresses based on the real surface condition.

## 7.2 Investigations on corroded weld seams

Steel structures contain a great number of welded joints which, due to their geometry, already have high stress concentrations. In addition, residual stresses are present at welds, which must be considered in the calculation with local approaches. The influence of corrosion on welds requires therefore additional experimental investigations in order to quantify the influence of the individual effects. For this purpose, fatigue tests on fillet- and butt-welded specimens, which were pre-corroded in a salt spray chamber for one month, were performed. Additionally, fatigue tests on as-welded and clean blasted specimens were carried out as reference for the corroded tests. Moreover, 3D-surface scans and residual stress measurements for different specimen geometries and surface conditions were carried out.

1. The fatigue tests revealed that the fatigue strength of as-welded specimens was the lowest but remained within established guidelines. After clean blasting, the fatigue strength improved; however, subsequent corrosion led to a reduction in fatigue strength.
2. The differences in fatigue strength were mainly associated with the crack initiation stage, as shown by the crack detection with DIC, while the fatigue life in the crack propagation stage differed only marginally.
3. Surface roughness measurements showed that clean blasting led to higher roughness as in the as-welded condition, but did not increase further due to corrosion. The visible changes in the surface scans could be attributed to the changes in waviness, as the changes were caused by longer wavelengths.
4. Utilizing 3D scans, a digital surface analysis was conducted to compare conditions before and after corrosion exposure. This analysis revealed material removal in both the base metal area and at the weld toe, which is the critical location with regard to fatigue. This removal occurred across a considerable surface area and also manifested locally in the form of pitting.
5. Both, butt and fillet welds, showed geometrical changes due to the effects of clean blasting and corrosion. Clean blasting resulted in a decrease of stress concentrations, while corrosion led to an increase of stress concentrations back to the level observed in the initial as-welded condition. However, as the fatigue strength showed differences despite similar stress concentrations values, it became apparent that the stress concentrations are not the sole driving factor of the fatigue strength.
6. The residual stress measurements at the fatigue driving area of the weld toe have revealed the highest tensile residual stresses in the as-welded specimen, whereas the clean-blasted specimen displayed compressive residual stresses. The corrosion-induced material removal reduced the initially applied compressive stresses on the surface, resulting in relatively minor tensile residual stresses. Nevertheless, these residual tensile stresses were significantly lower than those observed in the as-welded specimens. This provided a clear correlation with the different fatigue strengths from the test.

In order to take these findings into account for the prediction of the fatigue strength, the fatigue tests were evaluated with local fatigue approaches in the fifth paper. For this purpose, the entire specimen geometry was transformed into a numerical 3D-model using the previous 3D-scans and the reverse engineering method. This made it possible to consider both the weld seam, including changes due to corrosion, and imperfections such as misalignments. The IGM was used to account for the micro-support effect and the residual stresses were acknowledged by the mean stress correction factor according to Smith-Watson-Topper (SWT).

7. The stress analysis demonstrated that the global stress magnification due to misalignments and stress concentrations from the weld geometry partly had opposing impacts on the stresses. Hence, it was necessary to account for their combined effect on one single numerical model. If these effects were considered separately and then superimposed, it would have resulted in either an overestimation or underestimation of the actual stress, increasing the scatter of the resulting SN-curves.

8. The examination of bending stresses resulting from the clamping procedure indicated high stresses at the weld toe for butt-welded specimens. For fillet-welded specimens the stresses even reached the yield point. Thus, in fatigue analysis the stresses from the clamping process should not be neglected.
9. With consideration of the effective notch stresses, the scatter in the SN-curve for all specimens could be reduced. Further reduction could be achieved by considering the residual stresses and the bending stresses from clamping.
10. Despite a low scatter, a noticeable distinction among the as-welded, clean blasted - uncorroded, and clean blasted - corroded specimens remains. This arises from the material properties at the surface, which differs for each series of specimens.
11. The crack location measured by DIC and the hotspot of stress concentrations from the numerical analysis have shown good agreement for most specimens and thus underlined the approach.

### 7.3 Outlook

Despite new findings, the investigations carried out in the framework of this thesis have shown that there is still a need for further research.

One of the future research areas is the accelerated corrosion process in a salt spray chamber and its correlation to real environmental condition, as in this study the welded specimens were exposed to artificial environmental condition in a salt spray chamber. In order to transfer the results of the fatigue tests and all other investigations to real structures, the correlation has to be examined.

Different types of investigations carried out in this thesis, such as 3D scans, hardness measurements and residual stress measurements, represent only a snapshot of the time they were carried out. Due to the degradation process, the surface geometry changes over time, which in the case of welded specimens may also involve changes in the residual stresses. Therefore, the development of the relevant parameters such as the surface geometry and the residual stresses over time needs further investigation.

Besides the change of the residual stresses resulting from the degradation process, the residual stresses also change due to cyclic loading. This has already been shown in some publications on welded joints, without considering the influence of corrosion. More detailed analyses for corroded welded joints in the future are needed.

It is known from the literature that corrosion, in addition to changing the surface geometry, also changes the near-surface material by increasing its brittleness. Using local methods, the embrittlement can be considered with the micro-support effect via the weighting factor  $a$ , which is coupled to the intrinsic material length  $L$ . This in turn depends on the fatigue crack propagation threshold  $\Delta K_{th}$  and the fatigue limit  $\Delta\sigma_0$  of the base material. In the investigations in paper III, the parameter  $a$  was calibrated based on the minimization of the scatter in the notch stress SN-curve, while in paper V an equal value of  $a = 0.01 \text{ mm}^2$  was assumed for all specimens (as-welded, clean-blasted and corroded material). A realistic consideration of the near-surface material, however, can only be achieved via



the material parameters  $\Delta K_{th}$  and  $\Delta\sigma_0$ , which have to be derived for corroded material in the context of future research. In this context, the corresponding values for clean-blasted and clean-blasted corroded material can also be derived.

Finally, it is worth pointing out that all investigations were carried out on pre-corroded specimens, where the simultaneous influence of corrosion and fatigue was not considered. However, it is known from the literature that the simultaneous exposure to corrosion and cyclic loading leads to a lower fatigue strength than separate exposure. The reason for this is the time component of corrosion, which cannot be accelerated in the same magnitude as it is done with cyclic loading. Future research should therefore focus on reducing the time component to the change in surface geometry and embrittlement of the material, in order to decouple the experimental and numerical investigations from the time component.



## 8 Lists

### 8.1 List of Figures

Figure 1-1: Examples of corroded steel structures.....	1
Figure 1-2: Definition of stresses in accordance with [28–30].....	3
Figure 1-3: Analysis of effective notch stress according EC [27], DNV [28], and IIW [29] using a fictitious notch radius.....	4
Figure 1-4: (a) SN-curves for butt-welded plates (Curve D) for different environments according DNV [28], (b) diagram of ERF-values for welded plates and tubular joints for free corrosion environment according [32]. .....	5
Figure 1-5: Definition of the intrinsic material length $L$ according Taylor [54].....	8
Figure 1-6: Illustration of TCD-methods, (a) point method, (b) line method, (c) volume method and (d) Radaj 1 mm method .....	9
Figure 1-7: Haigh-diagram.....	11
Figure 1-8: Mean stress effect according IIW .....	11
Figure 1-9: Procedure of calculating the local mean stress ratio $R_{local}$ .....	12
Figure 1-10: Schematic overview of the thesis .....	14
Figure 2-1: Schematic overview of the investigated models and the associated workflow steps .....	28
Figure 2-2: High resolution shot of a corroded sample .....	30
Figure 2-3: Examples for double pits on the real corroded surface scanned in high resolution .....	31
Figure 2-4: Frequency diagram for pit depth (left) and pit width ratio (right) .....	32
Figure 2-5: Faceted 3D-scan of corroded sample with ATOS Core in STL-format (left) and original (right) .....	32
Figure 2-6: Numerical model of single-pit (left) and double-pit (right) with corresponding stress concentrations (von Mises stress in [Pa]).....	33
Figure 2-7: Correlation between pit depth and pit ratio for original data (left) and generated data (right) for the Monte-Carlo simulation .....	34
Figure 2-8: Realization of random field (left) and calibrated random field, model 1 (right) ...	36
Figure 2-9: Extraction of pit number and radius of model 1 (upper left) and real surface (lower left) with matlab tool and frequency plot for 50 samples for real surface and random fields (right).....	36

Figure 2-10: Random field (model 2) calibrated on 5%-quantile radius (left) and frequency plot for 50 samples for real surface and random fields (right) .....	37
Figure 2-11: Numerical model of random field, model 1 (upper), model 2 (lower) and corresponding stress concentrations (von Mises stress in [Pa]) .....	37
Figure 2-12: NURBS-surface of a 20x20mm sample with grid rate 10 (left) and grid rate 50 (right).....	38
Figure 2-13: Numerical model of real corroded samples with solid model (left), mesh (middle) and result plot of stress concentrations (right) for 40x40mm (upper) and 20x20mm (lower) sample size.....	38
Figure 2-14: Stress concentrations for a wide pit $a=1.60$ (upper) and narrow pit $a=0.70$ (lower) .....	39
Figure 2-15: Stress concentration against pit depth (left) and pit ratio (right) .....	39
Figure 2-16: Stress concentration as a function of overlapping distance and pit ratio (left) and overlapping distance and pit depth (right).....	40
Figure 2-17: Correlation matrix of random field parameters.....	41
Figure 2-18: Random fields with varying KL-terms and correlation length .....	42
Figure 2-19: Results of numerical investigation of the single-pit model, frequency plot (left) and PDF/CDF plot (right).....	42
Figure 2-20: Results of the Monte-Carlo simulation .....	43
Figure 2-21: Correlation matrix from the Monte-Carlo simulation.....	44
Figure 2-22: Results of numerical investigation of random fields.....	45
Figure 2-23: Exemplary results of 50 numerical simulation of 40x40mm real corroded surfaces .....	46
Figure 2-24: Results of numerical investigation of 40x40mm samples with real corroded surface .....	47
Figure 2-25: Results of numerical investigation of 20x20mm samples with real corroded surface .....	47
Figure 2-26: CDF of stress concentration for all models and 95%-quantile values .....	48
Figure 3-1: Geometry of fatigue test specimen.....	58
Figure 3-2: Fatigue test setup.....	59
Figure 3-3: Force-displacement diagram for static and dynamic test.....	60
Figure 3-4: Specimen preparation for DIC, white sprayed surface .....	60
Figure 3-5: 3D-scan with Keyence VR-3000 .....	61

Figure 3-6: High resolution shots of a corroded sample from all sides .....	62
Figure 3-7: Assembling the scans into a 3D-model as STL-data. ....	63
Figure 3-8: Faceted 3D-model in STL-format with non-continuous surface in a) and b). Solid model with NURBS-patches with continuous surface in c) and d) - both for specimen P.01 .....	64
Figure 3-9: Specimen P.01 a) cross section A at maximum stress concentration, b) solid 3D-model, c) initial surface mesh of solid model, d) results of numerical simulation, e) maximum stress concentration before convergence study .....	65
Figure 3-10: Specimen P.01, adaptive convergence study applied on in the area of maximum stress concentrations. a) refined surface mesh at last stage, b) converged stress concentration c) convergence plot.....	66
Figure 3-11: Impact of mesh element size on surface description for 0.2mm (a), 1.0mm (b) and 1.8mm (c).....	66
Figure 3-12: Fatigue test results for different R-ratios and corresponding 50%-quantile S-N curves.....	68
Figure 3-13: Fatigue test results for different R-ratios and corresponding 97.7%-quantile S-N curves.....	68
Figure 3-14: Haigh-diagram for fatigue life endurance $N=5 \times 10^5$ .....	69
Figure 3-15: Comparison of test data to design S-N curves from DNV .....	69
Figure 3-16: DIC plot for crack initiation, crack propagation and fracture of Spec. No. 07 ....	70
Figure 3-17: Frequency plot for the ratio of cycles until crack initiation to total cycles (a) and relationship between crack initiation ratio and the corresponding stress level (b) .....	71
Figure 3-18: Comparison of DIC results with numerical determined stress concentration results for specimen No. 01 – coincidence level 1 .....	72
Figure 3-19: Comparison of DIC results with numerical determined stress concentration result for specimen No. 05 – coincidence level 2 .....	73
Figure 3-20: Specimens of coincidence level 1 with corresponding crack location and max. stress concentrations location (red banner) .....	75
Figure 3-21: Specimens of coincidence level 2 with corresponding crack location (blue banner) and max. stress concentrations location (red banner) .....	76
Figure 3-22: Stress concentrations from numerical analysis of all specimens with corresponding stress concentrations at the crack location.....	77
Figure 3-23: Frequency plot of stress concentrations from numerical analyses of all specimens .....	77

Figure 3-24: Frequency plot of stress concentration ratio $r_\alpha$ .....	77
Figure 3-25: Stress concentration along the thickness for max. stress concentration and crack location .....	77
Figure 4-1: Illustration of TCD-methods, (a) point method, (b) line method, (c) area method and (d) volume method.....	91
Figure 4-2: Hardness measurement results, (a) cross section of tested specimen, (b) measured area, (c) hardness map .....	94
Figure 4-3: (a) Tested specimen geometry and (b) fatigue test setup from [2] .....	95
Figure 4-4: Fatigue test results from [2] for different R-ratios .....	96
Figure 4-5: Flowchart of numerical analysis using the IGM approach .....	96
Figure 4-6: Numerical model for structural-mechanical analysis of stress concentrations, a) solid 3D-model and boundary conditions, b) mesh before convergence study, c) cross section at crack location, d-f) elastic stress concentrations before convergence study .....	98
Figure 4-7: Maximum stress concentrations from numerical analysis of all specimens with the corresponding stress concentrations at the crack location from Shojai et al. [2] .....	99
Figure 4-8: Effective stress concentrations for different magnitudes of parameter a compared to initial stress concentrations from structural analysis.....	100
Figure 4-9: Effective stress concentrations $\alpha_f$ against parameter a for specimen Nos. 03 and 11 at different locations .....	101
Figure 4-10: Comparison of (a1-a4) DIC-shot with crack initiation, (b1-b4) elastic notch stresses (von Mises stress criterion) from structural analysis without consideration of micro-support effect, and (c1-c4, d4) effective notch stresses with consideration of micro-support-effect for a=0.01 – Conformity Levels 1 to 4 .....	102
Figure 4-11: Comparison of maximum effective notch stresses and effective notch stresses at the crack location for conformity levels 1 to 4 with the governing effective stress concentration factors $\alpha_{f,cal}$ from based on calibration of parameter a....	105
Figure 4-12: Ratio $r_{\alpha,f}$ of the effective notch stresses at the crack location and maximum effective notch stress for conformity levels 1 to 4 .....	106
Figure 4-13: Notch stress SN-curves, (a) SN-curve based on effective notch stress ranges without micro-support consideration, (c) SN-curve based on effective notch stress ranges with micro support consideration for a=0.0045 .....	107
Figure 4-14: Scatter $T_\sigma$ and conformity rate in dependence of parameter a .....	108

- Figure 4-15: Results for the point method and the line method, (a) Scatter of  $T_{\sigma}$  and conformity rate as a function of the distance  $d^*$ /equivalent length  $\rho^*$ , (b) SN-curve based on effective notch stress ranges with micro support consideration for  $d^* = 0.04$  mm and  $\rho^* = 0.11$  mm.....109
- Figure 4-16: Comparison between original specimen and replica with (a1) image of original specimen, (a2) 3D-scan of original specimen, (b1) image of replica and (b2) 3D-scan of replica .....112
- Figure 4-17: Reverse Engineering from STL-data (a) and (d) to solid model (b) and (d) for the original specimen and the replica, with corresponding boundary condition in (c) and (f).....113
- Figure 4-18: (a1) to (d1) Elastic stress concentration based on von Mises stress criterion for the original and replica scan and for upper and lower side, and (a2) to (d2) effective stress concentration with consideration of the micro-support effect with a weighting factor  $a=0.0045$  mm<sup>2</sup> .....114
- Figure 5-1: Specimen geometries for base material (G), butt weld (S), and fillet weld (K) ..126
- Figure 5-2: Surface conditions of the specimen, (a) blasted surface with cleanliness grade Sa 3, (b) specimen after 1 month of NSS test, (c) specimen after rust removal ..127
- Figure 5-3: 3D-surface scans with ATOS Core 5M: (a) test setup, (b) scan of butt-welded specimen and (c) scan of fillet-welded specimen.....129
- Figure 5-4: (a) Geometrical weld parameters according ISO 5817 [16] and (b) Implementation in the MATLAB tool .....130
- Figure 5-5: Fatigue test setup, (a) test setup for butt-welded specimen, (b) butt-welded specimen with stochastic pattern, (c) DIC capturing frame .....131
- Figure 5-6: Technical crack definition in DIC: (a) high-resolution shot during fatigue testing of fillet-welded specimen with ARAMIS, (b) and (c) corresponding DIC strain plot, (d) displacement in axial direction, (e1) illustration of crack detection at technical crack stage, (e2) illustration of crack detection at propagated stage .....133
- Figure 5-7: Surface measurement results for (a) as-welded specimen, (b) clean blasted – uncorroded specimen and (c) clean blasted – corroded specimen .....134
- Figure 5-8: Results of surface scans for fillet welds, (a) scan without corrosion, (b) scan after one-month corrosion, (c) deviation plot of the surface scans, (d) deviation plot with deviation banners.....135
- Figure 5-9: Results of surface scans for butt welds, (a) scan without corrosion, (b) scan after one-month corrosion, (c) deviation plot of the surface scans, (d) deviation plot with deviation banners.....136

- Figure 5-10: Frequency plots for (a) radius, (b) the flank angle, and (c) the SCF for different specimen geometry and surface conditions .....137
- Figure 5-11: Macrographs and hardness values HV 0.1 for different surface conditions, (a1) to (c1) for as-welded specimen, (a2) to (c3) for clean blasted – uncorroded specimen, (a3) to (c3) for clean blasted – corroded specimen .....139
- Figure 5-12: Residual stress measurement with results for (a) transversal stresses and (b) for longitudinal stresses .....140
- Figure 5-13: Fatigue test results: (a1) to (a3) without consideration of misalignment and (b1) to (b3) with consideration of misalignment .....143
- Figure 5-14: DIC results for butt and fillet welds with different surface conditions, (a) crack initiation lifetime, (b) crack propagation lifetime and (c) crack initiation ratio  $r_c$  as a function of the stress range.....145
- Figure 6-1: Notch stress analysis methods(a) point method, (b) line method, (c) area/volume method, summarized in [28] and (d) Radaj 1 mm method [24]However, all presented methods show deficiencies when the effective stresses shall be investigated on the basis of a real 3D geometry. The application of 1 mm approach of Radaj requires a change of geometry, which is not possible for 3D-models. The analysis with PM, LM, and VM is possible, but requires a lot of post processing because of the great number of notches in real corroded geometries, requiring all the stress paths to be evaluated individually. ....161
- Figure 6-2: Procedure of calculating the local mean stress ratio  $R_{local}$  (a) illustration of load steps in fatigue tests and (b) resulting stress-strain behaviour at the notch base with typical hysteresis .....163
- Figure 6-3: (a) Specimen geometries for butt weld (S) and fillet weld (K), (b) Fatigue test and DIC-system setup .....164
- Figure 6-4: Fatigue test results for as-welded, clean blasted – uncorroded and clean blasted – corroded specimens with corresponding scattering of the SN-curve for (a) butt welds and (b) fillet welds .....165
- Figure 6-5: Reverse engineering procedure shown exemplarily for a corroded butt-welded specimen , (a) scanning of the whole specimen with ATOS Core 300, (b) scanning of the welded area with Keyence VR-3000 with higher resolution than in (a), (c) STL-geometry as result of ATOS Core 300, (d) result of the welded area from Keyence VR-3000, (e) assembled STL- model from (c) and (d), (f) generation of a NURBS-patch based on the STL-model, (g) generated NURBS-patch, (h) 3D-solid model assembled from individual NURBS-patches .....167
- Figure 6-6: Numerical 3D-model of a fillet welded specimen in corroded condition , (a1-a3) 3D-solid model after reverse engineering process and generation of NURBS-



- patches, (b1-b3) discretization of the solid model with different element lengths for weld toe and base material area .....168
- Figure 6-7: Numerical analysis of the clamping process, (a) 3D-model with angular misalignment and the resulting offset at the lower side of the specimen (compared to the plain line), (b) straightened 3D-model after application of the offset  $u_z$ , (c-e) resulting von Mises stresses from the clamping process with nonlinear material definition for the whole specimen and the weld area.....169
- Figure 6-8: Numerical analysis of stress concentrations based on linear elastic material definition, (a) straightened 3D-model from clamping process with corresponding boundary conditions, (b-c) resulting von Mises stresses for the whole specimen and (d-e) at the weld area .....170
- Figure 6-9: Effective stress concentrations  $\alpha_f$  in dependence of the weighting factor  $a$  for specimen No. 1-K-1 .....171
- Figure 6-10: Comparison of DIC results for different load cycles (a1-f1) with numerical determined stress concentration (a2-g2) for corroded fillet weld specimen no. 1-K-03 .....173
- Figure 6-11: Comparison of DIC results for different load cycles (a1-f1) with numerical determined stress concentration (a2-g2) for corroded butt weld specimen no. 1-S-09 .....174
- Figure 6-12: SN-curves based on 4R-method for (a1-a3) butt welded joints, and (b1-b3) for fillet welded joints .....176
- Figure 6-13: Evaluation of all data based on (a) nominal stresses, (b) notch stresses without consideration of bending and residual stresses, (c) mean stress corrected notch stresses with consideration of bending and residual stresses, and (d) comparison of obtained SN-curve from this study to existing master curves for butt and fillet welds. ....177
- Figure 6-14: Replica technique applied on corroded fillet-welded specimen, (a,b) corroded welded specimen, (c) original specimen, (d) original scan, (e) replica imprint, (f) replica scan .....180
- Figure 6-15: Misalignment equations according IIW [10]: .....182

## 8.2 List of Tables

Table 2-1: Statistical evaluation of the geometric pit data.....	31
Table 2-2: Input parameters for Monte-Carlo simulation.....	34
Table 2-3: Input data of 20 simulations and the corresponding stress concentrations .....	34
Table 2-4: Statistical Data for stress concentration distribution of random fields.....	45
Table 2-5: Statistical Data for stress concentration distribution for real corroded surfaces .....	45
Table 2-6: Comparison of stress concentration for different models.....	48
Table 3-1: Mechanical properties from tensile tests by Biglu [38].....	58
Table 3-2: Fatigue testing scope .....	59
Table 3-3: S-N curve parameters .....	68
Table 3-4: Detail categories according to DNV.....	69
Table 3-5: Fatigue test results .....	79
Table 3-6: Results of DIC measurements .....	80
Table 3-7: Stress concentrations from numerical analysis.....	81
Table 4-1. Four different conformity levels suggested in this study. ....	101
Table 4-2: Fatigue curve parameter resulting from different methods for micro-support consideration .....	109
Table 4-3: Weighting parameter from literature for low alloy mild steel compared to result of this study.....	110
Table 5-1: Test matrix including different surface conditions and weld types.....	126
Table 5-2: Mean values for surface measurements.....	134
Table 5-3: Fatigue curve parameter .....	142
Table 5-4: Statistical results of radius, flank angle, and corresponding stress concentrations for different surface conditions .....	148
Table 5-5: Fatigue test data and DIC results.....	149
Table 6-1: Material properties S 355 ML .....	164
Table 6-2: Match of crack location and numerical prediction .....	173
Table 6-3: Comparison of nominal stress curves with mean stress corrected notch stress curves.....	175
Table 6-4: Bending stresses from clamping process.....	182

## **Eidesstaatliche Erklärung**

Hiermit erkläre ich, Mohammad Sulaiman Shojai, geboren am 27.09.1991, wohnhaft in Bothfelder Straße 32 in 30916 Isernhagen, dass ich die nachfolgenden Punkte im Zusammenhang mit meiner Dissertation einhalte und bestätige:

- a) Ich erkläre, dass ich die Regeln der geltenden Promotionsordnung der Leibniz Universität vollständig kenne und diese in vollem Umfang eingehalten habe. Ich bin damit einverstanden, meine Dissertation gemäß den Bestimmungen der Promotionsordnung zu prüfen.
- b) Ich bestätige, dass ich meine Dissertation selbstständig verfasst habe. Alle Textabschnitte, die nicht von mir stammen, wurden ordnungsgemäß gekennzeichnet und als Zitate oder Paraphrasen aus fremden Quellen gekennzeichnet. Ich habe alle von mir in meiner Arbeit benutzten Hilfsmittel und Quellen in meinem Literaturverzeichnis ordnungsgemäß angegeben.
- c) Ich versichere, dass ich weder unmittelbar noch mittelbar geldwerte Leistungen an Dritte für Vermittlungstätigkeiten oder für die inhaltliche Ausarbeitung meiner Dissertation erbracht habe. Das bedeutet, dass meine wissenschaftliche Arbeit weder in Teilen noch in ihrer Gesamtheit von Dritten gegen Entgelt oder sonstige Gegenleistungen erworben oder vermittelt wurde.
- d) Ich habe meine Dissertation noch nicht als Prüfungsarbeit für eine staatliche oder andere wissenschaftliche Prüfung eingereicht. Diese Arbeit ist meine originäre wissenschaftliche Leistung und wurde nicht zuvor für andere Prüfungen verwendet.
- e) Ich erkläre, dass ich keine gleiche oder in wesentlichen Teilen ähnliche Arbeit bei einer anderen Hochschule als Dissertation eingereicht habe.

Mohammad Sulaiman Shojai, Hannover, 24.10.2023

## Curriculum Vitae

Name: Mohammad Sulaiman Shojai  
Date of birth: 27.09.1991  
Place of birth: Kabul, Afghanistan

### Education

2010: Abitur, Söderblom Gymnasium Espelkamp, Germany  
2010 – 2013: Bachelor of Science, Civil Engineering,  
Technische Universität Braunschweig, Germany  
2013 – 2016: Master of Science, Civil Engineering  
Technische Universität Braunschweig, Germany

### Professional Experience

2016 – 2019: Structural Engineer, Engineering Office Dr. Binnewies,  
Hamburg, Germany  
Since 2019: Research Associate at Institute for Steel Construction,  
Leibniz University Hannover, Germany

### Journal Papers:

1. Shojai, Sulaiman; Brömer, Tim; Ghafoori, Elyas; Schaumann, Peter (2023): Application of local fatigue approaches on corroded welded joints with consideration of weld geometry and residual stresses. In: *Theoretical and Applied Fracture Mechanics*, S. 104215. DOI: 10.1016/j.tafmec.2023.104215.
2. Shojai, Sulaiman; Schaumann, Peter; Ghafoori, Elyas (2024): Micro-support effect consideration in fatigue analysis of corroded steel based on real surface geometry. In: *Journal of Constructional Steel Research* 212, S. 108259. DOI: 10.1016/j.jcsr.2023.108259.
3. Shojai, Sulaiman; Brömer, Tim; Ghafoori, Elyas; Woitzik, Christian; Braun, Moritz; Köhler, Markus; Schaumann, Peter (2023): Assessment of corrosion fatigue in welded joints using 3D surface scans, digital image correlation, hardness measurements, and residual stress analysis. In: *International Journal of Fatigue* 176, S. 107866. DOI: 10.1016/j.ijfatigue.2023.107866.

4. Shojai, Sulaiman; Schaumann, Peter; Braun, Moritz; Ehlers, Sören (2022): Influence of pitting corrosion on the fatigue strength of offshore steel structures based on 3D surface scans. In: *International Journal of Fatigue* 164, S. 107128. DOI: 10.1016/j.ijfatigue.2022.107128.
5. Shojai, Sulaiman; Schaumann, Peter; Brömer, Tim (2022): Probabilistic modelling of pitting corrosion and its impact on stress concentrations in steel structures in the offshore wind energy. In: *Marine Structures* 84, S. 103232. DOI: 10.1016/j.marstruc.2022.103232.
6. Momber, A. W.; Nattkemper, T. W.; Langenkämper, D.; Möller, T.; Brün, D.; Schaumann, P.; Shojai, S. (2022): A data-based model for condition monitoring and maintenance planning for protective coating systems for wind tower structures. In: *Renewable Energy* 186, S. 957–973. DOI: 10.1016/j.renene.2022.01.022.
7. Momber, Andreas; Nattkemper, Tim; Langenkämper, Daniel; Möller, Torben; Brün, Daniel; Schaumann, Peter; Shojai, Sulaiman (2021): Digitalisierung und Verarbeitung von Sensordaten für die Zustandsbewertung von Oberflächenschutzsystemen stählerner Türme von Onshore-Windenergieanlagen. In: *Stahlbau*. DOI: 10.1002/stab.202100020.

#### Conference Papers:

1. Shojai, Sulaiman; Schaumann, Peter; Momber, Andreas; Ghafoori, Elyas (2023): Fatigue stress concentrations analysis of real corroded steel structures based on replica imprints. In: *ce papers* 6 (3-4), S. 2527–2533. DOI: 10.1002/cepa.2568.
2. Woitzik, C.; Braun, M.; Ehlers, S.; Shojai, S.; Schaumann, P. (2023): Fatigue assessment of offshore wind turbine support structures subjected to seawater. In: J. W. Ringsberg und C. Guedes Soares (Hg.): *Advances in the Analysis and Design of Marine Structures*. London: CRC Press, S. 521–528.